Coherent transfer of Ultracold Molecules: From weakly to deeply bound

Dissertation
zur Erlangung des akademischen Grades
Doktor der Naturwissenschaften

eingereicht an der

Fakultät für Mathematik, Informatik und Physik
der Universität Innsbruck

von

Florian Lang

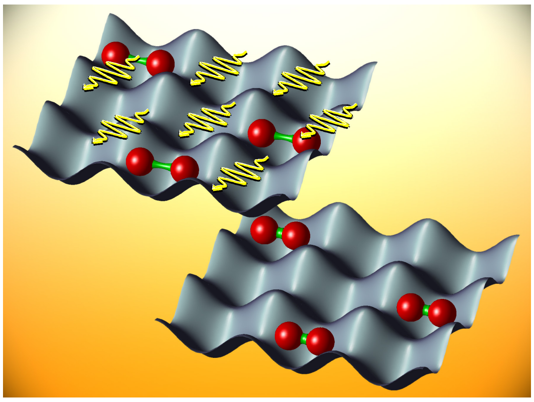

unter der Betreuung von
Univ.-Prof. Dr. Johannes Hecker Denschlag
Institut für Experimentalpyhsik

Innsbruck, Juni 2009

Abstract

In this thesis I report the coherent transfer of ultracold molecules from weakly to deeply bound states using two different techniques. While these transfers allow the manipulation of the internal quantum state of the molecules, their external state is determined by confining them in an optical lattice. This gives ultimate control over all molecular degrees of freedom and opens the way towards controlled quantum chemistry.

Our experiments start from an atomic Bose-Einstein condensate of ^{87}Rubidium that is loaded into a three-dimensional optical lattice. A pure sample of diatomic molecules is formed by ramping over a magnetic Feshbach resonance at 1007.4 G, and removing the remaining unbound atoms. These very weakly bound Feshbach molecules are transferred to more deeply bound states with two different methods.

We have developed a novel transfer scheme based on the combination of a radio frequency pulse with an adiabatic ramp of the magnetic bias field. Using this method, molecules can be transferred across avoided crossings of different molecular states with an efficiency of more than 99%. The broad applicability of this scheme is demonstrated by bringing the Feshbach molecules from a magnetic field of more than 1000 G to 0 G with a series of nine radio frequency transfers. The molecular binding energy thereby increases from 24 MHz$\times h$ to about 3.6 GHz$\times h$.

In order to transfer the Feshbach molecules to deeply bound states we use STimulated Raman Adiabatic Passage (STIRAP), an optical Raman transfer scheme. Feshbach molecules are transferred with an efficiency of close to 90% into the rovibrational ground state of the $a^3\Sigma_u^+$ triplet potential, where they have a binding energy of more than 7 THz$\times h$.

After the transfer into the triplet ground state we observe coherent molecular oscillations in the optical lattice. These oscillations occur because the lattice potential is much weaker for the ground state molecules than for the Feshbach molecules. A numerical model taking the lattice band structure into account reproduces this behavior. For the molecules remaining after the lattice-induced dynamics we find a lifetime exceeding 200 ms. This allows the investigation of the presently unknown collisional properties of triplet ground state molecules and marks an important step towards the realization of a Bose-Einstein condensate of deeply bound molecules.

Zusammenfassung

In der vorliegenden Arbeit beschreibe ich den kohärenten Transfer ultrakalter Moleküle von schwach- zu tief gebundenen Zuständen mit zwei unterschiedlichen Verfahren. Während durch diese Transfers der interne Quantenzustand der Moleküle manipuliert werden kann, ist ihr externer Zustand durch den Einschluss in ein optisches Gitter bestimmt. Dies erlaubt ultimative Kontrolle über alle molekularen Freiheitsgrade und weist den Weg Richtung kontrollierte Quantenchemie.

Unsere Experimente werden ausgehend von einem Bose-Einstein Kondensat aus ^{87}Rubidium-Atomen durchgeführt, welches in ein dreidimensionales optisches Gitter geladen wird. Ein reines Ensemble zweitomiger Moleküle wird durch Rampen über eine magnetische Feshbachresonanz sowie das Entfernen der verbleibenden einzelnen Atome erzeugt. Diese äußerst schwach gebundenen Feshbachmoleküle werden anschließend mit zwei unterschiedlichen Techniken in tiefer gebundene Zustände transferiert.

Wir haben ein neuartiges Transferschema entwickelt, das auf der Kombination eines Radiofrequenzpulses mit einer adiabatischen Rampe des magnetischen Feldes beruht. Mit dieser Methode können Moleküle mit einer Effizienz von mehr als 99% über vermiedene Kreuzungen unterschiedlicher molekularer Zustände transferiert werden. Wir demonstrieren die breite Anwendbarkeit dieses Verfahrens durch eine Serie von neun Radiofrequenztransfers, mit denen die Feshbachmoleküle von einem Magnetfeld von mehr als 1000 G zu 0 G transferiert werden. Die molekulare Bindungsenergie erhöht sich dabei von 24 MHz$\times h$ auf etwa 3.6 GHz$\times h$.

Um die Feshbachmoleküle in tief gebundene Zustände zu transferieren, verwenden wir STimulated Raman Adiabatic Passage (STIRAP), eine optische Raman-Transfermethode. Damit werden Feshbachmoleküle mit einer Effizienz von nahezu 90% in den rovibronischen Grundzustand des $a^3\Sigma_u^+$ Triplettpotentials transferiert, wo sie eine Bindungsenergie von mehr als 7 THz$\times h$ aufweisen.

Nach dem Transfer in den Triplett-Grundzustand beobachten wir kohärente Oszillationen der Moleküle im optischen Gitter. Diese treten aufgrund der Tatsache auf, dass das Gitterpotential für die Grundzustandsmoleküle wesentlich schwächer ist als für die Feshbachmoleküle. Mit Hilfe eines numerisches Modells, welches die Bandstruktur des Gitters berücksichtigt, kann dieses Verhalten reproduziert werden. Für die nach den gitterbedingten Oszillationen verbleibenden Moleküle messen wir eine Lebenszeit von über 200 ms. Dies erlaubt die Untersuchung der derzeit unbekannten Kollisionseigenschaften von Molekülen im Triplett-Grundzustand und stellt einen wichtigen Schritt auf dem Weg zur Realisierung eines Bose-Einstein Kondensats tiefgebundener Moleküle dar.

Contents

1 Introduction

The development of laser cooling and trapping techniques for atoms during the 1980s [Metc 02] allowed unprecedented control over their internal and external degrees of freedom. With the added benefit of evaporative cooling one can reach the regime where the de-Broglie wavelength associated with the atomic motion becomes comparable with the mean interparticle distance, and the behavior of the system is strongly governed by quantum statistics. Bose-Einstein condensation (BEC) occurs when at extremely low temperatures the single-particle ground state of the system becomes occupied by a macroscopic particle number, and a macroscopic matter wave is formed. In 1995, 70 years after Einstein's initial proposal [Eins 25] based on paper of Bose [Bose 24], this effect was finally observed in dilute atomic gases [Ande 95, Davi 95]. This achievement, as well as the pioneering work in laser cooling were honored with Nobel prizes in 1997 and 2001.

In the following years Bose-Einstein condensates were employed in numerous spectacular experiments. An - inevitably incomplete - list of highlights comprises for example the confirmation of the predicted behavior of a BEC as a macroscopic quantum matter wave by interference of two independent condensates [Andr 97] and the realization of an atom laser [Mewe 97]. The superfluid nature of a BEC was proven through the excitation of vortices [Matt 99, Abo 01], and the observation of solitons [Dens 00] demonstrated the nonlinear behavior of BEC matter waves.

With the implementation of an optical lattice, a periodic potential for the atoms can be added. This regime closely resembles solid state systems, but has the advantage of offering various tunable parameters, while lattice defects and undesired relaxation mechanisms are strongly suppressed. Hence, ultracold Bosons in an optical lattice represent an almost perfect realization of the Bose-Hubbard-Hamiltonian [Jaks 98], which was confirmed by the observation of the quantum phase transition from the superfluid BEC to a Mott insulator [Grei 02].

1.1 Ultracold molecules

After the great successes achieved with ultracold atoms, there has been a growing interest in the investigation of cold molecules. Compared to atoms, molecules have additional rotational and vibrational degrees of freedom. Furthermore heteronuclear molecules carry in general a permanent electric dipole moment, and have been suggested to be employed in quantum computation [DeMi 02], the search for an electric dipole moment of the electron [Hind 97, Huds 05] or the realization of novel phases in ultracold gases [Sant 00, Buch 07].

Due to their rich internal structure and the resulting numerous decay channels, molecules cannot be laser cooled as easily as atoms. Accordingly, alternative methods like buffer gas cooling [Wein 98], Stark deceleration [Beth 99], velocity filtering [Rieg 05], or single collision scattering [Elio 03] have been developed. While these methods were shown to work for a broad range of molecules, the phase-space densities presently achieved are still far from quantum degeneracy.

An alternative approach for the production of cold molecules is to form them from pre-cooled atoms. Photoassociation via one or two photons is widely applied for this purpose [Jone 06], and the production of molecules in the vibrational ground state has been recently demonstrated [Vite 08, Deig 08]. However, the transfer schemes applied to date suffer from relatively low efficiency, and as photoassociation is commonly carried out in magneto-optical traps, only modest phase space densities have been reached.

Starting from an atomic sample that is close to quantum degeneracy, however, magnetic Feshbach resonances can be employed to associate molecules. Feshbach resonances are scattering resonances which occur when two colliding particles resonantly couple to a bound state. They were introduced in the context of nuclear physics [Fesh 64], where two colliding particles are brought into resonance with a bound state by changing their kinetic energy. In the field of ultracold gases magnetic Feshbach resonances have been used with impressive success over the last decade. For such a magnetic Feshbach resonance a vibrationally highly excited molecular state is shifted into resonance with the state of two colliding atoms by changing an external magnetic field. Their first application was to demonstrate controlled tuning of the atomic scattering properties [Inou 98, Cour 98, Robe 98]. Three years after the suggestion to form molecules by adiabatically ramping over a magnetic Feshbach resonance [Mies 00], this scheme could be realized for many different species [Herb 03, Xu 03, Rega 03, Cubi 03, Durr 04]. As the association process is adiabatic and reversible, the molecular sample inherits the high phase space density of the atoms. However, while being translationally cold, Feshbach molecules are vibrationally highly excited. This excitation energy greatly exceeds the typical trap depths, and can be released by collisional relaxation to lower vibrational states, leading to loss of the respective particles.

For molecules associated from fermionic atoms, however, collisional decay is strongly suppressed by Pauli blocking [Petr 04]. This allowed the formation of the first molecular Bose-Einstein condensates in the year 2003 [Joch 03, Grei 03a, Zwie 03].

In the case of bosonic molecules Pauli blocking is absent, and collision-induced transitions to lower lying vibrational states are much more favorable. This leads to a dramatic decrease of molecular lifetime in dense samples. By preparing Feshbach molecules in separate sites of a three-dimensional optical lattice they can be shielded from detrimental collisions, and long molecular lifetimes can be reached [Thal 06].

One of the major goals in the field of ultracold molecules has been the production of molecules in the rovibrational ground state. Being potentially stable under collisions, they could condense to form a BEC of bosonic molecules. A possible procedure for the formation of ultracold ground state molecules is to load an atomic BEC into an optical lattice, where molecules can be associated and subsequently transferred into the rovibrational ground state with a series of optical Raman pulses [Jaks 02]. In a similar approach, we have demonstrated the reduction of the vibrational quantum number of Feshbach molecules by one unit in 2007 [Wink 07a]. In this thesis I will show amongst others things how we transferred Feshbach molecules into the rovibrational triplet ground state with this scheme.

1.2 This thesis

The first chapter of this thesis gives an overview of the setup in which the experiments are performed. ^{87}Rb atoms from background vapor are collected in a magneto-optical trap and transferred into a glass cell over a magnetic transfer line. They are brought to the Bose-Einstein condensate phase transition through rf-induced evaporative cooling and loaded into a three-dimensional optical lattice. Feshbach molecules are created via an adiabatic sweep over a magnetic Feshbach resonance, and remnant unpaired atoms are removed by a purification pulse. The result of this procedure is a pure sample of Feshbach molecules in the ground state of the optical lattice, which serves as a starting point for the further experiments.

Chapter 2 focuses on radio frequency induced transfer of Feshbach molecules to more deeply bound states. A two-level model for rf-transitions at an avoided crossing of bound molecular states is introduced and analyzed using a Floquet approach. We then present two different molecular rf-spectroscopy methods and a newly-developed scheme to adiabatically transfer population across an avoided crossing. This method is used to transfer $^{87}\mathrm{Rb}_2$ Feshbach molecules from more than 1000 G to zero magnetic field. Finally, the possible realization of an rf-induced Feshbach resonance is investigated. All measurements are simulated with a numerical model and the outcomes are compared to the experimental results.

While radio frequency transfers allow only modest differences in binding energy to be bridged, molecules can be transferred from weakly to deeply bound states with optical transfer schemes. The third chapter of this thesis starts with a brief discussion of STIRAP and then presents the laser system that has been set up to meet the requirements of this transfer method. Feshbach molecules are transferred into the rovibrational ground state of the $a^3\Sigma_u^+$ triplet potential of $^{87}\mathrm{Rb}_2$ with a one-way transfer efficiency close to 90%. Compared to the Feshbach molecules, those in the ground state experience a much weaker lattice potential, leading to coherent on-site molecular oscillations. A numerical model taking the lattice band structure into account reproduces this behavior, and allows the determination of the lattice depth for the ground state molecules.

This thesis ends with an outlook on future work with ultracold molecules.

2 Preparation of a pure ensemble of Feshbach molecules

A pure ensemble of ultracold Feshbach molecules is prepared in an ultra-high vacuum apparatus. Its construction was started in 2001 using a design similar to the one developed in the group of Theodor Hänsch in Munich. The main feature of this system is a magnetic transport line [Grei 01] connecting the MOT vacuum chamber with the glass cell where the experiments are carried out. The advantage of this design is that the experimental glass cell has ultra-high vacuum and offers excellent optical access. The magnetic transport- and vacuum systems of our setup are described in the diploma thesis of Klaus Winkler [Wink 02] and doctoral thesis of Matthias Theis [Thei 05] respectively. In the doctoral thesis of Gregor Thalhammer [Thal 06] a detailed description of the laser system, the magnetic field- and the computer-control-system of the experiment can be found. For completeness I will give a brief overview of the apparatus and the preparation procedure for a pure sample of Feshbach molecules, in a similar way as in [Wink 07b]. Such a molecular ensemble is the starting point for all the experiments described in the following chapters of my thesis.

2.1 Vacuum apparatus and magnetic transport

The vacuum apparatus consists of the MOT-chamber, which is connected via a differential pumping tube to the glass cell, where the actual experiments are carried out (see Fig. 2.1). In the first step, ^{87}Rb atoms are trapped in a magneto-optical trap (MOT) directly from the background vapor at a pressure of about 5×10^{-8} mbar. About 3×10^{9} atoms are trapped in 10 s and further cooled to about 50 μK in a molasses cooling phase. The atoms are optically pumped into the lowest spin state $|f = 1, m_f = -1\rangle$, with f the total atomic angular momentum and m_f its projection, and subsequently loaded into a magnetic quadrupole trap.

In the next step the atomic cloud is transferred into the experimental glass cell over a magnetic transport line consisting of 13 pairs of quadrupole coils (see Fig. 2.2). The current through the coils is ramped in such a way that the trap minimum shifts smoothly along the transport line (for details see [Wink 02, Thei 05, Thal 07]). The atoms cover a distance of 48 cm including an angle of 120° and pass a differential pumping tube with an inner diameter of 6.2 mm and a length of 115 mm. An ion getter pump after the tube allows us to reach a pressure of less than 10^{-11} mbar in the glass

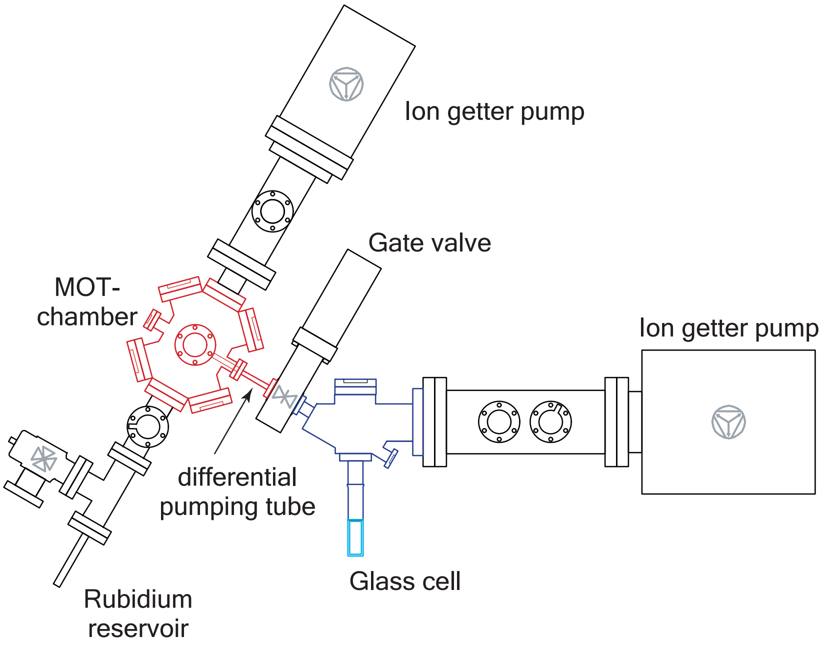

Figure 2.1:
Vacuum system. A differential pumping tube connects the MOT chamber to the experimental glass cell . ^{87}Rb atoms are trapped in the MOT and transferred over a magnetic transport line into the experimental glass cell (see Fig. 2.2). Figure adapted from [Wink 07b].

cell. After the transport the last quadrupole trap is changed into a Quadrupole-Ioffe-Configuration (QUIC) trap [Essl 98] by ramping up the current through an additional coil (Ioffe coil) to the same value as through the quadrupole coils. In contrast to a quadrupole trap, the QUIC trap has a non-zero minimum of the magnetic field with approximately harmonic characteristics. At an operating current of 40 A the trap frequencies are $\omega_r = 2\pi \times 150\,\text{Hz}$ in the radial- and $\omega_a = 2\pi \times 15\,\text{Hz}$ in the axial direction. After loading into the QUIC trap we typically end up with 4×10^8 atoms at a temperature of $250\,\mu$K.

2.2 Preparation of an atomic BEC

In the QUIC trap we apply forced radio frequency induced evaporation (For a detailed treatment see [Luit 96].) to further reduce the temperature. After 14 seconds a Bose-Einstein condensate of typically 10^6 ^{87}Rb atoms in the spin state $|f = 1, m_f = -1\rangle$ is formed. During the last second of evaporation the trap current is reduced to 30 A to avoid oscillations of the BEC, which are induced if the trap frequencies are higher

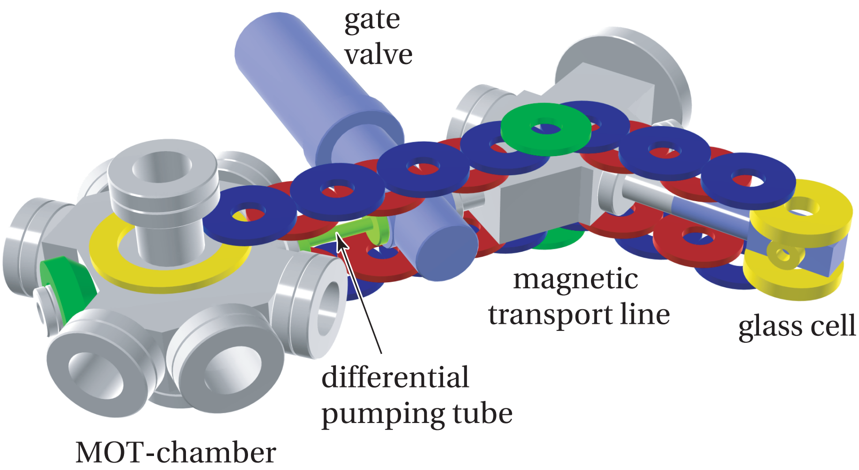

Figure 2.2:
Magnetic transport line. Shown are the coils used for the MOT (yellow, left-hand side), the QUIC trap (yellow, right-hand side) and for the magnetic transport between them (red, blue and green). Figure adapted from [Wink 07b].

harmonics of the line frequency of 50 Hz. Note that for the following procedure we typically do not use a pure condensate but a BEC plus a thermal component to increase the efficiency of molecule formation in the optical lattice.

The magnetic field minimum of the QUIC trap is displaced by about 8 mm from the center of the quadrupole coils. These coils are later switched into a Helmholtz configuration to create a homogeneous magnetic field used to form Feshbach molecules (see Sec. 2.4). In order to shift the trap minimum into the center of the quadrupole-coils the current through the quadrupole coils is reduced from 30 A to about 16.2 A while keeping the current through the Ioffe coil constant. The resulting trap frequencies are $\omega_{x,y,z} = 2\pi \times (7, 19, 20)$ Hz. We use additional coils for gravity compensation and the fine-adjustment of the BEC position in all three directions (see [Wink 07b] for details).

2.3 Optical lattice

For the production of Feshbach molecules, an optical lattice offers several advantages compared to a large-volume trap. Due to the high atomic density at the lattice sites the atom-molecule coupling is strongly enhanced, allowing efficient molecule association.

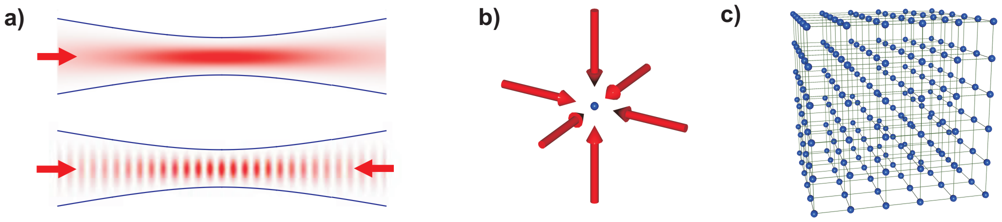

Figure 2.3:
3D optical lattice. a) Dipole potential of a single (upper part) and two counterpropagating (lower part) focused Gaussian laser beams. b) A three-dimensional cubic optical lattice can be formed by superposing six laser beams. c) After loading a BEC into a red-detuned lattice the atoms are trapped at the sites of maximum intensity. Note that depending on the exact loading conditions there can be multiple atoms per lattice site.

As Feshbach molecules are only very weakly bound, they are highly instable under collisions with each other. In a sufficiently deep optical lattice with no more than a single molecule per site they are shielded from each other, leading to a strong increase in lifetime [Thal 06]. Furthermore mean-field effects present in dense samples do not occur in an optical lattice. A detailed discussion of ultracold atoms in optical lattices can be found in [Grei 03b, Thal 07].

For the realization of a cubic three-dimensional optical lattice we use retroreflected laser beams at a wavelength $\lambda = 830\,\mathrm{nm}$ in all three spatial directions (Fig. 2.3). The intensity distribution for the resulting standing optical wave in one dimension reads

$$I(r,z) = 4I_0 \exp\left(-\frac{2r^2}{w(z)^2}\right)\cos^2(k_L z), \tag{2.1}$$

with I_0 the peak intensity, $k_L = 2\pi/\lambda$ the wavenumber of the laser beam, and

$$w(z) = w_0\sqrt{1+\left(\frac{z}{z_R}\right)} \tag{2.2}$$

the $\frac{1}{e^2}$-radius as function of the distance z from the focus. $z_R = \pi w_0^2/\lambda$ is the Rayleigh length and w_0 the $\frac{1}{e^2}$-radius at the focus. The optical dipole potential for large detunings $\Delta \gg \Gamma$ is approximately [Grim 00]

$$V(\mathbf{r}) = \frac{3\pi c^2\Gamma}{2\omega_0^3\Delta} I(\mathbf{r}), \tag{2.3}$$

where $\Gamma = 2\pi \times 6\,\mathrm{MHz}$ is the natural linewidth for Rb and Δ is the detuning from the weighted center of the D1 and D2 lines at $\lambda_{1,2} = (795, 780)\,\mathrm{nm}$ respectively. The resulting trap frequencies in the harmonic approximation are

$$\omega_z = \sqrt{\frac{2V_0 k_L}{m}} \tag{2.4}$$

in the axial and

$$\omega_r = \sqrt{\frac{4V_0}{m w_0^2}} \tag{2.5}$$

in the radial direction, where V_0 is the trap depth and m the mass of the atom. As generally $\omega_z \gg \omega_r$ this results in an array of microtraps with trap frequency

$$\omega_{ho} = \sqrt{\frac{2V_0 k_L}{m}} \tag{2.6}$$

in all three directions at the intersection of the laser beams.

For the optical lattice we use three laser beams which are derived from a Ti:Sapphire laser at $\lambda = 830.44\,\mathrm{nm}$. Each laser beam is coupled through a separate AOM and sent to the glass cell over an optical fiber. After passing through the glass cell the beams are retroreflected by cavity mirrors with a reflectivity of $R = 0.99$. The transmitted light is used to intensity-stabilize the laser beams via feedback to the AOMs. The laser beams are polarized perpendicular to each other, and their frequencies differ by tens of MHz in order to avoid interference effects. The laser beams have a $\frac{1}{e^2}$-waist radius of $170\,\mu\mathrm{m}$ at the site of the atoms, corresponding to a Rayleigh length of 11 cm. A power of 100 mW per laser beam results in a lattice depth of $37\,\mathrm{E}_r$, where $\mathrm{E}_r = \pi^2\hbar^2/2ma^2\mathrm{E}_r$ is the recoil energy and $a = \lambda/2$ is the lattice spacing. When the second Ti:Sapphire laser is used for spectroscopy or STIRAP, the pump power from the Verdi V18 laser has to be split between the two Ti:Sapphire lasers, reducing the power available for the optical lattice (see Sec. 4.2). In this configuration we typically operate with lattice depths of $15\,\mathrm{E}_r$ for atoms, corresponding to $60\,\mathrm{E}_r$ for Feshbach molecules.

Before reaching the glass cell the lattice beams are superimposed with the absorption imaging beams using polarizing beam splitter (PBS) cubes in all three directions (see Fig. 2.4). They are separated after the glass cell in the same way. A small fraction of the lattice light leaks through the PBS, allowing the detection of the size and position of the beams on the CCD-cameras. This makes it easy to align the lattice beams onto the BEC.

After the BEC is moved into the center of the quadrupole-coils as described in the previous section, it is adiabatically loaded into the optical lattice by ramping up the lattice power to its maximum value in 100 ms.

2.4 Production of Feshbach molecules

Magnetic Feshbach resonances have been extensively used in ultracold atomic physics for purposes like the association of molecules or the manipulation of atomic properties

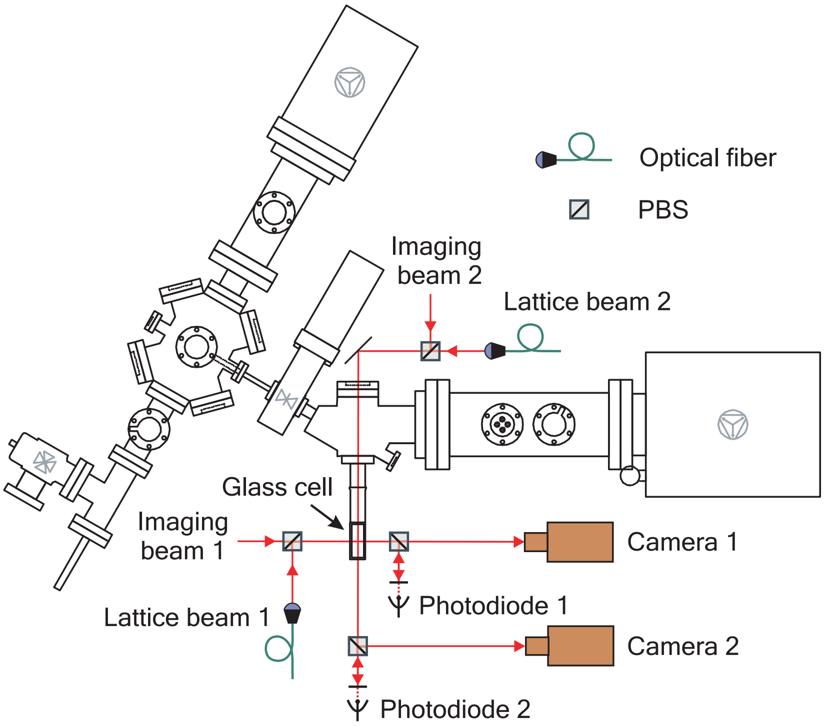

Figure 2.4:
Lattice beam alignment. After the optical fibers the lattice laser beams are superimposed with the absorption imaging light on polarizing beam splitters (PBS). Using the same method the beams are separated again after passing through the glass cell. The lattice beams are retroreflected by cavity mirrors, which transmit about 1% of the light. After detecting this light on photodiodes their signal is used to intensity-stabilize the lattice beams. Beam alignment in the vertical direction is implemented in an analogous way and is not shown here. Figure adapted from [Wink 07b].

(for reviews see [Chin 08, Kohl 06]). The broadest magnetic Feshbach resonance that has been observed in ^{87}Rb to date is in the spin state $|f=1, m_f=+1\rangle$ [Mart 02]. It lies at a magnetic field of 1007.4 G and has a width of 210 mG [Mart 02, Volz 03]. In order to use this Feshbach resonance we transfer the molecules from the magnetically trappable spin state $|f=1, m_f=-1\rangle$ into the high-field seeking state $|f=1, m_f=+1\rangle$. For this we ramp down the magnetic trap and then suddenly reverse the direction of the residual magnetic bias field. The magnetic moment of the atoms cannot follow the direction of the magnetic field, and they are diabatically transferred into state $|f=1, m_f=+1\rangle$. The quadrupole coils used for the QUIC trap are then switched into Helmholtz-configuration to create a homogenous magnetic field. Within 3 ms the current is ramped up to about 80.5 A corresponding to a magnetic field of 1012 G,

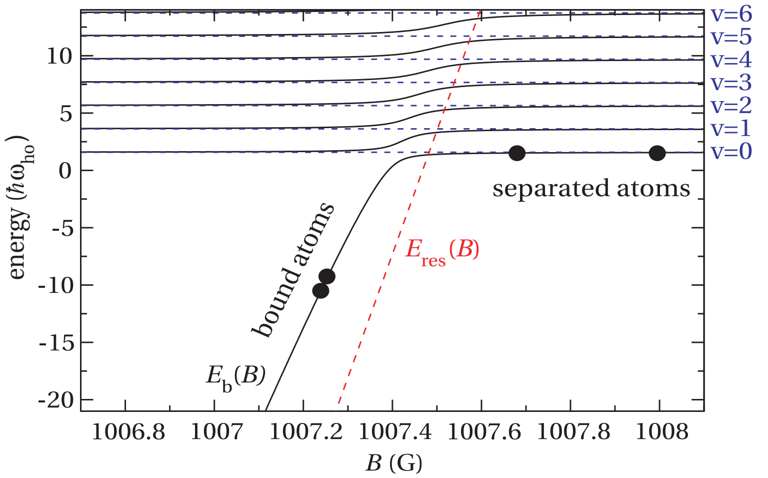

Figure 2.5:
Feshbach resonance in an optical lattice. The dashed blue lines represent the seven lowest trap states of two ^{87}Rb atoms with spin $|f = 1, m_f = +1\rangle$ in a spherical harmonic trap. The trap frequency is $\omega_{ho} = 2\pi \times 39\,\mathrm{kHz}$, which at a wavelength of $\lambda = 830\,\mathrm{nm}$ corresponds to a lattice depth of $35\,\mathrm{E}_r$. The atomic states are crossed by a molecular level (dashed red line) at 1007.5 G. Coupling between the molecular and atomic states leads to avoided crossings adiabatically connecting e.g. the molecular state with the lowest trap state. This coupling shifts the Feshbach resonance to 1007.4 G. Figure adapted from [Kohl 06].

i.e., on the "atomic" side above the Feshbach resonance. The atoms are basically not affected by this ramp, and they remain in the ground state of the lattice. The magnetic field is then slowly lowered to 1000 G with a ramp speed of typically 5 G/ms. At multiply occupied lattice sites this leads to adiabatic association of molecules with close to unit efficiency [Thal 06]. In the next step we quickly switch off the magnetic field and apply standard absorption imaging (see Sec. 2.6). As molecules cannot be detected using this technique they are dissociated by ramping back over the Feshbach resonance before the magnetic field is switched off. During the final switch-off the Feshbach resonance is crossed with a speed of more than 1000 G/ms, ensuring that effectively no molecules are formed.

The results of a typical measurement can be seen in Fig. 2.6. After Feshbach association we observe a loss of about 40% of the initially detected atoms. About 15% of the atoms reappear after Feshbach dissociation, while a fraction of about 25% of the initial signal is irretrievably lost. This can be understood in the following way: The adiabatic loading of a BEC[1] into the vibrational ground state of a deep optical lattice

---

[1] As explained in Sec. 2.2 we generally do not use a pure BEC for the experiments described here.

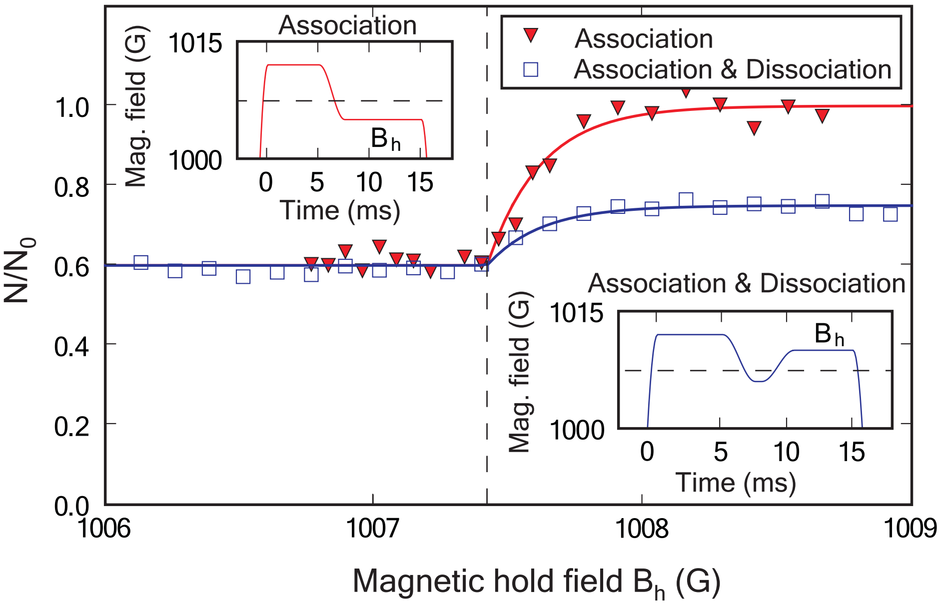

Figure 2.6:
Association and dissociation of Feshbach molecules. Feshbach association: The red triangles represent the fraction of detected atoms after ramping the magnetic field from 1013 G, above the resonance, to a hold value B_h (see left inset). About 40% of the atoms are lost for magnetic fields below the Feshbach resonance at 1007.4 G (dashed lines). Association and dissociation: After ramping back to a magnetic field B_h above the resonance (right inset) atoms in doubly occupied lattice sites reappear (blue squares). At lattice sites with higher initial occupation number inelastic atom-molecule and molecule-molecule collisions occur after Feshbach association. These particles are lost and correspond to the difference between the red triangles and blue squares. Figure adapted from [Thal 07].

leads to a Mott-insulator state [Jaks 98, Grei 02]. Due to the external harmonic confinement it has a wedding-cake like structure with alternating shells of superfluid and insulating regions of different occupation number [Jaks 99, Foll 06]. Atoms at singly occupied sites are detected independent of the magnetic field. While the association of molecules at sites with two atoms is reversible, inelastic atom-molecule- or molecule-molecule-collisions lead to loss of the particles at sites with atomic occupation number three or higher. From measurements similar to those presented in Fig. 2.6, we typically find 50-60% of the atoms in singly, 10-20% in doubly, and 20-30% in more highly occupied sites [Thal 06].

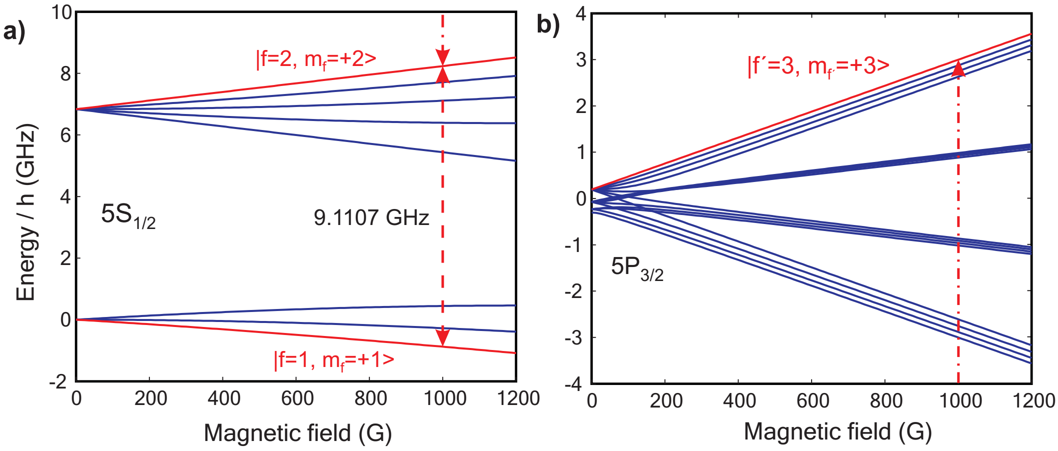

Figure 2.7:
Purification scheme. We simultaneously apply a microwave- and laser pulse for about 5 ms at a magnetic field of 1000G. a) The microwave indicated by the dashed red line drives the transition between the levels $|f=1, m_f=+1\rangle$ and $|f=2, m_f=+2\rangle$. b) The laser (dash-dotted red line) is resonant with the closed transition from the level $|f=2, m_f=+2\rangle$ to the electronically excited level in the $5\mathrm{P}_{3/2}$ manifold that correlates with $|f'=3, m_f'=+3\rangle$ at 0 G.

2.5 Purification of the molecular sample

After Feshbach association we remove the remaining single atoms which account for about 60% of the initial particles to end up with a pure molecular sample. For this we apply a combined microwave- and laser pulse at a magnetic field of 1000 G for about 5 ms. The microwave drives the atomic transition $|f=1, m_f=+1\rangle \leftrightarrow |f=2, m_f=+2\rangle$ at a frequency of 9.1107 GHz (see Fig. 2.7a). The molecules are out of resonance and not affected by the microwave. As an antenna we use a rectangular waveguide that is open on one side and supplied by an amplifier with an output power of 2 W. In order to remove the atoms we shine in resonant laser light at the same time as the microwave. It drives the closed transition $|f=2, m_f=+2\rangle \leftrightarrow |f'=3, m_{f'}=+3\rangle$, and is 1402 MHz blue detuned compared to the transition at zero magnetic field (compare Fig. 2.7b). The atoms are removed from the lattice by the recoil momentum transferred from the scattered photons [Xu 03]. After a purification pulse of about 5 ms no more atoms can be detected. We do not observe a decrease in molecule number for additional pulses and typically end up with a pure molecular sample of about 3×10^4 Feshbach molecules in the vibrational ground state of the lattice.

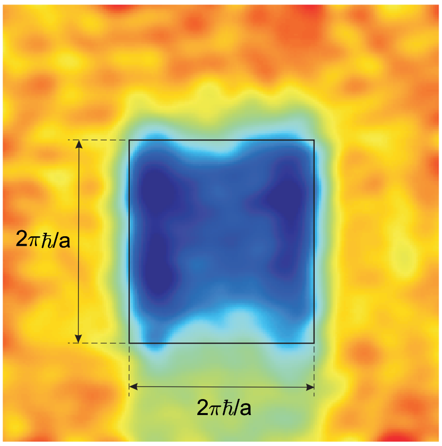

Figure 2.8:
Time-of-flight absorption image. After Feshbach dissociation and ramp-down of the optical lattice the atoms expand in a magnetic gradient field for 13 ms. The center square corresponds to the first Brillouin zone, i.e., the lowest band of the lattice. In the region below the first Brillouin zone residual atoms in a different spin state can be seen. They are produced by non-ideal switching of the magnetic fields.

2.6 Absorption imaging

In our experiments data acquisition mainly based on absorption imaging [Kett 99] at the end of the experimental cycle. Feshbach molecules are dissociated into atoms by adiabatically ramping over the Feshbach resonance. As a next step the optical lattice is ramped down in typically 5 ms. This process is adiabatic with respect to the lattice band gap, i.e., no higher bands are excited. On the other hand it is fast enough that the atomic quasi-momentum distribution does not change during the ramp-down, and is directly converted into free particle momentum. After releasing the atoms from the lattice they expand in free[2] fall, and the momentum distribution is mapped into a spatial distribution. In other words, this release procedure converts Brillouin zones from quasi-momentum- into real space [Grei 03b]. After typically 13 ms of expansion the atoms are exposed to resonant light driving the closed transition $|f = 2\rangle \leftrightarrow |f' = 3\rangle$ at a magnetic field $B = 2\,\mathrm{G}$ for $100\,\mu\mathrm{s}$. In order to detect atoms in the state $|f = 1\rangle$ and to retain atoms that are lost from the closed transition we simultaneously shine in repumping light at the transition $|f = 1\rangle \leftrightarrow |f' = 2\rangle$. The resulting absorption image can be observed with CCD cameras in all three directions (see Fig. 2.4). In general, however, only one high-quality camera (model S285 from Theta System Elektronik) is

---

[2] During the expansion of the atoms, a vertical magnetic gradient field is switched on to separate different atomic spin states.

used for imaging. For all the experiments presented in this thesis only atoms in the lowest Brillouin zone are counted as signal. A typical absorption image of an atomic sample in the lowest Brillouin zone is shown in Fig. 2.8.

3 Rapid adiabatic passage with radio frequency fields

In the past few years the production of ultracold Feshbach molecules permitted the realization of a numerous spectacular experiments. For many of these the fact that Feshbach molecules are produced in particular, well-defined quantum states was crucial. However, only a very limited number of states are directly accessible via magnetic Feshbach resonances, and there is strong interest in transferring Feshbach molecules to arbitrary quantum states. As recently demonstrated in our group, a transfer of Feshbach molecules to neighboring states can be realized by appropriate ramps of the magnetic bias field [Mark 07]. Depending on the ramp speed avoided crossings are adiabatically followed or diabatically crossed. Due to limited ramp speed, however, transfers over avoided crossings are possible only for very small energy splittings up to about 200 kHz×h. In a different approach, Feshbach molecules can be transferred via optical Raman schemes like STIRAP [Wink 07a]. While such techniques allow much more deeply bound states to be addressed, they typically require a complex setup including frequency-stabilized lasers at different wavelengths with fast intensity control [Danz 08, Ni 08, Lang 08b]. The efficiency of STIRAP transfers could potentially be considerably increased by starting from a molecular state having more favorable Franck-Condon factors than the initial Feshbach state [Danz 08].

Since the first half of the 20^{th} century magnetic radio frequency fields have been widely used for spectroscopic measurements in physics, chemistry and medicine [Rabi 38, Ingr 56, Bove 88]. In the field of ultracold molecules, rf-spectroscopy has been employed to determine the molecular binding energies near magnetic Feshbach resonances [Rega 03, Chin 04] and to probe the excitation spectrum of a Fermi gas in the BEC-BCS crossover regime [Bart 04, Grei 05]. It has also been used for the resonant production of molecules in the vicinity of a magnetic Feshbach resonance [Thom 05, Ospe 06, Bert 06]. We have developed a simple, robust and highly efficient method for transfer of molecules between different quantum states, which relies on the combination of a radio frequency pulse with an adiabatic magnetic field ramp [Lang 08a].

This chapter starts with a general discussion of how transitions between different molecular states can be driven by radio waves. We then apply this to the specific case of an avoided crossing between two bound molecular states. A two-level model describing such a system is introduced and analyzed using Floquet theory, and the results are compared to the well-known rotating wave approximation. Two different methods to spectroscopically determine the energy splitting of an avoided crossing are presented and our adiabatic transfer scheme is discussed in detail. The versatility of this method is demonstrated by increasing the binding energy of the Feshbach molecules from 24 MHz to 3.6 GHz×h with a series of nine transfers. Finally we investigate if we can use this transfer scheme to realize an rf-induced Feshbach resonance, and draw an analogy to the well-known magnetic Feshbach resonance. For all of these steps the experimental results are simulated with numerical models.

3.1 Molecules in oscillating magnetic fields

3.1.1 Experimental radio frequency setup

For the generation of the magnetic radio frequency fields used to drive molecular transitions we employ the same setup as for forced evaporative cooling (Sec. 2.2). A sinusoidal signal with a frequency of up to 150 MHz is provided by a DDS-based AD9865 frequency generator board (for details see [Schm 06]). The ADwin Gold computer control system controls the AD9854, whose amplitude and frequency can thus be changed in timesteps of 50 μs. The rf-signal is amplified by a ZFL-500LN amplifier from Minicircuits in a first, and by a Frankonia FLL25 amplifier with a maximum output power of 25 W in a second stage. The output is then transmitted via two coil antennas, which are located directly above and below the glass cell. They both have three windings, a diameter of 25 mm and produce a magnetic rf-field in the same direction as the magnetic bias field. The magnetic field along the axis of a thin coil is given as

$$B = \frac{\mu_0 N I r^2}{2(r^2 + a^2)^{3/2}} , \tag{3.1}$$

where N is the number of windings, I the current through the coil, r its radius, and a the distance along the axis through the center of the coil. For our maximum current of 0.8 A we find the two coils to produce a magnetic field of about 300 mG. However, at high rf-power cross-talk from the rf-signal to the stabilization of the magnetic bias field used for Feshbach association occurs. This cross-talk leads to oscillations in the bias field and consequently to loss of molecules. We assume that the cross-talk is due to pickup of the current transducers used to measure the magnetic bias field, which is caused by the radio frequency currents. The system shows particularly high sensitivity from relatively low frequencies up to 5 MHz. We have thus chosen the rf-amplitudes to be considerably lower than 300 mG in this frequency range.

3.1.2 Magnetic dipole transitions

We now want to analyze how magnetic dipole transitions between different molecular states can be driven. For an oscillating magnetic field with frequency ω_{rf}

$$\mathbf{B}_{\text{rf}}(t) = \mathbf{B}_{\text{rf}} \sin(\omega_{\text{rf}} t) \tag{3.2}$$

we can write the Hamiltonian for magnetic dipole transitions [Cohe 77] as

$$\hat{H}_{\text{md}} = \mathbf{B}_{\text{rf}}(t).(\frac{\mu_B}{\hbar}(\hat{\mathbf{l}} + g_s \hat{\mathbf{s}}) + \frac{\mu_N g_i}{\hbar}\hat{\mathbf{i}}) \equiv \mathbf{B}_{\text{rf}}(t).\hat{\mu}, \tag{3.3}$$

where $\hat{\mathbf{l}}$, $\hat{\mathbf{s}}$ and $\hat{\mathbf{i}}$ are the electron orbital angular momentum, electron spin and nuclear spin operators respectively. μ_B and μ_N are the Bohr- and nuclear magneton, g_s and g_i are the g-factors for electron- and nuclear spin, and $\hat{\mu}$ is the magnetic dipole moment operator. For the case where $\mathbf{B}_{\text{rf}}$ is parallel to the direction of the magnetic bias field (i.e. the z-axis), we find the selection rules

$$\Delta l = 0, \tag{3.4}$$

$$\Delta m_l = 0, \tag{3.5}$$

$$\Delta m_s = 0, \tag{3.6}$$

$$\Delta m_F = 0, \tag{3.7}$$

where m_l and m_s are the magnetic quantum numbers for the electronic orbital angular momentum and spin, respectively, and m_F is the magnetic quantum number of the total angular momentum.

We define the matrix element for an rf-induced transition from state $|i\rangle$ to $|j\rangle$, which gives the coupling strength between the states as

$$\mu_{i,j} = \frac{\langle i|\hat{H}_{\text{md}}|j\rangle}{|B_{\text{rf}}|}. \tag{3.8}$$

For different vibrational levels $|i\rangle$ and $|j\rangle$ of a single molecular potential $\mu_{i,j}$ vanishes due to the orthogonality of the respective wavefunctions. In real molecules like $^{87}\text{Rb}_2$, however, interactions like spin-orbit coupling, hyperfine- and exchange interactions cause coupling of different molecular potentials. This leads to mixing of molecular levels and thus to new eigenstates of the system, between which rf-transitions can then be driven. This mixing effect is strongest at avoided crossings of two molecular levels, where the transition matrix element $\mu_{u,l}$ between the upper $|u\rangle$ and lower branch $|l\rangle$ is resonantly peaked (see Fig. 3.1). Further away from avoided crossings the transition strength is generally too low to efficiently drive radio frequency transitions. In our experiments we thus mainly focus on the regions around avoided crossing to induce rf-transitions.

3.2 Two-level model for radio frequency transitions at avoided crossings

In this section a two-level model describing magnetic radio frequency transitions at an avoided crossing of two molecular levels is introduced. We first use this model to derive an analytic expression for the magnetic transition strength. The system is then investigated with a Floquet approach, and the results are compared to that for electric dipole transitions and the rotating wave approximation. Finally we present a numerical model including magnetic field noise, which is used to simulate our experiments.

3.2.1 Analytic model

In our model two bare molecular levels $|b_1\rangle = \binom{1}{0}$ and $|b_2\rangle = \binom{0}{1}$ with magnetic moments μ_1 and μ_2 respectively cross at a magnetic field $B = B_0$ (see Fig. 3.1a). Without the radio frequency field the Hamiltonian for this system reads

$$\hat{H}_0 = (B - B_0)\begin{pmatrix}\mu_1 & 0\\ 0 & \mu_2\end{pmatrix} + \frac{\hbar}{2}\begin{pmatrix}0 & \Omega\\ \Omega & 0\end{pmatrix}, \tag{3.9}$$

where Ω is a coupling between $|b_1\rangle$ and $|b_2\rangle$ that can arise for example from exchange- or dipole-dipole interaction. We diagonalize this Hamiltonian to find the new eigenstates

$$|u\rangle = \cos(\theta)|b_1\rangle + \sin(\theta)|b_2\rangle \tag{3.10}$$

$$|l\rangle = -\sin(\theta)|b_1\rangle + \cos(\theta)|b_2\rangle, \tag{3.11}$$

with mixing angle $\theta = \arctan(\frac{\delta+\sqrt{\delta^2+\Omega^2}}{\Omega})$, where $\delta = \frac{(\Delta\mu\Delta B)}{\hbar}$, $\Delta\mu = \mu_2 - \mu_1$ and $\Delta B = B - B_0$. The corresponding eigenenergies are

$$E_u = \frac{1}{2}\left(\Delta B(\mu_1 + \mu_2) + \sqrt{\Delta B^2\Delta\mu^2 + \hbar^2\Omega^2}\right) \tag{3.12}$$

$$E_l = \frac{1}{2}\left(\Delta B(\mu_1 + \mu_2) - \sqrt{\Delta B^2\Delta\mu^2 + \hbar^2\Omega^2}\right). \tag{3.13}$$

The eigenstates $|u\rangle$ and $|l\rangle$ form the upper and lower branch of an avoided crossing (Fig. 3.1a). In order to include magnetic radio frequency radiation into this model we add a time-dependent part $\hat{H}_{\mathrm{md}}(t)$ describing an oscillating magnetic field to the Hamiltonian. The total Hamiltonian then becomes

$$\begin{aligned}\hat{H}^{\mathrm{tot}}_{\mathrm{md}}(t) &= \hat{H}_0 + \hat{H}_{\mathrm{md}}(t)\\ &= (B - B_0)\begin{pmatrix}\mu_1 & 0\\ 0 & \mu_2\end{pmatrix} + \frac{\hbar}{2}\begin{pmatrix}0 & \Omega\\ \Omega & 0\end{pmatrix} + B_{\mathrm{rf}}\cos(\omega_{\mathrm{rf}}t)\begin{pmatrix}\mu_1 & 0\\ 0 & \mu_2\end{pmatrix}.\end{aligned} \tag{3.14}$$

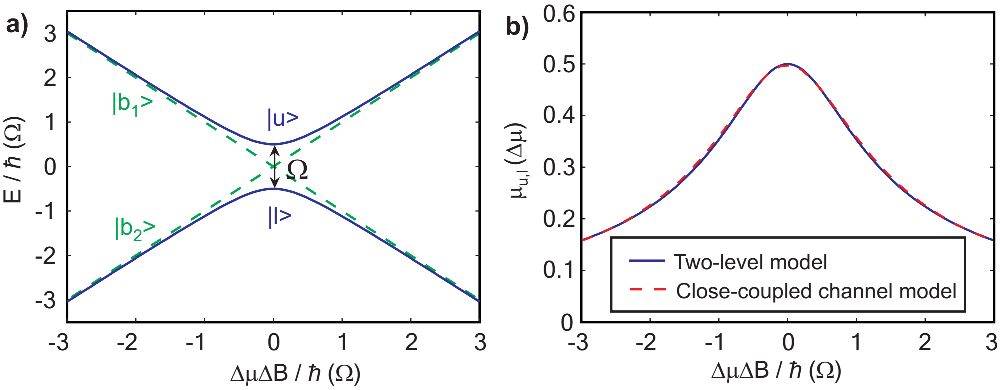

Figure 3.1:
Coupling strength at avoided crossing. a) The bare molecular states $|b_1\rangle$ and $|b_2\rangle$ (dashed green lines) are coupled with coupling strength Ω. The new eigenstates (solid blue lines) form the upper $|u\rangle$ and lower branch $|l\rangle$ of an avoided crossing. b) The matrix element $\mu_{u,l}$ for magnetic dipole transitions between $|u\rangle$ and $|l\rangle$ is peaked at the avoided crossing. The solid blue line is from our two-level model (Eq. 3.15), while the dashed red line is computed with the close-coupled channel model described in Sec. 3.3.1.

Inserting Eqs. 3.10, 3.11 and 3.14 into Eq. 3.8 we can calculate the matrix element for magnetic dipole transitions between $|u\rangle$ and $|l\rangle$ as

$$\mu_{u,l} \equiv \langle u| \begin{pmatrix} \mu_1 & 0 \\ 0 & \mu_2 \end{pmatrix} |l\rangle = \frac{\Delta\mu \sin(2\theta)}{2} = \Delta\mu \frac{\Omega(\delta + \sqrt{\delta^2 + \Omega^2})}{\Omega^2 + (\delta + \sqrt{\delta^2 + \Omega^2})^2}. \tag{3.15}$$

The matrix element $\mu_{u,l}$ is maximum for $B = B_0$ with a full width at half maximum (FWHM) of $2\sqrt{3}\,\Omega$ and vanishes as $1/\Delta B$ away from the avoided crossing. We find good agreement between our analytic expression with matrix elements calculated using the close-coupled-channel model that will be presented in Sec. 3.3.1 (see Fig. 3.1b).

In the basis of the eigenstates $|u\rangle$ and $|l\rangle$ of $\hat{H}_0$ the total Hamiltonian from Eq. 3.14 becomes

$$\begin{aligned} \hat{H}^{u,l}_{\mathrm{md}}(t) &= \begin{pmatrix} E_u & 0 \\ 0 & E_l \end{pmatrix} + B_{\mathrm{rf}} \cos(\omega_{\mathrm{rf}} t) \begin{pmatrix} \mu_1 + \Delta\mu \sin^2(\theta) & \Delta\mu \sin(2\theta)/2 \\ \Delta\mu \sin(2\theta)/2 & \mu_1 + \Delta\mu \cos^2(\theta) \end{pmatrix} \\ &\equiv \begin{pmatrix} E_u & 0 \\ 0 & E_l \end{pmatrix} + \hbar \cos(\omega_{\mathrm{rf}} t) \begin{pmatrix} \Omega_u & \Omega_R \\ \Omega_R & \Omega_l \end{pmatrix}, \end{aligned} \tag{3.16}$$

with

$$\begin{aligned}
\Omega_R &= B_{\mathrm{rf}}\Delta\mu\sin(2\theta))/(2\hbar), && (3.17)\\
\Omega_u &= B_{\mathrm{rf}}(\mu_1+\Delta\mu\sin^2(\theta))/\hbar, && (3.18)\\
\Omega_l &= B_{\mathrm{rf}}(\mu_1+\Delta\mu\cos^2(\theta))/\hbar. && (3.19)
\end{aligned}$$

A comparison of Eq. 3.17 to the matrix element $\mu_{u,l}$ for magnetic dipole transitions between $|u\rangle$ and $|l\rangle$ as defined in Eq. 3.15 shows

$$\Omega_R = \frac{\mu_{u,l}B_{\mathrm{rf}}}{\hbar}. \tag{3.20}$$

3.2.2 Rotating wave approximation

The qualitative difference of the Hamiltonian for magnetic dipole transitions at an avoided crossing (Eq. 3.16) to the one describing for example the interaction of a two-level system with a monochromatic electromagnetic field in the electric dipole approximation, is that $\hat{H}_{u,l}(t)$ contains periodically time-dependent diagonal elements. Hence, we can obtain the Hamiltonian formally equivalent[1] to the one for electric dipole transitions from Eq. 3.16 by setting $\Omega_l = \Omega_u = 0$,

$$\hat{H}_{\mathrm{ed}}(t) \;=\; \begin{pmatrix} E_u & 0 \\ 0 & E_l \end{pmatrix} + \hbar\cos(\omega_{\mathrm{rf}}t)\begin{pmatrix} 0 & \Omega_R \\ \Omega_R & 0 \end{pmatrix}. \tag{3.21}$$

Even though this commonly used Hamiltonian is not relevant for magnetic radio frequency transitions, we will discuss it in the following section to emphasize principal differences between electric- and magnetic dipole transitions. With the assumptions[2] of low field amplitude,

$$\Omega_R \ll (E_u - E_l)/\hbar \tag{3.22}$$

and small detuning,

$$\Delta \equiv (E_u - E_l)/\hbar - \omega_{\mathrm{rf}} \ll (E_u - E_l)/\hbar + \omega_{\mathrm{rf}} \tag{3.23}$$

the well-known rotating wave approximation (RWA, see e.g. [Cohe 77]) can be applied to $\hat{H}_{\mathrm{ed}}(t)$. This results in the time-independent Hamiltonian for the so-called dressed states $|u\rangle$ and $|l+\hbar\omega_{\mathrm{rf}}\rangle$

---

[1] In the case of electric dipole transitions $\Omega_R = Ed/\hbar$ with E the electric field amplitude and $d = \langle u|\hat{d}|l\rangle$ the electric dipole matrix element between $|u\rangle$ and $|l\rangle$, and ω_{rf} has to be replaced by the electromagnetic field frequency.

[2] For our experimental parameters these criterions are generally well fulfilled. Their validity will be studied in detail in the following sections.

$$\hat{H}_{RWA} = \begin{pmatrix} E_u & \hbar\Omega_R/2 \\ \hbar\Omega_R/2 & E_l + \hbar\omega_{\mathrm{rf}} \end{pmatrix}. \tag{3.24}$$

For zero detuning $\Delta = 0$ this Hamiltonian leads to sinusoidal oscillations between $|u\rangle$ and $|l\rangle$, allowing us to identify Ω_R as Rabi frequency. In the following section we will introduce generalized Floquet theory to perform a more rigorous treatment of $\hat{H}_{u,l}(t)$ and compare it to the rotating wave approximation.

3.2.3 Floquet approach

Floquet theory can be applied for the investigation of time periodic Hamiltonians [Autl 55, Shir 65] and is today widely used, for example in the case of high-amplitude external fields, where perturbative approaches are not applicable [Potv 88]. An overview is given e.g. in the review article [Chu 04]. Here, we will first summarize the derivation of the Floquet framework using a similar notation as in Ref. [Gao 08]. This formalism is used to analyze the Hamiltonians from Eqs. 3.16 and 3.21, describing magnetic- and electric dipole transitions, respectively. The results are compared to the rotating wave approximation.

We consider the time-dependent Schrödinger equation

$$i\hbar \frac{\partial \Psi(r,t)}{\partial t} = \hat{H}(t)\Psi(r,t) \tag{3.25}$$

for the case of a periodic Hamiltonian

$$\hat{H}(t) = \hat{H}_0 + \hat{V}(t), \tag{3.26}$$

where $\hat{V}(t) = \hat{V}(t+T)$ is a periodic perturbation[3]. The unperturbed Hamiltonian $\hat{H}_0$ has a complete orthonormal set of eigenfunctions

$$E_\alpha \psi_\alpha(r) = \hat{H}_0 \psi_\alpha(r), \tag{3.27}$$

with $\langle\psi_\alpha|\psi_\beta\rangle = \delta_{\alpha,\beta}$. For the sake of nomenclature we will refer to these as "molecular states". According to the Floquet theorem [Floq 83] we can write the solution of Eq. 3.25 as

$$\Psi_\varepsilon(r,t) = e^{-i\varepsilon t/\hbar}\Phi_\varepsilon(r,t), \tag{3.28}$$

where the Floquet state $\Phi_\varepsilon(r,t)$ has the same periodicity as $\hat{V}(t)$,

$$\Phi_\varepsilon(r,t) = \Phi_\varepsilon(r,t+T). \tag{3.29}$$

---

[3] Note that in contrast to perturbation theory, $\hat{V}(t)$ is not restricted to small amplitudes.

Inserting Eq. 3.28 into Eq. 3.25 we obtain the eigenequation

$$\varepsilon\Phi_\varepsilon(r,t) = \left(\hat{H}(t) - i\hbar\frac{\partial}{\partial t}\right)\Phi_\varepsilon(r,t), \tag{3.30}$$

where ε will be called the quasienergy. The term quasienergy emphasizes the analogy of the states $\Psi_\varepsilon(r,t)$ to the Bloch eigenstates with quasimomentum k for spatially periodic Hamiltonians. We note that the transformation

$$\varepsilon' = \varepsilon + m\hbar\omega, \tag{3.31}$$

$$\Phi_{\varepsilon'}(r,t) = e^{im\omega t}\Phi_\varepsilon(r,t), \tag{3.32}$$

with m an arbitrary integer and $\omega = \frac{2\pi}{T}$ converts an eigenstate $\Phi_\varepsilon(r,t)$ in Eq. 3.30 into another eigenstate. The wavefunction $\Psi_\varepsilon(r,t)$ from Eq. 3.28, however, remains unchanged [Samb 73, Hsu 06]. The quasienergies for physically different Floquet states can thus be restricted to an energy range $-\frac{\hbar\omega}{2} < \varepsilon < \frac{\hbar\omega}{2}$.

To solve for the eigenvalues of Eq. 3.30 we choose the molecular states $\psi_\alpha(r)$ as basis for the spatial part of $\Phi_\varepsilon(r,t)$. Since $\Phi_\varepsilon(r,t)$ is periodic with period T, we can make the Fourier expansion

$$\Phi_\varepsilon(r,t) = \sum_\alpha \sum_{n=-\infty}^{\infty} C^\varepsilon_{\alpha,n} e^{in\omega t}\psi_\alpha(r), \tag{3.33}$$

where $C^\varepsilon_{\alpha,n}$ are coefficients to be determined. Using Dirac notation we define the Floquet state $|\alpha,n\rangle$ such that

$$\langle r,t|\alpha,n\rangle = e^{in\omega t}\psi_\alpha(r), \tag{3.34}$$

and get the inner product

$$\langle\beta,m|\alpha,n\rangle = \frac{1}{T}\int_0^T dt \int dr e^{-im\omega t} e^{in\omega t}\psi^*_\beta(r)\psi_\alpha(r) = \delta_{\beta,\alpha}\delta_{m,n}. \tag{3.35}$$

Substituting Eq. 3.33 into Eq. 3.30 and using Eqs. 3.34 and 3.35 we obtain the system of coupled equations

$$\sum_\alpha \sum_{n=-\infty}^{\infty} \left(\langle\alpha|\hat{V}^{(m-n)}(r)|\beta\rangle + (E_\alpha - \varepsilon + n\hbar\omega)\delta_{\beta,\alpha}\delta_{m,n}\right) C^\varepsilon_{\alpha,n} = 0, \tag{3.36}$$

with

$$\hat{V}^{(m-n)}(r) \equiv \frac{1}{T}\int_0^T \hat{V}(r,t)e^{i(m-n)\omega t}dt. \tag{3.37}$$

We can rewrite Eq. 3.36 in the form of a matrix eigenvalue equation

$$\varepsilon C^{\varepsilon}_{\alpha,n} = \sum_{\beta} \sum_{m=-\infty}^{\infty} \langle \alpha, n | \hat{\mathcal{H}} | \beta, m \rangle C^{\varepsilon}_{\beta,m}, \tag{3.38}$$

where we call $\hat{\mathcal{H}}$ the Floquet Hamiltonian with matrix elements

$$\langle \alpha, n | \hat{\mathcal{H}} | \beta, m \rangle = \hat{V}^{(n-m)}_{\alpha,\beta} + (E_\alpha - n\hbar\omega)\delta_{\beta,\alpha}\delta_{m,n}. \tag{3.39}$$

The Floquet Hamiltonian is an infinite Hermitian matrix where the columns are identified by pairs of indices n and α and the rows by m and β. Hence, we have transformed the time-dependent Schrödinger equation from Eq. 3.25 into an equivalent time-independent, infinite-dimensional eigenvalue problem.

Let us now consider the probability to make a transition from an initial molecular state $|\alpha\rangle$ at time t_0 to a final state $|\beta\rangle$ at time t. The matrix form of the time-evolution operator $\hat{U}(t, t_0)$ can be expressed [Shir 65] as

$$\hat{U}_{\beta\alpha}(t, t_0) \equiv \langle \beta | \hat{U}(t, t_0) | \alpha \rangle = \sum_{n=-\infty}^{\infty} \langle \beta, n | e^{-i\hat{\mathcal{H}}(t-t_0)} | \alpha, 0 \rangle e^{in\omega t}. \tag{3.40}$$

This means that the amplitude for a system to evolve from an initial state $|\alpha\rangle$ at time t_0 to a state $|\beta\rangle$ at time t according to the time-dependent Hamiltonian $\hat{H}(t)$ is equal to the amplitude to evolve from a Floquet state $|\alpha, 0\rangle$ at t_0 to the Floquet state $|\beta, n\rangle$ at t according to the time-independent Floquet Hamiltonian $\hat{\mathcal{H}}$, summed over n with weighting factors $e^{in\omega t}$. Methods used to solve problems involving time-independent Hamiltonians can thus be applied to periodically time-dependent Hamiltonians.

a) Electric dipole Floquet vs. RWA

As an example we will apply the Floquet framework to the electric dipole Hamiltonian (Eq. 3.21). This is a common approach for high field amplitudes such as in pulsed laser experiments, where the rotating wave approximation (see Eq. 3.24) is not valid [Ho 83, Dres 99]. Mathematically the electric dipole Hamiltonian can be obtained from the one describing magnetic dipole transitions at an avoided crossing by setting the time-dependent diagonal elements to zero (see Sec. 3.2.2).

From Eq. 3.39 we can calculate the matrix elements of the time-independent Floquet Hamiltonian $\hat{\mathcal{H}}_{\text{ed}}$, which is equivalent to the time-dependent Hamiltonian $\hat{H}_{\text{ed}}$ (Eq. 3.21). Ordering the Floquet states $|n, \alpha\rangle$ such that α runs over the molecular states before each change in n, the matrix representation of $\hat{\mathcal{H}}_{\text{ed}}$ is

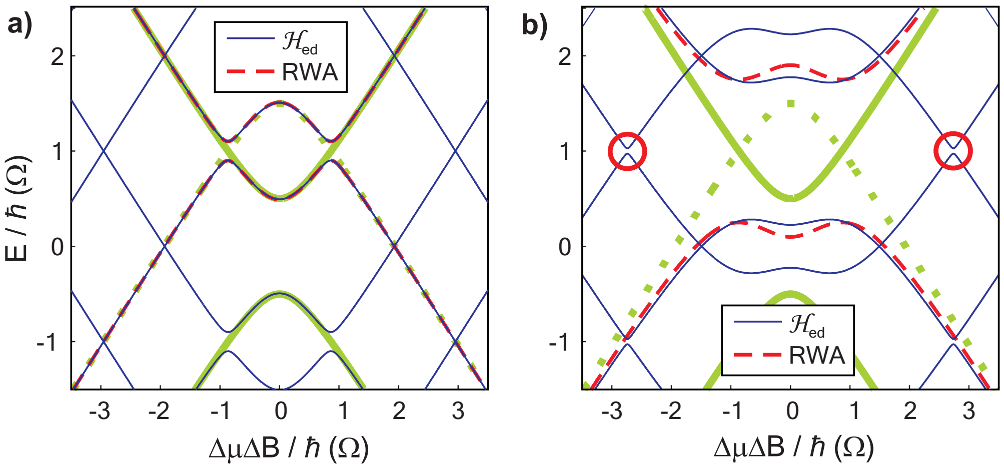

Figure 3.2:
Rotating wave approximation and Floquet states for electric dipole interaction at different Rabi frequencies. The thick solid lines show the upper and lower branch $|u\rangle$ and $|l\rangle$ of an avoided crossing of two molecular states having a coupling strength Ω (compare Fig. 3.1). The dashed green line represents the state $|l,+1\rangle$ for a field frequency $\omega_{\mathrm{rf}} = 2\Omega$. The eigenstates of the rotating wave Hamiltonian $\hat{H}_{RWA}$ are shown as dashed red lines, those of the electric dipole Floquet Hamiltonian $\hat{\mathcal{H}}_{\mathrm{ed}}$ as solid blue lines. The Rabi frequency Ω_R is considered to be independent of the magnetic bias field B. a) Eigenenergies for low Rabi frequency $\Omega_R = \Omega/5$. b) At higher Rabi frequency $\Omega_R = 3\Omega/2$ higher order coupling causes deviations of the Floquet states from the RWA. As an example the three-photon coupling between the states $|l,+2\rangle$ and $|u,-1\rangle$ is indicated by the red circles. Note that there is no coupling for even photon number (see text).

$$\hat{\mathcal{H}}_{\mathrm{ed}} = \begin{pmatrix} \cdot & \cdot & \cdot & \cdot & \cdot & \cdot & \cdot & \cdot & \cdot & \cdot \\ \cdot & E_l{-}2\hbar\omega_{\mathrm{rf}} & \Omega_R/2 & 0 & 0 & 0 & 0 & 0 & 0 & \cdot \\ \cdot & \hbar\Omega_R/2 & E_u{-}\hbar\omega_{\mathrm{rf}} & 0 & 0 & \hbar\Omega_R/2 & 0 & 0 & 0 & \cdot \\ \cdot & 0 & 0 & E_l{-}\hbar\omega_{\mathrm{rf}} & \hbar\Omega_R/2 & 0 & 0 & 0 & 0 & \cdot \\ \cdot & 0 & 0 & \hbar\Omega_R/2 & E_u & 0 & 0 & \hbar\Omega_R/2 & 0 & \cdot \\ \cdot & 0 & \hbar\Omega_R/2 & 0 & 0 & E_l & \hbar\Omega_R/2 & 0 & 0 & \cdot \\ \cdot & 0 & 0 & 0 & 0 & \hbar\Omega_R/2 & E_u{+}\hbar\omega_{\mathrm{rf}} & 0 & 0 & \cdot \\ \cdot & 0 & 0 & 0 & \hbar\Omega_R/2 & 0 & 0 & E_l{+}\hbar\omega_{\mathrm{rf}} & \hbar\Omega_R/2 & \cdot \\ \cdot & 0 & 0 & 0 & 0 & 0 & 0 & \hbar\Omega_R/2 & E_u{+}2\hbar\omega_{\mathrm{rf}} & \cdot \\ \cdot & \cdot & \cdot & \cdot & \cdot & \cdot & \cdot & \cdot & \cdot & \cdot \end{pmatrix}. \tag{3.41}$$

We see that $\hat{\mathcal{H}}_{\mathrm{ed}}$ is periodic with only the diagonal elements changing by integer multiples of $\hbar\omega_{\mathrm{rf}}$ from block to block. In principle, to calculate the eigenenergies of the Floquet Hamiltonian we have to solve the infinite-dimensional secular equation

$$\det(\hat{\mathcal{H}}_{\mathrm{ed}} - \varepsilon I) = 0. \tag{3.42}$$

In practice, however, it is sufficient to truncate $\hat{\mathcal{H}}_{\text{ed}}$ at a certain Fourier component depending on the interaction strength. A straightforward way to determine the boundaries of this truncation is to check for consistency when including higher Fourier components.

Figure 3.2 shows the upper $|u\rangle$ and lower branch $|l\rangle$ of an avoided crossing as solid green lines, and the state $|l,+1\rangle$ as dashed green line. Within the rotating wave approximation $|u\rangle$ and $|l,+1\rangle$ are coupled with coupling strength Ω_R, leading to new eigenstates represented by the dashed red lines. These eigenstates show an avoided crossing at $E_u - E_l = \hbar\omega_{\text{rf}}$, i.e. the coupling is mediated by a single photon. The eigenenergies of the Floquet Hamiltonian $\hat{\mathcal{H}}_{\text{ed}}$, which are shown as solid blue lines, are periodic with $\Delta E = \hbar\omega_{\text{rf}}$. At low Rabi frequency Ω_R the eigenenergies of $\hat{\mathcal{H}}_{\text{ed}}$ and $\hat{H}_{RWA}$ do not deviate noticeably from each other (see Fig. 3.2a, where $\Omega_R = \Omega/5$[4]).

In contrast to the rotating wave approximation, the Floquet approach also takes into account higher order coupling. With increasing Rabi frequency the discrepancy between the Floquet states and the RWA become significant (Fig. 3.2b, with $\Omega_R = 3\Omega/2$). For the Floquet case we find transitions involving the exchange of an odd number of photons to be allowed, while those for even photon numbers are forbidden. This can be seen directly from Eq. 3.41: The off-diagonal elements $\Omega_R/2$ couple only Floquet states with different molecular state, $|u,n\rangle \leftrightarrow |l,n\pm 1\rangle$. The fact that two Floquet states can become energetically degenerate only if their molecular state differs implies that resonant coupling can only occur for odd photon numbers. As an example the three-photon coupling between the Floquet states $|l+2\rangle$ and $|u,-1\rangle$ is highlighted by the red circles in Fig. 3.2b, while it is too weak to be resolved in Fig. 3.2a.

b) Magnetic- vs. electric dipole Floquet

After becoming acquainted to the Floquet framework in the context of electric dipole transitions we will now use it to analyze the Hamiltonian for magnetic dipole transitions at an avoided crossing (Eq. 3.16). In this case we obtain the Floquet Hamiltonian

$$\hat{\mathcal{H}}_{\text{md}} = \begin{pmatrix}
\cdot & \cdot & \cdot & \cdot & \cdot & \cdot & \cdot & \cdot & \cdot & \\
\cdot & E_l-2\hbar\omega_{\text{rf}} & \hbar\Omega_R/2 & \hbar\Omega_u/2 & 0 & 0 & 0 & 0 & 0 & \cdot \\
\cdot & \hbar\Omega_R/2 & E_u-\hbar\omega_{\text{rf}} & 0 & \hbar\Omega_l/2 & \hbar\Omega_R/2 & 0 & 0 & 0 & \cdot \\
\cdot & \hbar\Omega_u/2 & 0 & E_l-\hbar\omega_{\text{rf}} & \hbar\Omega_R/2 & \hbar\Omega_u/2 & 0 & 0 & 0 & \cdot \\
\cdot & 0 & \hbar\Omega_l/2 & \hbar\Omega_R/2 & E_u & 0 & \hbar\Omega_l/2 & \hbar\Omega_R/2 & 0 & \cdot \\
\cdot & 0 & \hbar\Omega_R/2 & \hbar\Omega_u/2 & 0 & E_l & \hbar\Omega_R/2 & \hbar\Omega_u/2 & 0 & \cdot \\
\cdot & 0 & 0 & 0 & \hbar\Omega_l/2 & \hbar\Omega_R/2 & E_u+\hbar\omega_{\text{rf}} & 0 & \hbar\Omega_l/2 & \cdot \\
\cdot & 0 & 0 & 0 & \hbar\Omega_R/2 & \hbar\Omega_u/2 & 0 & E_l+\hbar\omega_{\text{rf}} & \hbar\Omega_R/2 & \cdot \\
\cdot & 0 & 0 & 0 & 0 & 0 & \hbar\Omega_l/2 & \hbar\Omega_R/2 & E_u+2\hbar\omega_{\text{rf}} & \cdot \\
\cdot & \cdot & \cdot & \cdot & \cdot & \cdot & \cdot & \cdot & \cdot &
\end{pmatrix}. \qquad (3.43)$$

This matrix has a block structure which is similar to that of $\hat{\mathcal{H}}_{\text{ed}}$ (Eq. 3.41), but contains additional off-diagonal elements Ω_u and Ω_l which couple Floquet states for identical molecular states ($|u,n\rangle \leftrightarrow |u,n\pm 1\rangle$ and $|l,n\rangle \leftrightarrow |l,n\pm 1\rangle$ respectively).

---

[4] This value of Ω_R is still considerably larger than typically applied in our experiments and was chosen for better visibility of the interaction-induced avoided crossings in Fig. 3.2a.

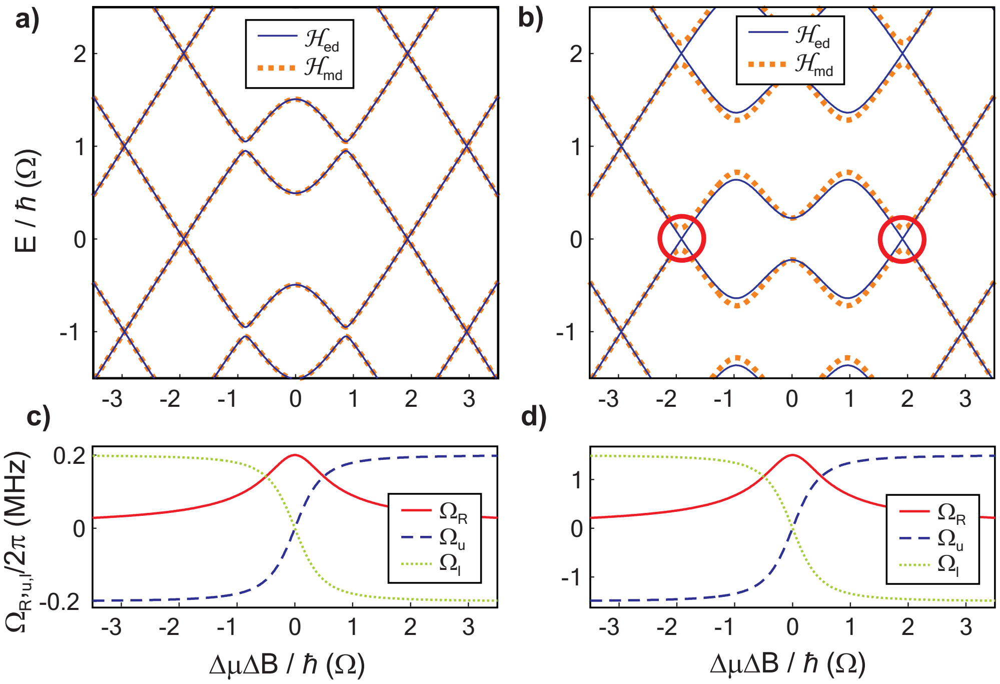

Figure 3.3:
Floquet states for electric- and magnetic dipole coupling at different coupling strength. a) and b) Comparison of quasienergies. Similar to Fig. 3.2 the thin solid lines show the eigenenergies of $\hat{\mathcal{H}}_{\text{ed}}$, while the thick dotted lines represent those of $\hat{\mathcal{H}}_{\text{md}}$. The red circles in b) indicate two-photon coupling, which is allowed for magnetic-, but not for electric dipole transitions. c) and d) Coupling strengths for subplots a) and b). The solid, dashed and dotted lines show the coupling strengths Ω_R, Ω_u and Ω_l respectively. They are computed according Eqs. 3.17-3.19 assuming a constant rf-amplitude B_{rf}.

In Fig. 3.3 we compare the quasienergies of $\hat{\mathcal{H}}_{\text{md}}$ and $\hat{\mathcal{H}}_{\text{ed}}$. In contrast to Fig. 3.2 where the Rabi frequency Ω_R was kept constant, we now assume the experimentally more relevant case of constant magnetic radio frequency field amplitude B_{rf}. According Eqs. 3.17-3.19 this leads to a variation of the couplings Ω_R, Ω_u and Ω_l, depending on the magnetic bias field B (see Fig. 3.3c and d). The rf-amplitude B_{rf} was thereby chosen such that the maxima of Ω_R equal its values from Fig. 3.2a and b respecively. For low B_{rf} as typically applied in our experiments[5] we find the quasienergies of $\hat{\mathcal{H}}_{\text{md}}$ and $\hat{\mathcal{H}}_{\text{ed}}$ to closely match each other (Fig. 3.3a) and thus also the rotating wave approximation

---

[5] For the parameters chosen in Fig. 3.3 the Rabi frequency at the point of one-photon transitions, i.e. at $\Delta B \Delta\mu/\hbar \simeq 1$ is $\Omega_R \simeq 2\pi \times 90\,\text{kHz}$, about twice the typical experimental value.

energies (compare Fig. 3.2a)[6]. In this regime, one-photon processes dominate, while higher-order coupling is negligible.

For large rf-amplitudes the eigenenergies of $\hat{\mathcal{H}}_{\text{md}}$ and $\hat{\mathcal{H}}_{\text{ed}}$ show significant deviations (see Fig. 3.3b). In particular processes under the exchange of even photon numbers become allowed for $\hat{\mathcal{H}}_{\text{md}}$. As an example, the coupling between the Floquet states $|u, -1\rangle$ and $|l, +1\rangle$ is indicated by the red circles in Fig. 3.3b. From Eq. 3.41 we see that this second-order coupling can occur via the off-diagonal elements Ω_R and Ω_u or Ω_R and Ω_l respectively. Higher order processes are allowed as well. Unlike in Fig. 3.2, however, three-photon-coupling is suppressed due to the resonant behavior of Ω_R.

In conclusion, from this investigation we find that for that for our experimental parameters the rotating wave approximation is an adequate description. At larger field amplitudes, however, processes involving the exchange of multiple photons become relevant. The main difference between rf-induced magnetic transitions and electric dipole transitions is that in the latter case coupling occurs for both even and odd photon numbers.

3.2.4 Rabi oscillations

Assuming the rotating wave approximation to be valid, sinusoidal Rabi oscillations of frequency Ω_R between $|u\rangle$ and $|l\rangle$ can be driven by subjecting molecules to resonant rf-radiation. However, gradients over the molecular sample for the magnetic bias- as well as for the rf-field cause dephasing between molecules at different sites, leading to damping of the oscillations. Additionally, fluctuations due to noise in the magnetic bias field lead to shot-to-shot noise for different experimental cycles. These imperfections in the magnetic bias field reduce the timespan over which Rabi oscillations can be observed. Dephasing as well as shot-to-shot noise can be strongly suppressed by setting the magnetic field to the center of an avoided crossing, where the transition frequency is in first order independent of the magnetic bias field. In Fig. 3.4 Rabi oscillations observed close to the center of the avoided crossing A from Figs. 3.7 and 3.14 are shown, where we find a coherence time of about 1 ms.

3.2.5 Numerical model

In Sec. 3.2.1 a Hamiltonian describing the interaction of molecules at an avoided crossing with radio frequency radiation (Eq. 3.16) was derived. From the discussion of Sec. 3.2.3 we have learned that for the low rf-amplitudes typically used in our experiments, the RWA is an adequate approximation for this Hamiltonian. However, Eq. 3.16 does not include noise in the magnetic bias field, which is caused by imperfections of the coil current stabilization. In this section we will introduce a numerical model for rf-transitions which in a first step will be used to test the validity of the RWA for the

---

[6] The eigenstates of the RWA are not shown in Fig. 3.3 for better visibility.

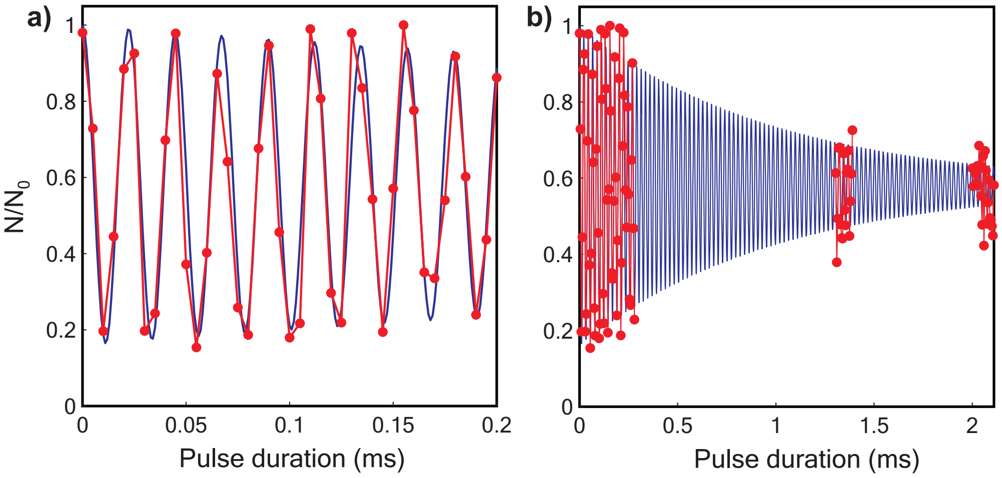

Figure 3.4:
Rabi oscillations. Shown is the fraction N/N_0 of molecules detected in $|u\rangle$ after subjecting them to a square pulse of magnetic rf-radiation as a function of pulse duration. a) For short pulses Rabi oscillations between $|u\rangle$ and $|l\rangle$ can clearly be observed. b) For longer pulse duration the oscillations are damped due to dephasing caused by inhomogeneities of the magnetic fields. The blue line is an exponentially damped sinusoidal fit to the experimental data (red circles), and gives a Rabi frequency $\Omega_R = 2\pi \times 44.6\,\mathrm{kHz}$ and a damping time of 1.1 ms. The data was taken close to the center of the avoided crossing A (see Figs. 3.7 and 3.14) at a magnetic bias field of 1001.4 G, for rf-pulses with $\omega_{\mathrm{rf}} = 2\pi\times 13.35\,\mathrm{MHz}$ and $B_{\mathrm{rf}} = 25\,\mathrm{mG}$.

Rabi oscillation measurements shown in Fig. 3.4. We will then add magnetic field noise to this model and investigate the consequences.

For the numerical model, we return to the time-dependent Hamiltonian in the basis of bare states $|b_1\rangle$ and $|b_2\rangle$ (Eq. 3.14). The time evolution is then numerically solved with the Crank-Nicolson method [Cran 47]. In order to check the quality of the rotating wave approximation we apply this model to the data from Fig. 3.4, showing Rabi oscillations between the upper and lower branch of the avoided crossing A. For these parameters, i.e. $(E_u - E_l)\hbar = \omega_{\mathrm{rf}} = 2\pi\times 13.35\,\mathrm{MHz}$ and $B_{\mathrm{rf}} = 25\,\mathrm{mG}$ corresponding to $\Omega_R = 2\pi \times 44.6\,\mathrm{kHz}$, the conditions for the RWA (Eqs. 3.22) and 3.23) are well satisfied. Indeed, the model shows sinusoidal Rabi oscillations between the molecular states $|u\rangle$ and $|l\rangle$ (solid lines in Fig. 3.5a).

We now compare this to the case where resonant rf of the same amplitude is applied at a very narrow avoided crossing, where the energy splitting is reduced by a factor of 100 to $\Omega = 2\pi \times 133\,\mathrm{kHz}$. In this case we find the Rabi frequency $\Omega_R = 2\pi \times 44.6\,\mathrm{kHz}$

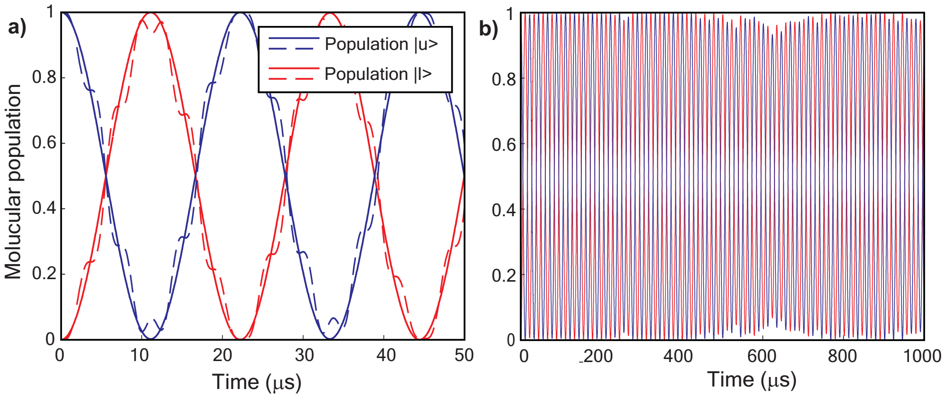

Figure 3.5:
Numerical model simulation of Rabi oscillations. a) Validity check of rotating wave approximation. The solid lines represent a numerical calculation for the Rabi oscillation measurement of Fig. 3.4. For these parameters the conditions for the RWA (Eqs. 3.22 and 3.23) are well fulfilled (see text), and sinusoidal oscillations between the molecular states $|u\rangle$ (solid blue line) and $|l\rangle$ (solid red line) can be observed. The dashed lines show a simulation for the same rf-amplitude B_{rf} but a transition frequency reduced by a factor of 100, leading to a violation of Eq. 3.22. b) Rabi oscillations including noise of the magnetic bias field (for a detailed discussion see following subsection). Shown is a simulation for the same parameters as the solid lines in a), but with magnetic noise included. Compared to the ”perfect” sinusoidal Rabi oscillations observed in a), the noise leads to a temporary reduction of the oscillation amplitude.

to be on the same order of magnitude as the energy difference between $|u\rangle$ and $|l\rangle$, $(E_u - E_l)\hbar = \omega_{\mathrm{rf}} = 2\pi\times 133\,\mathrm{kHz}$, and thus a violation of the condition from Eq. 3.22. A corresponding numerical model simulation shows that an oscillation of higher frequency is superimposed on the Rabi oscillation (dashed lines in Fig. 3.5a).

Magnetic field noise

Due to the imperfections in the stabilization of the magnetic bias field the molecules are subjected to magnetic field noise. Before including this noise into the model, however, we briefly analyze the experimental magnetic bias field stabilization setup. In order to control the magnetic field we have implemented an active digital stabilization circuit. The current through the Feshbach coils is generated by an SM 30-100D power supply from Delta Elektronika and measured with an Ultrastab 866 current transducer from Danfysik with a relative stability better than 10^{-5}. This signal is fed back to the

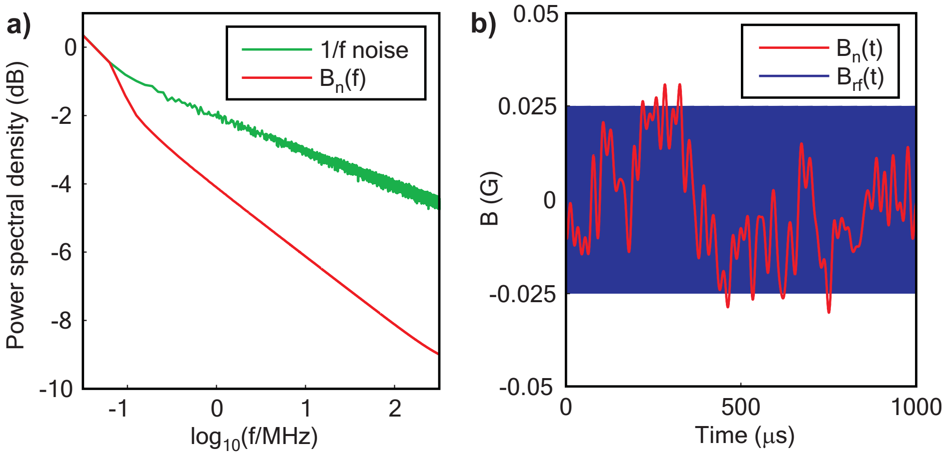

Figure 3.6:
Simulated magnetic noise. a) Noise spectrum. The magnetic noise B_n used in our numerical model (red line) is constructed by filtering out frequency components higher than 50 kHz from 1/f-noise (green line). b) The red line shows the time signal of the magnetic noise $B_\mathrm{n}(t)$ corresponding to the red line in a) (low-pass filtered 1/f-noise). The magnetic rf-field as used in the simulation of Rabi oscillations from Fig. 3.5 is shown in blue. Due to the high radio frequency $\omega_\mathrm{rf} = 2\pi \times 13.35\,\mathrm{MHz}$ the oscillations of the rf-field are not resolved in this plot.

power supply over a digital PID controller implemented via our ADwin Gold computer control system, which has a cycle rate of 20 kHz. From the measured signal of the current transducer we find magnetic field noise with a root mean square (rms) of about 35 mG (see [Thal 07]). However, this value could deviate from the real magnetic field noise due to instabilities in the current measurement or noise caused by the analog-to-digital converter. Filtering this noise with a low pass with a cut-off frequency of 1.5 kHz, i.e. the bandwidth of the total system, reduces the noise to about half of its original value. Due to the sampling rate of the control system, the range of the noise spectrum recorded via the digital PID controller is limited to a maximum value of 10 kHz.

We include magnetic field noise into our model by introducing a time-dependent noise term $B_\mathrm{n}(t)$. The total Hamiltonian now reads as

$$\hat{H}^\mathrm{tot}(t) = (B - B_0 + B_\mathrm{rf}\cos(\omega_\mathrm{rf}t) + B_\mathrm{n}(t)) \begin{pmatrix} \mu_1 & 0 \\ 0 & \mu_2 \end{pmatrix} + \frac{\hbar}{2}\begin{pmatrix} 0 & \Omega \\ \Omega & 0 \end{pmatrix} . \tag{3.44}$$

In order to generate realistic noise we start with 1/f-noise (”pink noise”), i.e. noise where the power spectral density is proportional to the inverse of the frequency (see

Fig. 3.6a). Frequency components higher than 50 kHz are then filtered out to account for the low-pass behavior of the control loop including the Feshbach coils. Finally $B_{\mathrm{n}}(t)$ is scaled to fit the experimentally measured noise level. In Fig. 3.6b an example for $B_{\mathrm{n}}(t)$ is plotted versus time. For comparison, the magnetic rf-field used for the simulation of the Rabi oscillations from Fig. 3.5 is depicted as well.

We now repeat the simulation for the Rabi oscillations from Fig. 3.5a with magnetic noise included. As can be seen from Fig. 3.5b, the noise temporarily reduces the amplitude of the oscillations. This effect, however, is much weaker than other effects like magnetic field gradients over the molecular sample, which limit the coherence time in the measurement.

3.3 Molecular level structure of ^{87}Rb$_2$

An important prerequisite for the transfer of molecules to lower lying states is precise knowledge of the level structure involved. We use a theoretical coupled-channel model to be described in the following as a tool to predict the energy spectrum of bound ^{87}Rb$_2$ molecules. Taking these calculations as a guideline we have carry out spectroscopic measurements with two different methods and generally find good agreement with the calculations.

3.3.1 Coupled channel model

In order to calculate the molecular level structure of ^{87}Rb$_2$ we use a coupled-channel model [Duli 95, Ties 98] based on adjusted *ab-initio* Born-Oppenheimer potentials, which was provided by Paul Julienne at NIST. This model allows the computation of the wavefunctions, eigenvalues and spin structure of the bound molecular states. From this data the magnetic dipole transition strength between the different levels as defined in Eq. 3.8 can be determined. In our group the model code was set up by Birgit Brandstätter and Peter van der Straten. A detailed description can be found in [Bran 07]. As an example, the molecular energy spectrum of states with angular

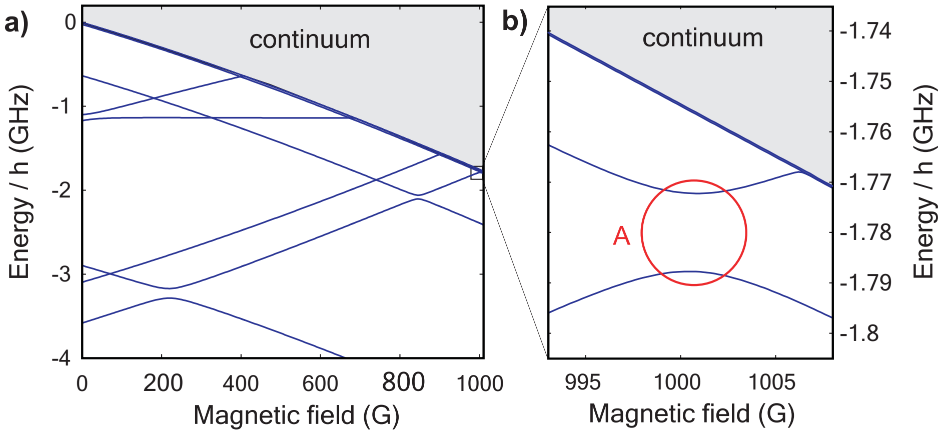

Figure 3.7:
Molecular energy spectrum. a) Shown is the Zeeman-like energy spectrum of bound s-wave states ($l = 0$) in ^{87}Rb$_2$ for $m_F = 2$ as calculated from the coupled channel model provided by NIST (see text). The grey area represents the continuum of free atom pairs $|f_1 = 1, m_{f1} = +1\rangle + |f_2 = 1, m_{f2} = +1\rangle$. b) Magnified view of the boxed region in a), showing the Feshbach resonance at 1007.4 G and an avoided crossing of two bound molecular states marked by the red circle (A).

momentum $l = 0$ ("s-wave states") for the region of interest in our experiments is shown in Fig. 3.7. In our experimental setup with the radio-frequency field aligned parallel to the magnetic bias field the selection rule $\Delta m_F = 0$ holds (see Sec. 3.1.2). Hence, only states with $m_F = 2$, same as for the Feshbach molecules, are shown.

3.3.2 Radio frequency spectroscopy

In order to permit rf-induced transfers over avoided crossings, the energy splitting between the two branches has to be determined in a first step. For this purpose we use two different spectroscopic methods which will be described in the following.

a) Resonant rf-spectroscopy

For this very intuitive method we expose the molecules to square rf-pulses at constant magnetic bias field B, and scan for the frequency of maximum transfer efficiency (see Fig. 3.8a). Repeating such measurements for different bias fields we find a hyperbolic dependence of the resonance frequency on the magnetic bias field B, as expected from our two-level model (compare Eqs. 3.12 and 3.13). In Fig. 3.8b data from a set of such

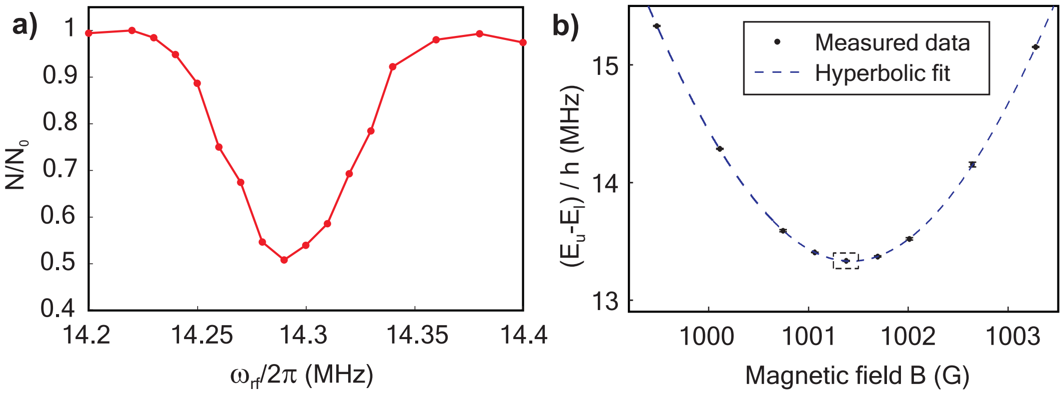

Figure 3.8:
Resonant rf-spectroscopy. a) Radio frequency scan. Shown is the fraction N/N_0 of molecules remaining in the upper branch of an avoided crossing after exposing them to rf-pulses of varying frequency. The data is taken at a magnetic field $B = 1000.1\,\mathrm{G}$, close to the avoided crossing A from Fig. 3.7b. The radio frequency pulses have a duration of 0.5 ms and a field amplitude $B_{\mathrm{rf}} = 16\,\mathrm{mG}$. b) The resonance frequency measured from scans as shown in a) has a hyperbolic dependence of the magnetic bias field B. The depicted data was taken at the avoided crossing A. The dashed line is a hyperbolic fit yielding a coupling $\Omega = 2\pi \times (13.331 \pm 0.005)\,\mathrm{MHz}$ and a center magnetic field $B_0 = (1001.4 \pm 0.002)\,\mathrm{G}$.

measurements at different magnetic fields is shown for the avoided crossing A from Fig. 3.7b. We have carried out similar measurements at the avoided crossings labeled C, E, and J in Fig 3.14. The data is given in Tab. 3.1.

b) Ramsey spectroscopy

We have also developed an alternative, Ramsey-type method to increase the precision of the previously described spectroscopic measurements. For this method we expose molecules in $|u\rangle$ to a slightly detuned $\pi/2$-pulse, which creates a 50/50-superposition of molecules in $|u\rangle$ and $|l\rangle$ (see Fig. 3.9a). After a hold time τ_h a second $\pi/2$-pulse is applied, which transfers the molecules to $|u\rangle$ or $|l\rangle$, depending on the relative phase between the molecular superposition state and the radio frequency field. Observing the number N of molecules detected in $|u\rangle$ as a function of τ_h we find an oscillation at a frequency ω_{osc} (Fig. 3.9b). The energy difference between $|u\rangle$ and $|l\rangle$ is then $E_u - E_l = \hbar(\omega_{\mathrm{rf}} \pm \omega_{osc})$ for red- and blue detuned rf-pulses respectively. In our measurements we reach coherence times up to 1 ms. In Fig. 3.10 data from a series of measurements at different magnetic fields corresponding to the dashed box in Fig. 3.8b is shown. The measured resonance frequencies clearly deviate from the ideal hyperbolic curve (dashed line in Fig. 3.10). This deviation is caused by a magnetic field

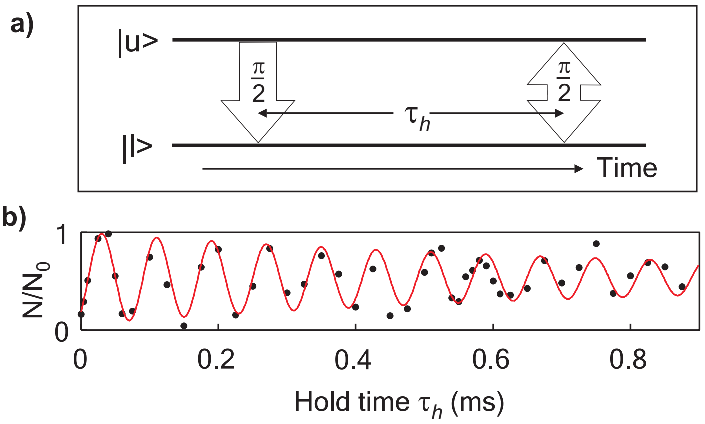

Figure 3.9:
Ramsey measurement. a) Schematic view. A $\pi/2$-pulse creates a 50/50-superposition of molecules in $|u\rangle$ and $|l\rangle$. After a certain hold time τ_h we apply a second $\pi/2$-pulse, and detect the number N of Feshbach molecules in $|u\rangle$. b) The fraction of detected molecules is shown as a function of hold time τ_h. The data was taken at avoided crossing A and a magnetic field $B = 1001.4\,\mathrm{G}$ with radio frequency pulses of $\omega_{\mathrm{rf}} = 2\pi \times 13.32\,\mathrm{MHz}$. We find an oscillation frequency $\omega_{osc} = 2\pi \times (12.43 \pm 0.14)\,\mathrm{kHz}$, corresponding to $E_u - E_l = (13.33243 \pm 0.00014) \times h\,\mathrm{MHz}$.

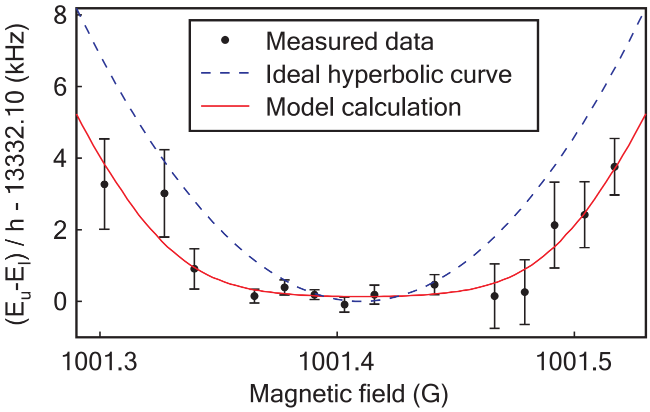

Figure 3.10:
Ramsey spectroscopy. Shown are the measured resonance frequencies for different magnetic fields in the region of the dashed box in Fig. 3.8a. The deviation of the data from the ideal hyperbolic curve (dashed blue line) is reproduced by a model calculation (solid red line) which takes experimental imperfections in to account (see text). The error bars represent a 95% uncertainty for the fit of ω_{osc}.

gradient over the molecular sample of about 2 Gmm^{-1} in combination with magnetic field fluctuations of about 20 mG during the scan. A model calculation taking these experimental imperfections into account (solid line in Fig. 3.10) reproduces the deviations. The 150 Hz difference between the minimum of the model curve and the hyperbola is due to an averaging effect over the magnetic field inhomogeneities. From the model we get a best estimate for the minimum splitting of the hyperbolic curve of $\Omega = 2\pi \times (13.33210 \pm 0.00015)$ MHz.

	partial waves	Ω ($2\pi\times$MHz)	B_0 (G)
A	s-s	13.33210 ± 0.00015	1001.4 ± 0.2
C	s-s	44.756 ± 0.006	845.8 ± 0.2
E	s-d	2.36 ± 0.01	466.1 ± 0.2
J	s-s	110.48 ± 0.01	218.8 ± 0.2

Table 3.1:
Data for avoided crossings. Given are the minimum splitting Ω and center magnetic field B_0 for the avoided crossings A, C, E and J of Fig. 3.14. The second column indicates the rotational quantum numbers of the involved molecular states. Splitting A is measured with both methods, while splittings C, E and J are determined via resonant spectroscopy only.

3.4 Transfer to more deeply bound states

Having spectroscopically determined the energy splitting of an avoided crossing, we can now tackle the problem of transferring molecules to the other branch. In this section an adiabatic transfer method that we have developed for this purpose will be introduced. This method was used to transfer the Feshbach molecules from more than 1000 G to 0 G, where they have a binding energy of about 3.6 GHz$\times h$.

3.4.1 Adiabatic Transfer across Avoided Crossings (ATAC)

Similar to the Rabi oscillations demonstrated in Sec. 3.2.4, molecules could in principle be transferred from $|u\rangle$ to $|l\rangle$ with a π-pulse of resonant rf-radiation. Such a transfer, however, is very sensitive to both pulse duration and amplitude. Magnetic field gradients lead to different pulse areas at different lattice sites, prohibiting unit transfer efficiency over the whole molecular sample. Additionally, even small fluctuations or drifts of the experimental parameters can cause significant deviations in transfer efficiency on both short and long timescales. We have thus developed an alternative method for efficient and robust radio frequency induced transfer between different

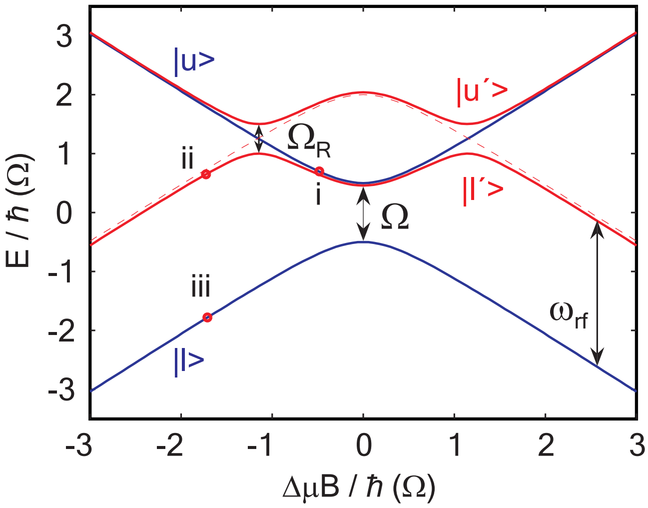

Figure 3.11:
ATAC transfer scheme. The upper and lower branch of an avoided crossing, $|u\rangle$ and $|l\rangle$ (solid blue lines), are coupled by rf of frequency ω_{rf}. Within the rotating wave approximation this gives rise to the dressed states $|u'\rangle$ and $|l'\rangle$ (solid red lines), with a splitting corresponding to the Rabi frequency Ω_R. Adiabatically following the path (i)-(ii)-(iii), molecules are transferred from $|u\rangle$ to $|l\rangle$ (see text). Note that for better visibility Ω_R was chosen larger than typically used in our experiments.

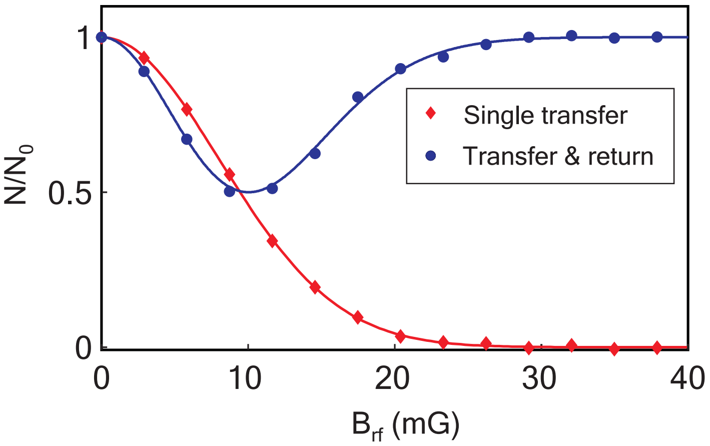

Figure 3.12:
ATAC transfer efficiency. Shown is the fraction of detected molecules after a single (red diamonds) and double (blue circles) ATAC transfer at avoided crossing A. The solid lines are fits from a Landau-Zener-model (see text). For the depicted data the magnetic field is ramped from 1001.4 G to 1000.1 G in 1 ms while molecules are exposed to an rf-pulse of frequency $\omega_{\mathrm{rf}} = 2\pi \times 13.6\,\mathrm{MHz}$.

molecular states. As an example, this method of Adiabatic populations Transfer across Avoided Crossings (ATAC) will now be discussed for the avoided crossing A.

Neglecting magnetic field noise we consider the RWA-Hamiltonian in the basis of the molecular states $|u\rangle$ and $|l\rangle$ from Eq. 3.24. The diagonalization of this Hamiltonian yields the new eigenstates $|u'\rangle$ and $|l'\rangle$, the so-called dressed states (see Fig. 3.11). For a transfer of molecules from $|u\rangle$ to $|l\rangle$ we start at a magnetic field at point (i) in Fig. 3.11 with the rf-field off. Switching on the blue-detuned radio frequency leads to a projection onto the dressed state $|l'\rangle$. With an adiabatic ramp-down of the magnetic field the molecules follow this state to the other side of the rf-induced avoided crossing (ii). After switching off the radio frequency, the molecules end up in level $|l\rangle$ (iii).

Experimental data for such an ATAC transfer at the avoided crossing A is shown in Fig. 3.12, where the fraction of detected Feshbach molecules is shown as function of rf-field amplitude B_{rf}. For sufficiently high B_{rf} no more molecules can be detected after a single transfer (red data). In order to detect the molecules again, a second ATAC transfer brings them back to the upper branch $|u\rangle$. The solid lines are calculations from a Landau-Zener-model [Vita 96], where the transfer probability for a single transition is given by

$$P_t = 1 - \exp(-\pi\Omega_R^2\hbar/2|\dot{B}|\Delta\mu_{u,l}). \qquad (3.45)$$

Here $|\dot{B}|$ is the ramp speed of the magnetic bias field and $\Delta\mu_{u,l} = |\mu_u - \mu_l|$ is the relative magnetic moment of $|u\rangle$ and $|l\rangle$[7]. From similar measurements with multiple transfers we deduce a single transfer efficiency of up to 99.5%.

For stronger rf-fields we observe a reduction in transfer efficiency, which is caused by loss due to the projections of the initial bare state $|u\rangle$ onto the dressed state $|l'\rangle$ at the beginning of the radio frequency pulse, and the projection from $|l'\rangle$ to the bare state $|l\rangle$ at the end of the rf-pulse. We have experimentally verified that this loss can be overcome by ramping the rf-amplitude up and down instead of switching it on and off.

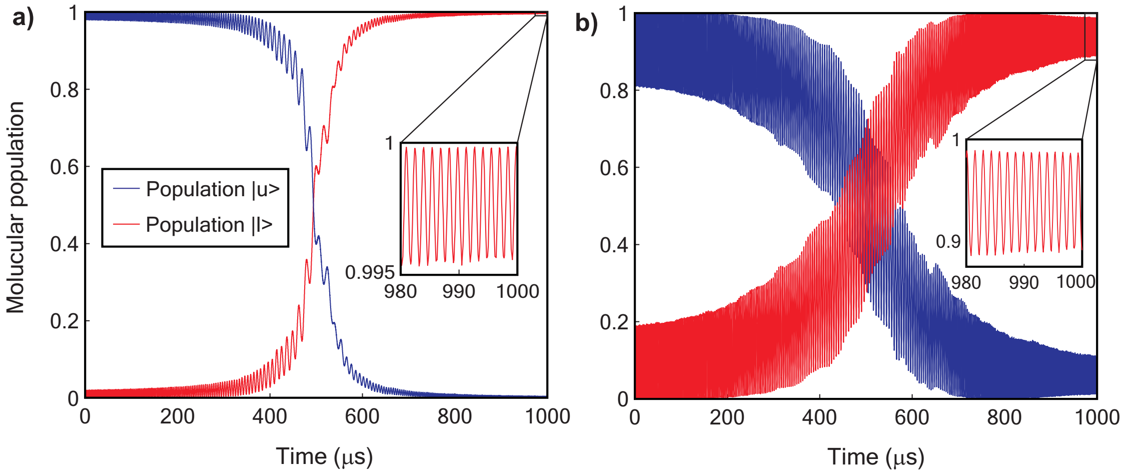

Figure 3.13:
Model simulation of ATAC transfer. a) The blue (red) line represent the population in state $|u\rangle$ ($|l\rangle$) during an ATAC transfer at avoided crossing A for typical experimental parameters, i.e. a magnetic field ramp from 1001.4 G to 1000.1 G in 1 ms and an rf-pulse with $\omega_{\mathrm{rf}} = 2\pi \times 13.6\,\mathrm{MHz}$ and $B_{\mathrm{rf}} = 0.03\,\mathrm{G}$. b) Same as a), but with the rf-amplitude increased to $B_{\mathrm{rf}} = 0.1\,\mathrm{G}$.

3.4.2 ATAC model simulation.

In order to test the approximations made in the previous section and to investigate the influence of magnetic field noise to such an ATAC population transfer we use the numerical model with the Hamiltonian from Eq. 3.44. In Fig. 3.13 simulations of ATAC transfers for the parameters of the data from Fig. 3.12 are shown. For a typical rf-amplitude of $B_{\mathrm{rf}} = 0.03\,\mathrm{G}$ we find an average efficiency higher than 99.5% (Fig. 3.13a), and only marginal fluctuations caused by magnetic field noise. This in good agreement

---

[7] Note that this differs from $\Delta\mu$ as defined in Sec. 3.2.1, which was defined with respect to the bare states $|b_1\rangle$ and $|b_2\rangle$.

with the experimentally determined value and the predictions of the Landau-Zener model from Sec. 3.4.1.

Fig. 3.13b shows a simulation for an increased rf-amplitude $B_{\mathrm{rf}} = 0.1\,\mathrm{G}$. In this case the projection of the bare state $|u\rangle$ onto the dressed state $|l'\rangle$ at the beginning of the transfer causes strong oscillations of the molecular populations and in consequence a reduction in transfer efficiency.

3.4.3 Transfer to zero magnetic field

In order to demonstrate the versatility of the ATAC scheme transfer, we transfer the Feshbach molecules to a more deeply bound state at zero magnetic field. We follow the state $|l = 0, F = f_1 = f_2 = m_F = 2, \nu = -5\rangle$ which induces the Feshbach resonance and has a binding energy of about $3.6\,\mathrm{GHz}\times h$ at $0\,\mathrm{G}$ (Fig. 3.14).

After a transfer over the first avoided crossing A as described in Sec. 3.4.1, the magnetic field is lowered to about 875 G. Just below this value we find an avoided crossing B with a d-wave state. Instead of traversing B, however, we use the ATAC scheme to transfer the molecules directly to the lower branch of the avoided crossing C (see right inset in Fig. 3.14). This is made possible by the large energy splitting of the avoided crossing C, which leads to a broad region of high magnetic coupling strength. In Fig. 3.15 the magnetic dipole matrix elements $\mu_{u,l}$ as calculated from the coupled-channel model are shown for the avoided crossings A and C. In agreement with Eq. 3.15, which was derived from our two-level model, the width of $\mu_{u,l}$ is proportional to the energy splitting of the respective avoided crossing.

Following the level $|l = 0, F = f_1 = f_2 = m_F = 2, \nu = -5\rangle$ to lower energies we encounter five avoided crossings with d-wave states (D,E,F,H,I). Their widths are all in the range of 1 MHz, and we use the ATAC scheme to cross them (as an example avoided crossing E is shown in the left inset in Fig. 3.14). In principle avoided crossings between s- and d-waves can be traversed in an analogous way as such purely consisting of s-waves. The narrow widths of the s-d-avoided crossings, however, make it technically more challenging to overcome them with the ATAC method. According Eq. 3.15 the matrix element $\mu_{u,l}$ and thus also Ω_R are resonantly peaked at the position of an avoided crossing, with a width proportional to the coupling strength Ω. In consequence Ω_R changes strongly during a magnetic field ramp in the vicinity of a narrow avoided crossing. This makes it demanding to find a compromise between losses due to the projection between bare and dressed state at the side of the ramp which is close to the avoided crossing and losses due to nonadiabaticity at the other side. The narrow region of strong coupling also increases the susceptibility to long-term drifts in the bias field and to magnetic field noise which can lead to undesired non-adiabatic transitions.

At 380 G we further observe an avoided crossing G with a g-wave, which due to its weak coupling can be crossed by diabatically ramping the magnetic field. After using the ATAC scheme to traverse the wide avoided s-wave crossing J and another crossing with a d-wave, K, we finally end up at 0 G in state $|l = 0, F = f_1 = f_2 = m_F = 2, \nu =$

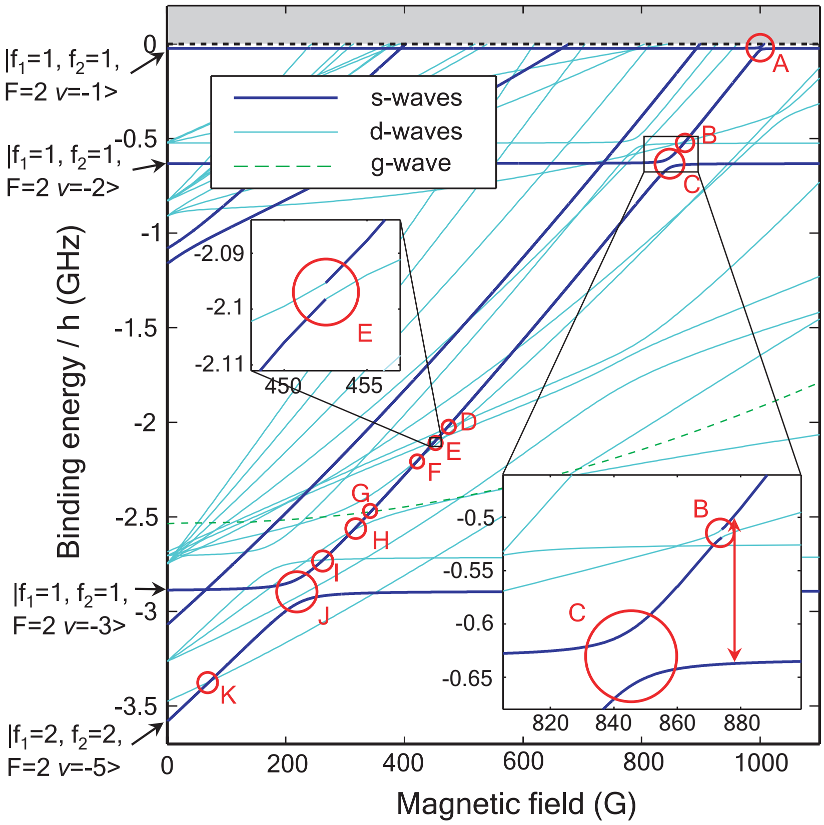

Figure 3.14:
ATAC transfer to 0 G. Shown are the molecular levels with $m_F = 2$ in the region relevant for our experiments. All states with $l = 0$ (solid blue lines, "s-waves") and $l = 2$ (solid cyan lines, "d-waves") as well as a single state with $l = 4$ (dashed green line, "g-wave") are depicted. In our experiments we follow the level $|l = 0, F = f_1 = f_2 = m_F = 2, v = -5\rangle$ to transfer the molecules to 0 G. For this we traverse the avoided crossings marked A-K with nine ATAC transfers (see text for details). Note that in contrast to Fig. 3.7 where the absolute energies of the different molecular states are plotted, this diagram shows the binding energies relative to the atomic $(|f_1 = 1, m_{f1} = +1\rangle + |f_2 = 1, m_{f2} = +1\rangle)$ dissociation threshold.

$-5\rangle$, at a binding energy of about 3.6 GHz×h. Alternatively we have skipped the last transfer to produce d-wave molecules by adiabatically following the avoided crossing K into the state $|l = 2, F = 0, f_1 = f_2 = m_F = 2, \nu = -5\rangle$.

The transfer to 0 G over 10 avoided crossings takes a total time of about 90 ms and has an overall efficiency of about 50%. The losses can mainly be explained by optical excitations by the lattice light (280 ms lifetime), and by not fully optimized transfers

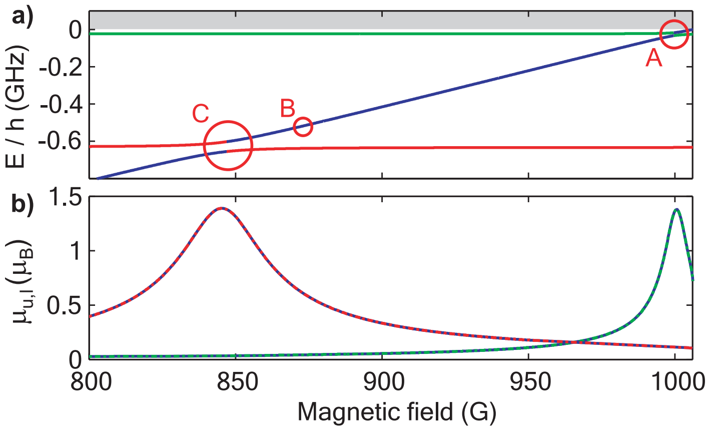

Figure 3.15:
Matrix elements for avoided crossings A and C. a) Magnification of the energy spectrum of Fig. 3.14, showing the avoided s-s-wave crossings A and C as well as the position of the avoided crossing B with a d-wave. The color coding identifies the bare molecular states which form the avoided crossing. b) The widths of the matrix elements $\mu_{u,l}$ for A and C calculated from the coupled-channel-model are proportional to the respective energy splittings.

at several avoided crossings.

3.4.4 Verification of molecular states

As the more deeply bound molecules can be observed only indirectly by reversing the previous transfer and dissociating them at the Feshbach resonance, we need a way to ensure that they really are in the desired quantum state. For this we use two methods. First, we check for consistency between the positions and energy splittings of the avoided crossings predicted by the coupled-channel model (Sec. 3.3.1) with the measured data. We generally find good agreement, with deviations of no more than a few Gauss for the center magnetic field, and about 5% for the energy splitting of the various avoided crossings.

In a second method we use optical spectroscopy to measure the binding energy of the molecules. The molecules are exposed to laser light tuned on the transition to the electronically excited level $|0_g^-, \nu = 31, J = 0\rangle$, located $6.87\,\mathrm{cm}^{-1}$ below the $(S_{1/2} + P_{3/2})$ dissociation asymptote [Fior 01]. On resonance, this excitation causes loss of molecules and thus a reduction in the signal observed after reconversion. From the measured shift of the resonance frequency and the known shift of the optically excited state, the binding energy can be deduced and compared to the predicted value.

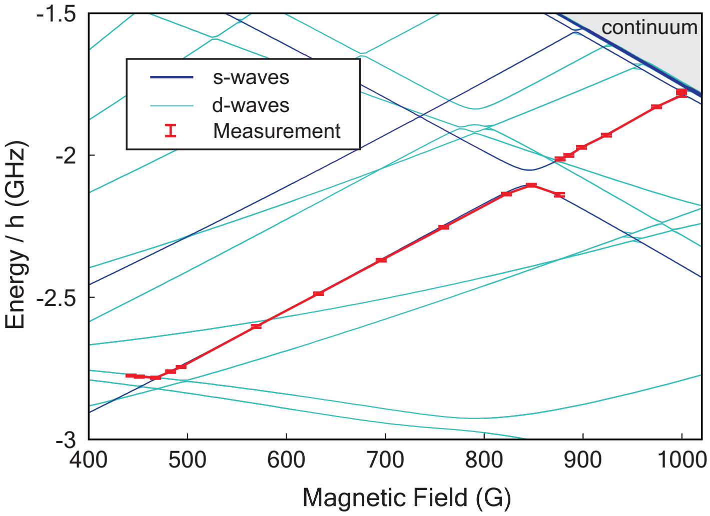

Figure 3.16:
Verification measurement. The red errorbars show the molecular binding energies measured by laser excitation to the molecular level $|0_g^-, \nu = 31, J = 0\rangle$ (for details see text). The solid red line connecting the error bars, which are barely resolved in this plot, is a guide to the eye.

Within the accuracy of our measurements of about $15\,\mathrm{MHz}\times h$ we find good agreement between theory and experimental data (see Fig. 3.16).

3.5 Rf-induced Feshbach resonances

In the last few years magnetic Feshbach resonances have proven to be a powerful tool in the field of ultracold gases, as they allow both control of atomic interactions and the formation of molecules (for reviews see e.g. [Kohl 06, Chin 08]). In different approaches, the manipulation of atomic scattering properties by optically induced Feshbach resonances [Fate 00, Thei 04, Thal 05] and by tuning magnetic Feshbach resonances with laser light [Baue 09] has been demonstrated. The following section will address the question of whether we can use rf to induce Feshbach resonances. For example, is it possible to exploit such a radio frequency Feshbach resonance to associate molecules from atom pairs? We will now discuss how an rf-induced Feshbach resonance would work within the adiabatic picture of the rotating wave approximation and compare it to a magnetic Feshbach resonance. A possible experimental implementation and our current limitations are discussed, and the experimental results are simulated with a numerical four-level model.

3.5.1 Magnetic- vs. rf-induced Feshbach resonances

In contrast to the bound-bound transitions treated in the previous sections, we now examine dynamics occurring directly at the molecular dissociation threshold, where the different atomic states have to be considered. As our experiments are carried out in an optical lattice with a depth of about $30\,\mathrm{E}_r$ for atoms, we can assume harmonic confinement. In this regime, the different lattice bands have a constant energy spacing $\hbar\omega_t$, where ω_t is the trap frequency. In Fig. 3.17 the molecular state $|m\rangle$ inducing the magnetic Feshbach resonance as well as the three lowest atomic pair states in the optical lattice, $|a_0\rangle$, $|a_1\rangle$ and $|a_2\rangle$ are shown as solid lines for the region around the magnetic Feshbach resonance at 1007.4 G. Note that this notation strictly holds only for magnetic fields below the Feshbach resonance. For $|m\rangle$, e.g., the molecular state is adiabatically connected to the lowest atomic trap state at magnetic fields above the resonance. The molecular and atomic states can be coupled with rf of Rabi frequency Ω_R. This leads to the formation of dressed states indicated by the dashed lines in Fig. 3.17, and an rf-induced Feshbach resonance marked by the red circle.

A key feature of a Feshbach resonance is sensitivity to the direction in which it is crossed. Detecting different outcomes for upward- and downward ramps of the magnetic field would thus experimentally distinguish a Feshbach resonance from non-adiabatic molecule formation.

In order to associate molecules via a magnetic Feshbach resonance we start with atom pairs in the lattice ground state above the resonance (point (k) in Fig. 3.17). By adiabatically ramping down the magnetic field to (kk) those pairs are converted into molecules. If we start with atom pairs in the lattice ground state at a magnetic field below the Feshbach resonance (l) and adiabatically ramp to higher values, the atoms are transferred into the first excited band of the lattice (ll).

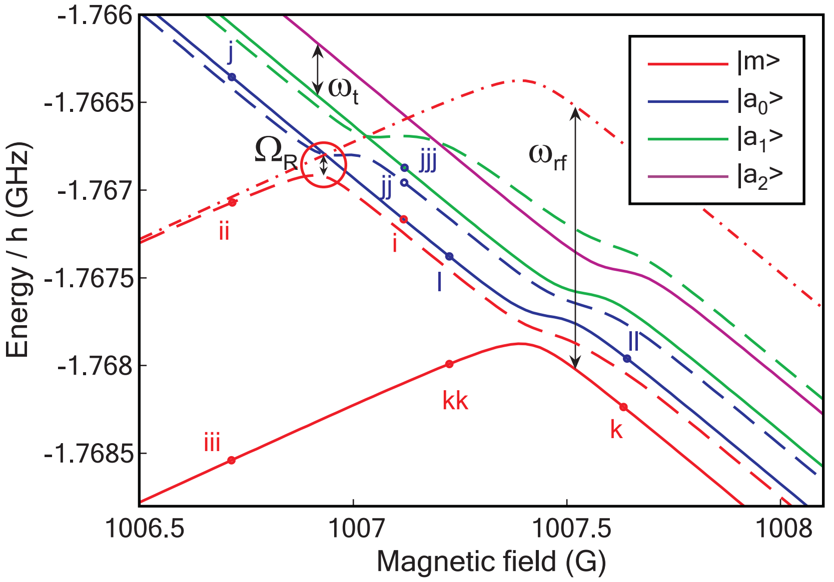

Figure 3.17:
Rf-induced Feshbach resonance. The solid lines represent the molecular $|m\rangle$ and atomic states $|a_0\rangle$, $|a_1\rangle$, $|a_2\rangle$ for the region around the Feshbach resonance at 1007.4 G. The radio frequency field couples these levels to form dressed states (dashed lines) and an rf-induced Feshbach resonance (red circle). For the association of molecules we ramp the magnetic bias field to follow the path (i)-(ii)-(iii), while the reverse ramp (j)-(jj)-(jjj) transfers the atoms to the first excited band of the lattice (see text for details). These processes are analogous to molecule association (k)-(kk) and excitation into a higher band (l)-(ll) via a magnetic Feshbach resonance. Note that for this diagram Ω_R and ω_t are chosen larger than in our experiments for better visibility.

We can now compare this to an rf-induced Feshbach resonance. Here the molecule association starts with atom pairs at a magnetic field above the rf-induced Feshbach resonance (i). After switching on the rf the magnetic bias field is ramped down, adiabatically following the rf-induced avoided crossing to the molecular side of the dressed state (ii). The radio frequency is then switched off, and the molecules end up at the point (iii) in state $|m\rangle$. The opposite process starts with atom pairs below the rf-induced Feshbach resonance (j). After adiabatically following the rf-induced dressed state to (jj) and switching off the radio frequency field, the atoms are in the first excited band of the lattice, $|a_1\rangle$ (jjj).

3.5.2 Magnetic dipole matrix elements for atom-molecule transitions

In general magnetic dipole matrix elements $\mu_{a,m}$ between the states of free (or trapped) atomic pairs $|a\rangle$ and bound molecules $|m\rangle$ of ^{87}Rb are too small to be experimentally exploited to drive rf-transitions (see [Bran 07]). Close to magnetic Feshbach resonances, however, atomic and molecular states mix, and $\mu_{a,m}$ can become on the order of μ_B. In Fig. 3.18 the matrix elements between the molecular state $|m\rangle$ and the three lowest atomic trap states $|a_0\rangle$, $|a_1\rangle$ and $|a_2\rangle$ as calculated from the close-coupled channel model (see Sec. 3.3.1) are plotted for the region around the magnetic Feshbach resonance at 1007.4 G. The matrix elements are peaked at the position of the Feshbach resonance, and quickly vanish away from it with FWHMs on the order of 100 mG. In contrast to the case of an avoided crossing of two molecular levels, the coupling strength is asymmetric with respect to the Feshbach resonance and does not reach a maximum value of $\Delta\mu/2$ (compare Eq. 3.15). These effects are due to the other atomic lattice states which also mix with the molecular state and lead to a reduction of $\mu_{a,m}$. This reduction and the small width of the coupling strength imply that the challenges arising for ATAC at narrow avoided crossings as discussed in Sec. 3.4.3 become even more delicate for the implementation of rf-induced Feshbach resonances. In particular, according to the Landau-Zener-model from Sec. 3.4.1, the transfer probability for ATAC is in first order proportional $\Omega_R^2 \propto \mu_{a,m}^2$.

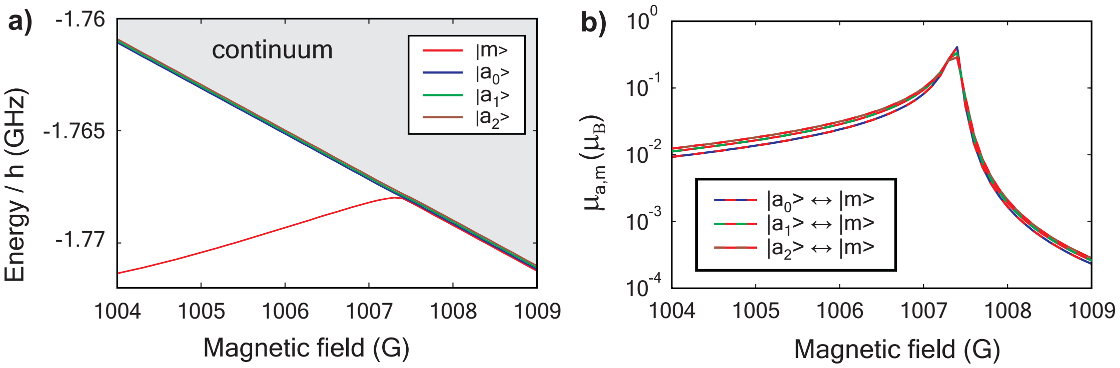

Figure 3.18:
Matrix elements for free-bound transitions. a) As in Fig. 3.17 an energy diagram of the states $|m\rangle$, $|a_0\rangle$, $|a_1\rangle$ and $|a_2\rangle$ is shown for a region around the magnetic Feshbach resonance at 1007.4 G. b) The matrix elements $\mu_{a,m}$ for magnetic dipole transitions between the state $|m\rangle$ and the states $|a_0\rangle$, $|a_1\rangle$, $|a_2\rangle$ as calculated from the close-coupled channel model (see Sec. 3.3.1) are given for the region shown in a). Note the logarithmic scale for the axis of ordinates. Plot adapted from [Bran 07].

3.5.3 A possible experimental realization

Compared to adiabatic transfer at an avoided crossing of two molecular states, the implementation of an rf-induced Feshbach resonance is much more challenging. This is mainly due to the reduced maximum coupling strength, the narrow region of strong coupling and the numerous close-lying atomic lattice states which can lead to parasitic coupling. In this section we will discuss the possible experimental realization of such an association scheme and its technical limitations.

Preparation of atomic pairs

The starting point for our rf-association experiments is a pure sample of atomic pairs in the lowest band of the optical lattice at a magnetic field below the magnetic Feshbach resonance (point (i) in Fig. 3.17). To prepare such a sample, we begin with the same experimental procedure as for the pure ensemble of Feshbach molecules described in Chap. 2. At the end of this preparation cycle the molecules are in the lowest band of the optical lattice at a magnetic field of about 995 G, slightly below the Feshbach resonance. The molecules are then dissociated into pairs of atoms by adiabatically ramping the magnetic field to a value above the Feshbach resonance. In a next step we quickly switch off the magnetic field within 250 μs, so that the atom pairs diabatically cross the Feshbach resonance without being associated to molecules again. Finally the magnetic field is ramped up to a value just below the magnetic Feshbach resonance. From subsequent association measurements via the magnetic Feshbach resonance we deduce that about 85% of the atoms are in doubly occupied sites at the end of this procedure.

Atom-molecule spectroscopy

In order to determine the resonance frequency for magnetic dipole transitions between atom pairs and molecules, we adapt a procedure analogous to that for resonant molecular spectroscopy described in Sec. 3.3.2. The magnetic bias field is kept constant at a value just below the magnetic Feshbach resonance, while the atom pairs are exposed to a square rf-pulse of varying frequency. After the pulse, the number of remaining atoms is detected without ramping over the Feshbach resonance again, so that molecules produced by the radio frequency radiation lead to a reduction of the observed signal. If the rf is resonant with the free-bound transition, Rabi oscillations between pairs of atoms and molecules are driven. Inhomogeneities in the magnetic bias- and rf-field cause dephasing of the oscillations over the atomic/molecular cloud. For long pulse times $\tau_p \gg 2\pi/\Omega_R$ this finally leads to a 50/50 distribution of atomic pairs and molecules averaged over the sample, and the fraction of observed atoms drops to 1/2 (Fig. 3.19a). For shorter pulse times $\tau_p \gtrsim 2\pi/\Omega_R$ we observe strong fluctuations in the number of detected atoms ranging from $N_0/2$ to N_0 (Fig. 3.19b). We attribute this to noise in the magnetic bias field, which can shift the atom-molecule transition out of resonance with

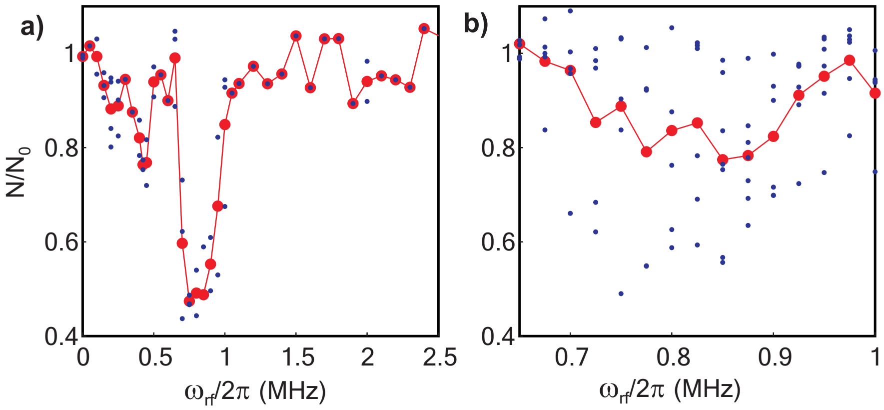

Figure 3.19:
Free-bound spectroscopy. a) Atomic pairs are held at a constant magnetic bias field slightly below the magnetic Feshbach resonance at 1007.4 G. Shown is the fraction of detected atoms after subjecting the pairs to square rf-pulses of varying frequency. Each small dot represents a single measurement, while the red circles show the average over the different experimental runs at a specific magnetic bias field. The broad resonance around 0.8 MHz indicates the association of molecules. We attribute the more narrow resonance features at 0.4 MHz and 0.2 MHz to higher harmonics of the rf-radiation. The data was taken at a bias field $B_0 = 1007.1$ G with rf-pulses of $B_{\text{rf}} = 50$ mG and $\tau_p = 2$ ms. The solid line connecting the data points is a guide to the eye. b) Same as a), but for shorter pulse time $\tau_p = 0.2$ ms.

the radio frequency field. From the width of the resonance and the relative magnetic moment between the atomic and molecular state we deduce a peak-to-peak magnetic field noise amplitude of about 60 mG. This value is in agreement with the noise level previously determined through other techniques (Sec. 3.2.5).

Association of molecules

As discussed in Sec. 3.5.1, the association of molecules starts from atom pairs held at a magnetic bias field below the magnetic Feshbach resonance. The magnetic field is then ramped to a lower value while the atoms are exposed to a radio frequency field. Due to the narrow region of high magnetic coupling strength $\mu_{a,b}$ this whole process should be carried out as close to the magnetic Feshbach resonance as possible. At the same time, however, we have to guarantee that the magnetic Feshbach resonance is not accidentally crossed due to fluctuations in the magnetic bias field, which would lead to the production of molecules simply by "ramping" over the magnetic Feshbach

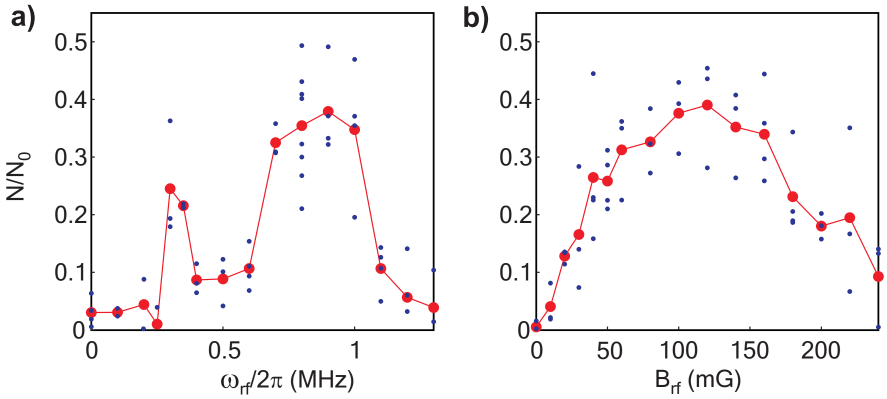

Figure 3.20:
Molecule association. a) Shown is the fraction of atom pairs converted into molecules with our ATAC-like association scheme as a function of rf-frequency. The blue dots represent single measurements while the red circles are the respective values averaged over all experimental cycles. For this scan the magnetic bias field is ramped from 1007.2 G to 1007.0 G in 0.6 ms while magnetic radio frequency with an amplitude of $B_{\mathrm{rf}} = 100\,\mathrm{mG}$ is applied. The broad signal between 0.6 MHz and 1.1 MHz stems from association at the rf carrier frequency, while we attribute the narrow signal around 0.4 MHz to the higher harmonic. b) Same as a) but for constant frequency $\omega_{\mathrm{rf}} = 2\pi \times 0.9\,\mathrm{MHz}$ and varying amplitude B_{rf}.

resonance. Additionally, the low-pass behavior of the magnetic field regulation circuit requires a certain time until the desired ramp speed is reached. Due to these technical limitations we start the rf-pulse at leasst 0.2 G from the magnetic Feshbach resonance. After the association has occurred, we have to ensure that only molecules, but none of the remaining atoms are detected. We thus apply a second purification pulse of combined microwave- and laser radiation (see Sec. 2.5), which removes the unbound atoms. Finally the molecules are dissociated by ramping over the magnetic Feshbach resonance and detected with our standard absorption technique.

In Fig. 3.20a the number of molecules associated with this scheme is shown as a function of rf-frequency. We observe a broad association signal around 0.8 MHz with a maximum efficiency of about 40% and a more narrow feature at 0.4 MHz. We attribute the latter to the second harmonic of the radio frequency radiation which is an artifact of the final amplification stage (Frankonia FLL25 amplifier). The number of molecules produced at constant frequency is shown as a function of rf-amplitude in Fig. 3.20b. The association efficiency reaches a maximum of about 40% at $B_{\mathrm{rf}} \approx 120\,\mathrm{mG}$ and decreases again for higher amplitudes. We attribute this decrease mainly to losses caused by cross-talk between the radio frequency field and the stabilization circuit of the magnetic bias field (for a discussion see Sec. 3.1.1). This cross-talk occurs at high rf-amplitudes and leads to an oscillation of the magnetic bias field and subsequent loss of atoms and molecules.

In the data from Fig. 3.20 strong shot-to-shot fluctuations in transfer efficiency are also evident. Numerical simulations from our time-dependent model suggest that these fluctuations as well as the limited average transfer efficiency are due to noise in the magnetic bias field (see Sec. 3.5.4).

Reverse ramp direction

The fact that the association efficiency of the experiments presented in the previous section is lower than 0.5 shows that we are not in the adiabatic regime. However, we can distinguish an rf-induced Feshbach resonance from "incoherent" formation of molecules at constant bias by detecting different outcomes for different ramp directions of the magnetic bias field. For adiabatic ramps, we expect to form molecules in the case of decreasing magnetic bias field, while an increasing ramp should lead to the excitation of atoms into higher bands (see Sec. 3.5.1). We thus repeat the association measurements from the previous section, but with the magnetic bias field ramp reversed. In Fig. 3.21a the number of produced molecules at constant rf-amplitude is shown as a function of ω_{rf}. We generally find strong fluctuations of the observed signal, where the average fraction

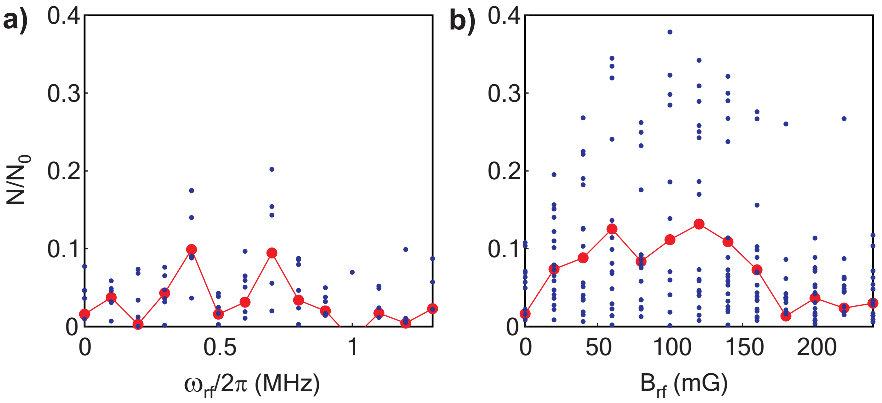

Figure 3.21:
Reverse ramp direction. Shown are measurements for conditions similar to those in Fig. 3.20, but with the magnetic bias field ramped from lower to higher values. a) Atom pairs are exposed to an rf-pulse of fixed amplitude $B_{\mathrm{rf}} = 120\,\mathrm{mG}$, while the magnetic bias field is ramped from 1007 G to 1007.2 G in 0.6 ms. b) The magnetic bias field is ramped from 1006.9 G to 1007.2 G in 1 ms while rf is applied at constant frequency $\omega_{\mathrm{rf}} = 2\pi \times 0.7\,\mathrm{MHz}$.

of produced molecules has two maxima of about 0.1 around 0.4 MHz and 0.7 MHz. As in the previous measurements from Figs. 3.19 and 3.20 we attribute the latter to the rf carrier frequency and the former to the second harmonic. In Fig. 3.21b the number of molecules produced at constant frequency is shown as a function of rf-amplitude. Again the signal is very noisy, with an average "efficiency" around 0.1 for $B_{\rm rf}$ between 50 mG and 150 mG. While this signal is obviously not zero in contrast to what is expected for an adiabatic ramp, it is clearly lower than for association measurements at decreasing bias field ramps (compare Fig. 3.20). From our numerical model we find that the deviations from the ideal case as well as the fluctuations are primarily caused by magnetic bias field noise (see Sec. 3.5.4).

3.5.4 Four-level model for rf-induced Feshbach resonance

We use an extended version of our previously discussed numerical model to simulate an rf-induced Feshbach resonance. This takes place at the atomic dissociation threshold, where there are many different lattice states separated from each other by multiples of the trap frequency ω_t (about $2\pi\times 30$ kHz for our typical parameters). These states have to be considered as well, and a two-level model is no longer sufficient. We thus extend our previous model to four levels including the molecular state which causes the Feshbach resonance and the three lowest atomic pair states in the optical lattice[8]. In the basis of these bare states the Hamiltonian for the system then reads

$$\begin{aligned}\hat{H} &= (B - B_0 + B_{\rm rf}\cos(\omega_{\rm rf}t) + B_{\rm n}(t))\begin{pmatrix}\mu_m & 0 & 0 & 0\\ 0 & \mu_a & 0 & 0\\ 0 & 0 & \mu_a & 0\\ 0 & 0 & 0 & \mu_a\end{pmatrix} + \\ &+ \frac{\hbar}{2}\begin{pmatrix}0 & \Omega_{a,m} & \Omega_{a,m} & \Omega_{a,m}\\ \Omega_{a,m} & 0 & 0 & 0\\ \Omega_{a,m} & 0 & 2\omega_t & 0\\ \Omega_{a,m} & 0 & 0 & 4\omega_t\end{pmatrix},\end{aligned} \tag{3.46}$$

where μ_m and μ_a are the magnetic moment of the molecular and atomic states respectively and $\Omega_{a,m}$ is the coupling between atomic and molecular state which induces the magnetic Feshbach resonance.

We first simulate rf-induced association of molecules (path (i)-(ii)-(iii) in Fig. 3.17), in particular the measurement shown in Fig. 3.20. For this we start with atom pairs in $|a_0\rangle$ and ramp the magnetic bias field from 1007.2 G to 1007.0 G in 0.6 ms, while the atom pairs are exposed to rf of $B_{\rm rf} = 100$ mG and $\omega_{\rm rf} = 2\pi\times 0.9$ MHz. Our lattice trap frequency is $\omega_t = 2\pi \times 30$ kHz, and for the magnetic Feshbach resonance at 1007.4 G

---

[8] These states are not equivalent to $|m\rangle$, $|a_0\rangle$, $|a_1\rangle$ and $|a_2\rangle$, which we have defined as the respective eigenstates of the magnetic Feshbach resonance including the atom-molecule coupling, $\Omega_{a,m}$.

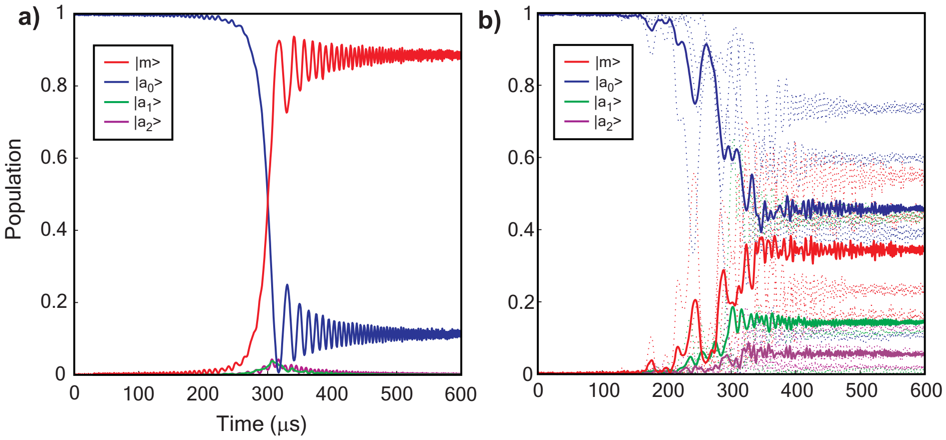

Figure 3.22:
Model simulation of an rf-induced molecule association. a) Shown is the time evolution of the population in the states $|m\rangle$, $|a_0\rangle$, $|a_1\rangle$ and $|a_2\rangle$ for the same parameters as in the measurement from Fig. 3.20, but without magnetic bias field noise. b) Same as a), but with included magnetic noise. The dotted lines show four individual runs of the simulation, while the solid lines represent their average. In these simulations the magnetic bias field is ramped from 1007.2 G to 1007.0 G in 0.6 ms, while the atom pairs are exposed to magnetic radio frequency with $B_{\rm rf} = 100\,{\rm mG}$ and $\omega_{\rm rf} = 2\pi \times 0.9\,{\rm MHz}$.

we have $\Omega_{a,m} = 2\pi \times 0.3\,{\rm MHz}$ [Thal 06, Syas 07] and $\mu_m - \mu_a = h \times 3.6\,{\rm MHz/G}$. In Fig. 3.22a the corresponding time evolution of the populations in the different states is shown for negligible magnetic bias field noise. The association process is mostly adiabatic with an efficiency of about 90%. Figure 3.22b shows a simulation for the same parameters but with magnetic field noise at a level typically occurring in our experiments (i.e. same amplitude as shown in Fig. 3.6). Four different runs are plotted as dashed lines, while their average is represented by the solid lines. We find strong variations over the different runs, and a reduction of the average transfer efficiency to about 40%. In some of the runs diabatic transfer of a sizable fraction of the atoms into excited lattice bands can be observed.

In the next step we investigate the "inverse" ramp over the rf-induced Feshbach resonance, corresponding to the path (j)-(jj)-(jjj) in Fig. 3.17 and the data shown in Fig. 3.21 respectively. For this we use the same parameters as in the previous simulation, but ramp the magnetic field in the opposite direction, from 1007.0 G to 1007.2 G. Again, we first neglect the noise of the magnetic bias field, and find mostly adiabatic behavior (see Fig. 3.23a). About 85% of the atoms are transferred into the first excited lattice band $|a_1\rangle$, while the states $|a_2\rangle$ and $|m_0\rangle$ remain almost unpopulated.

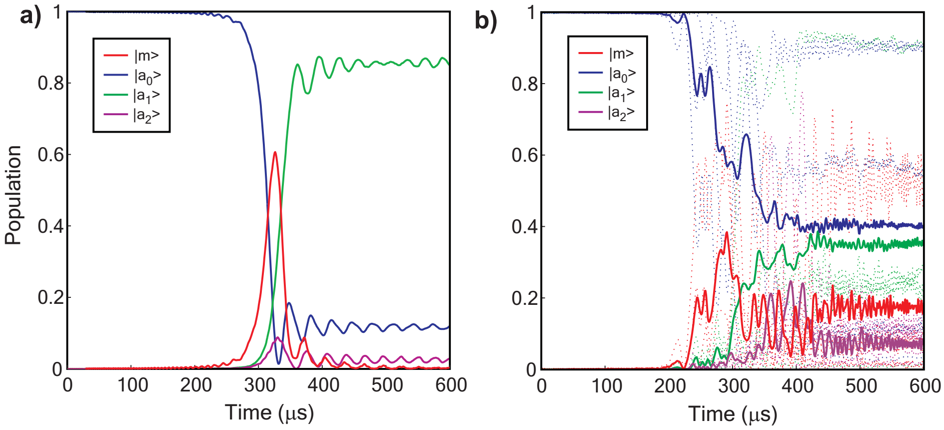

Figure 3.23:
Simulation of the reverse path over the rf-induced Feshbach resonance, corresponding to (j-jjj) in Fig. 3.17. Apart from the reversed direction of the magnetic bias field ramp the parameters are the same as for Fig. 3.22 a) Time evolution without magnetic field noise. The atoms are mostly transferred into the first excited lattice band $|a_1\rangle$, in accordance with the expectations for an adiabatic ramp. b) Same as a), but with included magnetic field noise. As in Fig. 3.22b dashed lines give the populations for four individual runs of the simulation, while the solid lines show their respective average. Again the noise leads to strong fluctuations between the different runs, where in this case the average final population in the molecular state $|m\rangle$ is increased.

If we include magnetic noise in the simulation we again find strong fluctuations over the different runs (see Fig. 3.23b). On average the fraction of atoms transferred into the first excited band drops to about 40%, while the number of molecules produced increases considerably to almost 20%, about half the value for the association procedure.

These simulations show that noise in the magnetic bias field is a limiting factor in our experiments. From further investigations we find that noise from practically the entire frequency spectrum used in the simulations has a detrimental influence. A reduction of this noise could be reached e.g. by using a power supply with ultra-high stability for the generation of the magnetic bias field, or by a considerable improvement of the field stabilization control circuit.

3.5.5 Width of rf-induced Feshbach resonance

In order to characterize the rf-induced Feshbach resonance we compare its width $\Delta B'$ with that of the magnetic Feshbach resonance which was used to induce it, ΔB. According to [Syas 07] the matrix element between open and closed channels for a magnetic Feshbach resonance with two atoms in the ground state of an optical lattice as entrance channel can be written as

$$\langle\Psi_a|H|\Psi_m\rangle = \left[\frac{4\pi\hbar^2 a_{bg}\Delta\mu\Delta B}{m(\sqrt{2\pi}a_{ho})^3}(1+0.49\frac{a_{bg}}{a_{ho}})\right]^{1/2} \equiv \hbar\Omega_{a,m}/2, \tag{3.47}$$

where a_{bg} is the background scattering length, and $a_{ho} = \sqrt{\hbar/(m\omega_t)}$ the harmonic oscillator length. Implicitly defining $\Delta B'$ we can write an analogous expression for the rf-induced Feshbach resonance,

$$\langle\Psi_a|H_{rf}|\Psi_m\rangle = \left[\frac{4\pi\hbar^2 a_{bg}\Delta\mu\Delta B'}{m(\sqrt{2\pi}a_{ho})^3}(1+0.49\frac{a_{bg}}{a_{ho}})\right]^{1/2} = \hbar\Omega_R/2, \tag{3.48}$$

where the second equality implies that the rotating wave approximation is valid. Comparing Eqs. 3.47 and 3.48 and using Eq. 3.20 we obtain

$$\Delta B' = \Delta B\left(\frac{\Omega_R}{\Omega_{a,m}}\right)^2 = \Delta B\left(\frac{\mu_{a,m}B_{\mathrm{rf}}}{\hbar\Omega_{a,m}}\right)^2. \tag{3.49}$$

Hence, the width of the rf-induced Feshbach resonance is proportional to the square of the Rabi frequency. For typical experimental parameters used in the simulations shown in Figs. 3.22 and 3.23 we have a Rabi frequency of $\Omega_R = 2\pi\times 11\,\mathrm{kHz}$. Compared to the magnetic Feshbach resonance with $\Delta B = 210\,\mathrm{mG}$ [Mart 02, Volz 03] this leads to a reduction in width by a factor $(\Omega_{a,m}/\Omega_R)^2 \simeq 750$ to $\Delta B' = 0.28\,\mathrm{mG}$. For a radio frequency field of same amplitude but applied directly at the center of the magnetic Feshbach resonance, these values would increase only moderately to $\Omega_R = 2\pi\times 16\,\mathrm{kHz}$ and $\Delta B' = 0.60\,\mathrm{mG}$. This can be mainly attributed to the reduced maximum coupling strength $\mu_{a,m}$, which is caused by the admixture of higher lattice bands (see Sec. 3.5.2). For a hypothetical value $\mu_{a,m} = |\mu_a - \mu_m|/2$ obtained at the center of an avoided crossing of only two states (see Eq. 3.15), we could expect a Rabi frequency $\Omega_R = 2\pi\times 180\,\mathrm{kHz}$ and a width $\Delta B' = 75\,\mathrm{mG}$.

4 Coherent optical transfer of Feshbach Molecules into the rovibrational triplet ground state

The production of ultracold molecules via magnetic Feshbach resonances is highly effective, reversible and adiabatic, and mostly conserves the phase space density of the atomic sample. While translationally cold, however, these molecules are produced in highly excited vibrational states. When composed of bosonic atoms, such vibrationally excited molecules are susceptible to collisional relaxation to more deeply bound states [Staa 06, Zahz 06]. The energy released in this process easily exceeds typical trap depths, leading to loss of the colliding particles. This decay mechanism can be circumvented by transferring Feshbach molecules into the rovibrational ground state, where they should be stable under collisions. A way to realize such a transfer is to to load an atomic BEC into a three-dimensional optical lattice, form molecules and transfer them into the rovibrational ground state with a series of Raman pulses. By subsequently ramping down the optical lattice, a molecular BEC could be produced [Jaks 02]. Heteronuclear molecules in deeply bound vibrational states possess a much stronger dipole moment than Feshbach molecules, allowing them to be used for quantum computation [DeMi 02], the realization of novel quantum phases [Sant 00, Buch 07] or the search for an electric dipole moment of the electron [Hind 97, Huds 05].

In 2007 our group performed a proof-of-principle experiment where the vibrational quantum number of Feshbach molecules held in a three-dimensional optical lattice is reduced by one unit with a STIRAP transfer. This transfer, which is described in detail in the doctoral thesis of Klaus Winkler [Wink 07b], increases the binding energy of the Feshbach molecules from about $24\,\mathrm{MHz}\times h$ to $637\,\mathrm{MHz}\times h$ [Wink 07a]. In the following year we reported the transfer of Feshbach molecules into the rovibrational ground state of the $a^3\Sigma_u^+$ triplet potential using the same scheme [Lang 08b]. This chapter is mainly dedicated to a detailed discussion of these experiments.

Bound states of diatomic alkaline molecules can be described by a triplet- and a singlet potential, depending on whether the configuration of the valence electron spins is symmetric or antisymmetric. The absolute ground state of the system is in the singlet potential, which is typically one order of magnitude deeper than the triplet potential. Our choice of using the rovibrational triplet ground state as final state for the STIRAP transfer has several reasons. In contrast to the singlet, triplet states have a magnetic moment and thus a rich level structure, with the possibility of molecule-molecule Feshbach resonances. The collisional properties of molecules in the triplet ground state have not yet been investigated and are to date subject of speculation. Additionally a transfer to the triplet ground state of $^{87}\mathrm{Rb}_2$ has the advantage of being technically less involved than one to the ground state of singlet potential. Due to unfavorable Franck-Condon overlaps the transfer of Feshbach molecules to the rovibrational $X^1\Sigma_g^+$ ground state requires two STIRAP transfers [Danz 09], while the triplet ground state can be reached in a single step.

In the first section of this chapter the concept of STIRAP is introduced. This optical Raman transfer scheme is based on adiabatic ramping of a dark state, leading to a coherent population transfer. In the following the resulting requirements on the utilized laser system are analyzed. To bridge the binding energy of the triplet ground state of about $7\,\mathrm{THz}\times h$, two lasers operating at different wavelength have to be stabilized relative to each other. In Sec. 4.2 the laser system we set up for this purpose is described in detail.

A mandatory requirement for successful STIRAP is precise knowledge of the involved states. "Conventional" spectroscopy in thermal Rb_2 has, generally, investigated the singlet potential, while at the time we started our experiments the $a^3\Sigma_u^+$ triplet potential was mostly unexplored. In Sec. 4.3 the spectroscopic measurements carried our to identify appropriate intermediate and final states for the STIRAP transfer are briefly described. A more detailed analysis will follow in the doctoral thesis of Christoph Strauss.

The actual transfer into the triplet ground state is presented in Section 4.4. We reach a single transfer efficiency of close to 90% and simulate the experiment with a master-equation based numerical model.

The ground state molecules experience a much weaker lattice potential than those in the Feshbach state. This leads to coherent molecular oscillations, which are discussed in Sec. 4.5. We present a numerical model taking into account the Bloch band structure, which reproduces these lattice-induced molecular dynamics.

4.1 STimulated Raman Adiabatic Passage (STIRAP)

STimulated Raman Adiabatic Passage (STIRAP) was developed in the group of Klaas Bergmann [Berg 98] and is known as a fast and efficient tool for population transfer. We will now introduce the basic concept of STIRAP following the lines of [Vita 01].

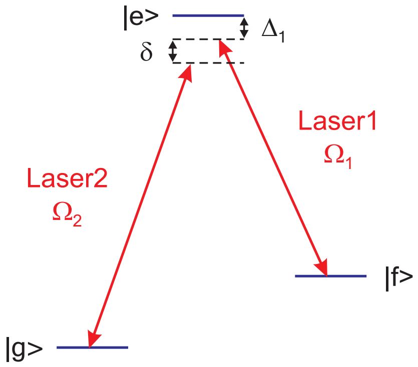

Figure 4.1:
λ-type three-level system. The electronic ground states $|f\rangle$ ($|g\rangle$) are coupled to the excited state $|e\rangle$ by laser 1 (2). The one- and two photon detuning are denoted Δ_1 and δ respectively (see text).

In a λ-type three-level system the lasers 1 and 2 couple the initial state $|f\rangle$ and final state $|g\rangle$ to the electronically excited state $|e\rangle$ (see Fig. 4.1). The one-photon detuning for laser 1 is $\Delta_1 = (E_e - E_f)/\hbar - \omega_1$ and the two-photon detuning $\delta = (E_f - E_g)/\hbar - \omega_2 + \omega_1$, with $\omega_{1,2}$ the frequencies of laser 1,2 respectively. In the rotating-wave approximation (RWA) the Hamiltonian driving the probability amplitudes

$$\mathbf{c} = \begin{pmatrix} c_f \\ c_g \\ c_e \end{pmatrix} \tag{4.1}$$

reads

$$\hat{H} = \hbar \begin{pmatrix} 0 & 0 & \Omega_1/2 \\ 0 & \delta & \Omega_2/2 \\ \Omega_1/2 & \Omega_2/2 & \Delta_1 \end{pmatrix} . \tag{4.2}$$

Here $\Omega_{1,2}$ are the Rabi frequencies for lasers 1,2 with

$$\Omega_1 = \frac{\langle f|\hat{\mathbf{d}}|e\rangle \mathbf{E_0}}{\hbar}, \tag{4.3}$$

where $\hat{\mathbf{d}}$ is the electric dipole operator and $\mathbf{E_0}$ is the amplitude of the electric field. In the Hamiltonian from Eq. 4.2 we have neglected the spontaneous decay rate Γ of the excited state $|e\rangle$, which is justified for

$$\Omega_{\text{eff}} \gg \Gamma, \tag{4.4}$$

with $\Omega_{\text{eff}} = \sqrt{\Omega_1^2 + \Omega_2^2}$ the effective Rabi frequency. For zero two-photon detuning $\delta = 0$ the eigenstates of this Hamiltonian are

$$\begin{aligned} |BS^+\rangle &= \sin\theta\sin\phi|f\rangle + \cos\phi|e\rangle + \cos\theta\sin\phi|g\rangle, && (4.5)\\ |DS\rangle &= \cos\theta|f\rangle - \sin\theta|g\rangle, && (4.6)\\ |BS^-\rangle &= \sin\theta\cos\phi|f\rangle - \sin\phi|e\rangle + \cos\theta\cos\phi|g\rangle, && (4.7) \end{aligned}$$

with mixing angles

$$\begin{aligned} \theta &= \arctan(\Omega_1/\Omega_2), && (4.8)\\ \phi &= \tfrac{1}{2}\arctan(\sqrt{\Omega_1^2 + \Omega_2^2}/\Delta_1). && (4.9) \end{aligned}$$

The respective eigenenergies are

$$\begin{aligned} \epsilon_{DS}(t) &= 0, && (4.10)\\ \epsilon_{BS}^{+,-}(t) &= \frac{\hbar}{2}\left(\Delta_1 \pm \sqrt{\Delta_1^2 + \Omega_1^2 + \Omega_2^2}\right). && (4.11) \end{aligned}$$

We note that the so-called bright states $|BS^{+,-}\rangle$ have contributions from the electronically excited state $|e\rangle$ and are thus subject to radiative decay. The dark state $|DS\rangle$ is a coherent superposition of the electronic ground states $|f\rangle$ and $|g\rangle$ only and thus intrinsically stable [Arim 76]. The population transfer via STIRAP occurs through the state $|DS\rangle$: By ramping the Rabi frequencies from the case $\Omega_1/\Omega_2 = 0$ ($\theta = 0$) to $\Omega_2/\Omega_1 \to \infty$ ($\theta = \pi/2$), the dark state changes from a state with pure $|f\rangle$ character to one consisting of $|g\rangle$ only. This transfer scheme is often referred to as "counterintuitive" because at its beginning only state $|f\rangle$ and laser 2, which do not couple to each other are present, while the situation is reversed at the end of the sequence. Given that the ramp is conducted in an adiabatic fashion, the system stays in the dark state during the transfer, and losses due to excitation to $|e\rangle$ are negligibly small. More specifically, the condition for adiabaticity is that the coupling between dark and bright states is much smaller than the energy difference between those states,

$$|\langle \dot{DS}|BS^{+,-}\rangle| \ll |\epsilon_{ds} - \epsilon_{bs}^{+,-}|. \tag{4.12}$$

For zero one-photon detuning $\Delta_1 = 0$ this condition simplifies to

$$|\dot{\theta}| \propto 1/T \ll \Omega_{\text{eff}}, \tag{4.13}$$

where T is the transfer time. Numerical simulations show a value $\Omega_{\text{eff}}T$ exceeding 10 to be sufficient to provide adiabatic transfer [Berg 98].

For our experimental parameters we typically find $\Omega_{\text{eff}} \approx 10\,\text{MHz}$, on the same order as $\Gamma = 8\,\text{MHz}$ and thus violating the condition from Eq. 4.4. In the limit $\Omega_{\text{eff}}^2 T \gg \Gamma$, an approximate solution for the STIRAP transfer efficiency from $|f\rangle$ to $|g\rangle$ is given by [Vita 96, Wink 07b]

$$P_t = \exp\left(\frac{\pi^2\Gamma}{\sqrt{2}\Omega_{\text{eff}}^2 T}\right), \tag{4.14}$$

where Gaussian pulse shapes $\Omega_{1,2}(t)$ separated by twice their width have been assumed. Our experiments, where typical transfer times $T \approx 2\mu\text{s}$ are used, are well within this limit.

As can be shown by a more general treatment [Vita 01], STIRAP is robust against fluctuations in one-photon detuning Δ_1, but depends critically on two-photon detuning δ. In order to reach high STIRAP efficiency it is thus crucial to keep $\delta \simeq 0$ during the transfer process.

4.2 STIRAP laser system

The application of STIRAP to transfer molecules into tightly bound states sets stringent requirements on the laser system utilized. The two Raman lasers have to be phase-stable during the STIRAP pulses to ensure the coherence of the process. Phase fluctuations would lead to an admixture of the bright states $|BS^{+,-}\rangle$ to $|DS\rangle$ and thus induce loss due to radiative decay. The lasers have to bridge the energy difference between $|f\rangle$ and $|g\rangle$, which is about $7\,\mathrm{THz}\times h$ when transferring Feshbach molecules into the ro-vibrational ground state of the $a^3\Sigma_u^+$ triplet potential. For a laser wavelength around 1000 nm this corresponds to a wavelength difference of about 23 nm. Additionally, the laser powers have to be sufficiently high to provide the Rabi frequencies $\Omega_{1,2}$ required for fast STIRAP transfers. A high long-term frequency stability of the Raman lasers is needed to keep them on resonance over many experimental cycles. As STIRAP is considerably more sensitive to two-photon detuning δ than to one-photon detuning Δ_1 (see Sec. 4.1), the relative stability of the lasers is of primary importance, while absolute stability is less crucial. The STIRAP laser system is also used for molecular spectroscopy. We have thus built a setup which allows us to change between two configurations meeting the different requirements for these purposes. After a brief presentation of the general properties of the two Raman lasers and the Pound-Drever-Hall locking scheme, a detailed description of these two configurations is given in this section.

Laser properties

As Raman lasers, we use a commercial grating-stabilized diode laser with a mode-hop free tuning range of about 20 GHz (model TOPTICA DL100) and a Ti:Sapphire laser (Coherent 899-01). The Ti:Sapphire laser is pumped by a Verdi V18 laser from Coherent at 532 nm with a maximum output power of 18 W. The output of the Verdi V18 is split on a high-power polarizing thin-film beamsplitter to simultaneously pump a second Ti:Sapphire laser which provides the light for the optical lattice (see Sec. 2.3). Due to the limited pump power, a certain trade-off between Raman laser power and lattice depth has to be made. The Ti:Sapphire laser is equipped with a long wavelength mirror set (output wavelength 900-1070 nm) and delivers up to 80 mW of optical power at the molecular sample at our typical operation wavelength of 1017 nm. It can be frequency stabilized by a mirror mounted on a piezoelectric transducer with a bandwidth of about 3 kHz. The diode laser has a range of 985-1066 nm and yields a few mW at the molecular sample. Its frequency can be tuned by shifting the grating angle via a piezoelectric transducer (bandwidth about 1 kHz) or the diode current.

The Ti:Sapphire laser is coupled through an AOM with a resonance frequency of 110 MHz to allow fast control of the laser power. For the DL100 we have set up a second AOM with the same frequency but in a double pass configuration. In addition to power control this yields a frequency tunability of about 50 MHz. The output powers of the AOM drivers for both single- and double pass are controlled by two arbitrary waveform generators (Agilent 33220A) with a bandwidth of 20 MHz. This allows us to independently switch and ramp the power of both laser 1 and 2 on a μs-timescale.

After the AOMs, the Raman lasers are coupled into optical fibers and guided to the experimental glass cell. They are almost superposed onto one of the lattice laser beams via two mirrors. The absorption imaging system is used to ensure that both lasers strike the molecular sample (compare Sec. 2.3). At the molecules, both Raman lasers have a $\frac{1}{e^2}$-waist radius of 130 μm. They are linearly polarized parallel to the magnetic bias field, and can thus only drive π transitions. We use a photodiode with a bandwidth of 1 GHz to monitor the Raman laser power after transmission through the glass cell.

Pound-Drever-Hall lock

To stabilize our Raman lasers we use a technique developed by Pound, Drever and Hall (PDH) [Drev 83]. In this locking scheme, a laser is phase-modulated with an electro-optical modulator (EOM), giving rise to sidebands. The laser beam is then coupled into an optical cavity over a $\lambda/4$-waveplate and a polarizing beam splitter (see Fig. 4.2). Because of the $\lambda/4$-waveplate, the retroreflected beam diverted by the PBS and detected on a high-bandwidth photodiode. Close to the transmission frequencies of the cavity, the carrier- and sideband components of the reflected laser beam experience different reflection coefficients and phase shifts. This combination of phase- and amplitude modulation is converted into an error signal by mixing the

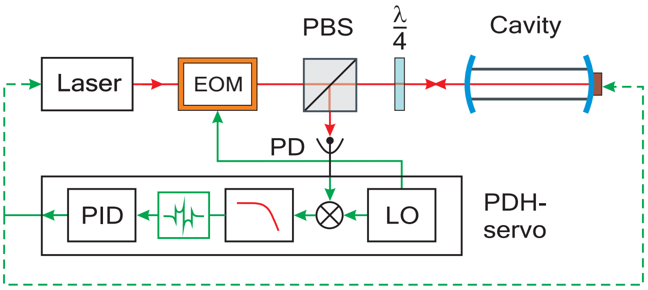

Figure 4.2:
Pound-Drever-Hall locking scheme. The phase-modulated laser beam is retroreflected by the cavity and detected on a photodiode (PD). A steep error signal is generated by mixing the PD-output with a local oscillator and fed back to either the laser or the cavity through a PID-controller (for details see text).

output of the photodiode with a local oscillator (LO) at the modulation frequency and filtering out the AC-component with a low-pass. The error signal has a steep zero crossing when the laser is resonant with the cavity, and can thus be used to stabilize either the cavity or the laser through a PID-controller.

4.2.1 Locking configurations

As an absolute frequency reference for the other lasers, we use a home-built grating stabilized diode laser (”master laser”) which is locked to an atomic ^{87}Rb-line at 780 nm via modulation transfer spectroscopy. A second ”offset laser” of the same kind is offset-locked to the master laser via a beat lock with a range of about 1.2 GHz (see Figs. 4.3 and 4.4). The details of these locking schemes can be found in [Thal 06].

The Raman lasers are locked to these lasers via two transfer cavities. The ”main cavity” is made of a low-expansion glass (Zerodur) spacer and has a free spectral range of 1.5 GHz and a finesse of about 300 [Kins 05]. One of the cavity mirrors is mounted on a piezoelectric actuator, allowing modulation of the cavity transmission frequency with a bandwidth of about 2 kHz. The second ”spectroscopy cavity” has a spacer made of silica glass but otherwise has the same properties as the main cavity.

During the work described here, these two lasers were utilized for both molecular spectroscopy and STIRAP transfer. As the two applications set different requirements on the stability, tunability and power of the lasers system, we use two different stabilization- and scanning setups which will be described in the following.

a) Spectroscopy setup.

For one-photon spectroscopy either of the two lasers can be used depending on the specific requirements concerning laser power, linewidth and tunability (Sec. 4.2). In our two-photon spectroscopy scheme, laser 1 is kept on resonance with the molecular transition from $|f\rangle$ to $|e\rangle$ while laser 2 is scanned (see Sec. 4.3.2). As the observed linewidth for this scheme is proportional Ω_2^2 (see Sec.4.3.2), the more powerful Ti:Sapphire serves as laser 2 to maximize the probability to detect molecular resonances. While for laser 1 only a limited tuning range is required to ensure it is on resonance, laser 2 has to be scanned independently of laser 1. Laser 1 is thus locked to the spectroscopy cavity, which itself is locked to the master laser and cannot be scanned (see Fig. 4.3). A limited scanning ability for laser 1 is added with an acousto-optical modulator (AOM) in double-pass configuration. Laser 2 is locked to the main cavity, which can be tuned by scanning the offset laser.

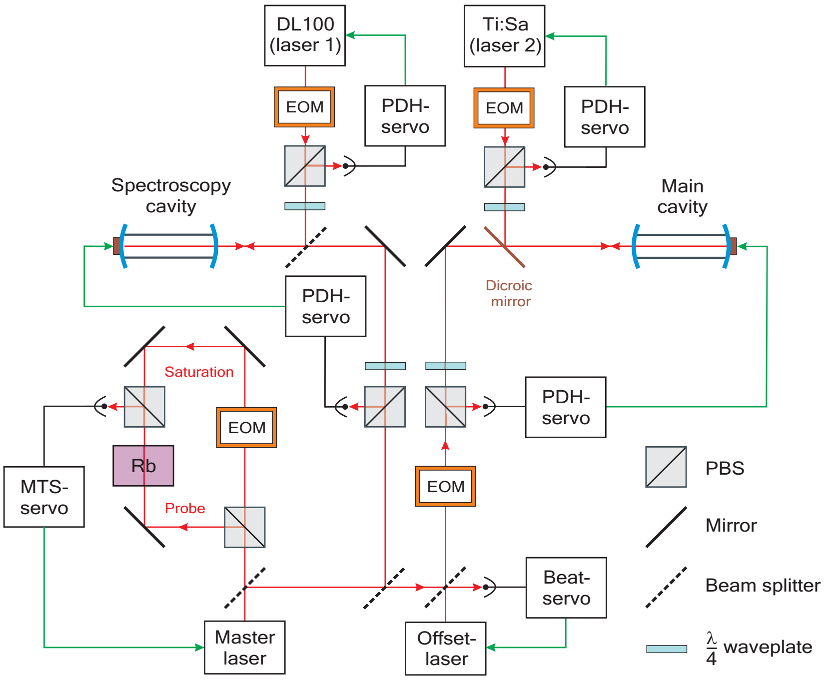

Figure 4.3:
Laser lock configuration for molecular two-photon spectroscopy. The master laser is stabilized to an atomic ^{87}Rb-line by modulation transfer spectroscopy (MTS). The spectroscopy cavity is Pound-Drever-Hall (PDH) locked directly to the master laser and thus cannot be scanned. The DL100 diode laser, which acts as laser 1 in this configuration is locked to the spectroscopy cavity with a PDH-scheme as well. The main cavity is PDH-locked to the offset laser, which itself is locked to the master laser via a beat lock. The Ti:Sapphire laser (laser 2) is PDH-locked to the main cavity and can thus be scanned by shifting the offset laser frequency over $\pm 1.2\,\mathrm{GHz}$, i.e. more than the FSR of the cavity of $1.5\,\mathrm{GHz}$.

b) STIRAP setup.

After the spectroscopic determination of the involved molecular levels, the transition frequencies for the STIRAP lasers are fixed. Hence, individual scanning ability for the two lasers is thus not necessary in this configuration. The main requirements for efficient STIRAP are high relative frequency stability between laser 1 and 2, and sufficiently large Rabi frequencies on both transitions. As the Franck-Condon factors for the transition $|f\rangle \leftrightarrow |e\rangle$ are much smaller than those for $|g\rangle \leftrightarrow |e\rangle$, we use the Ti:Sapphire laser as laser 1 and the DL100 as laser 2. In order to increase the relative frequency stability of the two lasers they are both PDH-locked to the main cavity

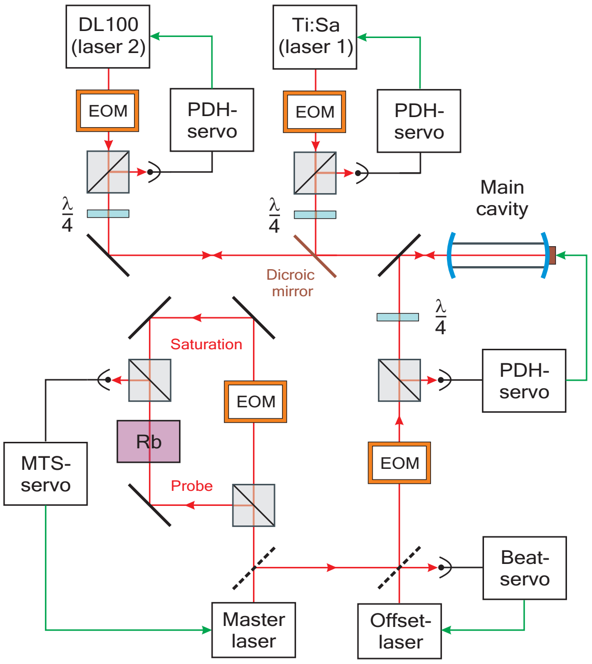

Figure 4.4:
Laser setup for STIRAP transfer. The locking configuration for master-, offset- and Ti:Sapphire laser as well as for the main cavity are the same as in the spectroscopy setup (see Fig. 4.3). In contrast to the previous scheme, however, also the DL100 diode laser is also locked onto the main cavity to increase the relative stability of lasers 1 and 2. The Ti:Sapphire laser which now acts as laser 1 can be brought on resonance by shifting the offset laser, while laser 2 can be fine-tuned via an AOM in double-pass configuration (not shown here).

in this setup (see Fig. 4.4). Compared to the case where the two lasers are locked to different cavities, this has the advantage that the sensitivity to instabilities of the cavity are reduced by a factor $\Delta\lambda/\lambda \approx 40$. As in the spectroscopy setup, the main cavity is locked to the offset laser and can be shifted via the offset lock. Again, a limited independent scanning ability for the DL100 (laser 2) is implemented with a double-pass AOM.

4.3 ^{87}Rb$_2$ triplet spectroscopy

At the time these experiments were started, both the electronically excited and ground triplet potentials were experimentally mostly unexplored, making extensive spectroscopic studies necessary. This section starts with a presentation of one-photon spectroscopy measurements performed to identify an appropriate excited state $|e\rangle$. We then stimulate the Raman scheme used for Raman spectroscopy of the triplet ground potential with a simple three-level model. Only a brief outline of the experimental results is given. A detailed discussion will follow in the doctoral thesis of Christoph Strauss.

4.3.1 One-photon spectroscopy

The choice of the intermediate state $|e\rangle$ is mainly governed by two conditions: Sufficiently strong coupling to both initial $|f\rangle$ and final state $|g\rangle$ is required to allow high Rabi frequencies Ω_1 and Ω_2. Additionally the separation from other molecular resonances has to be large enough to avoid losses due to off-resonant excitation.

A resonant absorption process can occur if the energy difference between the Feshbach state $|f\rangle$ and an electronically excited molecular state $|e\rangle$ matches the energy $\hbar\omega$ of a photon (see Fig. 4.5). For exact resonance and low intensity $\Omega_1 \ll \Gamma$ the transition

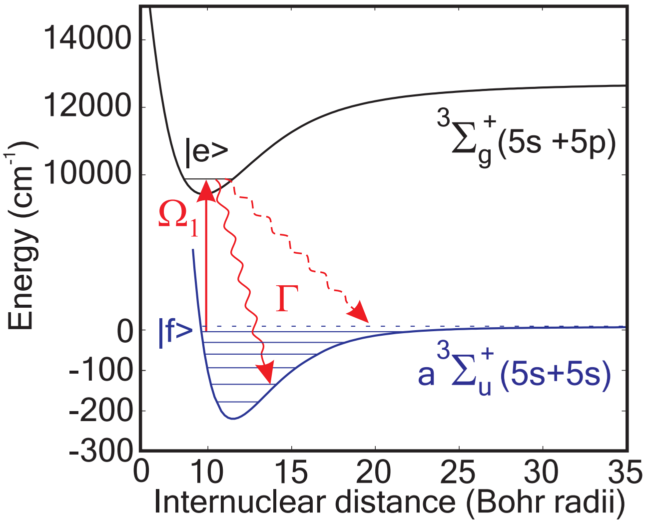

Figure 4.5:
One-photon spectroscopy. After excitation into state $|e\rangle$ the molecule can decay into a bound state of the electronic ground molecular potential (solid wavy arrow) or into a pair of unbound atoms (dashed wavy arrow) with total decay rate Γ. In both cases, the particles are not detected.

rate is given as

$$\gamma = \frac{\Omega_1^2}{\Gamma}, \tag{4.15}$$

where Γ is the natural linewidth of the transition. The excited molecule is instable and can either decay into one of the bound states of the electronic ground molecular potential, or dissociate into two atoms with high kinetic energy. As the decay back into the state of the Feshbach molecules generally is much less favorable than the other processes, an excited molecule is very likely to be lost from detection. For one-photon excitation, the transition rate γ can thus be considered equal to the experimentally observed molecular loss rate.

Vibrational progression. Prior to the work described here very limited experimental data about electronically excited $^{87}\mathrm{Rb}_2$ triplet potentials was available [Fior 01]. Model calculations from *ab-initio* potentials predicted suitable coupling strength from the states of the Feshbach molecules $|f\rangle$ and triplet ground state $|g\rangle$ to a number of vibrational levels of the electronically excited $^3\Sigma_g^+$ potential, suggesting the use of one of those levels as intermediate state $|e\rangle$ [Koch 07]. These calculations showed about 200 vibrational levels for this potential, with the vibrational ground state at an excitation energy of about 283 THz×h, corresponding to a laser wavelength of about 1060 nm.

In order to map out this vibrational progression, we used the Ti:Sapphire spectroscopy laser (model Coherent 899-01) as laser 1. The laser frequency was measured with a WS6-IR wavemeter from High Finesse with a precision of about 200 MHz. We have recorded the 16 lowest vibrational levels ($v = 0 - 15$) of the $^3\Sigma_g^+$ potential. For each vibrational level we observe two series of lines with 0_g^- and 1_g character respectively. We find the vibrational ground state at an excitation energy of 281.07 THz×h with respect to $|f\rangle$, corresponding to a wavelength of 1066.61 nm.

Rotational and hyperfine structure. We use the DL100 diode laser as laser 1 to resolve the rotational- and hyperfine structure of the $^3\Sigma_g^+$ potential. The wavelength of the laser is again measured with the WS6-IR wavemeter. For the 0_g^- manifold we find three strong absorption lines separated by about 3 GHz×h, while we we observe 15 lines with a total spacing of about 12 GHz×h in the 1_g manifold.

4.3.2 Raman spectroscopy

In contrast to the electronically excited molecular states, those in the electronic ground state are not directly accessible via one-photon laser spectroscopy. We thus use a Raman-scheme to determine the position of the bound states in the $a^3\Sigma_u^+$ potential. This scheme relies on Autler-Townes splitting, and is discussed briefly here.

Theoretical discussion

For the case of a λ-type three-level system with only laser 2 switched on (see Fig. 4.6a) we can set $\Omega_1 = \Delta_1 = 0$ and $\delta \equiv \Delta_2$ in the Hamiltonian of Eq. 4.2, where Δ_2 is the one-photon detuning of laser 2 . This results in a mixing angle $\theta = 0$ and the eigenstates from Eqs. 4.5-4.7 become

$$\begin{aligned} |BS^+\rangle &= \cos\phi|e\rangle + \sin\phi|g\rangle, && (4.16)\\ |DS\rangle &= |f\rangle, && (4.17)\\ |BS^-\rangle &= \sin\phi|e\rangle + \cos\phi|g\rangle, && (4.18) \end{aligned}$$

with mixing angle $\phi = \frac{1}{2}\arctan(\Omega_2/\delta)$ and eigenenergies

$$\begin{aligned} \epsilon_{DS}(t) &= 0, && (4.19)\\ \epsilon_{BS}^{+,-}(t) &= \frac{\hbar}{2}\left(\Delta_2 \pm \sqrt{\Delta_2^2 + \Omega_2^2}\right). && (4.20) \end{aligned}$$

The decay rates of the bright states $|BS^+\rangle$ and $|BS^-\rangle$ are

$$\begin{aligned} \Gamma^+ &= \Gamma\cos^2\phi, && (4.21)\\ \Gamma^- &= \Gamma\sin^2\phi. && (4.22) \end{aligned}$$

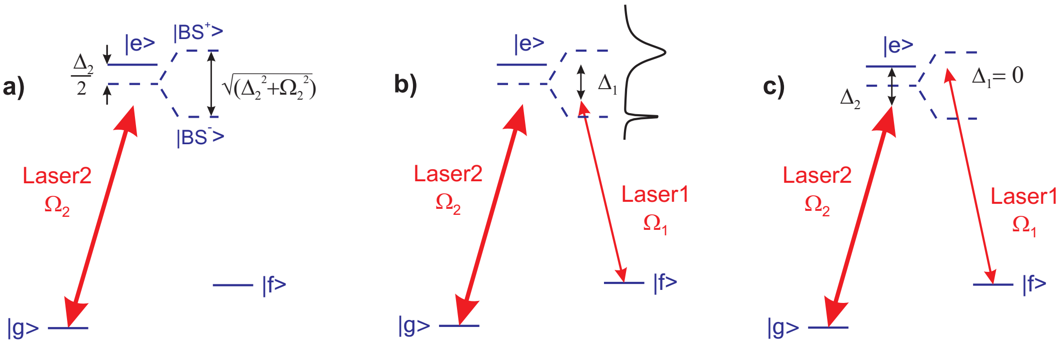

Figure 4.6:
Autler-Townes spectroscopy. a) The bare states $|e\rangle$ and $|g\rangle$ (solid blue lines) are coupled by laser 2, resulting in a splitting of the dressed states $|BS^+\rangle$ and $|BS^-\rangle$ (dashed blue lines). b) The energy splitting between $|BS^+\rangle$ and $|BS^-\rangle$ induced by laser 2 can be probed by scanning laser 1 at low intensity ($\Omega_1 \ll \Omega_2$). c) In our detection scheme laser 1 is kept on resonance, while laser 2 is scanned. If the two-photon resonance condition $\delta = 0$ is satisfied, a dark resonance appears.

As indicated in Fig. 4.6b, this so-called Autler-Townes splitting between the bright states $|BS^+\rangle$ and $|BS^-\rangle$ can be probed by scanning laser 1 at low Rabi frequency $\Omega_1 \ll \Omega_2$. In our detection scheme for bound molecular states we make use of this splitting, but apply a different scanning procedure: Laser 1 is kept on resonance $\Delta_1 = 0$ at low intensity, constantly inducing losses due to excitation to $|e\rangle$. At the same time, laser 2 is scanned at high intensity ($\Omega_2 \gg \Omega_1, \Gamma$). As laser 2 becomes resonant with the molecular transition $|g\rangle \leftrightarrow |e\rangle$, the bare state $|e\rangle$ evolves into the dressed state $|BS^+\rangle$ which is shifted out of resonance with laser 1. If the condition $\delta = 0$ is satisfied, a dark state is formed, and losses are strongly suppressed. Experimental data for such a dark resonance is shown in Fig. 4.7.

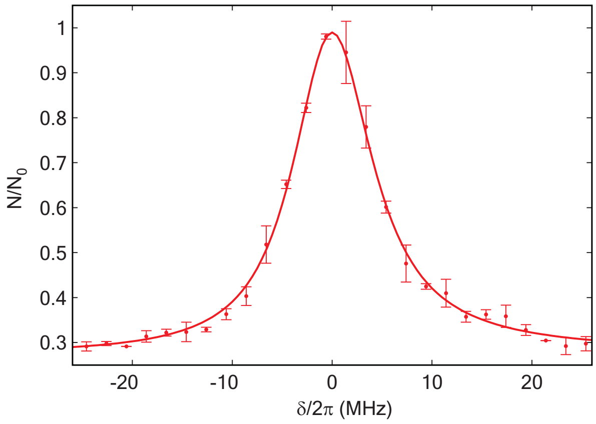

Figure 4.7:
Dark resonance. Shown is the number of molecules remaining in $|f\rangle$ after subjecting them to a $3\,\mu$s square pulse from both Raman lasers. The frequency of laser 1 is kept constant, while laser 2 is scanned. The Rabi frequencies are $\Omega_1 = 2\pi \times 0.7\,$MHz and $\Omega_2 = 2\pi \times 10\,$MHz. The solid line is a fit from a three-level model.

Linewidth. We now want to investigate what linewidth we can expect for such a dark resonance in our scanning scheme. For this, we compare the decay rate of $|BS^+\rangle$ to its shift from resonance with laser 1 (see Figs. 4.6 and 4.8a). More specifically, we calculate for which detuning of laser 2, $\Delta_2^{HWHM} = \delta^{HWHM}$, this shift equals half the linewidth of $|BS^+\rangle$. Using Eqs. 4.20 and 4.21, and neglecting saturation effects we get

$$\frac{\sqrt{\delta^2 + \Omega_2^2} - |\delta|}{2} = \Gamma \frac{\cos^2 \phi}{2} = \Gamma \frac{\sqrt{\delta^2 + \Omega_2^2} + \delta}{4\sqrt{\delta^2 + \Omega_2^2}}. \tag{4.23}$$

For our typical experimental conditions we have $\Omega_2 \gg \Gamma$, and the left side can become smaller than Γ only for $\delta \gg \Omega_2$. With the approximation

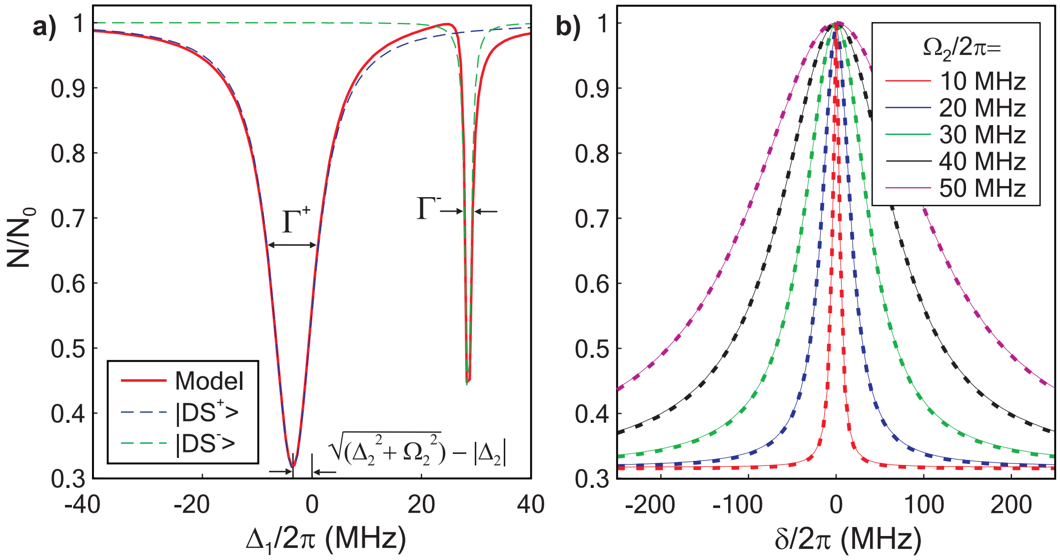

Figure 4.8:
Model simulation of Raman spectroscopy linewidth. a) Autler-Townes splitting. The solid red line shows a simulation from a three-level model, where laser 1 is scanned while laser 2 is kept at fixed detuning $\Delta_2 = 2\pi \times 25\,\mathrm{MHz}$ (compare Fig. 4.6b). The dashed blue (green) lines indicate the naive expectation of two Lorentzian lineshapes of width Γ^+ (Γ^-) at position $\epsilon^+_{BS}/\hbar$ ($\epsilon^-_{BS}/\hbar$) for the dressed states $|BS^+\rangle$ ($|BS^-\rangle$). The parameters used are $\Omega_1 = 2\pi \times 0.7\,\mathrm{MHz}$, $\Omega_2 = 2\pi \times 20\,\mathrm{MHz}$, and $\Gamma = 2\pi \times 8\,\mathrm{MHz}$. b) Linewidth of dark resonance in our Raman spectroscopy scheme. The solid lines are simulations for scans of laser 2 with laser 1 fixed at $\Delta_1 = 0$ for different Rabi frequencies $\Omega_2 = 2\pi\times(10, 20, 30, 40, 50)\,\mathrm{MHz}$ (see Fig. 4.6c). The dashed lines are Lorentzians with widths given by Eq. 4.25, i.e., $\delta^{HWHM} = 2\pi\times(6, 25, 56, 100, 156)\,\mathrm{MHz}$.

$$\sqrt{\delta^2 + \Omega_2^2} \approx |\delta| + \frac{\Omega_2^2}{2|\delta|} \tag{4.24}$$

and further neglecting terms of order $(\Omega_2/\delta)^2$ we solve for δ to get

$$\delta^{HWHM} = \frac{\Omega_2^2}{2\Gamma}. \tag{4.25}$$

For large Rabi frequency $\Omega_2 \gg \Gamma$ we can thus expect the observed width of a dark resonance to be proportional to Ω_2^2. This is in good agreement with simulations from a three-level model, which indeed show such a quadratic behavior not only for large Ω_2, but also for $\Omega_2 \simeq \Gamma$ (see Fig. 4.8b).

Experimental results

Previous to our work only the binding energies of the seven highest vibrational levels ($v = 34 - 40$) of the $a^3\Sigma_u^+$ electronic ground triplet potential had been experimentally observed [Best 04]. Detailed spectroscopic measurements were thus required to determine the binding energy of the vibrational ground state of the $a^3\Sigma_u^+$ potential which we had envisaged as final state $|g\rangle$ for our STIRAP transfer. From the previous section, the linewidths of dark states observed with our detection scheme is proportional to Ω_2^2. This suggests that in our "spectroscopy setup" the more powerful Ti:Sapphire should be used as laser 2 and the DL100 as laser 1 (see Sec. 4.2.1).

Vibrational progression. Theoretical calculations from a close-coupled channel model based on *ab-initio* potentials predicted 41 bound states for the $a^3\Sigma_u^+$ potential with the ground state at a binding energy of 7.114 THz×h [Tiem 08]. Using these calculations as a guideline, we have mapped out all of the 41 levels in the vibrational progression, and find the rovibrational ground state at a binding energy of 7.03806(3) THz×h. We have experimentally verified that no more molecular resonances appear where more deeply bound vibrational levels were to be expected.

Rotational- and hyperfine structure. For each vibrational level, we find rotational- and hyperfine structure which has a total width of about 20 GHz×h for the deeply bound levels. In order to verify that the lowest observed resonance is indeed the hyperfine ground state, we compare the measured structure to the close-coupled channel model. As excited state $|e\rangle$ for these measurements we use a solitary strong resonance in the 0_g^- manifold of the vibrational level $v = 13$ of the $^3\Sigma_g^+$ potential. This state has quantum number $I = 3$, considerably restricting the number of observed lines due to the selection rule $\Delta I = 0$ and the fact that I is a good quantum number for

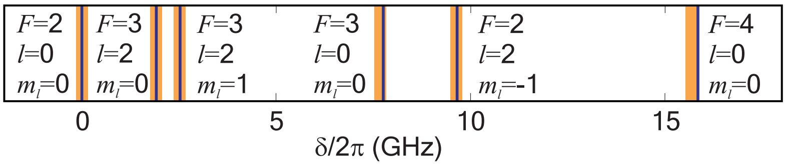

Figure 4.9:
Hyperfine- and rotational structure of the $a^3\Sigma_u^+$ vibrational ground state $v = 0$. The orange bars show the measured resonances, where the width indicates a typical error margin. The thin blue lines represent the positions of the states with quantum numbers F, l and its projection m_l as calculated from the close-coupled channel model. The two-photon detuning δ is taken relative to the absolute lowest state $|g\rangle$ of the $a^3\Sigma_u^+$ potential.

the deeply bound states in the $a^3\Sigma_u^+$ potential. We find good agreement between the measured data and the model calculations (see Fig. 4.9).

4.4 Transfer to the rovibrational triplet ground state

After determiing the intermediate $|e\rangle$ and final state $|g\rangle$ the STIRAP transfer into the rovibrational ground state can be carried out. As discussed in Sec. 4.1, such a transfer requires high relative frequency stability and similar Rabi frequencies for both Raman lasers. In our "STIRAP setup" both Raman lasers are Pound-Drever-Hall locked to the main cavity in order to minimize relative fluctuations in the laser frequency (see Sec. 4.2.1). The more powerful Ti:Sapphire laser acts as laser 1 and the DL110 diode laser as laser 2 to compensate for the unequal transition strength which is much lower for $|f\rangle \leftrightarrow |e\rangle$ than for $|g\rangle \leftrightarrow |e\rangle$.

For the STIRAP transfer, we apply a counter-intuitive pulse sequence as shown in Fig. 4.10. First only laser 2, which couples the levels $|g\rangle$ and $|e\rangle$ is switched on. In order to transfer the molecules from $|f\rangle$ to $|g\rangle$, laser 2 is ramped down while laser 1 is ramped up in about $2\,\mu$s. After a certain hold time τ_h, a second time-reversed STIRAP pulse sequence is applied. Note that τ_h is defined as the time between the actual transfers, i.e., from the time when laser 2 is switched off at the end of pulse 1 until it is switched on again at the beginning of pulse 2 (Fig. 4.10). We typically use a hold time of $2\,\mu$s for maximum transfer efficiency (compare Sec. 4.5). After ramping

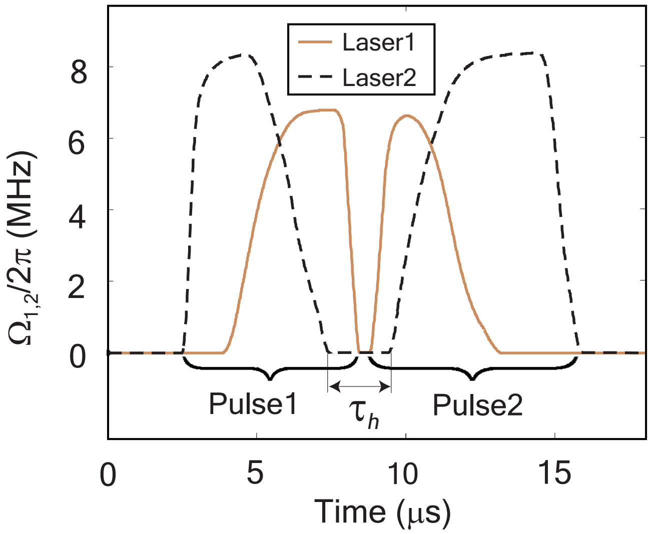

Figure 4.10:
STIRAP pulse sequence. For the transfer of molecules from $|f\rangle$ to $|g\rangle$ laser 2 (dashed black line) is ramped down while laser 1 (solid brown line) is ramped up. After a certain hold time τ_h a second, time-reversed pulse transfers the molecules back from $|g\rangle$ to $|f\rangle$.

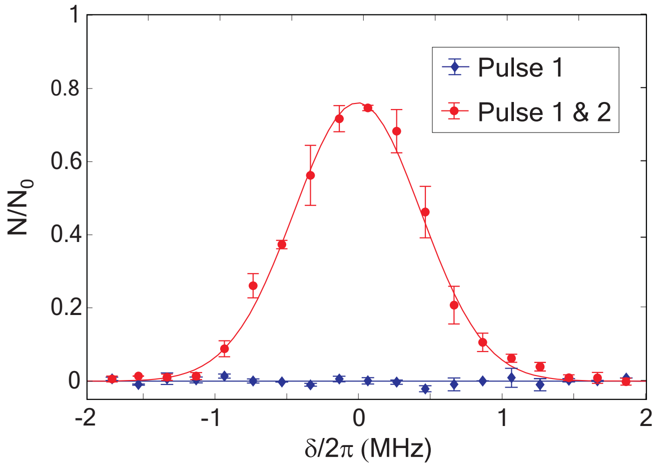

Figure 4.11:
STIRAP transfer efficiency. Shown is the fraction of detected Feshbach molecules for varying two-photon detuning δ. After a single STIRAP pulse no $|f\rangle$ molecules can be detected (blue diamonds). A maximum of 75% of the initial molecules reappear after a second, time-inverted STIRAP pulse (red circles). The solid lines are calculations from a master equation based three-level model (see Sec. 4.4.2).

down laser 2 in the first pulse sequence, laser 1 is left on at maximum intensity for about 1 μs to ensure that no molecules remain in $|f\rangle$.

In Fig. 4.11 the number of molecules observed in $|f\rangle$ after STIRAP pulse 1 (blue diamonds) and pulses 1 and 2 (red circles) is shown as a function of two-photon detuning δ. After the first pulse no more Feshbach molecules can be detected. When applying both STIRAP pulses about 75% of the initial molecules reappear in $|f\rangle$ in case of resonance ($\delta = 0$). Assuming equal transfer efficiency for both pulses, this corresponds to a one-way transfer efficiency of 87% and a total number of 2.6×10^4 ground state molecules. The resonance has a FWHM of about 1 MHz which is determined by Fourier- and power broadening. This width is in good agreement with our model calculations (Sec. 4.4.2).

4.4.1 Square pulse projection transfers

We have also performed a different kind of measurement, replacing the more elaborate STIRAP pulse sequence with simple square Raman pulses [Lang 09]. This procedure allows us to gain further insight into the system, and to demonstrate a very simple transfer method from $|f\rangle$ to $|g\rangle$.

The Feshbach molecules are exposed to a square Raman pulse with both lasers on

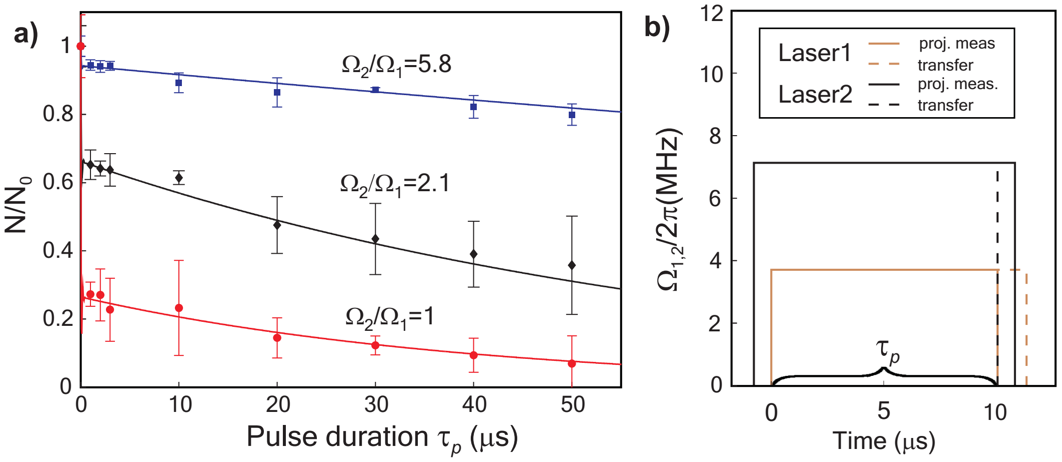

Figure 4.12:
Square pulse projection measurements. a) Shown is the fraction of remaining Feshbach molecules after subjecting them to square Raman laser pulses as a function of pulse duration for different Rabi frequency ratios Ω_2/Ω_1. After a fast initial projection from $|f\rangle$ to $|DS\rangle$, the dark state decays on a much longer timescale. The solid lines are simulations from a master equation based three-level model (Sec. 4.4.2). b) For the projection measurements shown in a), laser 2 (solid black line) is switched on earlier and switched off later than laser 1 (solid brown line). This is required to avoid excitation from $|f\rangle$ to $|e\rangle$ due to jitter in the laser timing. The pulse duration τ_p is defined as the time span when both lasers are on. If the square pulse scheme is used to transfer molecules into $|g\rangle$, laser 1 (dashed brown line) is turned off after laser 1 (dashed black line) to rule out excitation from $|g\rangle$.

resonance ($\Delta_1 = \delta = 0$) for a variable pulse duration τ_p. Laser 2 is switched on earlier and turned off later than laser 1 by about 1 μs to avoid excitation from $|f\rangle$ to $|e\rangle$ due to jitter in the laser timing (solid lines in Fig. 4.12(b)). After switching off the lasers the number of molecules remaining in $|f\rangle$ is detected. We observe an initial loss of molecules occurring in less than 1 μs which depends on the ratio Ω_2/Ω_1, followed by a much slower exponential decay (Fig. 4.12a).

This behavior can be understood in the following way: With Eqs. 4.5-4.7 we write $|f\rangle$ as superposition of dark and bright states,

$$|f\rangle = [\Omega_2|DS\rangle + \Omega_1(\sin\phi|BS^+\rangle + \cos\phi|BS^-\rangle)]/\sqrt{\Omega_1^2+\Omega_2^2}. \qquad (4.26)$$

When the lasers are switched on, the bright states are quickly lost due to excitation to $|e\rangle$, while the dark state remains. Using Eq. 4.6 we find that after the projection onto $|DS\rangle$, a fraction $\Omega_2^4/(\Omega_1^2+\Omega_2^2)^2$ of the initial molecules is in $|f\rangle$. This fact can be used to calibrate the ratio of Rabi frequencies Ω_2/Ω_1. Indeed we find good agreement with the values previously determined with other techniques. We note that after the projection of $|f\rangle$ onto $|DS\rangle$ a fraction $\Omega_1^2\Omega_2^2/(\Omega_1^2+\Omega_2^2)^2$ of the initial Feshbach molecules is in $|g\rangle$, with a maximum of 25% for $\Omega_1 = \Omega_2$. This provides a very simple and fast method to transfer a sizeable fraction of Feshbach molecules into the ground state. For such a transfer, however, the laser timing has to be slightly changed compared to the one for the projection measurements. To ensure that $|g\rangle$ molecules are not excited to $|e\rangle$ at the end of the Raman pulse, laser 2 is switched off earlier than laser 1 (dashed lines in Fig. 4.12b)).

After the initial projection, the dark state decays on a much slower timescale. This decay could, for example, be due to off-resonant coupling to states other than $|f\rangle$, $|g\rangle$ and $|e\rangle$. Exposing $|f\rangle$ ($|g\rangle$) molecules to laser 2 (1), however, we find losses due to laser excitation to be completely negligible on the timescale of our experiments. We have also tested for possible AC-Stark shifts of the dark resonance by measuring its position for different Rabi frequencies $\Omega_{1,2}$. Within the accuracy of the measurements of 200 kHz, however, no shifts could be detected. We thus attribute the decay of $|DS\rangle$ to phase fluctuations of the Raman lasers which causes the phase of the lasers to differ from that of the molecular superposition state. This can be viewed as an admixture of the bright states $|BS^{+,-}\rangle$ into $|DS\rangle$, followed by their excitation to $|e\rangle$. The decay time of $|DS\rangle$ depends on the Rabi frequency ratio Ω_2/Ω_1 and is lowest for equal Rabi frequencies, where we find it to be about $50\,\mu$s.

4.4.2 Master equation based three-level model

In order to numerically simulate the internal molecular dynamics of the STIRAP transfers and the square pulse projection measurements, we use our three-level-model (Eq. 4.2) in a master equation [Wall 94]. Compared to a Hamiltonian-based model this approach has the advantage that decoherence due to laser phase fluctuations is taken into account. As the system is comparatively insensitive to one-photon detuning, we set $\Delta_1 = 0$, but include the natural linewidth[1] Γ of the excited state $|e\rangle$; and the relative linewidth η of the two Raman lasers. Relabeling the levels $|f\rangle$, $|g\rangle$ and $|e\rangle$ as 1, 2, and 3 we can write the master equation as

---

[1] Γ is neglected in the Hamiltonian from Eq. 4.2 which was used to calculate $|DS\rangle$ and $|BS^{+,-}\rangle$, but is included in the three-level model applied in Figs. 4.7 and 4.8.

$$\begin{aligned}\frac{d\rho}{dt} &= -i\delta\left[\sigma^{22},\rho\right] - \frac{i}{2}\sum_{k=1}^{2}\Omega_k\left[\sigma_-^{3k}+\sigma_+^{3k},\rho\right]\\ &-\frac{1}{2}\Gamma\left(\sigma^{33}\cdot\sigma^{33}\cdot\rho+\rho\cdot\sigma^{33}\cdot\sigma^{33}\right)\\ &+\frac{1}{2}\eta\left(2\sigma^{22}\cdot\rho\cdot\sigma^{22}-\sigma^{22}\cdot\rho-\rho\cdot\sigma^{22}\right),\end{aligned} \tag{4.27}$$

where ρ is the density matrix. The matrices σ_-^{jk} and σ_+^{jk} are ladder operators and each is the transpose of the other. For example

$$\sigma_-^{32} = \begin{pmatrix} 0 & 0 & 0 \\ 0 & 0 & 0 \\ 0 & 1 & 0 \end{pmatrix} = \left(\sigma_+^{32}\right)^{\mathrm{T}}. \tag{4.28}$$

Implementing the time-dependent Rabi frequencies $\Omega_{1,2}$ for the two STIRAP pulses as shown in Fig. 4.10 we model the STIRAP transfers for varying two-photon detuning δ. The relative laser linewidth η is used as a fit parameter to give best agreement with the data from in Fig. 4.11, where the results of the simulations are shown as solid lines. Neglecting lattice dynamics we find $\eta = 2\pi \times 20\,\mathrm{kHz}$, indicating that about half of the losses are due to nonadiabaticity and half are due to the non-ideal laser system.

For the square pulse projection measurements from Sec. 4.4.1 we set $\Delta_1 = \delta = 0$ and apply pulses as shown in Fig. 4.12b for the Rabi frequencies $\Omega_{1,2}$. Again we use the relative laser linewidth as parameter to fit the data of Fig. 4.12a and find a best value of $\eta = 2\pi \times 16\,\mathrm{kHz}$. The results of the simulations are shown as solid lines in Fig. 4.12a.

4.5 Molecular dynamics in the optical lattice

In the preceding discussion we have neglected the influence of the optical lattice on the molecules. Due to their strong binding, however, ground state molecules do not have the same dynamic polarizability as Feshbach molecules. No details about the strength and even sign of the lattice potential for the ground state molecules were known. In our experiments we observe molecular oscillations in the lattice occurring after the transfer into the rovibrational ground state. This behavior is reproduced with a multi-band model, which allows one to deduce the polarizability of the ground state molecules.

4.5.1 Coherent molecular oscillations

In order to study the dynamics of the $|g\rangle$ molecules in the lattice, we repeat the STIRAP transfer experiment from Sec. 4.4 for variable hold time τ_h. Within about 40 μs the fraction of detected Feshbach molecules falls from 75% to around 30% (Fig. 4.13). Some of the "lost" molecules reappear in a damped oscillation with period and damping time both about 80 μs, which levels off at about 40% of the initial molecules.

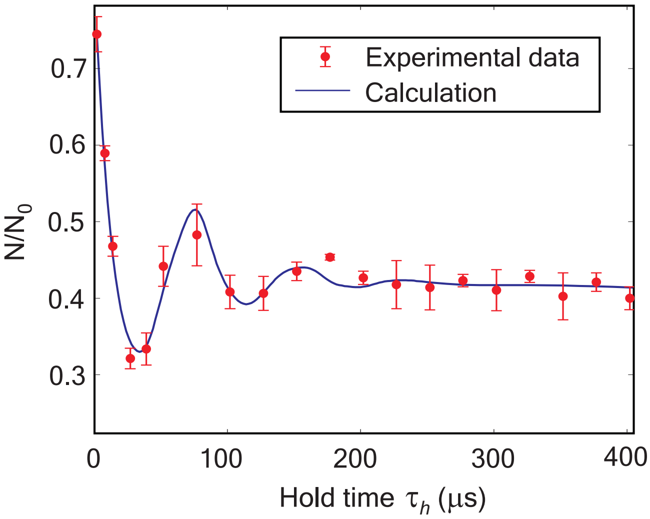

Figure 4.13:
Molecular oscillations. The fraction of recovered Feshbach molecules after two STIRAP pulses is plotted as a function of hold time τ_h. The oscillation in the molecule number is caused by breathing oscillations of molecules in $|g\rangle$, which experience a much weaker lattice potential than those in $|f\rangle$ (see text). Except for the varying hold time τ_h all parameters are the same as in Fig. 4.11. The solid line is a calculation from our multi-band model (Sec. 4.5.2).

This behavior can be explained as follows: During the first STIRAP transfer from $|f\rangle$ to $|g\rangle$ the spatial shape of the center-of-mass (c.o.m.) molecular wavepacket remains unchanged. The molecules in the ground state experience a lattice potential which is about a factor of 10 weaker than that for the Feshbach molecules. This leads to breathing oscillations of the molecular wavepacket at the lattice site trap frequency ω_t, which are damped by tunneling to neighboring sites. If the molecular wavepacket at the time of the return transfer differs from the original one (i.e. the lattice ground state for $|f\rangle$), the second STIRAP pulse leads to the excitation of higher bands for the Feshbach molecules. As we detect only particles in the lowest band (Sec. 4.5.2), this effect leads to an apparent oscillation in transfer efficiency in the data shown in Fig. 4.13. For a more detailed discussion of this behavior see Sec. 4.5.2.

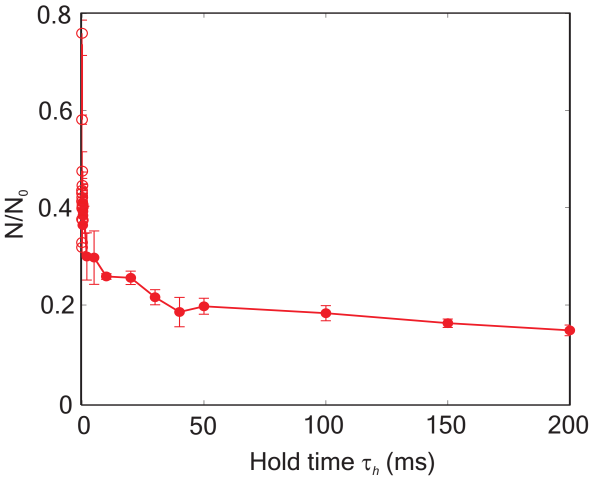

Figure 4.14:
Ground state molecular lifetime. Shown is the same set of data as in Fig. 4.13 (plotted as open circles), but extended to longer hold times (full circles). After the coherent initial dynamics we find a decay occurring within about 25 ms, which we attribute to tunneling of molecules in excited bands out of the lattice. The remaining molecules in the lowest band of the lattice have a lifetime exceeding our experimental observation time. The solid line is a guide to the eye and connects neighboring data points.

Fig. 4.14 shows the extension of these measurements to longer hold times. We find an additional decay occurring within about 25 ms, after which around 20% of the inial molecules are left. We attribute this loss mainly to essentially unbound molecules in higher bands, which simply fall out of the lattice. For the remaining molecules in the lowest band we find a lifetime exceeding our experimental observation time, which is limited to about 200 ms due to heating of the Feshbach coils.

4.5.2 Multi-band model

For the simulation of the dynamics caused by the modified lattice depth for the different molecular states, we extend the three-level model of the master equation approach discussed in Sec. 4.4.2. The levels $|f\rangle$, $|g\rangle$ and $|e\rangle$ now have a substructure, the lattice Bloch bands, which depends on the respective depth of the lattice for the different levels (Fig. 4.15). We assume the Feshbach molecules to be initially localized at a lattice site. As Bloch wavefunctions are delocalized over the whole lattice, a localized wavepacket has to be constructed. Integrating the Bloch waves of a specific band over all quasi-momenta gives the Wannier function for the respective band. Among the different localized wavefunctions constructed from Bloch waves, Wannier functions stand out as those with lowest total energy [Kohn 73]. They form a complete set of orthonormal functions, and closely resemble harmonic oscillator wavefunctions for deep lattices. We use Wannier functions as a basis to describe the molecules in the optical lattice and will denote the Wannier function for level $|\alpha\rangle$ and band n as $|\Psi_{\alpha n}\rangle$ in the following.

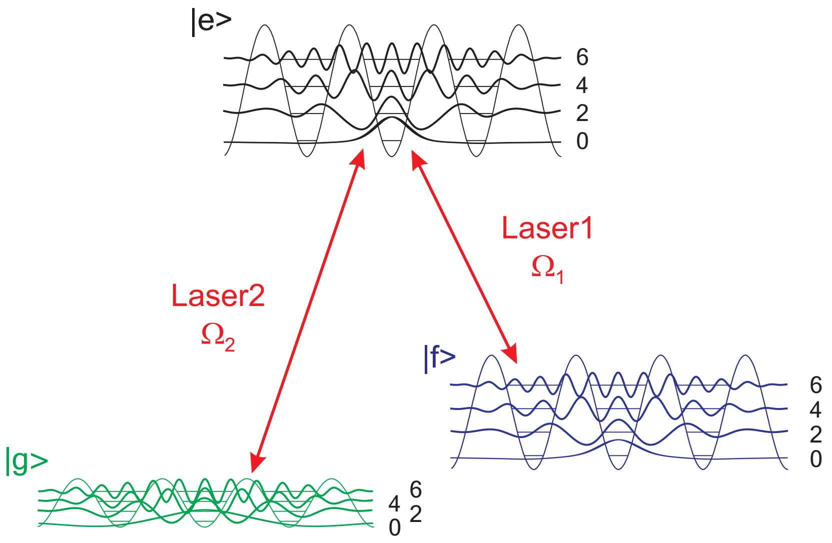

Figure 4.15:
Level-scheme for multi-band model. Due to the optical lattice, the molecular levels $|f\rangle$, $|g\rangle$ and $|e\rangle$ obtain a Bloch band substructure. The different bands $n = 0, 2, 4, 6$ of level $|f\rangle$ ($|g\rangle$) are coupled to $|e\rangle$ by laser 1 (2) according to the respective wave function overlaps.

As the initial wavepacket is symmetric, only symmetric bands (i.e., with even indices) can be excited. It turns out that for our typical parameters, the inclusion of bands with indices $n > 6$ has only negligible effect on the model. We thus restrict our calculations to the four lowest symmetric bands, corresponding to $n = 0, 2, 4, 6$. Each of the three dimensions of the system is now described by a twelve-level model, which we solve with a Schrödinger equation based approach. In contrast to the master-equation model from Sec. 4.4.2 it does not include losses due to laser phase fluctuations, but has the advantage of being numerically less involved. In order to describe tunneling of molecules to a neighboring lattice site we introduce a tunnel rate $J_{\alpha n}$ for band n in level $|\alpha\rangle$. For the time dependent Schrödinger equation

$$i\hbar\frac{\partial}{\partial t}|\Phi\rangle = \hat{H}|\Phi\rangle \tag{4.29}$$

we write a general state $|\Phi\rangle$ in terms of a 12-element probability amplitude vector

$$\mathbf{c} = \begin{pmatrix} c_{f0} \\ c_{g0} \\ c_{e0} \\ c_{f2} \\ \vdots \end{pmatrix}, \tag{4.30}$$

where $c_{\alpha n}$ is the amplitude for the basis state $|\Psi_{\alpha n}\rangle$. The Hamiltonian then has the form of a $12 \times 12-$matrix

$$\hat{H} = \hbar \begin{pmatrix} E_{f0}-\frac{i}{2}J_{f0} & 0 & \frac{1}{2}\Omega_1 \cdot M_{f0,e0} & 0 & \cdots \\ 0 & E_{g0}+\delta-\frac{i}{2}J_{g0} & \frac{1}{2}\Omega_2 \cdot M_{g0,e0} & 0 & \cdots \\ \frac{1}{2}\Omega_1 \cdot M_{e0,f0} & \frac{1}{2}\Omega_2 \cdot M_{e0,g0} & E_{e0}+\Delta_1-\frac{i}{2}\Gamma-\frac{i}{2}J_{e0} & \frac{1}{2}\Omega_1 \cdot M_{e0,f2} & \cdots \\ 0 & 0 & \frac{1}{2}\Omega_1 \cdot M_{f2,e0} & E_{f2}-\frac{i}{2}J_{f2} & \cdots \\ \vdots & \vdots & \vdots & \vdots & \end{pmatrix}, \tag{4.31}$$

where $E_{\alpha n}$ is the mean energy of Bloch band n in state $|\alpha\rangle$ and $M_{\alpha n,\beta k} = \langle\Psi_{\alpha n}|\Psi_{\beta k}\rangle$ the overlap integral of the respective Wannier functions.

We use the Crank-Nicolson method [Cran 47] to calculate the coherent time evolution of the 1D amplitudes for the non-tunneled molecules, $\mathbf{c}$. In order to extend the model to three dimensions, the elements of $\mathbf{c}$ are allocated to three 4-element vectors $\mathbf{c}_\mathbf{f}$, $\mathbf{c}_\mathbf{g}$ and $\mathbf{c}_\mathbf{e}$ for the respective states $|f\rangle$, $|g\rangle$ and $|e\rangle$, e.g.,

$$\mathbf{c}_\mathbf{f} = \begin{pmatrix} c_{f0} \\ c_{f2} \\ c_{f4} \\ c_{f6} \end{pmatrix}. \tag{4.32}$$

The $4 \times 4 \times 4-$array of the respective 3D amplitude distribution $c_f^{x,y,z}$ is then constructed as product of the 1D amplitudes which we assume to be equal for the three directions as $c_f^{x,y,z} = \mathbf{c}_\mathbf{f}^\mathbf{x} \otimes \mathbf{c}_\mathbf{f}^\mathbf{y} \otimes \mathbf{c}_\mathbf{f}^\mathbf{z}$, where $(\mathbf{c}_\mathbf{f}^\mathbf{x} = \mathbf{c}_\mathbf{f}^\mathbf{y} = \mathbf{c}_\mathbf{f}^\mathbf{z} \equiv \mathbf{c}_\mathbf{f})$. For example, the part of $c_f^{x,y,z}$ describing the amplitudes for the lowest band in the z-direction is a $4 \times 4-$matrix given as

$$c_f^{x,y,0} = \begin{pmatrix} c_{f0}c_{f0}c_{f0} & c_{f0}c_{f2}c_{f0} & c_{f0}c_{f4}c_{f0} & c_{f0}c_{f6}c_{f0} \\ c_{f2}c_{f0}c_{f0} & c_{f2}c_{f2}c_{f0} & c_{f2}c_{f4}c_{f0} & c_{f2}c_{f6}c_{f0} \\ c_{f4}c_{f0}c_{f0} & c_{f4}c_{f2}c_{f0} & c_{f4}c_{f4}c_{f0} & c_{f4}c_{f6}c_{f0} \\ c_{f6}c_{f0}c_{f0} & c_{f6}c_{f2}c_{f0} & c_{f6}c_{f4}c_{f0} & c_{f6}c_{f6}c_{f0} \end{pmatrix}. \tag{4.33}$$

Tunneling molecules are considered to remain in the same band, and are described by an amplitude vector $\tilde{\mathbf{c}}$. The 3D amplitude arrays $\tilde{c}_{f,g,e}^{x,y,z}$ for the tunneling molecules are constructed in an analogous was as $c_{f,g,e}^{x,y,z}$. In contrast to the non-tunneling molecules, however, the tunneling ones do not undergo a coherent evolution. They are considered to be transferred back from $|g\rangle$ to the different bands of $|f\rangle$ according to the respective wave function overlaps by the reverse STIRAP pulse[2]. This loss of coherence leads to damping of the molecular oscillation. The tunnel rates $J_{\alpha n}$ are slightly adjusted compared to the theoretically expected values to reach better agreement with the data from Fig. 4.13.

Molecule-atom band conversion

In our experiments only atoms that end up in the first Brillouin zone after dissociation of the Feshbach molecules are counted as signal (see Sec. 2.6). We will now discuss how the different Bloch bands for molecules are mapped into those for atoms. As the lattice for $|f\rangle$ is very deep (typically $60\,E_r$), we can us a harmonic approximation with trap frequency ω_t for the sinusoidal potential at a specific lattice site. The 1D eigenfunctions of the harmonic oscillator are

$$|\Phi_n\rangle = \frac{1}{\sqrt{2^n n! \sqrt{\pi} x_0}} \exp(-\frac{x^2}{2x_0^2})\ \mathrm{H}_n\left(\frac{x}{x_0}\right), \tag{4.34}$$

where $x_0 = \sqrt{\hbar/\omega_t m}$ is the oscillator length and H_n is the n$^{\mathrm{th}}$ Hermite polynomial. For two atoms at a specific lattice site we use the coordinates $x_{1,2}$. We can transform these into relative and center-of-mass coordinate as

$$x_r = \frac{(x_1 - x_2)}{\sqrt{2}} \tag{4.35}$$

$$x_c = \frac{(x_1 + x_2)}{\sqrt{2}}. \tag{4.36}$$

While the c.o.m. potential is harmonic with lattice site trap frequency ω_t, the relative potential is a combination of the harmonic and atomic interaction potential (Fig. 4.16). When a molecule is dissociated by ramping over a magnetic Feshbach resonance, the quantum level in the relative coordinate changes from a bound molecular state to

---

[2] A fraction of 10% of the molecules is assumed to be lost during the transfer due to the limited STIRAP efficiency.

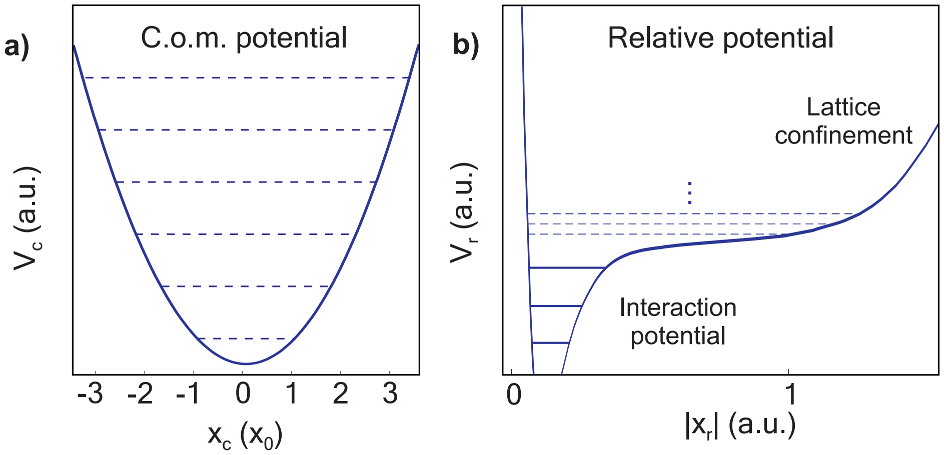

Figure 4.16:
Potentials for the center-of-mass and relative coordinates of two atoms trapped at a site of the optical lattice. a) The bound states (dashed lines) of the harmonic c.o.m. potential V_c correspond to the Bloch bands for molecules. b) At short interatomic distances the relative potential V_r is dominated by the interaction potential of two atoms, which allows the formation of bound molecular states (solid lines). Atoms that do not form such molecular states are trapped by the lattice potential at larger separation (dashed lines). With help of a Feshbach resonance the lowest trap state can be converted into a weakly-bound molecular state. Note that in this schematic view, both energy and distance for the two contributions to the relative potential are not to scale.

an atomic pair state, while the c.o.m. wavefunction remains unaffected. By applying the transformation from relative-/c.o.m.- to atomic coordinates we can calculate how molecular Bloch bands are converted into atomic ones. To illustrate, we write the wavefunction for an atomic pair produced by dissociation of a molecule in the lowest Bloch band as

$$|\Phi\rangle = \frac{1}{x_0\sqrt{2}}\exp(-\frac{x_c^2}{2x_0^2})\exp(-\frac{x_r^2}{2x_0^2}) = \frac{1}{x_0\sqrt{2}}\exp(-\frac{x_1^2}{2x_0^2})\exp(-\frac{x_2^2}{2x_0^2}), \tag{4.37}$$

i.e., both atoms end up in the lowest Bloch band as well. This analysis can be extended to higher bands. The conversion amplitudes for the four lowest symmetric molecular bands are given in Tab. 4.1.

In the absorption imaging process, the optical density is integrated in the direction of observation. We therefore assume atoms which are in higher bands in this direction to be counted as signal, while atoms in higher bands in the perpendicular directions are not detected.

		atomic Bloch band								
		0	1	2	3	4	5	6	7	$\dots$
molecular band	0	1	0	0	0	0	0	0	0	$\dots$
	2	$\frac{1}{2}$	$-\sqrt{\frac{1}{2}}$	$\frac{1}{2}$	0	0	0	0	0	$\dots$
	4	$\frac{1}{4}$	$-\sqrt{\frac{4}{16}}$	$\sqrt{\frac{6}{16}}$	$-\sqrt{\frac{4}{16}}$	$\frac{1}{4}$	0	0	0	$\dots$
	6	$\frac{1}{8}$	$-\sqrt{\frac{6}{64}}$	$\sqrt{\frac{15}{64}}$	$-\sqrt{\frac{20}{64}}$	$\sqrt{\frac{15}{64}}$	$-\sqrt{\frac{6}{64}}$	$\frac{1}{8}$	0	$\dots$
	$\vdots$	$\vdots$	$\vdots$	$\vdots$	$\vdots$	$\vdots$	$\vdots$	$\vdots$	$\vdots$	

Table 4.1:
Band conversion amplitudes in the harmonic oscillator approximation. Each row gives the amplitudes for a constituent atom of a molecule in a specific band to populate the different atomic bands after dissociation. Certain correlations for the conversion of the two atoms of a molecule are implied by energy conservation. If, for example, atom 1 from a molecule in band 2 ends up in the lowest band, the second atom has to be converted to band 2. Note that the squares of the amplitudes correspond to the binomial coefficients.

Molecular oscillations

We will now apply this model to the molecular oscillations observed in Sec. 4.5.1, and give a more detailed discussion of the results. For the simulation of the STIRAP transfers we use the same pulse shapes as for the master equation model (see Fig. 4.10). As already mentioned in Sec. 4.5.1, the shape of the molecular wavepacket does not change during the first STIRAP transfer. Directly after the transfer it essentially still corresponds to the lattice ground state for the Feshbach molecules, $|\Psi_{f0}\rangle$ (Fig. 4.17). In the much weaker lattice potential felt by the ground state molecules, such a wavepacket can only be formed by including excited bands. For the data from Fig. 4.13 we find 1D excitation probabilities of (84%, 13%, 3%, 0.2%)[3] for bands $b = (0, 2, 4, 6)$. This means that about 60% of the molecules are in the lattice ground state in all three dimensions after the first STIRAP pulse. In the following evolution, the molecular wavepacket undergoes breathing oscillations at the lattice site trap frequency ω_t (see Fig. 4.17), which are damped by tunneling to neighboring sites. Depending on the shape of molecular wavepacket at the time of the return STIRAP pulse, the excitation

---

[3] The given probabilities are normalized to sum up to 1, i.e., losses due to STIRAP or excitation of higher bands are not included.

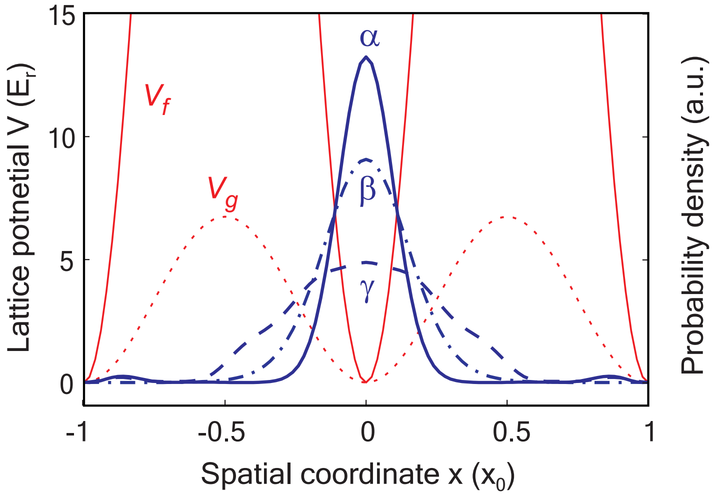

Figure 4.17:
Molecular breathing oscillations. Directly after the first STIRAP transfer the molecular wavepacket essentially has the shape of the ground state $|\Psi_{f0}\rangle$ (thick solid line, α) of the sinusoidal lattice potential for the Feshbach molecules, V_f. As this does not correspond to the ground state $|\Psi_{g0}\rangle$ (thick dash-dotted line, β) of the much weaker lattice potential for the ground state molecules, V_g, the wavepacket starts to oscillate. After 1/8 of the oscillation period $\tau_{osc} = 2\pi/\omega_t$ it roughly corresponds to $|\Psi_{g0}\rangle$, and reaches its maximum extension after $\tau_{osc}/4$ (thick dashed line, γ).

of higher bands is mapped back onto the $|f\rangle$ molecules. As we detect only atoms in the first Brillouin zone, this leads to an apparent oscillation in transfer efficiency for the data shown in Fig. 4.13. Fitting our model to this data we deduce that the lattice potential for $|g\rangle$ is shallower than for $|f\rangle$ by a factor of 10 ± 2. After one quarter of the oscillation period $\tau_{osc} = 2\pi/\omega_t$ the wavepacket reaches its maximum extension (dashed line γ in Fig. 4.17). At this point, the return STIRAP transfer leads to a maximum excitation of higher bands in $|f\rangle$, and a minimum of detected molecules. Neglecting tunneling, the excitation probabilities for the different bands in $|f\rangle$ would be (47%, 42%, 11%, 0.1%). In this case, the wavepacket would reach its initial shape again after half an oscillation period $\tau_{osc}/2$, and be completely transferred into the lowest band for $|f\rangle$ by the second STIRAP pulse. Due to tunneling to neighboring lattice sites, however, the coherence between the different bands is lost and the oscillation is damped. For a completely incoherent sample ($\tau_h \to \infty$) the 1D excitation probabilities after the second STIRAP transfer are (71%, 17%, 9%, 3%), i.e., about 35% of the molecules end up in the lowest band of $|f\rangle$ in all three dimensions.

Square pulse projection

The question now arises why we do not observe such molecular oscillations in the dark state projection measurements from Sec. 4.4.1, especially for the case $\Omega_1 \simeq \Omega_2$ where $|DS\rangle$ has a contribution of about 50% from $|g\rangle$. To gain deeper insight into the system, we simulate these square pulse experiments with our multi-band model. For this we set the detuning $\Delta_1 = \delta = 0$ and use square Raman pulses as shown in Fig. 4.12b. Diagonalizing the Hamiltonian from Eq. 4.31, we find twelve "eigenstates" with complex eigenvalues. In case of strong coupling ($\Omega_{1,2} \gg \omega_t$) four of them have negligible contribution from the excited state $|e\rangle$ and are thus long-lived. For our dark state projection measurements we typically have $\Omega_{1,2} \gtrsim 2\pi \times 1\,\mathrm{MHz}$ and $\omega_t \sim 2\pi \times 10\,\mathrm{kHz}$, and are well within this regime. The four quasi-dark eigenstates essentially correspond to the four bands of our model and will be denoted as $|DS_n\rangle$, with $n = 0, 2, 4, 6$. Neglecting a small contribution from $|e\rangle$ they can be considered to consist of

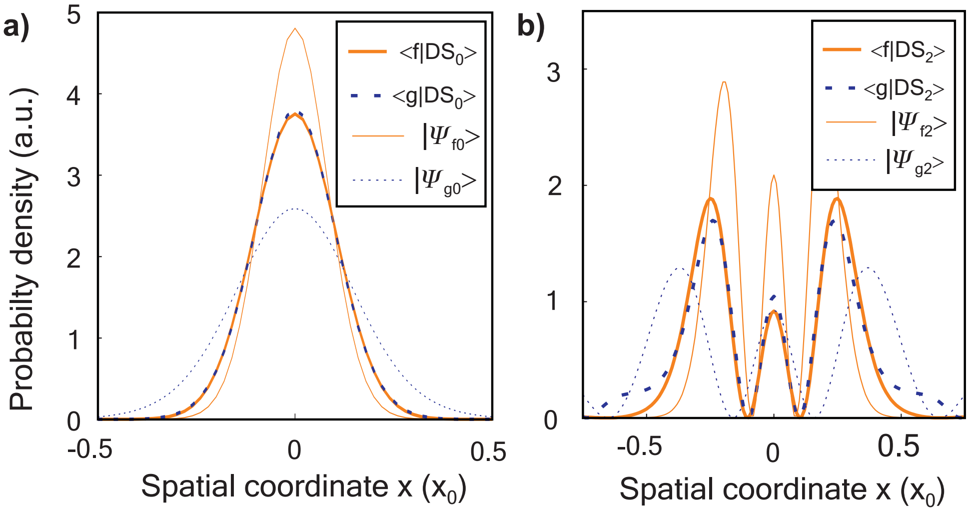

Figure 4.18:
Dark state wavepackets. a) The two components of the dark state with lowest energy $|DS_0\rangle$ having $|f\rangle$ and $|g\rangle$ character, $\langle f|DS_0\rangle$ (thick solid line) and $\langle g|DS_0\rangle$ (thick dashed line), essentially have the same shape. Their main contributions are from the respective lattice ground states $|\Psi_{f0}\rangle$ (thin solid line) and $|\Psi_{g0}\rangle$ (thin dotted line). All depicted states are normalized. b) Same as a), but for the dark state corresponding to the second band, $|DS_2\rangle$, and the according lattice states $|\Psi_{f2}\rangle$ and $|\Psi_{g2}\rangle$. For the higher dark states $|DS_{4,6}\rangle$ the situation is analogous. The parameters used are $\Omega_1 = \Omega_2 = 2\pi \times 7\,\mathrm{MHz}$, $V_f = 60\,E_r$ and $V_g = 6\,E_r$, typical for our experiments.

$|f\rangle$ and $|g\rangle$ components only, and we write them as

$$|DS_n\rangle = |g\rangle\langle g|DS_n\rangle + |f\rangle\langle f|DS_n\rangle. \tag{4.38}$$

It turns out that the $|f\rangle$- and $|g\rangle$ component wavepackets for the different $|DS_n\rangle$, $\langle g|DS_n\rangle$ and $\langle f|DS_n\rangle$, have the same spatial shape (Fig. 4.18). This fact ensures that the condition imposed by Eq. 4.6, that the ratio of $|f\rangle$- and $|g\rangle$ amplitudes equals Ω_2/Ω_1, is satisfied everywhere.

After subjecting the Feshbach molecules to a square Raman laser pulse, a dark state is formed in less than 1 μs. As in the STIRAP transfer, the shape of the molecular wavepacket does not change during this process, and still corresponds to $|\Psi_{f0}\rangle$, the lattice ground state for $|f\rangle$. The dark state can now be written as a superposition of the four dark eigenstates from Eq. 4.38

$$|DS\rangle = \sum_{n=0,2,4,6} c_n |DS_n\rangle. \tag{4.39}$$

The subsequent coherent evolution of these dark states will in principle lead again to breathing oscillations. The amplitude of these oscillations depends on the extent to which higher dark states (i.e., $|DS_n\rangle$ with $n > 0$) are excited. The excitation increases with increasing deviation of $|DS\rangle$ from the initial state $|f\rangle$, i.e., with rising Ω_1/Ω_2. For the projection measurement with $\Omega_1 = \Omega_2$ that is shown as a red line in Fig. 4.12a, we find 1D excitation probabilities for $|DS_n\rangle$ of (98.6%, 1.2%, 0.2%, <0.1%) for n = (0, 2, 4, 6).

This can also be understood in another picture. As for each of the individual eigenstates $|DS_n\rangle$, the $|f\rangle$- and $|g\rangle$ components of $|DS\rangle$ have identical shapes. The superposition state $|DS_n\rangle$ can thus be considered to experience an effective lattice potential which is the weighted average of the potentials for the two contributing states $|f\rangle$ and $|g\rangle$. For the case $\Omega_1 = \Omega_2$ this effective potential is about half as deep as that for the Feshbach molecules. Compared to the case of pure ground state molecules, where the lattice potential is reduced by a factor of 10, the oscillations of the wavepacket are strongly suppressed[4] and cannot be observed with our current experimental precision. For $\Omega_1 \gg \Omega_2$, the dark state $|DS\rangle$ has a dominant contribution from state $|g\rangle$, and the effective lattice potential essentially corresponds to the one for ground state molecules. In Fig. 4.19a a measurement for $|DS\rangle$ with $\Omega_1/\Omega_2 \approx 5$ is shown. In this case oscillations similar to the ones observed in the previously discussed STIRAP transfer appear despite the strong coupling. For these experiments we have ramped into the dark state and back in a fashion similar to STIRAP to avoid strong losses caused by direct projection into $|DS\rangle \approx |g\rangle\langle g|DS\rangle$ (see Fig. 4.19b). From our model, we deduce excitation probabilities of (87%, 10%, 2%, 0.2%) for the different $|DS_n\rangle$. These values are close to those we had for the different lattice bands during of a STIRAP transfer

---

[4] Note that in the harmonic approximation we have $x_0 \propto V_0^{-1/4}$, where x_0 is the oscillator length and V_0 the depth of the potential.

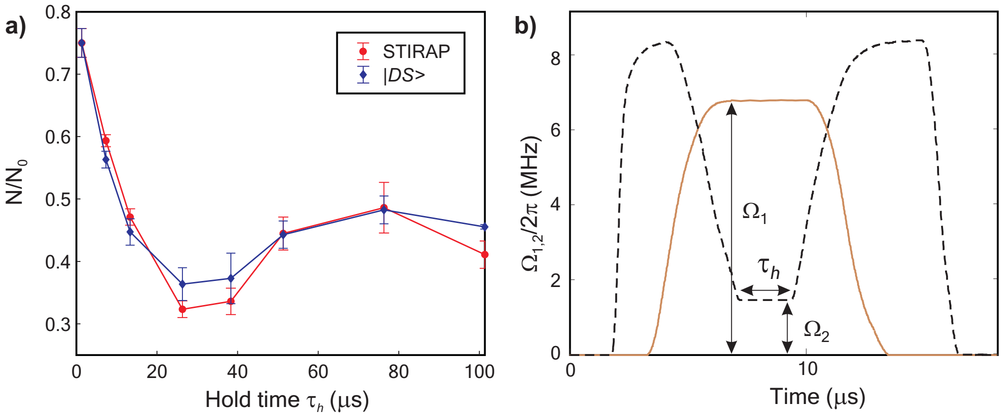

Figure 4.19:
Oscillation of dark state. a) The red circles show the same data as in Fig. 4.13, i.e., the fraction of detected Feshbach molecules after two STIRAP pulses as a function of hold time. The blue diamonds are from a similar measurement, but instead of completely transferring the molecules into the ground state, they are kept in a dark superposition state where about 95% of the population is in $|g\rangle$. b) Pulse shapes for the dark state measurement shown as blue diamonds in a). The pulses are similar to the ones used for the STIRAP transfer, but instead of ramping down, laser 1 is kept at its maximum value of $\Omega_1 = 7\,\text{MHz}$. Laser 2 is ramped to $\Omega_2 = 1.5\,\text{MHz}$ and kept at this value during the holding period of length τ_h.

(84%, 13%, 3%, 0.2%). This is expected, as in the limit $\Omega_1 \gg \Omega_2$ the dark states $|DS_n\rangle$ approach the lattice states $|\Psi_{gn}\rangle$.

5 Summary and outlook

Two methods to transfer molecules between different states have been presented. A radio frequency based scheme allows adiabatic transfer of molecules across avoided crossings. This technique is in principle applicable to arbitrary avoided crossings, but can only bridge a limited energy gap. Starting from Feshbach molecules, almost any molecular state up to a binding energy of a couple of GHz×h can be accessed. The intrinsic constraint, that the association of Feshbach molecules is possible only for a limited number of specific quantum states, can thus be overcome. In particular, the rf-transfer scheme can be utilized to prepare molecules in states that are ideal starting points for subsequent optical transfers, e.g. by optimizing Franck-Condon factors [Danz 08].

Using radio frequency spectroscopy, we have mapped out the energy spacing of avoided crossings between molecular states and thus the strength of the involved couplings with very high precision. The accuracy of this data surpasses that of current theoretical models employed for the calculation of molecular energy spectra by several orders of magnitude, and might lead to a considerable improvement of these models.

Molecules can be transferred from weakly to deeply bound states with optical transfer schemes like STIRAP. This brings the production of a molecular ground state Bose-Einstein condensate, which is a strongly pursued goal of this field, within reach. A possible route to achieve this, is to transfer molecules associated from an atomic Mott-insulator state in a three-dimensional optical lattice into their rovibrational ground state. These molecules are expected to be stable under collisions, and a Bose-Einstein condensate might be formed after subsequently melting the Mott-insulator [Jaks 02].

In our experiments, we have transferred Feshbach molecules in a 3D optical lattice into the rovibrational ground state of the $a^3\Sigma_u^+$ triplet potential. The collisional properties of these triplet molecules are presently unknown. In particular their stability with respect to relaxation into more deeply bound singlet states is subject to speculation. By ramping down the optical lattice in the two horizontal directions, an assembly of pancake-shaped traps could be created, which offers an environment for collisional studies [Krem 08].

In contrast to singlet molecules, those in triplet states have a non-zero magnetic moment, and thus a much richer level structure. Model calculations predict avoided crossings between different rotational- and hyperfine states to exist all the way to the vibrational ground state of the $a^3\Sigma_u^+$ triplet potential [Bran 07]. Hence, the combination of the optical STIRAP transfer with our radio frequency based scheme allows the preparation of triplet molecules in almost arbitrary quantum levels. Of special interest are, for example, states that are promising starting points for molecule-molecule Feshbach resonances.

A superlattice, which is currently set up in our laboratory, represents an ideal system for the investigation of such molecular Feshbach resonances. After preparing molecules in well-defined states, the superlattice can be used to enforce controlled collisions between pairs of molecules. This can be seen as a step towards novel multi-particle physics [Krae 06, Knoo 09] and coherent cold chemistry [Hein 00, Krem 08].

Spectroscopic measurements of molecular quantum states offer new perspectives for studies of the possible variation of physical constants. For example, the sensitivity of molecular vibrational energies to the electron-proton mass ratio permits the investigation of the time-dependence of this parameter. Zelevinsky and coworkers propose to use ultracold molecules in a three-dimensional optical lattice and probe the vibrational energy spacing with a Raman spectroscopy scheme [Zele 08]. In a different approach, a transfer of molecules into vibrational levels that are almost degenerate with those of another molecular potential (e.g. the $X^1\Sigma_g^+$ singlet- and $a^3\Sigma_u^+$ triplet ground potentials) has been suggested [Flam 07, DeMi 08]. The energy difference could then be measured via microwave spectroscopy, thereby considerably enhancing the relative sensitivity of such measurements.

Appendix A

Publications

In the course of this thesis the following paper have been published:

1. F. Lang, C. Strauss, K. Winkler, T. Takekoshi, R. Grimm, J. Hecker Denschlag.
   Dark state experiments with ultracold, deeply-bound triplet molecules.
   Faraday Discuss. **142**, 1-13, 2009.

2. F. Lang, K. Winkler, C. Strauss, R. Grimm, J. Hecker Denschlag.
   Ultracold triplet molecules in the rovibrational ground state.
   Phys. Rev. Lett. **101**, 133005, 2008

3. F. Lang, P.v.d. Straten, B. Brandstätter, G. Thalhammer, K. Winkler, P.S. Julienne, R. Grimm, J. Hecker Denschlag.
   Cruising through molecular bound state manifolds with radio frequency.
   Nat. Phys. **4**, 223, 2008.

4. K. Winkler, F. Lang, G. Thalhammer, P.v.d. Straten, R. Grimm, and J. Hecker Denschlag.
   Coherent optical transfer of Feshbach molecules to a lower vibrational state.
   Phys. Rev. Lett. **98**, 043201, 2007.

5. A.J. Daley, A. Kantian, H.P. Büchler, P. Zoller, K. Winkler, G. Thalhammer, F. Lang, R. Grimm, J. Hecker Denschlag.
   Repulsively bound atom pairs: Overview, simulations and links.
   Proceedings ICAP-2006 (Innsbruck).

6. K. Winkler, G. Thalhammer, F. Lang, R. Grimm, J. Hecker Denschlag, A. J. Daley, A. Kantian, H. P. Büchler, and P. Zoller.
   Repulsively bound atom pairs in an optical lattice.
   Nature **441**, 853, 2006.

7. S. Schmid, G. Thalhammer, K. Winkler, F. Lang, and J. Hecker Denschlag.
   Long distance transport of ultracold atoms using a 1D optical lattice.
   New J. Phys. **8**, 159, 2006

8. G. Thalhammer, K. Winkler, F. Lang, S. Schmid, R. Grimm, and J. Hecker Denschlag.
   Long-lived Feshbach molecules in a three-dimensional optical lattice.
   Phys. Rev. Lett. **96**, 050402, 2006.

Faraday Discussions 142: Cold and Ultracold Molecules RSC Publishing
DOI:10.1039/b818964a 2009

Dark state experiments with ultracold, deeply-bound triplet molecules

Florian Lang[a], Christoph Strauss[a], Klaus Winkler[a], Tetsu Takekoshi[a],
Rudolf Grimm[a,b], Johannes Hecker Denschlag*[a]

[a]Institut für Experimentalphysik und Zentrum für Quantenphysik,
Universität Innsbruck, A-6020 Innsbruck, Austria
[b]Institut für Quantenoptik und Quanteninformation
der Österreichischen Akademie der Wissenschaften, A-6020 Innsbruck, Austria
* E-mail: johannes.denschlag@uibk.ac.at

Received 27th October 2008, accepted 15th January 2009
First published online 8th May 2009

We examine dark quantum superposition states of weakly bound Rb_2 Feshbach molecules and tightly bound triplet Rb_2 molecules in the rovibrational ground state, created by subjecting a pure sample of Feshbach molecules in an optical lattice to a bichromatic Raman laser field. We analyze both experimentally and theoretically the creation and dynamics of these dark states. Coherent wavepacket oscillations of deeply bound molecules in lattice sites, as previously observed by Lang *et al.* (*Phys. Rev. Lett.*, 2008, **101**, 133005), are suppressed due to laser-induced phase locking of molecular levels. This can be understood as the appearance of a novel multilevel dark state. In addition, the experimental methods developed help to determine important properties of our coupled atom / laser system.

---

1 Introduction

Very recently, several groups have produced dense, ultracold ensembles of molecules that are deeply bound[1,2,3,4,5] and in a ro-vibrational ground state[1,2,4,5]. This was achieved by binary association of alkali atoms in ultracold ensembles via two different pathways: (1) photoassociation[6,7] and (2) magneto-association at Feshbach resonances[7,8] combined with stimulated Raman adiabatic passage (STIRAP)[9], a special coherent optical transfer method. In contrast to photoassociation, magneto-association only produces weakly-bound Feshbach molecules[7,8]. STIRAP can then be used to transfer these weakly-bound molecules to the rovibrational ground state. This method is coherent, efficient, fast, reversible, and highly selective. STIRAP is based on a counter-intuitive light pulse sequence giving rise to a dynamically changing dark superposition state (Fig. 1a)

$$|DS\rangle = (\Omega_2|f\rangle - \Omega_1|g\rangle)\,/\sqrt{\Omega_1^2+\Omega_2^2}. \tag{1}$$

In this paper, we deliberately replace the efficient but complex STIRAP transfer of Ref.[1] with a simple square laser pulse scheme. This reveals interesting fundamental processes and dynamics in

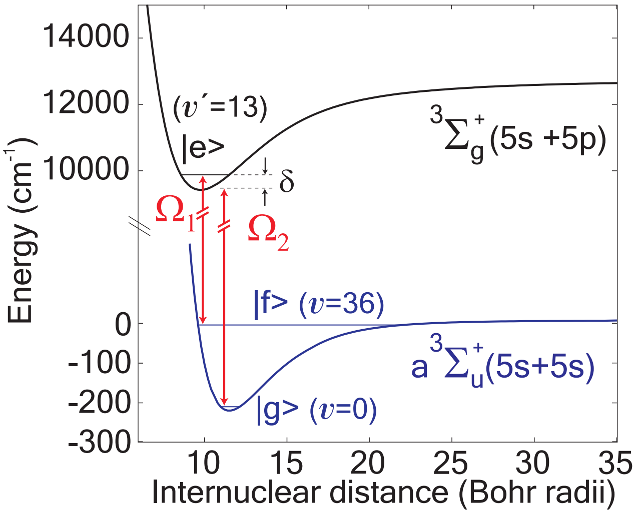

Figure 1: Λ-type three-level scheme for dark states. The lasers 1 and 2 couple the molecular levels $|f\rangle$, $|g\rangle$ to the excited level $|e\rangle$ with Rabi frequencies $\Omega_{1,2}$, respectively.

the coupled atom / laser system, that would otherwise be hidden. In addition, this procedure allows us to determine important properties and parameters of our system and to check for consistency with our theoretical model. We study the creation and lifetime of dark superposition states that contain a sizeable fraction of deeply bound molecules. These molecules are held in a 3D optical lattice. Because the lattice potential is much shallower for the deeply bound molecules than for the Feshbach molecules, and because the transfer is fast, the deeply bound molecules coherently populate several Bloch bands. In contrast to Ref.[1], where similar circumstances lead to coherent oscillations in the lattice, oscillations are suppressed in the experiment described here due to phase locking of all quantum levels involved. A novel dark state appears which is a superposition of up to 8 quantum levels. We investigate the limiting conditions under which oscillations set in.

2 Experimental setup and initial preparation of molecules

We carry out our dark state experiments with a 50 μm-size pure ensemble of 3×10^4 weakly bound Rb_2 Feshbach molecules. The molecules are trapped in the lowest Bloch band of a cubic 3D optical lattice with no more than a single molecule per lattice site[10] and an effective lattice filling factor of about 0.3. The lattice depth for the Feshbach molecules is $60\,E_r$, where $E_r = \pi^2\hbar^2/2ma^2$ is the recoil energy, with m the mass of the molecules and $a = 415.22\,\text{nm}$ the lattice period. Such deep lattices suppress tunneling between different sites. A pure ensemble of Feshbach molecules has been produced as follows. We prepare a cold cloud of 6×10^5 ^{87}Rb atoms that are either Bose condensed or *nearly*[1] Bose condensed in a Ioffe-type magnetic trap with trap frequencies $\omega_{x,y,z} = 2\pi \times (7, 19, 20)$ Hz. Within 100 ms we adiabatically load the atoms into the 3D optical lattice. After turning off the magnetic trap, we flip the spins of our atoms from their initial state $|F = 1, m_F = -1\rangle$ to $|F = 1, m_F = +1\rangle$ by suddenly reversing the bias magnetic field of a few G. This spin state features a 210 mG-wide Feshbach resonance at 1007.40 G[11]. By adiabatically ramping over this resonance, we efficiently convert atoms at multiply occupied lattice sites into Rb_2 Feshbach molecules. After conversion, inelastic collisions occur at lattice sites that contain more particles than

---

[1] It turns out that this increases the number of Feshbach molecules.

a single Feshbach molecule, leading to vibrational relaxation of these molecules, release of binding energy into kinetic energy and removal of all particles from these sites. A subsequent combined microwave and optical purification pulse removes all remaining chemically unbound atoms, creating a pure sample of 3×10^4 Feshbach molecules. Afterwards, the magnetic field is set to 1005.8 G, where the Feshbach molecules are in a quantum state $|f\rangle$ which correlates with $|F=2, m_F=2, f_1=2, f_2=2, v=36, l=0\rangle$ at 0 G. Here, F and $f_{1,2}$ are the total angular momentum quantum numbers for the molecule and its atomic constituents, respectively, and m_F is the total magnetic quantum number; v is the vibrational quantum number for the triplet ground state potential ($a^3\Sigma_u^+$) and l is the quantum number for rotation.

The bichromatic Raman laser field for the creation of the molecular dark states is based on two lasers (1 and 2) which connect the Feshbach molecule level $|f\rangle$, via an excited level $|e\rangle$, to the absolute lowest level in the triplet potential $|g\rangle$ (Fig. 1a). Laser 1 is a Ti:Sapphire laser and laser 2 is a grating-stabilized diode laser. Both lasers are Pound-Drever-Hall locked to a single cavity which itself is locked to an atomic ^{87}Rb-line. From the lock error signals, we estimate frequency stabilities on a ms-timescale of 40 kHz and 80 kHz for lasers 1 and 2, respectively. Both laser beams have a waist of 130 μm at the location of the molecular sample, propagate collinearly, and are polarized parallel to the direction of the magnetic bias field. Thus, the lasers can only induce π transitions.

The ground state $|g\rangle$ has a binding energy of 7.03806(3) THz$\times h$ and can be described by the quantum numbers $|F=2, m_F=2, S=1, I=3, v=0, l=0\rangle$ where S and I are the total electronic and nuclear spins of the molecule, respectively. At 1005.8 G $|g\rangle$ is separated by hundreds of MHz from any other bound level, so that there is no ambiguity as to which level is addressed. The level $|e\rangle$ is located in the vibrational $v=13$ manifold of the electronically excited $^3\Sigma_g^+$ (5s + 5p) potential and has 1_g character. It has an excitation energy of 294.62610(6) THz$\times h$ with respect to $|f\rangle$, and a width $\Gamma = 2\pi\times$ 8 MHz. The Rabi frequencies $\Omega_{1,2}$ of the two lasers depend on their respective intensities $I_{1,2}$, i. e., $\Omega_1 = 2\pi\times 0.4\,\text{MHz}\sqrt{I_1/(\text{Wcm}^{-2})}$ and $\Omega_2 = 2\pi\times 30\,\text{MHz}\,\sqrt{I_2/(\text{Wcm}^{-2})}$, and are typically chosen to be in the MHz regime.

3 Dark state evolution within a square pulse

Our square pulse projection experiments are carried out as follows. We expose the Feshbach molecules $|f\rangle$ in the lattice to square pulses of Raman lasers 1 and 2 of variable pulse duration. Laser 2 is switched on about 1 μs before laser 1 to avoid excitation from $|f\rangle$ to $|e\rangle$ due to jitter in the laser pulse timing. The Raman lasers are resonant ($\delta = 0$) and the Rabi frequency $\Omega_2 \approx 2\pi \times 7$ MHz while Ω_1 is varied (Fig. 2). After the pulse, we measure the fraction of molecules remaining in state $|f\rangle$ by dissociating them into pairs of atoms at the Feshbach resonance, releasing them from the lattice and applying standard absorption imaging. It is important to note that we actually only count atoms in the lowest Bloch band of the lattice. The release from the optical lattice is done as described in[12], where after 13 ms of ballistic expansion we map out the Bloch bands in momentum space (see Appendix for details).

Figure 2 shows the remaining fraction of molecules in state $|f\rangle$ versus pulse duration. Within 1 μs we observe a rapid loss of molecules that depends on the ratio Ω_2/Ω_1. The remaining molecules are stable on a much longer timescale. This can be understood in terms of formation of a dark state $|DS\rangle$. We can write

$$|f\rangle = (\Omega_2|DS\rangle + \Omega_1|BS\rangle)\,/\sqrt{\Omega_1^2+\Omega_2^2} \tag{2}$$

where

$$|BS\rangle = (\Omega_1|f\rangle + \Omega_2|g\rangle)\,/\sqrt{\Omega_1^2+\Omega_2^2} \tag{3}$$

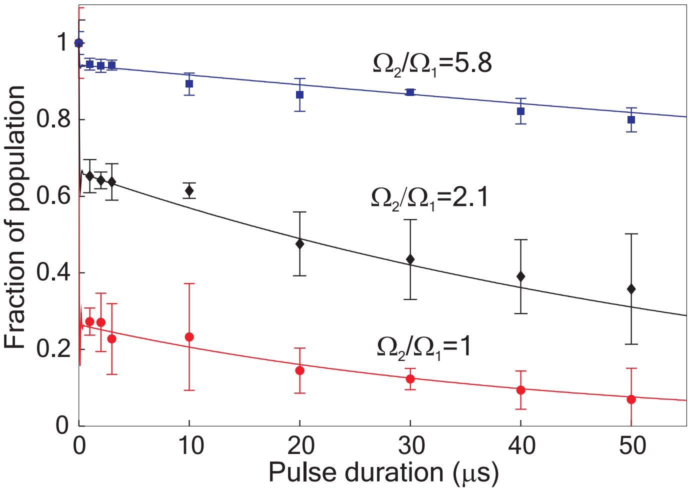

Figure 2: Dark state formation and lifetime. Shown is the fraction of Feshbach molecules remaining after subjecting them to a square pulse of Raman laser light of varying length for various Rabi frequency ratios Ω_2/Ω_1 ($\Omega_2 \approx 2\pi \times 7\,\mathrm{MHz}$). After switching on the lasers, a certain fraction of molecules is lost within 1 μs and a dark state has formed which has a much longer lifetime. The solid lines represent model calculations (Sec. 4) which can be used to determine the Rabi frequencies and short-term laser linewidths.

is a bright state which quickly decays via resonant excitation to level $|e\rangle$. The dark state remains after the lasers are switched on and can be detected as a fraction $\Omega_2^4/(\Omega_1^2+\Omega_2^2)^2$ of molecules projected back to $|f\rangle$ after switching off the lasers[2].

Also, after the pulse a fraction $\Omega_1^2\Omega_2^2/(\Omega_1^2+\Omega_2^2)^2$ of the initial molecules are in state $|g\rangle$ with a maximum of 25% for $\Omega_1 = \Omega_2$. Thus, a sizeable fraction of the molecules can be coherently transferred to the ground state. Remarkably, this transfer takes place in less than 1 μs! Such short transfer times cause Fourier broadening, resulting in considerably reduced laser stability requirements. In addition, due to the formation of a dark state, there is still a well-defined phase relation between the $|f\rangle$ and $|g\rangle$ molecules.

As can be seen from Fig. 2, the dark state slowly decays. Its lifetime is shortest for $\Omega_1 = \Omega_2$, where we measure it to be $\approx$50 μs. The decay of the dark state is likely due to phase fluctuations of the Raman lasers. Phase fluctuations lead to an admixture of a bright state component to the otherwise dark state, which causes losses. In Sec. 4 we will show that these fluctuations can be expressed in terms of the short-term relative linewidth of the lasers, γ, which we find to be about $2\pi \times 20\,\mathrm{kHz}$. In principle, the decay of the dark state could be due to other effects, such as coupling to levels other than $|f\rangle$, $|e\rangle$, and $|g\rangle$. However, we have verified that this is not the case, because losses due to optical excitation are completely negligible on the 100 μs-timescale when we expose a pure ensemble of $|f\rangle$ ($|g\rangle$) molecules to only laser 2 (1).

We also searched for laser power dependent shifts of the two-photon resonance. Using the Raman square pulse measurements, we scanned the relative detuning of the lasers for a fixed pulse duration and various laser powers. Within the accuracy of our measurements of $2\pi \times 200\,\mathrm{kHz}$, we could not detect any shifts of the resonance.

The behavior in Fig. 2 is described well by a closed three-level model (a Λ system) and its

---

[2] This fact can be used to conveniently calibrate the Rabi frequency ratio Ω_1/Ω_2. We found good agreement with other calibration methods for the Rabi frequencies.

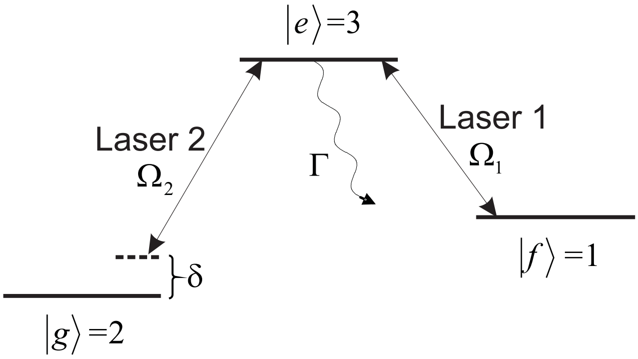

Figure 3: Level scheme for the master equation.

dynamics can be simulated with a master equation which we describe in the following.

4 Three-level model and master equation

Neglecting lattice effects, we can describe the internal dynamics of the molecules as they are subjected to the Raman laser fields with a three-level model. We use a master equation[13,14] which takes into account decoherence due to phase fluctuations of the Raman lasers. We consider the case where laser 1 is kept on resonance and laser 2 has a detuning δ (Fig. 3). Identifying the levels $|f\rangle$, $|g\rangle$, $|e\rangle$ with numbers 1, 2, 3, respectively, we can write the master equation as,

$$\begin{aligned}\frac{d\rho}{dt} &= -i\delta\left[\sigma^{22},\rho\right] - \frac{i}{2}\sum_{k=1}^{2}\Omega_k\left[\sigma_-^{3k}+\sigma_+^{3k},\rho\right] \\ &-\frac{1}{2}\Gamma\left(\sigma^{33}\cdot\sigma^{33}\cdot\rho+\rho\cdot\sigma^{33}\cdot\sigma^{33}\right) \\ &+\frac{1}{2}\gamma\left(2\sigma^{22}\cdot\rho\cdot\sigma^{22}-\sigma^{22}\cdot\rho-\rho\cdot\sigma^{22}\right),\end{aligned} \tag{4}$$

where ρ is the density matrix, $\Omega_{1,2}$ are the Rabi frequencies, Γ is the spontaneous decay rate of the excited level $|e\rangle$, and γ is the relative linewidth of the two Raman lasers. The matrices σ_-^{rs} and σ_+^{rs} are ladder operators and each is the transpose of the other. For example

$$\sigma_-^{32} = \begin{pmatrix} 0 & 0 & 0 \\ 0 & 0 & 0 \\ 0 & 1 & 0 \end{pmatrix} = \left(\sigma_+^{32}\right)^{\mathrm{T}}. \tag{5}$$

Setting the linewidth of the excited level Γ = 8 MHz, the detuning $\delta = 0$ and Rabi frequencies $\Omega_2 = 2\pi\times 7$ MHz and Ω_1 to give the ratios in Fig. 2, we fit all the data with a single fit parameter γ. As a best fit, we obtain a relative linewidth of the two Raman lasers $\gamma = 2\pi\times 20\,\mathrm{kHz}$, which is a reasonable value for our laser system.

5 Coherent oscillations and their suppression

In reference[1] coherent oscillations of molecular wavepackets of $|g\rangle$ molecules in the optical lattice were observed. We now investigate how these observations fit together with the experimental results

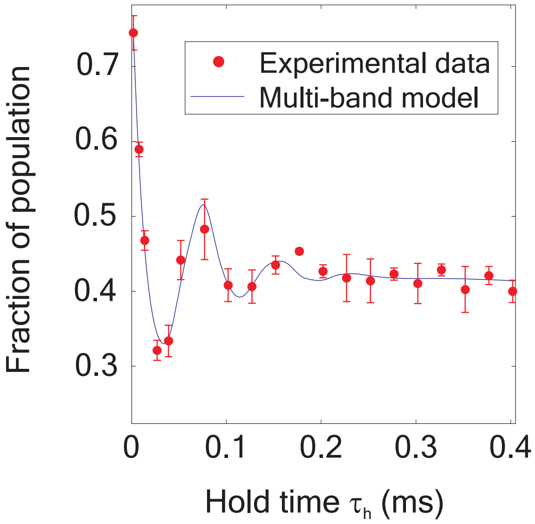

Figure 4: We plot the transfer efficiency for the round-trip STIRAP process as a function of the hold time τ_h between the two STIRAP pulses. With our procedure we only count molecules whose constituent atoms end up in the lowest Bloch band after transfer. The oscillations in the transfer efficiency are due to breathing oscillations of localized spatial wavepackets of molecules in the lattice sites. The solid line is from a multi-band model calculation (Sec. 6). This plot is taken from Ref.[1].

of the square pulse projection experiments presented here. For clarity, the oscillation data from Ref.[1] are presented again in Fig. 4 and briefly discussed.

Using a STIRAP pulse, Feshbach molecules are efficiently transferred to level $|g\rangle$. The Raman lasers are extinguished and the molecules are held for a time τ_h, after which they are transferred back to $|f\rangle$ with a reverse STIRAP pulse. The number of recovered Feshbach molecules is counted. However, we only detect atoms that end up in the lowest Bloch band after dissociation of the Feshbach molecules (see Appendix). The oscillation can be understood as follows. We consider the localized spatial center-of-mass (c.o.m.) wavepacket of a Feshbach molecule at a particular lattice site in the lowest Bloch band. The first STIRAP transfer projects this wavepacket onto the much shallower[3] lattice potential felt by the $|g\rangle$ molecules (Fig. 5) without changing its shape. As a consequence, $|g\rangle$ molecules are coherently spread over various Bloch bands, and the wavepacket undergoes "breathing" oscillations with the lattice site trap frequency ω_t. These coherent oscillations (period $\approx 80\,\mu$s) are damped by tunneling of $|g\rangle$ molecules in higher Bloch bands to neighboring lattice sites. The reverse STIRAP transfer maps this periodic oscillation back to the Feshbach molecule signal in Fig. 4. Higher Bloch bands are populated here as well, but are at most partially counted in our scheme (see Appendix), which leads to an apparent decrease in transfer efficiency.

The question arises why similar oscillations are not observed in our square pulse projection measurements shown in Fig. 2, especially for the case $\Omega_1 = \Omega_2$ where 50% of the population is in state $|g\rangle$. One might assume that the spatial wavepackets of the $|g\rangle$ molecules undergo similar breathing oscillations. These oscillations would then periodically break up the dark superposition state and lead to corresponding losses. They would also periodically produce population in higher Bloch bands of the Feshbach molecule lattice. As we will see, the oscillations are suppressed because the Raman lasers phase lock the involved quantum levels which stops, in a sense, the free evolution

---

[3] Due to a smaller dynamic polarizability, the lattice depth for the tightly bound $|g\rangle$ molecules is shallower than for the Feshbach molecules by a factor of $\approx$10.

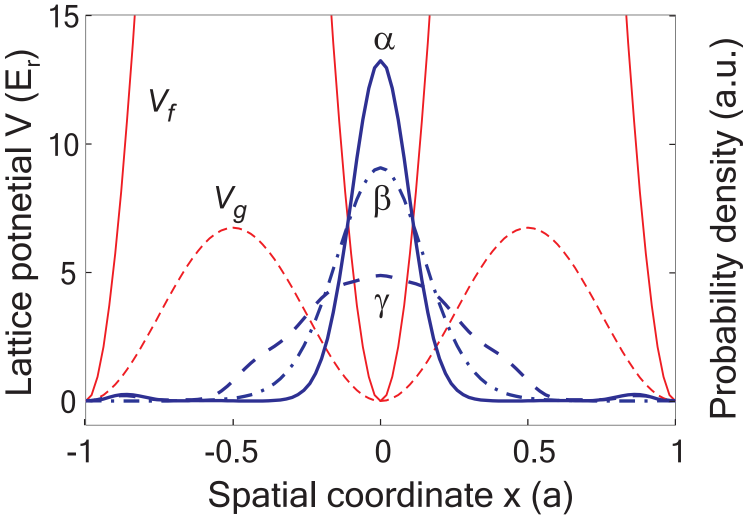

Figure 5: Wavepacket dynamics. Directly after the STIRAP transfer of a molecule from $|f\rangle$ to $|g\rangle$ the shape of its wavepacket (thick solid line α) essentially corresponds to the vibrational ground state of the sinusoidal lattice potential for Feshbach molecules V_f (thin solid line). In the much weaker potential felt by the ground state molecules V_g (thin dashed line) the wavepacket starts to oscillate. After 1/8 of the oscillation period $\tau_{osc} = 2\pi/\omega_t$ its shape roughly corresponds to the vibrational ground state for $|g\rangle$ (thick dash-dotted line β) and reaches its maximum extension after $\tau_{osc}/4$ (thick dashed line γ).

of the wavepackets. We can understand this behavior in detail with the help of a multi-band model, which we describe in the following.

6 Multi-band model

In an optical lattice the molecular levels $|f\rangle$, $|g\rangle$ and $|e\rangle$ from the previous model have a substructure given by the lattice Bloch bands. Because the lattice depths for the levels $|f\rangle$, $|g\rangle$ and $|e\rangle$ are in general different, the respective band structures will also vary. This combination of external (c.o.m. motion in the lattice) and internal degrees of freedom gives rise to a number of new quantum levels which are coupled by the laser fields (Fig. 6). We assume each Feshbach molecule to be initially localized in a singly-occupied lattice site. The corresponding localized molecular wavepacket can be described by Wannier functions[15] which form a complete set of orthonormal functions. In the following we will denote the Wannier function for level $|\alpha\rangle$ and band n as $|\Psi_{\alpha n}\rangle$. We note that for deep lattices, these Wannier functions closely resemble harmonic oscillator wavefunctions.

The Raman lasers couple different $|\Psi_{\alpha n}\rangle$ according to the respective wavefunction overlaps (Fig. 6). Since the initial wavepackets of the Feshbach molecules are symmetric, only even bands will be populated. We restrict our calculations to the four lowest Bloch bands with even symmetry,[4] corresponding to the band indices $n = 0, 2, 4, 6$. The dynamics in each of the three lattice directions is then described by a 12-level model, which can in principle be solved in terms of a master equation (Sec. 4). However, we have used a Schrödinger equation-based model since the numerical code is less involved. In this approach, laser phase fluctuations are neglected, and we introduce a lattice site tunnel rate for each band. These tunnel rates are chosen to match the expected tunnel rates for the

---

[4] The effect of including higher bands into the model was found to be negligible.

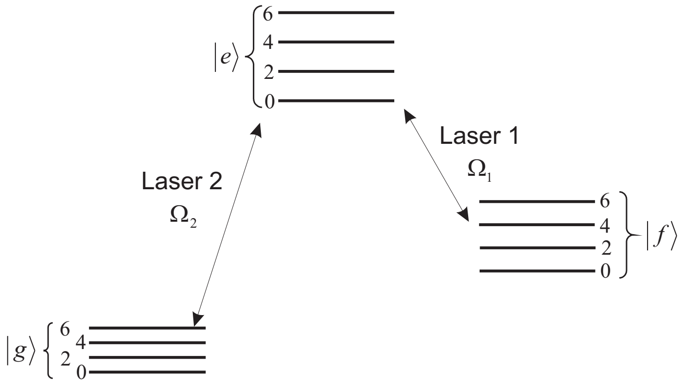

Figure 6: Multi-band model. The three molecular levels $|f\rangle$, $|e\rangle$ and $|g\rangle$ have a Bloch band substructure due to the optical lattice. We restrict the model to the 4 lowest Bloch bands with even symmetry (band index $n = 0, 2, 4, 6$).

different bands and are slightly adjusted for a better fit of the data in Fig. 4. We note that the results of the model calculations are essentially independent of the excited state lattice depth, which is not well known.

The Hamiltonian H of our time dependent Schrödinger equation

$$i\hbar\frac{\partial}{\partial t}|\Phi\rangle = H|\Phi\rangle \tag{6}$$

has the form of a 12×12 matrix,

$$\hat{H} = \hbar \begin{pmatrix} E_{f0} - \frac{i}{2}J_{f0} & 0 & \frac{1}{2}\Omega_1(t)\cdot M_{f0,e0} & 0 & \dots \\ 0 & E_{g0} + \delta - \frac{i}{2}J_{g0} & \frac{1}{2}\Omega_2(t)\cdot M_{g0,e0} & 0 & \dots \\ \frac{1}{2}\Omega_1(t)\cdot M_{e0,f0} & \frac{1}{2}\Omega_2(t)\cdot M_{e0,g0} & E_{e0} - \frac{i}{2}\Gamma - \frac{i}{2}J_{e0} & \frac{1}{2}\Omega_1(t)\cdot M_{e0,f2} & \dots \\ 0 & 0 & \frac{1}{2}\Omega_1(t)\cdot M_{f2,e0} & E_{f2} - \frac{i}{2}J_{f2} & \dots \\ \vdots & \vdots & \vdots & \vdots & \end{pmatrix}. \tag{7}$$

Here $E_{\alpha n}$ and $J_{\alpha n}$ are the energy and tunnel matrix element respectively for the Wannier function $|\Psi_{\alpha n}\rangle$ in band n of level $|\alpha\rangle$. $M_{\alpha n,\beta k} = \langle\Psi_{\alpha n}|\Psi_{\beta k}\rangle$ is the overlap integral of the respective Wannier functions.

Diagonalizing this Hamiltonian, we find twelve "eigenstates" of the coupled system which in general have complex eigenvalues. In the following, we study the case of strong coupling ($\Omega_{1,2} \gg \omega_t$),[5] which is the regime for phase locking. In this regime, four of these eigenstates have negligible contribution from the excited level $|e\rangle$ and thus a long lifetime. These 4 quasi-dark states essentially correspond to the 4 lattice bands in our model and will be denoted as $|DS_n\rangle$ with n = 0, 2, 4, 6. We now study the spatial waveforms of these dark states (Fig. 7) and compare the components with $|f\rangle$ and $|g\rangle$ character. Neglecting a small $|e\rangle$ component the dark superposition state, $|DS_n\rangle$ can be written as

$$|DS_n\rangle = |g\rangle\langle g|DS_n\rangle + |f\rangle\langle f|DS_n\rangle. \tag{8}$$

As an example ($\Omega_1 = \Omega_2$) Fig. 7 shows that the wavepackets $\langle g|DS_n\rangle$ and $\langle f|DS_n\rangle$ have the same shape. This is not surprising since this ensures that the ratio of the $|f\rangle$ and $|g\rangle$ amplitudes equals Ω_2/Ω_1 everywhere, as in Eq. 1.

---

[5] For our experiments where $\Omega_{1,2} \gtrsim 2\pi \times 1\,\mathrm{MHz}$ and $\omega_t \sim 2\pi \times 10\,\mathrm{kHz}$ this condition is satisfied.

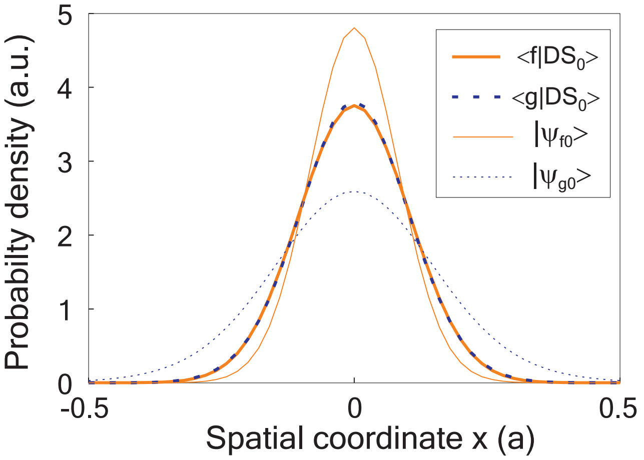

Figure 7: Spatial wavepackets of the dark state $|DS_0\rangle$ and the Wannier functions $|\Psi_{f0}\rangle$, $|\Psi_{g0}\rangle$. The dark state $|DS_0\rangle$ has two components, one having $|f\rangle$ character ($\langle f|DS_n\rangle$) and the other one having $|g\rangle$ character ($\langle g|DS_n\rangle$). The wavepackets of $\langle f|DS_n\rangle$ and $\langle g|DS_n\rangle$ essentially have the same shape. They are mainly composed of the lattice ground states $|\Psi_{f0}\rangle$ (thin solid line) and $|\Psi_{g0}\rangle$ (thin dotted line). All depicted states are normalized. The parameters used are $\Omega_1 = \Omega_2 = 2\pi \times 7$ MHz, $V_f = 60\,E_r$ and $V_g = 6\,E_r$, as in our experiments.

Let us now discuss the formation and evolution of the dark state that we have observed in the square pulse experiments of Sec. 3. A dark state $|DS\rangle$ is formed in less than $1\,\mu s$ by subjecting Feshbach molecules to a square Raman laser pulse. As in the STIRAP transfer (discussed in Sec. 5) the initial projection onto $|DS\rangle$ will not change the shape of the Feshbach molecule wavepacket, given by the Wannier function $|\Psi_{f0}\rangle$. The dark state can be expressed as a coherent superposition of the four dark eigenstates $|DS_n\rangle$ of the 12-level Hamiltonian

$$|DS\rangle = \sum_{n=0,2,4,6} c_n |DS_n\rangle. \tag{9}$$

The subsequent coherent evolution of these dark states will again in principle lead to breathing oscillations. The amplitude of these oscillations depends on the extent to which higher bands (i. e., $|DS\rangle_n$, $n > 0$) are excited. The excitation increases with increasing deviation of $|DS\rangle$ from the initial state $|f\rangle$, i. e., with rising Ω_1/Ω_2.

This can also be understood from another point of view. The effective lattice potential felt by the molecules in such a superposition state is the weighted average of the potentials for the two contributing states $|f\rangle$ and $|g\rangle$. For the case $\Omega_1 = \Omega_2$ this effective potential is about half as deep as that for the Feshbach molecules. Compared to the case of pure ground state molecules (Fig. 4) where the lattice potential is reduced by a factor of 10, the oscillations of the wavepacket are strongly suppressed and cannot be observed with our current experimental precision. For $\Omega_1 \gg \Omega_2$, the dark state $|DS\rangle$ has a dominant contribution from state $|g\rangle$, and the effective lattice potential essentially corresponds to the one for ground state molecules. In this case oscillations appear despite the strong coupling, a fact which we also have experimentally verified[6].

---

[6] For these experiments we have ramped into the dark state and back in a fashion similar to STIRAP transfer pulses to avoid strong losses caused by direct projection into $|DS\rangle \approx |g\rangle\langle g|DS\rangle$.

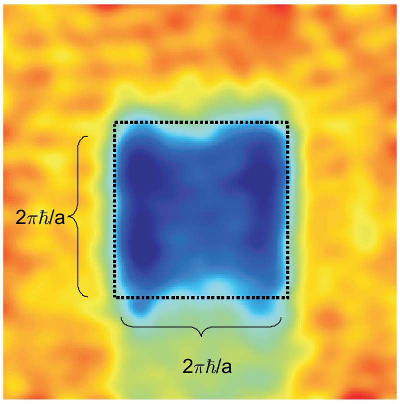

Figure 8: Shown is a typical absorption image which displays the atomic quasi-momentum distribution in the optical lattice after exposure to the Raman laser beams and subsequent adiabatic molecule dissociation. Atoms inside the square region come from the lowest Bloch band. $2\pi\hbar/a$ is the modulus of the reciprocal lattice vector.

Conclusion We have analyzed coherent wavepacket dynamics and their suppression in a 3D optical lattice. We observed optically induced phase locking of a number of quantum levels, which can also be viewed as the appearance of a novel multi-level dark state. The experiments were carried out with tightly bound molecules as a component of a dark quantum superposition state. Thus, the experiments demonstrate control of molecular motion in an optical lattice for the first time. In addition, different models have been introduced and discussed in detail, with which the lattice dynamics can be understood and quantitatively described.

Acknowledgements The authors thank Helmut Ritsch for very helpful discussions and support in model calculations. We also thank Gregor Thalhammer for early assistance in the lab, and Florian Schreck for loaning us a Verdi V18 pump laser. This work was supported by the Austrian Science Fund (FWF) within SFB 15 (project part 17).

Appendix: Theoretical band population analysis

As stated before, our signals only include molecules for which the constituent atoms end up in the lowest Bloch band of the lattice. A controlled lattice rampdown in a few milliseconds maps the bands and quasi-momentum distribution of the atoms into momentum space[16,12]. We image these distributions after 13 ms of time-of-flight via absorption imaging. Fig. 8 shows a typical distribution. The dotted square region corresponds to the lowest Bloch band and is dominantly populated.

An important question is how the Bloch bands for the Feshbach molecules map onto the Bloch bands for the atoms. In other words, if we measure the atomic population of the Bloch bands – do we know what the band population for the molecules was? As the lattice is very deep for the Feshbach molecules and atoms, we can approximate the potential at an individual lattice site as harmonic with trap frequency ω_t. In one dimension, the eigenfunctions of the harmonic oscillator are

$$|\Phi_n\rangle = \frac{1}{\sqrt{2^n n! \sqrt{\pi} x_0}} \exp\left(-\frac{1}{2}\left(\frac{x}{x_0}\right)^2\right) \mathrm{H}_n\left(\frac{x}{x_0}\right), \tag{10}$$

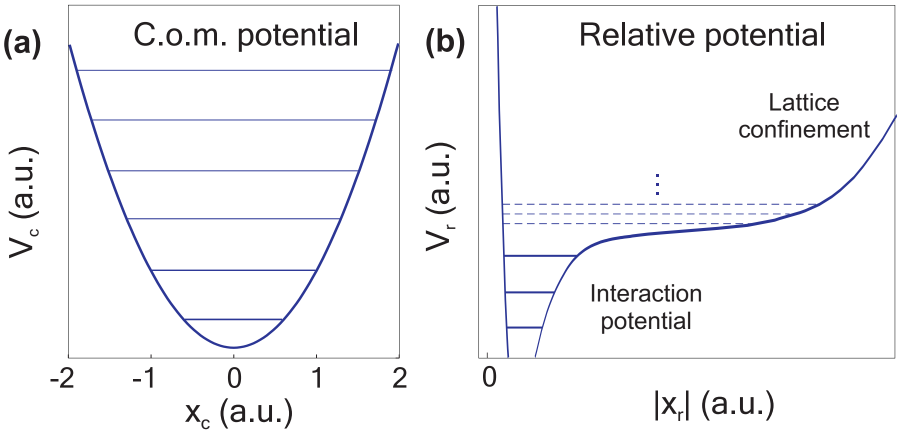

Figure 9: Potentials for the center-of-mass and relative coordinate of two atoms trapped at a site of the optical lattice. (a) The bound states (solid lines) of the harmonic center-of-mass potential V_c correspond to the molecular Bloch bands. (b) At short interatomic distances the relative potential V_r is dominated by the interaction potential, which allows the formation of bound molecular states (solid lines). Unbound atoms are trapped by the lattice potential at larger separation (dashed lines). With the help of a Feshbach resonance the lowest trap state can be converted into a high molecular state. Note that in this schematic view both energy and distance for the two contributions to the relative potential are not to scale.

where $x_0 = \sqrt{\hbar/\omega_t m}$ is the oscillator length and H_n is the n$^{\text{th}}$ Hermite polynomial. We assume that we have two atoms in a lattice site with coordinates $x_{1,2}$. The relative and c.o.m. coordinates of the atom pair are

$$x_r = 1/\sqrt{2}(x_1 - x_2) \tag{11}$$
$$x_c = 1/\sqrt{2}(x_1 + x_2) \tag{12}$$

The c.o.m. potential V_c for the pair will be harmonic with trap frequency ω_t and the potential V_r for the relative coordinate will be a sum of the harmonic potential and the interaction potential (Fig. 9).

When we form or dissociate a molecule by adiabatically ramping across a Feshbach resonance, only the quantum level in the V_r potential will change – from a molecular bound state to an unbound atomic pair state in the lowest Bloch band. The wavefunction in the c.o.m. coordinate remains unchanged. We can now calculate how band populations of Feshbach molecules converted to atomic band populations by using the coordinate transformations. As an example: A Feshbach molecule in the lowest Bloch band (i. e., center-of-mass coordinate) will produce an atom pair with the following wavefunction: $|\Psi\rangle \propto \exp(-1/2\, x_c^2)\exp(-1/2\, x_r^2) = \exp(-1/2\, x_1^2)\exp(-1/2\, x_2^2)$. This means that both atoms will also end up in the lowest Bloch band of the lattice. This analysis can be extended to any band. Table 1 gives the conversion amplitudes from molecular to atomic bands for the four lowest symmetric molecular bands. Correlations between the two constituent atoms of a molecule are not discussed here.

We finally note that when we apply absorption imaging, the optical density of the atomic sample is integrated in the direction of observation. Thus in this direction no band population analysis is possible. We accounted for this in our multi-band model described in Sec. 6.

		atomic Bloch band								
		0	1	2	3	4	5	6	7	…
molecular band	0	1	0	0	0	0	0	0	0	…
	2	$\frac{1}{2}$	$-\sqrt{\frac{1}{2}}$	$\frac{1}{2}$	0	0	0	0	0	…
	4	$\frac{1}{4}$	$-\sqrt{\frac{4}{16}}$	$\sqrt{\frac{6}{16}}$	$-\sqrt{\frac{4}{16}}$	$\frac{1}{4}$	0	0	0	…
	6	$\frac{1}{8}$	$-\sqrt{\frac{6}{64}}$	$\sqrt{\frac{15}{64}}$	$-\sqrt{\frac{20}{64}}$	$\sqrt{\frac{15}{64}}$	$-\sqrt{\frac{6}{64}}$	$\frac{1}{8}$	0	…
	⋮	⋮	⋮	⋮	⋮	⋮	⋮	⋮	⋮	

Table 1: Band conversion amplitudes in the harmonic oscillator approximation. Each line gives the amplitudes for a constituent atom of a molecule in a certain band to populate various atomic bands after dissociation. Note that the squares of the amplitudes correspond to the binomial coefficients.

Acknowledgements

The authors thank Helmut Ritsch for very helpful discussions and support in model calculations. We also thank Gregor Thalhammer for early assistance in the lab, and Florian Schreck for loaning us a Verdi V18 pump laser. This work was supported by the Austrian Science Fund (FWF) within SFB 15 (project part 17).

References

[1] F. Lang, K. Winkler, C. Strauss, R. Grimm, J. Hecker Denschlag *Phys. Rev. Lett.*, 2008, **101**, 133005.

[2] M. Viteau, A. Chotia, M.Allegrini, N. Bouloufa, O. Dulieu, D. Comparat and P. Pillet, *Science*, 2008, **321**, 232.

[3] J. G. Danzl , E. Haller, M. Gustavsson, M. J. Mark, R. Hart, N. Bouloufa, O. Dulieu, H. Ritsch, and H.-C. Nägerl, *Science*, 2008, **321**, 1062.

[4] K.-K. Ni, S. Ospelkaus, M. H. G. de Miranda, A. Pe'er, B. Neyenhuis, J. J. Zirbel, S. Kotochigova, P. S. Julienne, D. S. Jin and J. Ye, *Science*, 2008, **322**, 5899.

[5] J. Deiglmayr, M. Repp, A. Grochola, K. Mörtlbauer, C. Glck, O. Dulieu, J. Lange, R. Wester and M. Weidemüller, *Phys. Rev. Lett.*, 2008, **101**, 133004.

[6] K. M. Jones, E. Tiesinga, P. D. Lett, P. S. Julienne, *Rev. Mod. Phys.*, 2006, **78**, 483.

[7] J. M. Hutson, P. Soldán, *Int. Rev. Phys. Chem.*, 2006, **25**, 497.

[8] T. Köhler, K. Goral, P. S. Julienne, *Rev. Mod. Phys.*, 2006, **78**, 1311.

[9] K. Bergmann, H. Theuer, B. W. Shore, *Rev. Mod. Phys.*, 1998, **70**, 1003.

[10] G. Thalhammer, K. Winkler, F. Lang, S. Schmid, R. Grimm and J. Hecker Denschlag, *Phys. Rev. Lett.*, 2006, **96**, 050402.

[11] T. Volz, S. Dürr, S. Ernst, A. Marte, and G. Rempe, *Phys. Rev. A*, 2003, **68**, 010702(R).

[12] K. Winkler, G. Thalhammer, F. Lang, R. Grimm and J. Hecker Denschlag, *Nature*, 2006, **441**, 853.

[13] D. F. Walls, G. J. Milburn, in *Quantum Optics*, Springer-Verlag, Berlin, 1994.

[14] T. Haslwanter, H. Ritsch, J. Cooper, and P. Zoller, *Phys. Rev. A*, 1988, **38**, 5652.

[15] W. Kohn, *Phys. Rev. B*, 1973, **7**, 4388.

[16] J. Hecker Denschlag, J. E. Simsarian, H. Häffner, C. McKenzie, A. Browaeys, D. Cho, K. Helmerson, S. L. Rolston and W. D. Phillips,
J. Phys. B: At. Mol. Opt. Phys., 2002, **35**, 3095.

This journal is ©The Royal Society of Chemistry 2009

Selected for a Viewpoint in *Physics*

PRL **101,** 133005 (2008) PHYSICAL REVIEW LETTERS week ending 26 SEPTEMBER 2008

Ultracold Triplet Molecules in the Rovibrational Ground State

F. Lang,[1] K. Winkler,[1] C. Strauss,[1] R. Grimm,[1,2] and J. Hecker Denschlag[1]

[1]*Institut für Experimentalphysik und Zentrum für Quantenphysik, Universität Innsbruck, A-6020 Innsbruck, Austria*
[2]*Institut für Quantenoptik und Quanteninformation der Österreichischen Akademie der Wissenschaften, A-6020 Innsbruck, Austria*

(Received 5 September 2008; published 25 September 2008)

We report here on the production of an ultracold gas of tightly bound Rb_2 triplet molecules in the rovibrational ground state, close to quantum degeneracy. This is achieved by optically transferring weakly bound Rb_2 molecules to the absolute lowest level of the ground triplet potential with a transfer efficiency of about 90%. The transfer takes place in a 3D optical lattice which traps a sizeable fraction of the tightly bound molecules with a lifetime exceeding 200 ms.

DOI: 10.1103/PhysRevLett.101.133005 PACS numbers: 37.10.Mn, 37.10.Jk, 37.10.Pq, 42.50.−p

The successful production of quantum degenerate gases of *weakly bound* molecules has triggered a quest for quantum gases of *tightly bound* molecules. These can be used to investigate ultracold collisions and chemistry of molecules, to produce molecular Bose-Einstein condensates (BEC), and to develop molecular quantum optics. Standard laser cooling techniques as developed for atoms [1] do not work for molecules due to their complex internal structure. Other pathways to cold and dense samples of molecules are required, such as Stark or Zeeman deceleration [2,3] and sympathetic cooling [4] or association of ultracold atoms [5–7]. Association via Feshbach resonances [6,7] has directly produced quantum degenerate or near-degenerate ultracold molecular gases [8–12], but only in very weakly bound states with a high vibrational quantum number. Furthermore, such molecules are in general unstable when colliding with each other, particularly if they are composed of bosonic atoms.

Recently, optical schemes have been developed with the goal to selectively produce cold and dense samples of deeply bound molecules [13–18], ultimately in a rovibrational ground state. We report here the realization of this goal by optically transferring a dense ensemble of $^{87}Rb_2$ Feshbach molecules to a single quantum level in the rovibrational ground state of the Rb_2 triplet potential ($a\,^3\Sigma_u^+$). The transfer is carried out in a single step using stimulated Raman adiabatic passage (STIRAP) [14–16,19] with an efficiency of almost 90%, which is only technically limited. The molecules are held in a 3D optical lattice in which they exhibit a trap lifetime exceeding 200 ms, after an initial relaxation within 50 ms.

In contrast to singlet molecules, triplet molecules exhibit a magnetic moment giving rise to a rich energy level structure in the presence of magnetic fields. Thus, collisions of triplet molecules should exhibit magnetically tunable scattering resonances, e.g., Feshbach resonances. Molecules in the triplet rovibrational ground state can potentially relax to the singlet state $X\,^1\Sigma_g^+$ through inelastic collisions. This process has not yet been investigated and can possibly be suppressed. Such a regime would open interesting prospects for future experiments with molecular Bose-Einstein condensates and ultracold chemistry [20].

The starting point for our transfer experiments is a 50 μm-size pure ensemble of 3×10^4 weakly bound Rb_2 Feshbach molecules, produced from an atomic ^{87}Rb Bose-Einstein condensate using a Feshbach resonance at a magnetic field of 1007.4 G ($1\ \text{G} = 10^{-4}$ T). They are trapped in the lowest Bloch band of a cubic 3D optical lattice with no more than a single molecule per lattice site [21] and an effective lattice filling factor of about 0.3. The lattice depth for the Feshbach molecules is 60 E_r, where $E_r = \pi^2\hbar^2/2ma^2$ is the recoil energy, with m the mass of the molecules and $a = 415.22$ nm the lattice period. Such deep lattices suppress tunneling between different sites. The magnetic field is set to 1005.8 G where the Feshbach molecules are in a quantum state $|f\rangle$ which correlates with $|F = 2, m_F = 2, f_1 = 2, f_2 = 2, v = 36, l = 0\rangle$ at 0 G [22]. Here, F and $f_{1,2}$ are the total angular momentum quantum numbers for the molecule and its atomic constituents, respectively, and m_F is the total magnetic quantum number; v is the vibrational quantum number for the triplet potential and l is the quantum number for rotation.

For the transfer, we use a stimulated optical Raman transition. Two lasers (1 and 2) connect the Feshbach molecule level, $|f\rangle$, via an excited level, $|e\rangle$, to the absolute lowest level in the triplet potential, $|g\rangle$ [see Fig. 1(a)]. State $|g\rangle$ has a binding energy of 7.0383(2) THz × h and can be described by the quantum numbers $|F = 2, m_F = 2, S = 1, I = 3, v = 0, l = 0\rangle$ where S and I are the total electronic and nuclear spins of the molecule, respectively. At 1005.8 G, the ground state is separated by hundreds of MHz from any other bound level, so there is no ambiguity in what level is addressed. The level $|e\rangle$ is located in the vibrational $v' = 13$ manifold of the electronically excited $^3\Sigma_g^+$ $(5s + 5p)$ potential and has 1_g character. It has an excitation energy of 294.6264(2) THz × h with respect to $|f\rangle$, a width $\Gamma = 2\pi \times 8$ MHz, and a Zeeman shift of 3.4 MHz × h/G. From resonant excitation measurements, we deduce a coupling strength for the transition from $|f\rangle$ to

© 2008 The American Physical Society

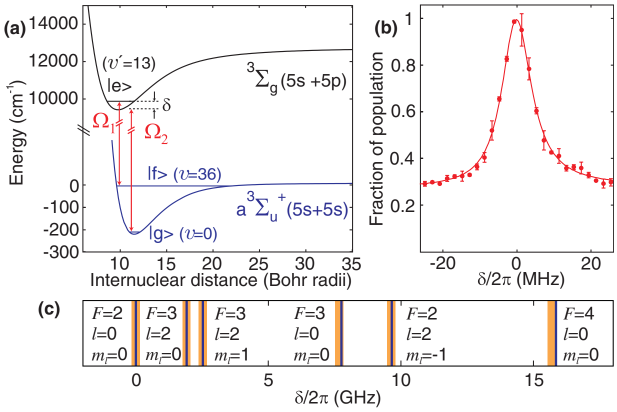

FIG. 1 (color online). (a) Molecular levels of Rb_2. The lasers 1 and 2 couple the molecule levels $|f\rangle$, $|g\rangle$ to the excited level $|e\rangle$ with Rabi frequencies $\Omega_{1,2}$, respectively. Note the different energy scales for the ground and excited triplet potentials. (b) Dark resonance. The data show the remaining fraction of Feshbach molecules $|f\rangle$ after exposing them to both Raman lasers in a 3 μs square pulse. The two-photon detuning δ is scanned by varying the wavelength of laser 2 while keeping laser 1 on resonance. The Rabi frequencies are $\Omega_1 = 2\pi \times 0.7$ MHz and $\Omega_2 = 2\pi \times 10$ MHz. The solid line is a fit from a simple three-level model [14]. (c) Hyperfine and rotational spectrum for the $v = 0$ manifold of the $a\,^3\Sigma_u^+$ potential. The shaded bars correspond to measurements, and their width represents the typical error margin. The thin solid lines are from theoretical calculations and are shown with respective quantum numbers F, l, and its projection m_l. The line at $\delta = 0$ corresponds to state $|g\rangle$ and is the absolute lowest level of the $a\,^3\Sigma_u^+$ potential.

$|e\rangle$ of $\Omega_1/\sqrt{I_1} = 2\pi \times 0.4\ \mathrm{MHz}/\sqrt{\mathrm{W\,cm}^{-2}}$ where Ω_1 is the Rabi frequency and I_1 is the intensity of laser 1. In comparison, the coupling strength for the transition from $|g\rangle$ to $|e\rangle$ is $\Omega_2/\sqrt{I_2} = 2\pi \times 30\ \mathrm{MHz}/\sqrt{\mathrm{W\,cm}^{-2}}$. As in Autler-Townes splitting [11], we deduce Ω_2 from the measured width of a dark resonance which appears when both lasers resonantly couple to level $|e\rangle$ [see Fig. 1(b)].

The positions of the deeply bound energy levels of the Rb_2 triplet potentials $^3\Sigma_g^+$ and $a\,^3\Sigma_u^+$ were not precisely known before this work. Therefore, we have carried out extensive single- and two-color spectroscopy on our pure ensemble of Feshbach molecules. We have mapped out the vibrational progression of both potentials to the ground state v (v') $= 0$ and find good agreement with theoretical calculations based on *ab initio* potentials [23]. In order to determine the hyperfine and rotational structure of the $a\,^3\Sigma_u^+$ vibrational ground state, we use a different intermediate level in the $^3\Sigma_g^+$ potential instead of $|e\rangle$. It has 0_g^- character and quantum number $I = 3$. Because of the selection rule $\Delta I = 0$ and the fact that I is a good quantum number for the deeply bound $a\,^3\Sigma_u^+$ states, this considerably restricts the number of observed lines. We find excellent agreement of the measured data with theoretical calculations based on a close-coupled channel model with essentially no free parameters [see Fig. 1(c)]. In particular, we identify the lowest observed state $|g\rangle$ as absolute ground state of the $a\,^3\Sigma_u^+$ potential. A detailed discussion of further spectroscopic measurements as well as their analysis will be presented elsewhere.

STIRAP is a very efficient transfer method based on a stimulated Raman transition. It uses a counterintuitive pulse sequence during which molecules are kept in a dynamically changing dark superposition state $|\Psi_{\mathrm{ds}}\rangle = (\Omega_2|f\rangle - \Omega_1|g\rangle)/\sqrt{\Omega_1^2 + \Omega_2^2}$. This dark state is decoupled from the light in the sense that there is no excitation of the short lived state $|e\rangle$, which suppresses losses during transfer [see, e.g., the dark resonance in Fig. 1(b)]. A vital condition for STIRAP is the relative phase stability between the two Raman lasers. Both of our Raman lasers, a Ti:Sapphire laser at 1017.53 nm (laser 1) and a grating-stabilized diode laser at 993.79 nm (laser 2) are Pound-Drever-Hall locked to a single cavity which itself is locked to an atomic ^{87}Rb-line. From the lock error signals, we estimate frequency stabilities on a ms time scale of 40 and 80 kHz for lasers 1 and 2, respectively. Thus, the transfer has to take place on a μs time scale in order not to lose phase coherence during STIRAP. Both laser beams have a waist of 130 μm at the location of the molecular sample, propagate collinearly, and are polarized parallel to the

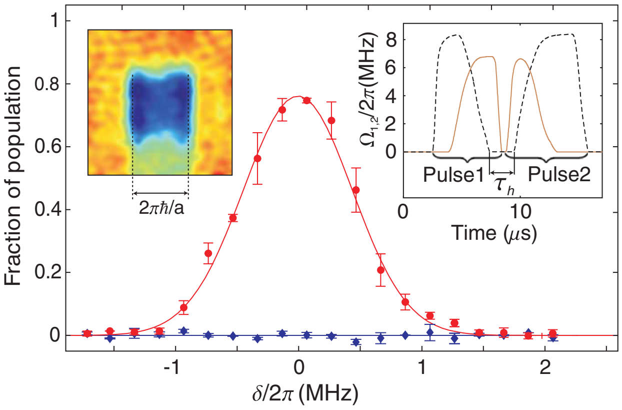

FIG. 2 (color online). STIRAP. We plot the efficiency for population transfer from state $|f\rangle$ to state $|g\rangle$ and back with two STIRAP pulses (circles) as a function of two-photon detuning δ. In the dead time between the two STIRAP pulses, no Feshbach molecules can be detected (diamonds). The continuous lines are from model calculations as described in the text. The right inset shows the corresponding pulse sequence indicating the Rabi frequencies of laser 1 (solid line) and laser 2 (dashed line). The hold time τ_h, the time between the actual population transfers, is equal to 2 μs. The left inset is an absorption image which displays the atomic quasimomentum distribution in the optical lattice after the round-trip STIRAP transfer and subsequent adiabatic molecule dissociation. Atoms located in the inner square stem from the lowest Bloch band. $2\pi\hbar/a$ is the modulus of the reciprocal lattice vector.

direction of the magnetic bias field. Thus, the lasers can only induce π transitions.

We perform STIRAP by adiabatically ramping the Raman laser intensities as shown in the right inset of Fig. 2. Pulse 1 efficiently transfers the molecules from $|f\rangle$ to $|g\rangle$. In order to detect the molecules in state $|g\rangle$ after the transfer, we bring them back to $|f\rangle$ with a second, reversed STIRAP pulse sequence. We then dissociate the molecules into pairs of atoms at the Feshbach resonance. By releasing these atoms from the optical lattice in the manner described in [24], we can map out the Bloch bands in momentum space. After 13 ms of ballistic expansion, the corresponding atomic distribution is recorded with standard absorption imaging (see left inset in Fig. 2). For our signals, we only count atoms in the central square zone, corresponding to the lowest Bloch band [24].

Figure 2 shows the total transfer efficiency after two STIRAP transfers which are separated by a hold time $\tau_h = 2\ \mu$s. The transfer efficiency for this *round-trip* STIRAP process is plotted as a function of the two-photon detuning δ and reaches about 75% at resonance ($\delta = 0$). Assuming equal efficiencies for both transfers, this corresponds to a single transfer efficiency of 87% and a total number of 2.6×10^4 molecules in state $|g\rangle$. We have experimentally verified that no molecules remain in state $|f\rangle$ between the two STIRAP pulses (diamonds in Fig. 2). Any such molecules would quickly be removed by laser 1 at the end of the first STIRAP pulse, which is kept on at maximum power for 1 μs after ramping down laser 2. Thus, all molecules that are retrieved after the second STIRAP transfer have been deeply bound in state $|g\rangle$. The 1 MHz width (FWHM) of the transfer efficiency is determined by power- and Fourier-broadening [25] and is in good agreement with a 3-level model (see solid lines in Fig. 2). We use a master equation which takes into account decoherence due to phase fluctuations of the Raman lasers [26]. These fluctuations can be expressed in terms of a short-term relative linewidth of the lasers, γ, which from fits, we determine to be about $2\pi \times 20$ kHz. Our calculations indicate that half of the losses are due to nonadiabaticity and half are due to the nonideal laser system. In principle, losses could also be due to other effects, such as coupling to levels outside of $|f\rangle$, $|e\rangle$, and $|g\rangle$. However, we have verified that this is not the case because losses due to optical excitation are completely negligible when we expose a pure ensemble of $|f\rangle$ ($|g\rangle$) molecules only to laser 2 (1). In addition, we did not detect any laser power dependent shift of the two-photon resonance within the accuracy of our measurements of $2\pi \times 200$ kHz.

We also investigate the dynamics and lifetime of the deeply bound molecules in the optical lattice. Because of their strong binding, molecules in state $|g\rangle$ cannot be expected to have a polarizability similar to that of Feshbach molecules, and it is not clear *a priori* what strength or even sign the optical lattice potential will have for them. Indeed, as we show below, the lattice potential is attractive for the $|g\rangle$ molecules, but a factor 10 ± 2 shallower compared to the potential for the Feshbach molecules. Repeating the transfer experiment, we now vary the hold time τ_h between the two STIRAP transfers (see Fig. 3). Interestingly, for short hold times, the transfer efficiency exhibits a damped oscillation (see inset). The period and damping time are both about 80 μs. After 250 μs, the efficiency levels off at 40% and then decays much more slowly. The initial oscillation can be understood as follows. We consider the localized spatial wave packet of a Feshbach molecule at a particular lattice site in the lowest Bloch band. The first STIRAP transfer projects this wave packet onto the much shallower lattice potential felt by the $|g\rangle$ molecules. As a consequence, $|g\rangle$ molecules are coherently spread over various Bloch bands, and the wave packet undergoes "breathing" oscillations with the lattice site trap frequency ω_t. These coherent oscillations are damped by tunneling of $|g\rangle$ molecules in higher Bloch bands to neighboring lattice sites. The reverse STIRAP transfer maps this periodic oscillation back to the Feshbach molecules. Higher Bloch bands are populated here as well, but are at most partially counted in our

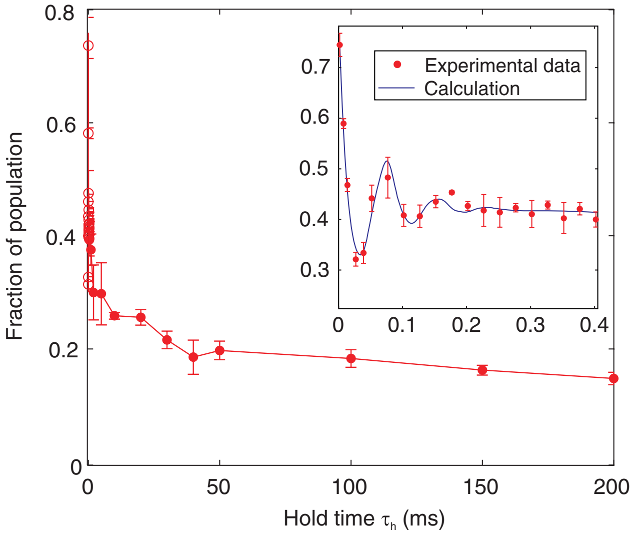

FIG. 3 (color online). Dynamics and lifetime of $|g\rangle$ molecules in the optical lattice. We plot the transfer efficiency for the round-trip STIRAP process as a function of the hold time τ_h between the two STIRAP pulses. We only count molecules whose constituent atoms end up in the lowest Bloch band after transfer (see left inset of Fig. 2). Except for τ_h, all other experimental parameters are the same as in Fig. 2. Molecules are lost on three different time scales, 100 μs, 50 ms, and ≈200 ms. The inset zooms into the first 400 μs. The oscillations in the transfer efficiency are due to breathing oscillations of localized spatial wave packets of molecules in the lattice sites. The solid line is from a multiband model calculation. The data shown in the inset are plotted with open plot symbols in the main plot. The line connects neighboring data points.

scheme, which leads to an apparent loss of our transfer efficiency. We can describe the data well using a 3D multiband model (see solid line, inset Fig. 3). In this model, the states $|f\rangle$, $|e\rangle$, and $|g\rangle$ have a substructure due to the Bloch bands of the optical lattice, and the resulting levels are coupled by the laser fields. From fits to the data, we extract the trap frequency ω_t in a single lattice site, which determines the lattice depth for the molecules in state $|g\rangle$. We note that the earlier analysis of Fig. 2 does not include optical lattice effects. However, because the hold time τ_h is so short (2 μs), molecule signal losses due to oscillation amount to only 4%. In fact, the multiband model leads to the same theoretical curve as shown when we use a short-term relative laser line width $\gamma = 2\pi \times 18$ kHz, close to the previous value.

For longer hold times of up to 200 ms, Fig. 3 shows the time dependent loss of the deeply bound molecules. Within the first 50 ms, the fraction of recovered molecules drops to 20%. We attribute this loss mainly to the fact that all molecules in excited bands will simply fall out of the lattice since they are essentially unbound. For the remaining molecules in the lowest band, we find a lifetime exceeding our maximum experimental observation time which is limited due to heating of the magnetic field coils.

To conclude, using a nearly 90% efficient STIRAP transfer, we have created a dense and ultracold ensemble of deeply bound Rb_2 molecules in the absolute lowest quantum state of the $a\,^3\Sigma_u^+$ potential. These deeply bound molecules were trapped in a 3D optical lattice, and we observed coherent motional dynamics of their spatial wave packets in the sites. This indicates that besides the internal degrees of freedom, the external degrees of freedom are also precisely defined after transfer. The transfer of molecules into a single Bloch band should be possible, either by matching the lattice depths of weakly and deeply bound molecules, or by spectroscopically resolving the Bloch bands [27]. The latter involves longer STIRAP pulses and more tightly phase-locked Raman lasers, with the added benefit of increasing the transfer efficiency further. Investigating the collisional behavior of the triplet molecules will be the next goal as it is of central importance for ultracold chemistry [20] and for achieving molecular BEC. An appealing way to reach BEC is by melting an optical-lattice-induced Mott insulator of rovibrational ground state molecules [28]. For this, we have to improve the lattice occupation of our initial ensemble of Feshbach molecules [12] and use a selective STIRAP transfer to the lowest Bloch band.

During the preparation of our Letter, we learned that rovibrational ground state molecules have been produced with KRb [29].

The authors thank Birgit Brandstätter, Olivier Dulieu, Paul Julienne, Christiane Koch, Roman Krems, Helmut Ritsch, Peter v. d. Straten, and Eberhard Tiemann for theoretical support. We acknowledge the usage of a close-coupled channel code from NIST. We thank Devang Naik, Tetsu Takekoshi, and Gregor Thalhammer for help in the lab as well as Florian Schreck and the group of Hanns-Christoph Nägerl for helpful exchange. This work was supported by the Austrian Science Fund (FWF) within SFB 15 (project part 17).

[1] H. J. Metcalf and P. van der Straten, *Laser Cooling and Trapping* (Springer-Verlag, New York, 1999).
[2] S. Y. T. van de Meerakker, H. L. Bethlem, and G. Meijer, Nature Phys. **4**, 595 (2008).
[3] M. S. Elioff, J. J. Valentini, and D. W. Chandler, Science **302**, 1940 (2003); N. Vanhaecke, U. Meier, M. Andrist, B. H. Meier, and F. Merkt, Phys. Rev. A **75**, 031402(R) (2007); E. Narevicius *et al.*, Phys. Rev. Lett. **100**, 093003 (2008).
[4] J. Doyle, B. Friedrich, R. V. Krems, and F. Masnou-Seeuws, Eur. Phys. J. D **31**, 149 (2004).
[5] K. M. Jones, E. Tiesinga, P. D. Lett, and P. S. Julienne, Rev. Mod. Phys. **78**, 483 (2006).
[6] T. Köhler, K. Goral, and P. S. Julienne, Rev. Mod. Phys. **78**, 1311 (2006).
[7] J. M. Hutson and P. Soldán, Int. Rev. Phys. Chem. **25**, 497 (2006).
[8] J. Herbig *et al.*, Science **301**, 1510 (2003).
[9] K. Xu *et al.*, Phys. Rev. Lett. **91**, 210402 (2003).
[10] S. Jochim *et al.*, Science **302**, 2101 (2003); M. Greiner, C. A. Regal, and D. S. Jin, Nature (London) **426**, 537 (2003); M. W. Zwierlein *et al.*, Phys. Rev. Lett. **91**, 250401 (2003); T. Bourdel *et al.*, Phys. Rev. Lett. **93**, 050401 (2004); G. B. Partridge *et al.*, Phys. Rev. Lett. **95**, 020404 (2005).
[11] K. Winkler *et al.*, Phys. Rev. Lett. **95**, 063202 (2005).
[12] T. Volz *et al.*, Nature Phys. **2**, 692 (2006).
[13] J. M. Sage, S. Sainis, T. Bergeman, and D. DeMille, Phys. Rev. Lett. **94**, 203001 (2005).
[14] K. Winkler *et al.*, Phys. Rev. Lett. **98**, 043201 (2007).
[15] S. Ospelkaus *et al.*, Nature Phys. **4**, 622 (2008).
[16] J. G. Danzl *et al.*, Science **321**, 1062 (2008).
[17] M. Viteau *et al.*, Science **321**, 232 (2008).
[18] J. Deiglmayr *et al.*, Phys. Rev. Lett. **101**, 133004 (2008).
[19] K. Bergmann, H. Theuer, and B. W. Shore, Rev. Mod. Phys. **70**, 1003 (1998).
[20] R. V. Krems, Phys. Chem. Chem. Phys. **10**, 4079 (2008).
[21] G. Thalhammer *et al.*, Phys. Rev. Lett. **96**, 050402 (2006).
[22] F. Lang *et al.*, Nature Phys. **4**, 223 (2008).
[23] S. J. Park, S. W. Suh, Y. S. Lee, and G.-H. Jeungy, J. Mol. Spectrosc. **207**, 129 (2001).
[24] K. Winkler *et al.*, Nature (London) **441**, 853 (2006).
[25] The actual population transfer in each STIRAP pulse takes place in 2 μs.
[26] D. F. Walls and G. J. Milburn, *Quantum Optics* (Springer-Verlag, Berlin, 1994).
[27] T. Rom *et al.*, Phys. Rev. Lett. **93**, 073002 (2004).
[28] D. Jaksch, V. Venturi, J. I. Cirac, C. Williams, and P. Zoller, Phys. Rev. Lett. **89**, 040402 (2002).
[29] K.-K. Ni *et al.*, Science, doi:10.1126/science.1163861, published online, 09 (2008).

Cruising through molecular bound-state manifolds with radiofrequency

F. LANG[1], P. V. D. STRATEN[2], B. BRANDSTÄTTER[1], G. THALHAMMER[1], K. WINKLER[1], P. S. JULIENNE[3], R. GRIMM[1,4] AND J. HECKER DENSCHLAG[1]*

[1] Institut für Experimentalphysik und Forschungszentrum für Quantenphysik, Universität Innsbruck, 6020 Innsbruck, Austria
[2] Debye Institute, Universiteit Utrecht, 3508 TA Utrecht, Netherlands
[3] Atomic Physics Division and Joint Quantum Institute, National Institute of Standards and Technology, Gaithersburg, Maryland 20899, USA
[4] Institut für Quantenoptik und Quanteninformation, Österreichische Akademie der Wissenschaften, 6020 Innsbruck, Austria
*e-mail: Johannes.Denschlag@uibk.ac.at

Published online: 27 January 2008; doi:10.1038/nphys838

The production of ultracold molecules with their rich internal structure is currently attracting considerable interest[1–4]. For future experiments, it will be important to efficiently transfer these molecules from their initial internal quantum state at production to other quantum states of interest. Transfer tools such as optical Raman schemes[5,6], radiofrequency transitions (see, for example, ref. 7) or magnetic field ramping[8,9] exist, but are either technically involved or limited in their applicability. Here, we demonstrate a simple, highly efficient hybrid transfer method that overcomes a number of the previous limitations. The scheme is based on magnetically tuned mixing of two neighbouring molecular levels, which enables otherwise forbidden radiofrequency transitions between them. By repeating this process at various magnetic fields, molecules can be successively transported through a large manifold of quantum states. Applying nine transfers, we convert very weakly bound Feshbach molecules to a much more deeply bound level with a binding energy corresponding to 3.6 GHz. As an important spin-off of our experiments, we demonstrate a high-precision spectroscopy method for investigating level crossings.

Radiofrequency has important applications for ultracold molecules, such as spectroscopy[7,10–14] and molecule production[15–17]. Using radiofrequency to transfer ground-state molecules between states of different vibrational quantum numbers, as demonstrated here, is not obvious. For simple molecular potentials, transition matrix elements for magnetic dipole transitions between different vibrational levels are expected to vanish on the basis of an overlap argument of the spatial wavefunctions. However, for real molecules such as Rb_2, the situation is more complex, for example, owing to exchange interaction, hyperfine structure and the Zeeman effect. The combined effect of these interactions induces mixing of states with different vibrational quantum numbers, leading to new eigenstates between which radiofrequency transitions can be driven (see the Methods section). This mixing effect is maximal at avoided crossings. (As a consequence, it is important for radiofrequency spectroscopy at Feshbach resonances[12].)

We carry out our experiments with a pure, ultracold ensemble of 2×10^4 ultracold $^{87}Rb_2$ Feshbach molecules, each of which is held in an individual optical microtrap (see the Methods section). Figure 1 shows the relevant molecular level spectrum for our experiment as calculated by a coupled-channel model[18,19] based on adjusted *ab initio* Rb_2 Born–Oppenheimer potentials[20]. It essentially consists of straight lines of *s*- and *d*-wave levels (corresponding to a rotational angular momentum $l = 0, 2$, respectively). In general, at magnetic fields where two levels intersect, coupling between them gives rise to an avoided crossing.

In the following, we will use the level spectrum like a street map, as the molecules move through the manifold of molecular bound states by sweeping the magnetic field. When arriving at a level intersection we can turn off or go straight, traversing the avoided crossing. In principle, the avoided crossing can be jumped via a fast magnetic field ramp[8,9]. This, however, is limited to very small splittings (typically $<200\,\text{kHz} \times h$) owing to practical limitations of the controllable magnetic ramp speed. This constraint can be easily overcome using a radiofrequency transition as we demonstrate below.

As an example for cruising through molecular bound-state levels, we choose the diagonal path in Fig. 1, as marked with the red circles A to K, each indicating an avoided crossing. This converts our Feshbach molecules with their weak binding energy of $24\,\text{MHz} \times h$ to a deeper bound level at zero magnetic field, $3.6\,\text{GHz} \times h$ below the $f = 1, m_f = 1$ dissociation limit.

Figure 2a shows an expanded view of the first avoided crossing A. The upper branch is connected to the Feshbach resonance at 1,007.4 G and is initially populated with Feshbach molecules at point i. We use adiabatic passage as a very efficient way for population transfer to the lower branch. We switch on a magnetic radiofrequency field which couples the upper and lower branches, inducing two narrow avoided crossings between the dressed states (Fig. 2b). An adiabatic magnetic field sweep to point ii and subsequent switching off the radiofrequency completes the transfer (see the Methods section).

Figure 2d shows the fraction N/N_0 of remaining molecules in the upper branch after the transfer to the lower branch (diamonds) as a function of the radiofrequency field amplitude B_{rf}. For sufficiently high amplitude, no more molecules are detected (see the Methods section). To verify that molecules are not simply lost for high amplitude, we also carry out a transfer back (ii → i) to the upper branch (circles). All molecules can be recouped again for strong enough radiofrequency fields.

From similar measurements with repeated transfers between the upper and lower branches, we infer single transfer efficiencies

© 2008 Nature Publishing Group

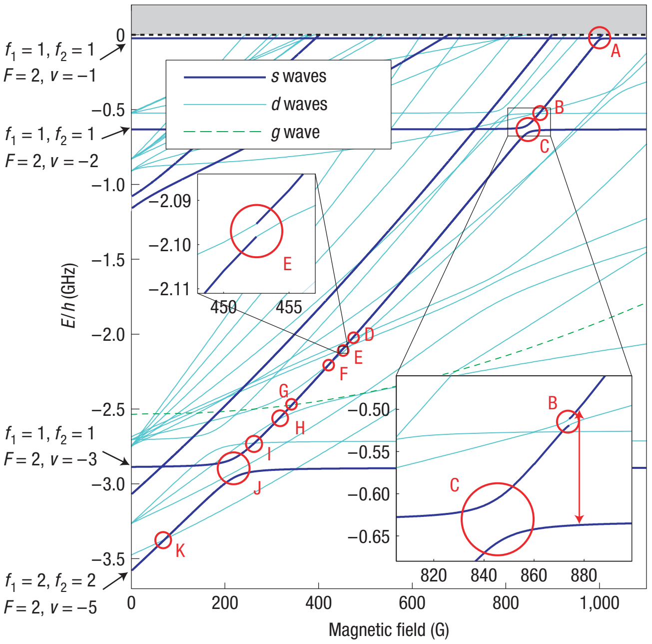

Figure 1 Path through manifold of molecular levels. Energy spectrum of relevant molecular levels of $^{87}Rb_2$ in the electronic ground state with $m_{F\mathrm{tot}} = 2$. The zero of energy is taken to be that of two separated atoms at each field strength and marks the dissociation threshold for a pair of $f = 1$; $m_f = 1$ ground-state atoms. Molecules are transported through the bound-level manifold by traversing avoided crossings, marked A–K. These levels are characterized by their respective quantum numbers at zero magnetic field, that is, global angular momentum F_{tot}, $m_{F\mathrm{tot}} = 2$, the angular momenta f_1, f_2 of the atomic constituents, their combined angular momentum F and the vibrational quantum number v. Out of the number of existing g-wave levels, we only show the single relevant one (1 G = 0.1 mT).

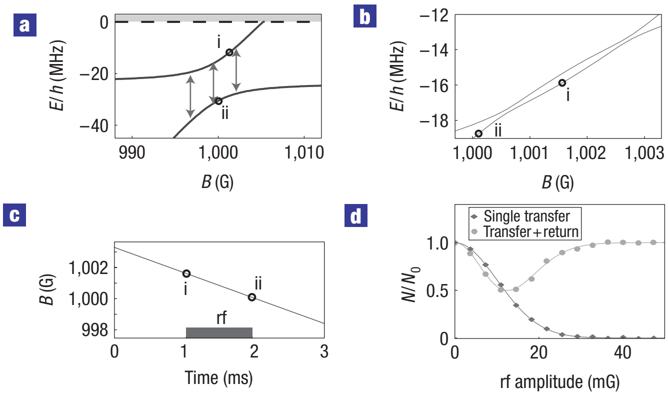

Figure 2 Adiabatic population transfer across avoided crossing with radiofrequency. a, Zoom into avoided crossing A of Fig. 1. Transitions between the upper and lower branches can be induced with radiofrequency. **b**, Dressed-state picture. Coupling the lower and upper branches in **a** with blue-detuned radiofrequency induces two avoided crossings. **c**, Experimental transfer sequence (rf: radiofrequency). **d**, Measured transfer efficiency for transfer from the upper branch to the lower branch (diamonds) and back (circles). The solid lines are fits to a Landau–Zener model. The radiofrequency amplitude is calibrated with a global uncertainty of about 40%.

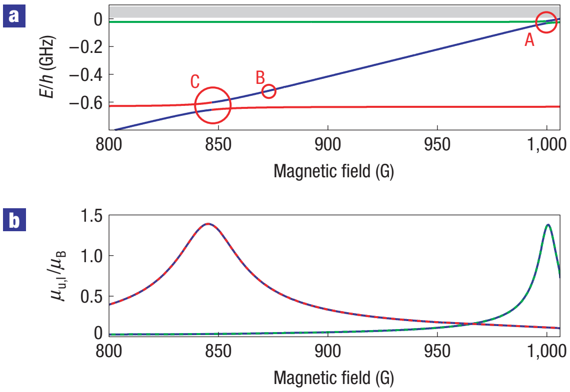

Figure 3 Calculated magnetic dipole matrix elements for the avoided crossings A and C of Fig. 1. a,**b**, Colour coding identifies the levels (**a**) with their respective transition (**b**).

of up to 99.5%. Our experimental data are well fitted with the well-known Landau–Zener model[21] (solid lines) where the transfer probability for a single transition is given by $1-\exp(-\pi\omega_{\mathrm{R}}^2\hbar/2|\dot{B}|\,|\mu_2-\mu_1|)$. Here ω_{R} is the Rabi frequency, $|\dot{B}|$ is the ramp speed and μ_1, μ_2 are the magnetic moments of the two states.

After this successful demonstration at crossing A, we will use such adiabatic transfers across avoided crossings (ATAC) repeatedly for traversing the remaining crossings on our path. We typically find avoided crossings to lie within a few Gauss of their predicted magnetic field position based on the coupled-channel calculation, which is within the accuracy of our model. This identification also helps us to verify that the molecules are in the right quantum level during transport (see the Methods section).

After traversing A, the next wide s-wave crossing is C. Before we get to C, however, we hit the avoided crossing B at 874 G with a $\sim$7 MHz × h splitting, on the basis of an intersecting d-wave level (see Fig. 1 inset). To circumvent crossing B, we carry out the ATAC transfer between the s-waves levels already at 876 G, far from the s-wave crossing. This raises the question, how far from an avoided crossing the radiofrequency transitions can still be driven. Figure 3a is a zoom into the energy spectrum showing the avoided crossings A and C. Figure 3b shows the corresponding calculated magnetic dipole matrix elements $\mu_{\mathrm{u,l}}$ between the corresponding upper and lower level branches using the coupled-channel model (see also the Methods section). The matrix elements are clearly peaked at their respective crossing, reaching values of more than a Bohr magneton. Such high coupling strengths are in agreement with our measurements in Fig. 2d, where $\mu_{\mathrm{u,l}}$ can be extracted from the fits by using $\omega_{\mathrm{R}} = B_{\mathrm{rf}}\mu_{\mathrm{u,l}}$ and measuring B_{rf}. The width of the peaks scales with the energy splitting of their avoided crossing. When moving away from the crossing at B_0, the matrix elements vanish inversely proportional to $|B - B_0|$ (see the Methods section).

Continuing our path down by lowering the magnetic field, we hit consecutively five avoided crossings (D,E,F,H,I) with d-wave states. The corresponding energy splittings are of the order of 1 MHz × h and are each crossed by the ATAC method, which demonstrates its universal character. In general, however, ATAC transfers at narrow avoided crossings are technically more challenging owing to a small magnetic field range of strong coupling and thus a greater susceptibility to magnetic field noise which can lead to unwanted non-adiabatic transitions. Coupling to a g-wave state is observed as well (crossing G), but it is weak enough to be overcome by diabatic ramping of the magnetic field. Finally, after crossing J and K we reach zero magnetic field, with

© 2008 Nature Publishing Group

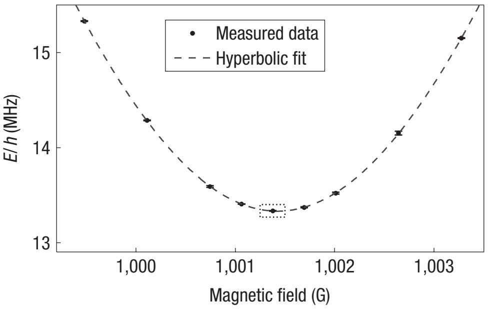

Figure 4 Spectroscopy of an avoided crossing. For the avoided crossing A, the splitting is measured for various magnetic fields by determining the resonant transition frequency using a lorentzian fit. The error bars represent a 95% confidence interval for the centre position of the lorentzian and are typically smaller than the size of the plot symbol. The dashed line is a hyperbolic fit yielding a minimum frequency of (13.331 ± 0.005) MHz.

the molecules in state $|l=0, F_{\mathrm{tot}}=F=f_1=f_2=m_{\mathrm{Ftot}}=2, v=-5\rangle$, 3.6 GHz below the $f_1=f_2=1, m_{f1}=m_{f2}=1$ threshold. We have also produced d-wave molecules at zero magnetic field ($|l=2, F_{\mathrm{tot}}=2, F=0, f_1=f_2=m_{\mathrm{Ftot}}=2, v=-5\rangle$) by adiabatically following the upper branch in crossing K, that is, taking a right turn. The complete transfer down across all 10 avoided crossings takes about 90 ms with a global transfer efficiency of about 50%. The losses during transfer can be explained mainly by the limited molecular lifetime of 280 ms in the lattice, due to inelastic scattering of lattice photons[22], and by not fully optimized transfers at several crossings.

We also developed a high-precision spectroscopy method for measuring the minimal energy splitting of an avoided crossing. For a given avoided crossing, the energy splitting is measured for various magnetic fields. We use two methods. Method 1 determines the resonance frequency for transfer of molecules between the two branches of the avoided crossing. Using a single radiofrequency pulse of a few milliseconds length, we look for the frequency of maximal transfer. The corresponding data for crossing A are shown in Fig. 4 and are very well fitted by a hyperbolic curve, yielding a splitting of (13.331 ± 0.005) MHz × h.

To increase the precision we use method 2, where we carry out a Ramsey-type interferometric measurement (Fig. 5a). A $\pi/2$-pulse of radiofrequency transfers 50% of the Feshbach molecules to the lower branch, creating a 50/50 coherent superposition. After a hold time t_{h} and a second $\pi/2$-pulse, the number of Feshbach molecules is detected. We observe an oscillation of this population N (Fig. 5b) that corresponds precisely to the detuning of the radiofrequency field from resonance. Coherence times reach 1 ms. Figure 5c shows a set of data taken in the region indicated by the dotted box in the centre of Fig. 4. The clear deviation from the hyperbolic curve results from a ~2 G mm^{-1} magnetic field gradient across the molecular cloud (~20 μm diameter) in combination with ~20 mG fluctuations of the magnetic field during the time of a scan. This behaviour is reproduced by our model calculation (solid line) taking these experimental imperfections into account. From the model, we obtain a best estimate of the minimum splitting of (13.33210 ± 0.00015) MHz × h for the ideal hyperbolic curve. The upshift of about 150 Hz of the minimum of the model curve with respect to the hyperbolic curve is due to averaging over the magnetic field inhomogeneities.

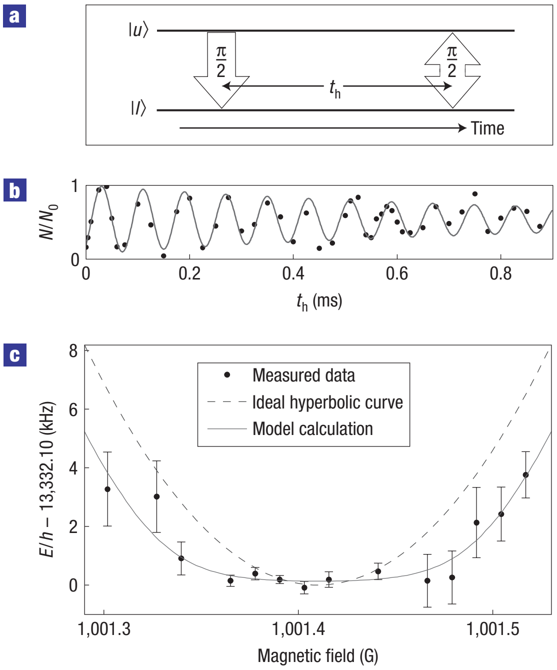

Figure 5 Spectroscopy with Ramsey interferometry. **a**, Ramsey scheme consisting of two $\pi/2$-pulses of radiofrequency and a holding time t_{h}. **b**, Fraction of remaining Feshbach molecules after a Ramsey measurement as holding time is varied (here, $B = 1{,}001.39$ G). The oscillation frequency corresponds to the detuning of the radiofrequency from the splitting and is determined by fitting an exponentially damped oscillation to the data. **c**, Measured splittings, in a narrow magnetic field region (indicated by the small dotted box in Fig. 4). The deviation from the hyperbolic curve (dashed line) results from magnetic field fluctuations and inhomogeneities and is reproduced by our model calculation (solid line). The error bars indicate a 95% confidence interval for the fit (**b**).

We have also carried out detailed measurements of the energy splitting at the avoided crossings marked C, E and J in Fig. 1. These data are shown in Supplementary Information, Table S1. The measurements are complementary to conventional bound-state spectroscopy because instead of measuring the plain energy spectrum of the bound states, our method determines the strength of the coupling between levels. The precision of our data is several orders of magnitude better than the accuracy of our current coupled-channel model. Thus, the data can serve to improve and test the theoretical models used to calculate molecular energy levels.

To conclude, we have demonstrated an efficient method (ATAC) to transfer molecules between neighbouring quantum states. It works for any kind of molecule, whether tightly or loosely bound, as long as the two levels for transfer exhibit a magnetically tunable avoided crossing in an accessible magnetic field range. For weakly bound Rb_2 molecules, our experiments highlight ATAC transfers between different vibrational levels. For tightly bound triplet Rb_2 levels, ATAC will be particularly useful for transfer between states of different rotational angular momentum l (see also Supplementary Information). This opens interesting perspectives for experiments in cold collisions[23–25], chemistry in the ultracold regime, high-resolution spectroscopy, matter-wave interferometry and molecular Bose–Einstein condensates. In particular, we plan to use the ATAC method to prepare Feshbach molecules in a convenient start position for an optical Raman transition to a deeply bound molecular state or even the vibrational ground state[6,26], optimizing in this way Franck–Condon factors and stability issues. Furthermore, the ATAC scheme can be extended in a straightforward manner to avoided crossings that are tuned by electrical fields.

© 2008 Nature Publishing Group

METHODS

PREPARATION OF FESHBACH MOLECULES IN MICROTRAPS

We load a Bose–Einstein condensate of ^{87}Rb atoms into the lowest Bloch band of a deep cubic three-dimensional optical lattice with lattice period 415 nm. After the atoms are prepared in state $f=1$, $m_{\mathrm{f}}=1$, ramping over a Feshbach resonance at 1,007.4 G (ref. 27) (1 G = 0.1 mT) produces Feshbach molecules. A final purification step removes all chemically unbound atoms[22]. There is no more than a single molecule per lattice site and the lattice potential is deep enough ($\approx$10 μK $\times k_{\mathrm{B}}$) to effectively isolate the molecules from each other, shielding them from detrimental collisions[22]. Thus, the sites can be viewed as microtraps holding single molecules in the trap ground state.

ADIABATIC TRANSFER ACROSS AN AVOIDED CROSSING

Exemplarily for all ATAC transfers, we discuss here in detail the transfer at avoided crossing A (Fig. 2a). At the beginning of the transfer sequence, the radiofrequency field is off (Fig. 2c). The Feshbach molecules are brought to point i by ramping the magnetic field to $B=1{,}001.4$ G. We then switch on a longitudinal radiofrequency magnetic field (that is, it points in the same direction as the magnetic bias field) which couples the upper and lower branches of the avoided crossing via a magnetic dipole transition. We use a frequency of 13.6 MHz, which is blue-detuned with respect to the minimal splitting of the avoided crossing of about 13.3 MHz. In the dressed-state picture, the radiofrequency field with field amplitude of $B_{\mathrm{rf}} \sim 50$ mG produces two radiofrequency-induced avoided crossings, one above and one below point i (Fig. 2b). Each avoided crossing shows an energy splitting corresponding to the Rabi frequency $\omega_{\mathrm{R}} \sim 2\pi \times 70$ kHz. Further lowering the magnetic field adiabatically, we reach point ii at 1,001.1 G after 1 ms. Subsequent switching off the radiofrequency field completes the transfer of the molecules to the lower branch.

DETECTION OF MOLECULES AND THEIR QUANTUM STATE

To detect the molecules at any stage during their transport through the manifold of molecular levels, we trace back exactly the path we have come before, adiabatically traversing all avoided crossings in the opposite direction. We end up with Feshbach molecules that are dissociated into unbound atoms by sweeping over the Feshbach resonance at 1,007.4 G. These atoms are then counted via standard absorption imaging, after switching off the optical lattice and the bias magnetic field.

We use two methods to verify that molecules are in the right quantum level during transport. (1) Checking for consistency between predicted and experimentally found avoided crossings, in terms of magnetic field location and energy splitting. (2) Optical spectroscopy to measure the binding energy of molecules. By irradiating the molecules with resonant laser light, we transfer them to an electronically excited molecular level, $|0_g^-, v=31, J=0\rangle$ (ref. 6), leading to losses. The shift of this laser frequency compared with the frequency of the photoassociation transition to the same excited molecular level corresponds to the binding energy of the molecules.

SIMPLE MODEL FOR RADIOFREQUENCY TRANSITIONS AT AN AVOIDED CROSSING

A simple two-level model gives insight into the mechanism of the radiofrequency transitions at the avoided crossing. Two molecular bare levels $|b1\rangle$, $|b2\rangle$ with magnetic moments μ_1 and μ_2 cross at a magnetic field $B=B_0$. The hamiltonian for these levels reads

$$\hat{H}=(B-B_0+B_{\mathrm{rf}}\cos(\omega_{\mathrm{rf}}t))\begin{pmatrix}\mu_1 & 0\\ 0 & \mu_2\end{pmatrix}+\frac{\hbar}{2}\begin{pmatrix}0 & \Omega\\ \Omega & 0\end{pmatrix}.$$

A coupling Ω between the two levels, for example, due to exchange interaction or dipole–dipole interaction, leads to mixing and the new eigenstates $|u\rangle$ and $|l\rangle$. These states form the upper and lower branches of an avoided crossing, similar to Fig. 2a. A longitudinal magnetic radiofrequency field with amplitude B_{rf} and frequency ω_{rf} can drive transitions between levels $|u\rangle$ and $|l\rangle$ which read

$$|u\rangle=\cos(\theta)|b1\rangle+\sin(\theta)|b2\rangle$$

$$|l\rangle=-\sin(\theta)|b1\rangle+\cos(\theta)|b2\rangle,$$

with mixing angle $\theta=\arctan((\delta+\sqrt{\delta^2+\Omega^2})/\Omega)$, where $\delta=((\mu_2-\mu_1)(B-B_0))/\hbar$. The matrix element for the radiofrequency transition is then

$$\mu_{\mathrm{u,l}} \equiv \langle u|\begin{pmatrix}\mu_1 & 0\\ 0 & \mu_2\end{pmatrix}|l\rangle=(\mu_2-\mu_1)\sin(2\theta)$$

$$= 2(\mu_2-\mu_1)\frac{\Omega(\delta+\sqrt{\delta^2+\Omega^2})}{\Omega^2+(\delta+\sqrt{\delta^2+\Omega^2})^2}.$$

Thus, $\mu_{\mathrm{u,l}}$ is resonantly peaked at the avoided crossing with a width (full-width at half-maximum) of $2\sqrt{3}\Omega$ and vanishes as $1/(B-B_0)$ far away from the crossing.

We find good agreement when comparing the matrix elements of our simple model to the ones of the coupled-channel model, given by $\mu_{\mathrm{u,l}}=\langle u|\mu_{\mathrm{B}}g_{\mathrm{s}}S_{\mathrm{z}}+\mu_{\mathrm{N}}g_{\mathrm{I}}I_{\mathrm{z}}|l\rangle$. Here $|u\rangle$, $|l\rangle$ are the wavefunctions as calculated with the coupled-channel model. μ_{B}, μ_{N} are the Bohr magneton and nuclear magneton, g_{s} and g_{I} are the g-factors of the electrons and nuclei, respectively, and S_{z}, I_{z} are the corresponding spin operator components in the direction of the magnetic field.

Received 30 August 2007; accepted 18 December 2007; published 27 January 2008.

References

1. Doyle, J., Friedrich, B., Krems, R. V. & Masnou-Seeuws, F. Quo vadis, cold molecules? *Eur. Phys. J. D* **31**, 149–164 (2004).
2. Jones, K. M., Tiesinga, E., Lett, P. D. & Julienne, P. S. Ultracold photoassociation spectroscopy: Long-range molecules and atomic scattering. *Rev. Mod. Phys.* **78**, 483–535 (2006).
3. Köhler, T., Goral, K. & Julienne, P. S. Production of cold molecules via magnetically tunable Feshbach resonances. *Rev. Mod. Phys.* **78**, 1311–1361 (2006).
4. Special issue on cold molecules. *J. Phys. B* **39**, S813–S1280 (2006).
5. Bergmann, K., Theuer, H. & Shore, B. W. Coherent population transfer among quantum states of atoms and molecules. *Rev. Mod. Phys.* **70**, 1003–1025 (1998).
6. Winkler, K. *et al.* Coherent optical transfer of Feshbach molecules to a lower vibrational state. *Phys. Rev. Lett.* **98**, 043201 (2007).
7. Bartenstein, M. *et al.* Precise determination of ^{6}Li cold collision parameters by radio-frequency spectroscopy on weakly bound molecules. *Phys. Rev. Lett.* **94**, 103201 (2005).
8. Mark, M. *et al.* Stückelberg interferometry with ultracold molecules. *Phys. Rev. Lett.* **99**, 113201 (2007).
9. Mark, M. *et al.* Spectroscopy of ultracold, trapped cesium Feshbach molecules. *Phys. Rev. A* **76**, 042514 (2007).
10. Regal, C. A., Ticknor, C., Bohn, J. L. & Jin, D. S. Creation of ultracold molecules from a Fermi gas of atoms. *Nature* **424**, 47–50 (2003).
11. Chin, C. *et al.* Observation of the pairing gap in a strongly interacting Fermi gas. *Science* **305**, 1128–1130 (2004).
12. Chin, C. & Julienne, P. Radio-frequency transitions on weakly bound ultracold molecules. *Phys. Rev. A* **71**, 012713 (2005).
13. Köhl, M., Moritz, H., Stöferle, T., Günter, K. & Esslinger, T. Fermionic atoms in a three-dimensional optical lattice: Observing Fermi surfaces, dynamics and interactions. *Phys. Rev. Lett.* **94**, 080403 (2005).
14. Schunck, C. H., Shin, Y., Schirotzek, A., Zwierlein, M. W. & Ketterle, W. Pairing without superfluidity: The ground state of an imbalanced Fermi mixture. *Science* **316**, 867–870 (2007).
15. Thompson, S. T., Hodby, E. & Wieman, C. E. Ultracold molecule production via a resonant oscillating magnetic field. *Phys. Rev. Lett.* **95**, 190404 (2005).
16. Ospelkaus, C. *et al.* Ultracold heteronuclear molecules in a 3D optical lattice. *Phys. Rev. Lett.* **97**, 120402 (2006).
17. Bertelsen, J. F. & Mølmer, K. Molecule formation in an optical lattice by resonantly modulated magnetic fields. *Phys. Rev. A* **73**, 013811 (2006).
18. Dulieu, O. & Julienne, P. S. Coupled channel bound states calculations for alkali dimers using the Fourier grid method. *J. Chem. Phys.* **103**, 60–66 (1995).
19. Tiesinga, E., Williams, C. J. & Julienne, P. S. Photoassociative spectroscopy of highly excited vibrational levels of alkali dimers: Greens function approach for eigenvalue solvers. *Phys. Rev. A* **57**, 4257–4267 (1998).
20. Krauss, M. & Stevens, W. J. Effective core potentials and accurate energy curves for Cs_2 and other alkali diatomics. *J. Chem. Phys.* **93**, 4236–4242 (1990).
21. Vitanov, N. V. & Garraway, B. M. Landau Zener model: Effects of finite coupling duration. *Phys. Rev. A* **53**, 4288–4304 (1996).
22. Thalhammer, G. *et al.* Long-lived Feshbach molecules in a 3D optical lattice. *Phys. Rev. Lett.* **96**, 050402 (2006).
23. Chin, C. *et al.* Observation of Feshbach-like resonances in collisions between ultracold molecules. *Phys. Rev. Lett.* **94**, 123201 (2005).
24. Staanum, P., Kraft, S. D., Lange, J., Wester, R. & Weidemüller, M. Experimental investigation of ultracold atom-molecule collisions. *Phys. Rev. Lett.* **96**, 023201 (2006).
25. Zahzam, N., Vogt, T., Mudrich, M., Comparat, D. & Pillet, P. Atom-molecule collisions in an optically trapped gas. *Phys. Rev. Lett.* **96**, 023202 (2006).
26. Jaksch, D., Venturi, V., Cirac, J. I., Williams, C. J. & Zoller, P. Creation of a molecular condensate by dynamically melting a Mott insulator. *Phys. Rev. Lett.* **89**, 040402 (2002).
27. Volz, T., Dürr, S., Ernst, S., Marte, A. & Rempe, G. Characterization of elastic scattering near a Feshbach resonance in ^{87}Rb. *Phys. Rev. A* **68**, 010702(R) (2003).

Acknowledgements

We thank W. Ketterle, C. Chin and S. Kokkelmans for valuable discussions. This work was supported by the Austrian Science Fund (FWF) within SFB 15 (project part 17). P.v.d.S. acknowledges support within the ESF-program QUDEDIS during his stay in Innsbruck. P.S.J. was partially supported by the US Office of Naval Research.
Correspondence and requests for materials should be addressed to J.H.D.
Supplementary Information accompanies this paper on www.nature.com/naturephysics.

Reprints and permission information is available online at http://npg.nature.com/reprintsandpermissions/

© 2008 Nature Publishing Group

Coherent Optical Transfer of Feshbach Molecules to a Lower Vibrational State

K. Winkler,[1] F. Lang,[1] G. Thalhammer,[1] P. v. d. Straten,[2] R. Grimm,[1,3] and J. Hecker Denschlag[1]
[1]*Institut für Experimentalphysik, Forschungszentrum für Quantenphysik, Universität Innsbruck, 6020 Innsbruck, Austria*
[2]*Debye Institute, Universiteit Utrecht, 3508 TA Utrecht, Netherlands*
[3]*Institut für Quantenoptik und Quanteninformation, Österreichische Akademie der Wissenschaften, 6020 Innsbruck, Austria*
(Received 8 November 2006; published 25 January 2007)

Using the technique of stimulated Raman adiabatic passage (STIRAP) we have coherently transferred ultracold $^{87}\mathrm{Rb}_2$ Feshbach molecules into a more deeply bound vibrational quantum level. Our measurements indicate a high transfer efficiency of up to 87%. Because the molecules are held in an optical lattice with not more than a single molecule per lattice site, inelastic collisions between the molecules are suppressed and we observe long molecular lifetimes of about 1 s. Using STIRAP we have created quantum superpositions of the two molecular states and tested their coherence interferometrically. These results represent an important step towards Bose-Einstein condensation of molecules in the vibrational ground state.

DOI: 10.1103/PhysRevLett.98.043201   PACS numbers: 34.50.Rk, 03.75.Nt, 32.80.Pj, 42.50.Gy

Recently, there has been a rapidly growing interest in ultracold molecules since they lend themselves to a large number of interesting studies in, for instance, few body collision physics [1–3], chemistry in the ultracold regime, high resolution spectroscopy, as well as quantum computation [4]. Furthermore, molecules in their vibrational ground state are of special interest, because they allow for the formation of an intrinsically stable molecular Bose-Einstein condensate (BEC). Current pathways towards the production of ultracold molecules in well-defined quantum states are either based on sympathetic cooling [5] or association of ultracold neutral atoms using photoassociation [6] or Feshbach resonances [7]. The method of Feshbach ramping has proved especially successful and efficient, but it only produces molecules in the last bound vibrational level. In order to selectively convert molecules into more deeply bound states, it has been proposed [8] to use a sequence of stimulated optical Raman transitions to step molecules down the vibrational ladder. This process takes place while the molecules are held in an optical lattice isolating them from each other and thus shielding them from detrimental collisions. Recently, optical transfer of molecules into their vibrational ground state was demonstrated experimentally using a "pump-dump" method without a lattice at a moderate efficiency and selectivity [9].

Here we report the realization of an efficient and highly selective transfer scheme, where an ensemble of $^{87}\mathrm{Rb}_2$ Feshbach molecules in an optical lattice is coherently converted to a deeper bound molecular state via stimulated Raman adiabatic passage (STIRAP). STIRAP is known as a fast, efficient, and robust process for population transfer based on a Raman transition [10]. During transfer it keeps the molecules in a dark superposition state, which decouples from the light and thus suppresses losses due to spontaneous light scattering. In our proof-of-principle experiment we transfer the Feshbach molecules with a STIRAP pulse from their last bound vibrational level (binding energy 24 MHz × h), which we denote $|a\rangle$, to the second-to-last bound vibrational level, $|g\rangle$ [see Fig. 1(a) and 1(b)]. Both levels have a rotational quantum number $l = 0$ and a total spin $F = 2$, $m_F = 2$. The level $|g\rangle$ is known from previous experiments [11–14]. It has a binding energy of 637 MHz × h at 973 G and can be conveniently reached via Raman beams generated with an acousto-optic modulator (AOM). In order to detect the more deeply bound molecules, a second STIRAP pulse converts the

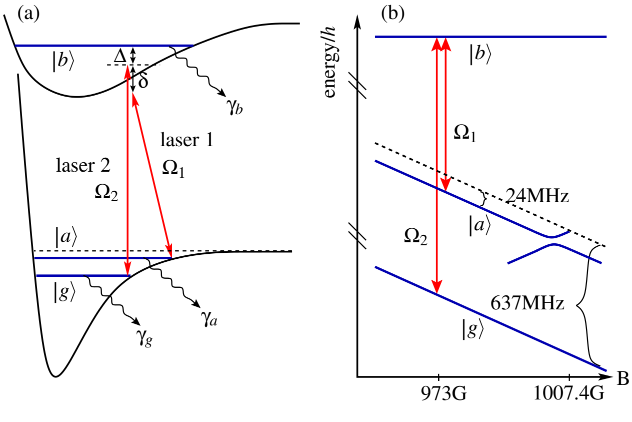

FIG. 1 (color online). (a) Level scheme for STIRAP. Lasers 1, 2 couple the ground state molecular levels $|a\rangle$, $|g\rangle$ to the excited level $|b\rangle$ with Rabi frequencies Ω_1, Ω_2, respectively. Δ and δ denote detunings. γ_a, γ_b, γ_g give effective decay rates of the levels. (b) Zeeman diagram of relevant energy levels. At 1007.4 G a molecular state crosses the threshold of the unbound two atom continuum (dashed line) giving rise to a Feshbach resonance. From there this molecular state adiabatically connects to the last bound vibrational level $|a\rangle$, the state of the Feshbach molecules.

© 2007 The American Physical Society

molecules back to the last bound vibrational level, where they are detected as atoms after dissociation via Feshbach ramping. The complete cycle has an efficiency of 75%, indicating a single STIRAP efficiency of 87%.

We use essentially the same setup as in Ref. [15]. Starting point for the experiments is a pure ensemble of 2×10^4 ultracold $^{87}\mathrm{Rb}_2$ Feshbach molecules which are held in the lowest Bloch band of a cubic 3D optical lattice. There is no more than a single molecule per site and the whole molecular ensemble occupies a volume of about $20 \times 20 \times 20\ \mu\mathrm{m}^3$. The lattice is 50 E_r deep for molecules ($E_r = 2\pi^2\hbar^2/m\lambda^2$, where m is the mass of the atoms and $\lambda = 830.44$ nm the wavelength of the lattice laser), suppressing tunneling between sites. The molecular ensemble is initially produced from an atomic ^{87}Rb BEC after loading it into the lattice, subsequent Feshbach ramping at 1007.40 G [16] and a final purification step [15] which removes all chemically unbound atoms. Lowering the magnetic field to 973 G transfers the atoms to the adiabatically connected state $|a\rangle$, which has nearly the same magnetic moment as $|g\rangle$ (see Fig. 1). This results in an almost magnetic field insensitive Raman transition [17].

In order to efficiently carry out STIRAP, a suitable excited molecular level, $|b\rangle$, has to be identified (see Fig. 1). We chose the electronically excited molecular state $|0_g^-, \nu = 31, J = 0\rangle$ located 6.87 cm^{-1} below the $S_{1/2} + P_{3/2}$ dissociation asymptote [18]. The corresponding line is strong and solitary; i.e., within a 2 GHz vicinity no other strong molecular lines are found which could interfere with STIRAP. Coupling to other excited molecular states leads to loss of the molecules, since these levels typically decay spontaneously into a variety of undetected vibrational levels in the ground state. Furthermore, it is advantageous that the chosen level $|b\rangle$ has a similar Franck-Condon overlap with states $|a\rangle$ and $|g\rangle$. It can be shown that this also helps to minimize losses through off-resonant coupling channels.

With this choice of states $|a\rangle$, $|b\rangle$, $|g\rangle$, we observe a clear molecular dark resonance when coupling the states with resonant Raman laser light (see Fig. 2). The corresponding molecular dark superposition state shows a long lifetime. This is a necessary precondition for our STIRAP experiments, because the molecules have to be kept in a dark state during the whole STIRAP process which in our case typically takes hundreds of μs. The Raman laser beams are both derived from a single Ti:sapphire laser with a short term linewidth of less than 1 MHz. The Ti:sapphire laser is offset locked relative to the D_2 line of atomic rubidium with the help of a scanning optical cavity, which yields an absolute frequency stability of better than 5 MHz. The frequency difference between the two beams is created with an acousto-optical modulator (AOM) with a frequency of about 307 MHz in a double-pass configuration. This allows precise control of the relative frequency difference between the beams over several tens of MHz and ensures phase locking. Both beams propagate collinearly and have a waist of about 290 μm at the location of the molecular ensemble. The polarization of the beams is parallel to the direction of the magnetic bias field of 973 G.

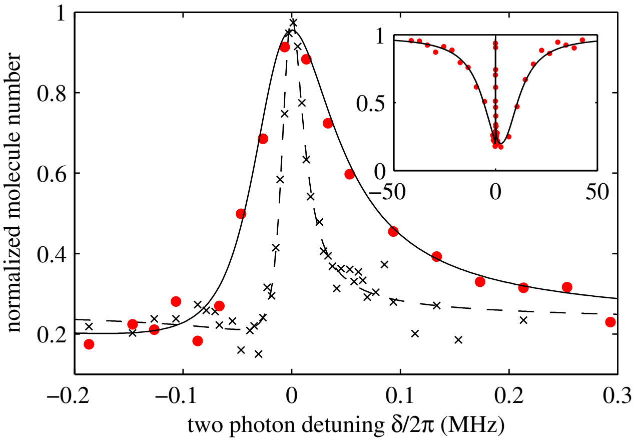

FIG. 2 (color online). Dark resonance. The data show the remaining fraction of Feshbach molecules in state $|a\rangle$, after subjecting them to a 200 μs square pulse of Raman laser light in a narrow range around 0 of the two-photon detuning δ. The inset shows the scan over the whole line of state $|b\rangle$. The strong suppression of loss at $\delta = 0$ is due to the appearance of a dark state. The laser intensities are $I_1 = 2.6\ \mathrm{mW/cm^2}$, $I_2 = 13\ \mathrm{mW/cm^2}$ (×), $I_2 = 51\ \mathrm{mW/cm^2}$ (●). Δ is in general tuned close to zero and for the shown measurements happens to be $\Delta/2\pi \approx 2.5$ MHz, which gives rise to the slightly asymmetric line shape of the dark states. The solid and dashed lines are model calculations (see text).

In order to transfer the molecules from state $|a\rangle$ to state $|g\rangle$, we carry out a STIRAP pulse which consists of a so-called counterintuitive succession of two laser pulses [see Fig. 3(a)]. We first switch on laser 2 and then ramp its intensity to zero within the pulse time $\tau_p = 200\ \mu$s. Simultaneously we ramp up the intensity of laser 1 from zero to its final value. We fix the ratio of the maximal pulse intensities of laser 1 and 2 to $I_2^{\max}/I_1^{\max} = 1/3.2$ in order to partially compensate for the unequal Franck-Condon factor of the $|a\rangle - |b\rangle$ and $|g\rangle - |b\rangle$ transitions. Ideally, after the first STIRAP pulse all molecules from state $|a\rangle$ should end up in state $|g\rangle$. In order to determine the population in state $|g\rangle$, we apply, after a holding time of $\tau_h = 5$ ms, a second STIRAP pulse which is the mirror image in time of pulse 1. This transfers the molecules back into state $|a\rangle$. We then ramp the magnetic field over the Feshbach resonance at 1007.4 G which dissociates the molecules with unit efficiency [15] into pairs of atoms. These are subsequently detected with standard absorption imaging. Figure 3(b) shows in a time resolved way how molecules in state $|a\rangle$ first disappear and then reappear during the course of the STIRAP sequence. After applying the first STIRAP pulse, no molecules can be observed in state $|a\rangle$. This is to be expected, since any molecule which is left over in state $|a\rangle$ at the end of the first STIRAP pulse is in a bright state and will be quickly removed by resonantly scattering photons from laser 1. This confirms, that after completion of the

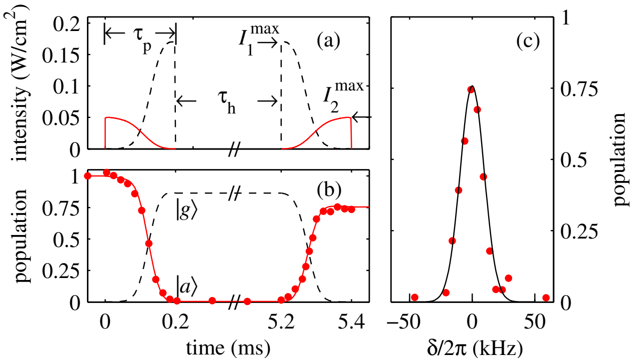

FIG. 3 (color online). STIRAP. (a) Counterintuitive pulse scheme. Shown are laser intensities as a function of time (laser 1: dashed line, laser 2: solid line). The first STIRAP pulse with length $\tau_p = 200\ \mu$s transfers the molecule from state $|a\rangle$ to state $|g\rangle$. After a holding time $\tau_h = 5$ ms, the second pulse (identical, but reversed) transfers the molecules back to $|a\rangle$. $I_{1,2}^{\max}$ indicates the maximal intensity of laser 1 (2) in the pulse, respectively. (b) Corresponding population in state $|a\rangle$ (data points, solid line) and state $|g\rangle$ (dashed line). The data points are measurements where at a given point in time the STIRAP lasers are abruptly switched off and the molecule population in state $|a\rangle$ is determined. For these measurements $\Delta \approx 0 \approx \delta$. The lines are model calculations (see text). (c) Efficiency for population transfer from state $|a\rangle$ to state $|g\rangle$ and back via STIRAP as a function of the two-photon detuning δ. The line is a model calculation, showing a Gaussian line shape with a FWHM width of ≈ 22 kHz.

second STIRAP pulse we only detect molecules that were previously in state $|g\rangle$. We observe an efficiency of 75% for the full cycle of conversion into state $|g\rangle$ and back. Figure 3(c) shows how this efficiency depends critically on the two-photon detuning δ.

In Fig. 4 we investigate further the complete STIRAP cycle efficiency as a function of the laser intensity and pulse length. In these measurements we use pulses with the same shape as in Fig. 3(a), which are rescaled to adjust pulse time τ_p and laser intensity. Again, for the best settings we reach an efficiency of about 75% for the two pulses, which corresponds to a transfer efficiency to state $|g\rangle$ of about 87%. The dependence of the efficiency on intensity and pulse length can be qualitatively understood as follows. For short pulse lengths or low intensities, the dark state cannot adiabatically follow the STIRAP pulse, resulting in a low transfer efficiency. For very long pulse lengths and high intensities the losses due to an imperfect dark state become dominant, also resulting in a low transfer efficiency. Thus in order to find an optimum value for the transfer efficiency there is a trade off between adiabaticity and inelastic photon scattering.

We are also able to quantitatively understand our data by using a three level model. It describes the evolution of the quantum mechanical probability amplitudes a, b, and g for a molecule in the respective states $|a\rangle$, $|b\rangle$, and $|g\rangle$ in terms of the following set of differential equations:

$$\begin{aligned} i\dot{a} &= (-i\gamma_a/2)a - \tfrac{1}{2}\Omega_1 b, \\ i\dot{b} &= [(\Delta + \delta) - i\gamma_b/2]b - \tfrac{1}{2}(\Omega_1 a + \Omega_2 g), \qquad (1) \\ i\dot{g} &= (\delta - i\gamma_g/2)g - \tfrac{1}{2}\Omega_2 b. \end{aligned}$$

Here, the Rabi frequencies Ω_1, Ω_2, the detunings Δ and δ, and the decay rates γ_a, γ_b, γ_g are defined as shown in Fig. 1. After experimentally determining Ω_1, Ω_2 and γ_a, γ_g and using $\gamma_b = 2\pi \times 12$ MHz, we are able to consistently describe all data in Figs. 2–4 with a single set of parameters. From one-photon and two-photon scans (as, e.g., in Fig. 2) we obtain $\Omega_1 = 2\pi \times 2.9\ \text{MHz}[I_1/(\text{W cm}^{-2})]^{1/2}$ and $\Omega_2 = 2\pi \times 6.0\ \text{MHz}[I_2/(\text{W cm}^{-2})]^{1/2}$. The effective decay rates γ_a, γ_g are intensity dependent and are mainly due to the off-resonant coupling of $|a\rangle$ with laser 2 and $|g\rangle$ with laser 1. We determine γ_a (γ_g) by shining laser 2 (laser 1) on the molecules in state $|a\rangle$ ($|g\rangle$) and measuring the off-resonant losses. We find that $\gamma_a/I_2 = 2\pi \times 0.72\ \text{kHz}/(\text{W cm}^{-2})$ and $\gamma_g/I_1 = 2\pi \times 0.40\ \text{kHz}/(\text{W cm}^{-2})$. From these independent measurements, all parameters of Eqs. (1) are determined without further adjustable parameters. In the calculations shown in Fig. 3(b), 3(c), and 4 the time dependent pulse shapes [see Fig. 3(a)] are included. The agreement between theory and experiment is very good.

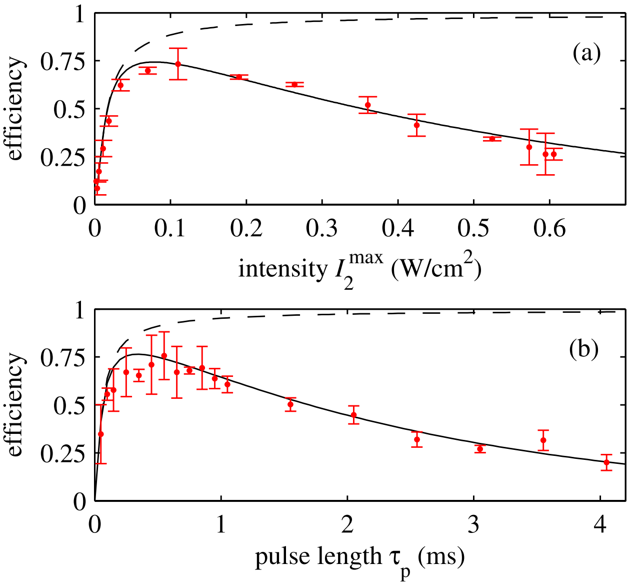

FIG. 4 (color online). Efficiency for population transfer from state $|a\rangle$ to state $|g\rangle$ and back with two STIRAP pulses. (a) Efficiency vs the laser intensity $I_2^{\max}$ (fixed pulse length of $\tau_p = 200\ \mu$s). (b) Efficiency vs the pulse length τ_p (fixed laser intensity $I_2^{\max} = 44\ \text{mW/cm}^2$). For (a) and (b) the intensity ratio $I_2^{\max}/I_1^{\max} = 1/3.2$. The lines are from calculations without free parameters using Eqs. (1). Setting $\gamma_a = \gamma_g = 0$, the efficiency would reach unity for a fully adiabatic transfer (dashed lines). Using for γ_a, γ_a the experimentally determined values, the calculations (solid lines) are in good agreement with the data. The error bars represent a 1σ statistical error.

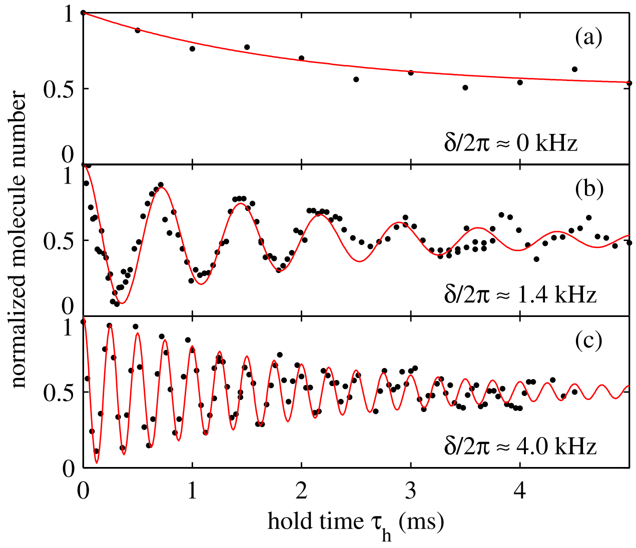

FIG. 5 (color online). Coherence of the $(|a\rangle - |g\rangle)$ superposition state. Shown is the molecule number in state $|a\rangle$ as a function of holding time τ_h for different detunings δ as indicated. The oscillations indicate coherent flopping of the molecular superposition state between the dark and a bright state. The lines are given by $0.5\exp(-\tau_h/\tau)\cos(\delta\tau_h) + 0.5$, with a damping time $\tau = 2$ ms.

During STIRAP the molecules are in a quantum superposition, $\Omega_2|a\rangle - \Omega_1|g\rangle$. In order to probe the coherence of this superposition, we perform a Ramsey-type experiment. First we create a dark superposition state with equal population in the two states, $|a\rangle - |g\rangle$, by going halfway into the first STIRAP pulse of Fig. 3(a). We then simultaneously switch off both STIRAP lasers for a variable holding time τ_h, after which we retrace in time the same STIRAP half pulse. As a result we observe oscillations in the number of molecules in level $|a\rangle$ as a function of the holding time τ_h (see Fig. 5). During the holding time, the superposition state freely evolves, coherently flopping between the dark and a bright state with a frequency equal to the two-photon detuning δ. At the end of the holding time, when we switch on again the STIRAP lasers, the dark state is transferred back to state $|a\rangle$ whereas the bright state will be immediately destroyed by the light and leads to complete loss of the corresponding molecules. The observed oscillations are exponentially damped on a time scale of about 2 ms. This damping can be explained by a magnetic field inhomogeneity of about 20 mG over the molecular cloud, which leads to a spatial variation of $2\pi \times 250$ Hz in the two-photon detuning δ. Additionally we observe a slight shift of the oscillation frequency with time on the order of $2\pi \times 50$ Hz/ms. This can be attributed to a small drift of the magnetic field.

Furthermore, we have performed lifetime measurements of the molecules in state $|g\rangle$ by varying the holding time τ_h between the two STIRAP pulses [see Fig. 3(a)]. At a lattice depth of 60 E_r for molecules, we observe a long lifetime of 0.8 s (assuming exponential decay), which is longer than the lifetime of 0.4 s for Feshbach molecules in state $|a\rangle$. At these deep lattices molecular decay is exclusively due to inelastic scattering of lattice photons.

To conclude, using STIRAP we have demonstrated a coherent transfer of a molecular quantum gas from a weakly bound molecular level to a more deeply bound molecular level with a high transfer efficiency of 87%. The method can be extended in a straightforward manner to create arbitrarily deeply bound molecules. With a *single* STIRAP pulse all vibrational levels down to level $X^1\Sigma_g^+(v = 116)/a^3\Sigma_u^+(v = 32)$ should be easily reached since the Franck-Condon factors to state $|b\rangle$ are of similar order as for level $|g\rangle$ [19]. This includes the level $X^1\Sigma_g^+(v = 119)/a^3\Sigma_u^+(v = 35)$ with its binding energy of 30 GHz × h, from which the vibrational ground state $X^1\Sigma_g^+(v = 0)$ of the singlet potential can be reached with two additional Raman (or STIRAP) transitions [8]. Thus STIRAP is a promising tool for the creation of a molecular BEC in the molecular ground state.

We thank Christiane Koch for providing Franck-Condon factors and Helmut Ritsch for valuable discussions. This work was supported by the Austrian Science Fund (FWF) within SFB 15 (project part 17) and the Cold Molecules TMR Network under Contract No. HPRN-CT-2002-00290. P. v. d. S. acknowledges support within the ESF-program QUDEDIS during his stay in Innsbruck.

[1] C. Chin *et al.*, Phys. Rev. Lett. **94**, 123201 (2005).
[2] P. Staanum, S. D. Kraft, J. Lange, R. Wester, and M. Weidemüller, Phys. Rev. Lett. **96**, 023201 (2006).
[3] N. Zahzam, T. Vogt, M. Mudrich, D. Comparat, and P. Pillet, Phys. Rev. Lett. **96**, 023202 (2006).
[4] D. DeMille, Phys. Rev. Lett. **88**, 067901 (2002).
[5] For an overview, see J. Doyle, B. Friedrich, R. V. Krems, and F. Masnou-Seeuws, Eur. Phys. J. D **31**, 149 (2004).
[6] For an overview, see K. M. Jones, E. Tiesinga, P. D. Lett, and P. S. Julienne, Rev. Mod. Phys. **78**, 483 (2006).
[7] For an overview, see T. Köhler, K. Goral, and P. S. Julienne, Rev. Mod. Phys. **78**, 1311 (2006).
[8] D. Jaksch, V. Venturi, J. I. Cirac, C. J. Williams, and P. Zoller, Phys. Rev. Lett. **89**, 040402 (2002).
[9] J. M. Sage, S. Sainis, T. Bergeman, and D. DeMille, Phys. Rev. Lett. **94**, 203001 (2005).
[10] K. Bergmann, H. Theuer, and B. W. Shore, Rev. Mod. Phys. **70**, 1003 (1998).
[11] R. Wynar, R. S. Freeland, D. J. Han, C. Ryu, and D. J. Heinzen, Science **287**, 1016 (2000).
[12] T. Rom *et al.*, Phys. Rev. Lett. **93**, 073002 (2004).
[13] K. Winkler *et al.*, Phys. Rev. Lett. **95**, 063202 (2005).
[14] G. Thalhammer *et al.*, Phys. Rev. A **71**, 033403 (2005).
[15] G. Thalhammer *et al.*, Phys. Rev. Lett. **96**, 050402 (2006).
[16] T. Volz, S. Dürr, S. Ernst, A. Marte, and G. Rempe, Phys. Rev. A **68**, 010702(R) (2003).
[17] At 973 G the dependence of the two-photon resonance on the magnetic field is about 12 kHz/G.
[18] A. Fioretti *et al.*, Eur. Phys. J. D **15**, 189 (2001).
[19] C. Koch (private communication).

arXiv:cond-mat/0608721v2 [cond-mat.other] 1 Sep 2006

Repulsively bound atom pairs: Overview, Simulations and Links

A. J. Daley[*,†], A. Kantian[*,†], H. P. Büchler[*,†], P. Zoller[*,†], K. Winkler[**], G. Thalhammer[**], F. Lang[**], R. Grimm[**,†] and J. Hecker Denschlag[**]

[*] *Institut für Theoretische Physik, Universität Innsbruck, A-6020 Innsbruck, Austria*
[†] *Institut für Quantum Optik und Quantum Information der Österreichischen Akademie der Wissenschaften, A-6020 Innsbruck, Austria*
[**] *Institut für Experimentalphysik, Universität Innsbruck, A-6020 Innsbruck, Austria*

Abstract. We review the basic physics of repulsively bound atom pairs in an optical lattice, which were recently observed in the laboratory [1], including the theory and the experimental implementation. We also briefly discuss related many-body numerical simulations, in which time-dependent Density Matrix Renormalisation Group (DMRG) methods are used to model the many-body physics of a collection of interacting pairs, and give a comparison of the single-particle quasimomentum distribution measured in the experiment and results from these simulations. We then give a short discussion of how these repulsively bound pairs relate to bound states in some other physical systems.

Keywords: optical lattices, repulsively bound pairs, Bose-Hubbard model, time-dependent Density Matrix Renormalization Group
PACS: 03.75.Lm, 42.50.-p

Introduction

Stable bound states, in which the composite object has a lower energy than the separated constituents, give rise to much diversity and complexity in many physical systems. Well-known examples ranging from chemically bound atomic molecules to excitons in solid state physics rely on attractive interactions to give rise to bound objects. The converse, particles bound by a repulsive interaction, is impossible in free space because interaction energy can be freely converted to kinetic energy of the constituent atoms. However, by placing particles on a lattice, kinetic energy is restricted to fall within the Bloch bands, and repulsively interacting atoms cannot always move apart and convert their interaction energy to kinetic energy. Recently we have reported on the first clear observation of such states, in the form of repulsively bound pairs of atoms in an optical lattice [1].

The stability of these pairs relies on the weak coupling of atoms in optical lattices to dissipative processes, which would otherwise lead to rapid relaxation of the system to its ground state (as is typically seen, e.g., in the context of solid state lattices). In this article we give an overview of repulsively bound atom pairs, beginning with a discussion of a single pair, and proceeding with a discussion of the experimental implementation, and many-body numerical simulations used to analyse a system of many interacting pairs. We then comment on analogies between these composite objects and bound states found

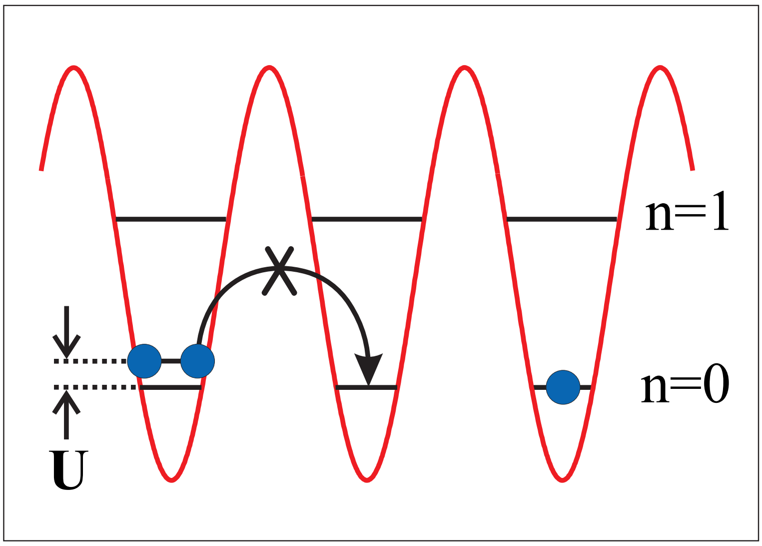

FIGURE 1. A state with two atoms located on the same site of an optical lattice has an energy offset $\approx U$ with respect to states where the atoms are separated. Breaking up of the pair is suppressed due to the lattice band structure and energy conservation, so that the pair remains bound as a composite object, which can tunnel through the lattice. In the figure, $n = 0$ denotes the lowest Bloch band and $n = 1$ the first excited band.

in other physical systems.

Repulsively bound atom pairs in an optical lattice

The existence of repulsively bound atom pairs is predicted by the Bose-Hubbard model [2], which describes well the dynamics of ultracold atoms loaded into the lowest band of a sufficiently deep optical lattice [3]. The corresponding Hamiltonian is

$$\hat{H} = -J \sum_{\langle i,j \rangle} \hat{b}_i^\dagger \hat{b}_j + \frac{U}{2} \sum_i \hat{n}_i \left(\hat{n}_i - 1\right), \tag{1}$$

where $\hat{b}_i$ ($\hat{b}_i^\dagger$) are destruction (creation) operators for the bosonic atoms at site i of the lattice, and $\hat{n}_i = \hat{b}_i^\dagger \hat{b}_i$ is the corresponding number operator. $J/\hbar$ denotes the nearest neighbor tunnelling rate, and U the on-site collisional energy shift. The relative value of U and J can be adjusted by varying the depth of the lattice V_0.

In the limit of $U/J \to \infty$, the repulsively bound pair can be seen as an object where two atoms are located on the same lattice site. Due to the interaction between atoms, this state has an energy offset of U compared with states where atoms are present on different lattice sites. The stability of the pair can then be understood by energy conservation arguments: Two separated atoms moving in the lowest Bloch band of a lattice can have a maximum combined kinetic energy of $8J$ (in 1D). Thus, the atoms cannot separate and convert their interaction energy to kinetic energy (see Figure 1).

More generally, repulsively bound pairs arise from the eigenstates of the Bose-Hubbard model with two atoms present on the lattice. Denoting the primitive lattice vectors in each of the d dimensions by $\mathbf{e}_i$, we can write the position of the two atoms by $\mathbf{x} = \sum_{i=1}^{d} x_i \mathbf{e}_i$ and $\mathbf{y} = \sum_{i=1}^{d} y_i \mathbf{e}_i$, where x_i, y_i are integers, and we can write the two atom wave function in the form $\Psi(\mathbf{x},\mathbf{y})$. The related Schrödinger equation from the Bose-Hubbard model then takes the form

$$\left[-J\left(\tilde{\Delta}_{\mathbf{x}}^{0}+\tilde{\Delta}_{\mathbf{y}}^{0}\right)+U\delta_{\mathbf{x},\mathbf{y}}\right]\Psi(\mathbf{x},\mathbf{y}) = E\,\Psi(\mathbf{x},\mathbf{y}), \tag{2}$$

where the operator

$$\tilde{\Delta}_{\mathbf{x}}^{\mathbf{K}}\Psi(\mathbf{x}) = \sum_{i=1}^{d}\cos\left(\mathbf{K}\mathbf{e}_i/2\right)\left[\Psi(\mathbf{x}+\mathbf{e}_i)+\Psi(\mathbf{x}-\mathbf{e}_i)-2\Psi(\mathbf{x})\right] \tag{3}$$

denotes the discrete lattice Laplacian on a cubic lattice. Writing the wavefunction in relative and centre of mass coordinates $\Psi(\mathbf{x},\mathbf{y}) = \exp(i\mathbf{K}\mathbf{R})\,\psi_{\mathbf{K}}(\mathbf{r})$, the Schrödinger equation can be reduced to a single particle problem in the relative coordinate

$$\left[-2J\tilde{\Delta}_{\mathbf{r}}^{\mathbf{K}}+E_{\mathbf{K}}+U\delta_{\mathbf{r},0}\right]\psi_{\mathbf{K}}(\mathbf{r}) = E\,\psi_{\mathbf{K}}(\mathbf{r}) \tag{4}$$

where $E_{\mathbf{K}} = 4J\sum_{i=1}\left[1-\cos(\mathbf{K}\mathbf{e}_i/2)\right]$ is the kinetic energy of the center of mass motion.

The short range interaction potential makes it possible to resum the perturbation expansion for the associated Lippman-Schwinger equation, and we obtain the scattering states

$$\psi_E(\mathbf{r}) = \exp(i\mathbf{k}\mathbf{r}) - 8\pi J f_E(\mathbf{K}) G_{\mathbf{K}}(E,\mathbf{r}) \tag{5}$$

with scattering amplitude

$$f_E(\mathbf{K}) = -\frac{1}{4\pi}\frac{U/(2J)}{1-G_{\mathbf{K}}(E,0)U} \tag{6}$$

with total energy $E = \varepsilon_{\mathbf{k},\mathbf{K}} + E_{\mathbf{K}}$, and $\varepsilon_{\mathbf{k},\mathbf{K}} = 4J\sum_{i=1}\cos(\mathbf{K}\mathbf{e}_i/2)\left[1-\cos(\mathbf{k}\mathbf{e}_i)\right]$. Furthermore, $G_{\mathbf{K}}(E,\mathbf{r})$ denotes the Greens function of the non-interacting problem, which in Fourier space takes the form $\tilde{G}_{\mathbf{K}}(E,\mathbf{k}) = 1/(E-\varepsilon_{\mathbf{k},\mathbf{K}}-E_{\mathbf{K}}+i\eta)$. The scattering states $\psi_E(\mathbf{r})$ correspond to two free atoms moving on the lattice and undergoing scattering processes.

In addition, the pole in the scattering amplitude indicates the presence of an additional bound state for each value of $\mathbf{K}$, which corresponds to the repulsively bound pair. The energy E_{bs} of the bound states is determined by $1 = UG_{\mathbf{K}}(E_{\mathrm{bs}},0)$ while the bound state wave function takes the form $\psi_{\mathbf{K}}^{\mathrm{bs}}(\mathbf{r}) = c\,G_{\mathbf{K}}(E_{\mathrm{bs}},\mathbf{r})$ with c a normalization factor. Note that in one dimension such bound states exists for arbitrary repulsive interaction, but for a three-dimensional lattice such bound states, and therefore repulsively bound pairs, appear only for a repulsive interaction above a critical value $U > U_{\mathrm{crit}} \approx 8J$ (for $K = 0$). These states have a square-integrable relative wavefunction $\psi_{\mathbf{K}}(\mathbf{r})$, as shown for two different values of U/J in Figure 2. For a deep lattice, i.e. $U/J \gg 1$, bound pairs essentially consist of two atoms occupying the same site, whereas for small U/J, the pair is delocalized over several lattice sites. A main feature of the repulsive pair wavefunction

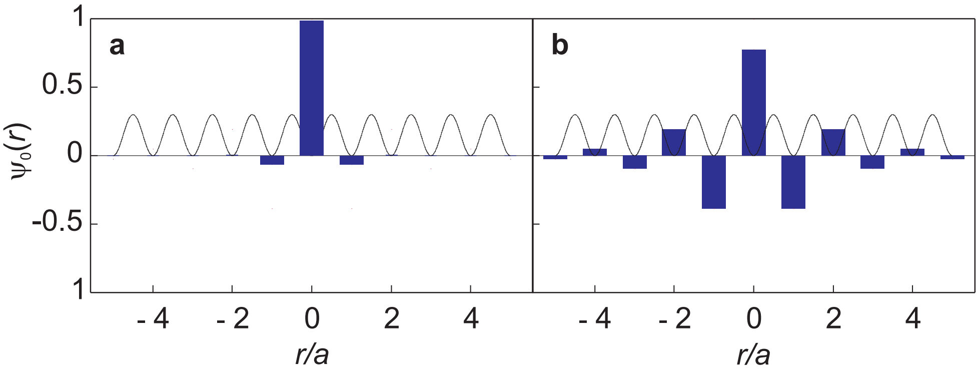

FIGURE 2. Relative wavefunctions $\psi_{\mathbf{K}}(\mathbf{r})$ for repulsively bound pairs ($a_s = 100a_0$) in 1D with $K = 0$, for (a) $U/J = 30$ ($V_0 = 10E_r$) and (b) $U/J = 3$ ($V_0 = 3E_r$), where E_r is the recoil energy. ($E_r = 2\pi^2\hbar^2/m\lambda^2$, where m is the mass of the atoms and λ is the twice the lattice period, a.)

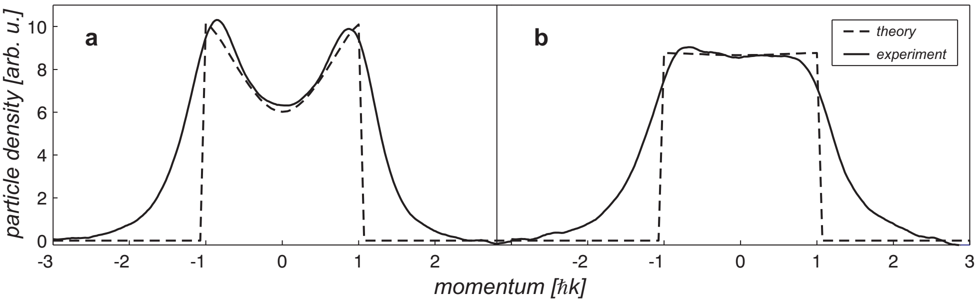

FIGURE 3. Single particle quasimomentum distributions for repulsively bound pairs in 1D from experiment and numerical simulations (see text) for (a) $V_0 = 5E_R$ and (b) $V_0 = 20E_R$. The density values have been scaled to facilitate comparison between experimental and theoretical results. These results agree well, up to experimental artifacts related to repulsion between atoms during expansion (before imaging) and also relatively long imaging times (many photons are scattered from each atom, which performs a random walk). This leads to smearing out of the sharp structure at the edge of the Brillouin zone.

is its oscillating character: the wavefunction amplitude alternates sign from one site to the next. In quasimomentum space this corresponds to a wavefunction which is peaked at the edges of the first Brillouin zone, as is shown in Figure 3.

When many repulsively bound pairs exist, they will interact with one another as described by the Bose-Hubbard model. This many-body behaviour can be computed numerically as described below.

Experimental realization of repulsively bound atom pairs

We experimentally create repulsively bound atom pairs from a sample of ultracold ^{87}Rb atoms in a cubic 3D optical lattice. About 2×10^4 atom pairs are initially prepared in a deep lattice of $35E_r$ depth, with each site of the lattice either doubly-occupied or unoccupied. By adiabatically ramping down the lattice depth afterwards the initially localized pair wavefunctions become delocalized (see Fig. 2). The initial preparation is carried out in several steps as described in the following. In the beginning, a Bose Einstein condensate of ^{87}Rb atoms is carefully loaded into the vibrational ground state of the optical lattice, such that many lattice sites are occupied with two atoms. Besides the doubly occupied sites, there are also sites which are occupied by single atoms or more than two atoms. In order to remove atoms from these sites we use a purification scheme which involves the use of a Feshbach resonance and a combined pulse of laser and radio-frequency (rf) radiation [4]. The laser and rf pulse resonantly blows atoms out of the lattice, whereas the Feshbach resonance serves to protect (shelve) the pairs temporarily from this pulse by converting pairs into Feshbach molecules and then back into atoms. Besides lifetime measurements, we have been able to experimentally map out the single particle momentum distribution (see Fig. 3) and to measure their binding energy. The properties and the dynamics of the pairs can be controlled by tuning the atom-atom interaction with the help of a Feshbach resonance at 1007G and by controlling the depth of the optical lattice and particle density. Consistent with our theoretical analysis, the repulsively bound pairs exhibit long lifetimes of hundreds of milliseconds, even under collisions with one another.

Many-Body simulations

Many-body numerical simulations for a gas of repulsively bound pairs are performed using time-dependent DMRG methods [5]. These methods allow for ground state calculation and time-dependent calculation of the dynamics of atoms for a variety of 1D situations, including many lattice and spin models. The basic algorithm provides near-exact integration of a many-body Schrödinger equation, with the Hilbert space being adaptively decimated. This works provided that the state of the system is always able to be efficiently represented as a matrix product state [6]. As a result, it is possible to compare the dynamics of a gas of interacting repulsively bound pairs in a 1D lattice with experimental data. For example, we can simulate a 1D Bose-Hubbard model with time dependent parameters, beginning with an initial state corresponding to a distribution of atoms situated in doubly occupied lattice sites. We compute the corresponding dynamics as the lattice depth is decreased by decreasing U and increasing J. These many-body simulations account for interactions between bound pairs, and let us compute final momentum distributions that agree well with the experimental results. We can also use these simulations to model lattice modulation spectroscopy of atoms in optical lattices. In figure 3 we show a comparison of quasimomentum distributions from the experiment and from many-body simulations.

Analogy to Other Bound States

Although no stable repulsively bound pairs have previously been observed, they have an interesting relationship to many bound states in other physical systems. For example, resonance behaviour based on similar pairing of Fermions of different spin in the Hubbard model was first discussed by Yang [7], and plays an important role in SO(5) theories of superconductivity [8]. There are several examples of many-body bound states that can occur for repulsive as well as attractive interactions, such as the resonances discussed in the context of the Hubbard model by Demler et al. [9]. Such resonance behaviour is common in many-body physics, although states of this type are normally very short-lived. Optical lattice experiments will now provide an opportunity to prepare and investigate stable versions of such states, which until now have only appeared virtually as part of complex processes.

The stability and many-body physics of repulsively bound pairs is perhaps most closely associated with that of excitons, which are bound pairs of a particle in the conduction band and a hole in the valence band of a periodic system [10]. These bind to form a composite boson, a gas of which can, in principle, Bose-condense. Excitons are excited states of the many-body system, but are bound by an attractive interaction between the particle and hole that form the pair. They are also discussed in the specific context of fermionic systems. However, a single exciton on a lattice could have a description very similar to that of a single repulsively bound pair, and could be realised and probed in optical lattices experiments [11].

Repulsively bound atom pairs in an optical lattice are also reminiscent of photons being trapped by impurities in photonic crystals [12], which consist of transparent material with periodically changing index of refraction. An impurity in that crystal in form of a local region of index of refraction can then give rise to a localized field eigenmode. In an analogous sense, each atom in a repulsively bound pair could be as an impurity that “traps” the other atom.

An analogy can also be drawn between repulsively bound atom pairs and gap solitons, especially as found in atomic gases [13, 14, 15, 16]. Solitons are normally a non-linear wave phenomenon, and in this sense have a very different behaviour to repulsively bound pairs, which exhibit properties characteristic of many-body quantum systems. However, there has been increasing recent interest in discussing the limit of solitons in atomic systems where very few atoms are present, giving rise to objects that are often referred to as quantum solitons [17]. These are N-body bound states in 1D, and thus a 2-atom bright quantum soliton is a bound state of two atoms moving in 1D. In this sense, the solution for a single repulsively bound pair in 1D is related to a single quantum soliton on a lattice.

Conclusion

In summary, a metastable bound state that arises from repulsion between the constituents and the lattice band structure has been demonstrated in the laboratory. This state exemplifies in a new way the strong correspondence between the optical lattice physics of ultracold atoms and the Hubbard model, a connection which has particular importance for applications of these cold atom systems to more general simulation of condensed matter models, to quantum computing. The existence of such metastable bound objects will be ubiquitous in cold atoms lattice physics, giving rise to new potential composite objects also in Fermions or in systems with mixed Bose-Fermi statistics.

These states could also be formed with more than two particles, or as bound states of existing composite particles. Repulsively bound pairs have no counterpart in condensed matter physics due to the strong inelastic decay channels observed in solid state lattices, and could be a building block of yet unstudied quantum many body states or phases.

ACKNOWLEDGMENTS

We would like to thank Eugene Demler for interesting discussions. We acknowledge support from the Austrian Science Fund (FWF) within the Spezialforschungsbereich 15, from the European Union within the OLAQUI and SCALA networks, from the TMR network "Cold Molecules", and the Tiroler Zukunftsstiftung.

REFERENCES

1. K. Winkler, G. Thalhammer, F. Lang, R. Grimm, J. Hecker Denschlag, A. J. Daley, A. Kantian, H. P. Büchler, and P. Zoller, *Nature* **441**, 853–856 (2006).
2. M. P. A. Fisher, P. B. Weichman, G. Grinstein, and D. S. Fisher, *Phys. Rev. B* **40**, 546–570 (1989).
3. D. Jaksch, and P. Zoller, *Annals of Physics* **315**, 52–79 (2005), and references therein.
4. G. Thalhammer, K. Winkler, F. Lang, S. Schmid, R. Grimm, and J. Hecker Denschlag, *Phys. Rev. Lett.* **96**, 050402 (2006).
5. G. Vidal, *Phys. Rev. Lett.* **91**, 147902 (2003); 93, 040502 (2004);
   A. J. Daley, C. Kollath, U. Schollwöck, and G. Vidal, *J. Stat. Mech.: Theory Exp.*, P04005 (2004);
   S. R. White and A. E. Feiguin, *Phys. Rev. Lett.* **93**, 076401 (2004);
   F. Verstraete, J. J. Garcia-Ripoll, and J. I. Cirac, *Phys. Rev. Lett.* 93, 207204 (2004).
6. U. Schollwöck, *Rev. Mod. Phys.*, **77**, 259–315 (2005).
7. C. N. Yang, *Phys. Rev. Lett.* **63**, 2144–2147 (1989).
8. E. Demler, W. Hanke, and S.-C. Zhang, *Rev. Mod. Phys.* **76** 909 (2004).
9. E. Demler, and S.-C. Zhang, *Phys. Rev. Lett.* **75**, 4126–4129 (1995).
10. S. A. Moskalenko and D. W. Snoke, *Bose-Einstein Condensation of Excitons and Biexcitons* (Cambridge University Press, Cambridge, 2000).
11. A. Kantian et al., in preparation.
12. J. D. Joannopoulos, R. D. Meade, and J. N. Winn, *Photonic Crystals: Molding the Flow of Light* Princeton University Press, Princeton, 1995.
13. P. J. Y. Louis, E. A. Ostrovskaya, C. M. Savage, and Yu. S. Kivshar, *Phys. Rev. A* **67**, 013602 (2003).
14. N. K. Efremidis, and D. N. Christodoulides, *Phys. Rev. A* **67**, 063608 (2003).
15. B. Eiermann, Th. Anker, M. Albiez, M. Taglieber, P. Treutlein, K.-P. Marzlin, and M. K. Oberthaler, *Phys. Rev. Lett.* **92**, 230401 (2004).
16. V. Ahufinger, A. Sanpera, P. Pedri, L. Santos, and M. Lewenstein, *Phys. Rev. A* **69**, 053604 (2004).
17. See, for example, P. D. Drummond, K. V. Kheruntsyan, and H. He, *J. Opt. B: Quant. Semiclass. Optics* **1**, 387–395 (1999); R. K. Bullough and M. Wadati, *J. Opt. B: Quant. Semiclass. Optics* **6**, S205– (2004); I. E. Mazets and G. Kurizki, *Europhysics Letters,* in press (2006).

Vol 441|15 June 2006|**doi:10.1038/nature04918**

nature

LETTERS

Repulsively bound atom pairs in an optical lattice

K. Winkler[1], G. Thalhammer[1], F. Lang[1], R. Grimm[1,3], J. Hecker Denschlag[1], A. J. Daley[2,3], A. Kantian[2,3], H. P. Büchler[2,3] & P. Zoller[2,3]

Throughout physics, stable composite objects are usually formed by way of attractive forces, which allow the constituents to lower their energy by binding together. Repulsive forces separate particles in free space. However, in a structured environment such as a periodic potential and in the absence of dissipation, stable composite objects can exist even for repulsive interactions. Here we report the observation of such an exotic bound state, which comprises a pair of ultracold rubidium atoms in an optical lattice. Consistent with our theoretical analysis, these repulsively bound pairs exhibit long lifetimes, even under conditions when they collide with one another. Signatures of the pairs are also recognized in the characteristic momentum distribution and through spectroscopic measurements. There is no analogue in traditional condensed matter systems of such repulsively bound pairs, owing to the presence of strong decay channels. Our results exemplify the strong correspondence between the optical lattice physics of ultracold bosonic atoms and the Bose–Hubbard model[1,2]—a link that is vital for future applications of these systems to the study of strongly correlated condensed matter and to quantum information.

Cold atoms loaded into a three-dimensional (3D) optical lattice provide a realization of a quantum lattice gas[1,2]. An optical lattice can be generated by pairs of counterpropagating laser beams, where the resulting standing wave intensity pattern forms a periodic array of microtraps for the cold atoms, with period a given by half the wavelength of the light, $\lambda/2$. The periodicity of the potential gives rise to a band structure for the atom dynamics with Bloch bands separated by bandgaps, which can be controlled by the laser parameters and beam configuration. The dynamics of ultracold atoms loaded into the lowest band of a sufficiently deep optical lattice is well described by the Bose–Hubbard model with hamiltonian[1,3]:

$$\hat{H} = -J\sum_{\langle i,j\rangle}\hat{b}_i^\dagger\hat{b}_j + \frac{U}{2}\sum_i \hat{n}_i(\hat{n}_i - 1) + \sum_i \varepsilon_i\hat{n}_i \qquad (1)$$

Here $\hat{b}_i$ ($\hat{b}_i{}^\dagger$) are destruction (creation) operators for the bosonic atoms at site i, and $\hat{n}_i = \hat{b}_i{}^\dagger\,\hat{b}_i$ is the corresponding number operator. $J/\hbar$ denotes the nearest-neighbour tunnelling rate, U the on-site collisional energy shift, and ε_i the background potential. The high degree of control available over the parameters in this system—for example, changing the relative values of U and J by varying the lattice depth, V_0—has led to seminal experiments on strongly correlated gases in optical lattices. These experiments include the study of the superfluid–Mott insulator transition[4], the realization of one-dimensional (1D) quantum liquids with atomic gases[5,6] (see also refs 7 and 8), and the investigation of disordered systems[9]. 3D optical lattices have also opened new avenues in cold collision physics and chemistry[10–13].

A striking prediction of the Bose–Hubbard hamiltonian (equation (1)) is the existence of stable repulsively bound atom pairs. These are most intuitively understood for strong repulsive interaction $|U| \gg J$, $U > 0$, where an example of such a pair is a state of two atoms occupying a single site, $|2_i\rangle \equiv (\hat{b}_i^{\dagger 2}|\mathrm{vac}\rangle)/\sqrt{2}$, where $|\mathrm{vac}\rangle$ is the vacuum state. This state has a potential energy offset U with respect to states where the atoms are separated (Fig. 1a). The pair is unable to decay by converting the potential energy into kinetic energy, as the Bloch band allows a maximum kinetic energy for two atoms given by $8J$, twice its width. The pair can move around the lattice, with both atoms tunnelling to a neighbouring site (Fig. 1b), but the atoms cannot move independently. The stability of repulsively bound pairs is intimately connected with the absence of dissipation, in contrast to solid state lattices, for example, where interactions with phonons typically lead to rapid relaxation.

We obtain experimental evidence for repulsively bound pairs with a sample of ultracold ^{87}Rb atoms in a cubic 3D optical lattice with lattice period $a = 415.22$ nm. The key tool used to prepare and observe the pairs is their adiabatic conversion into chemically

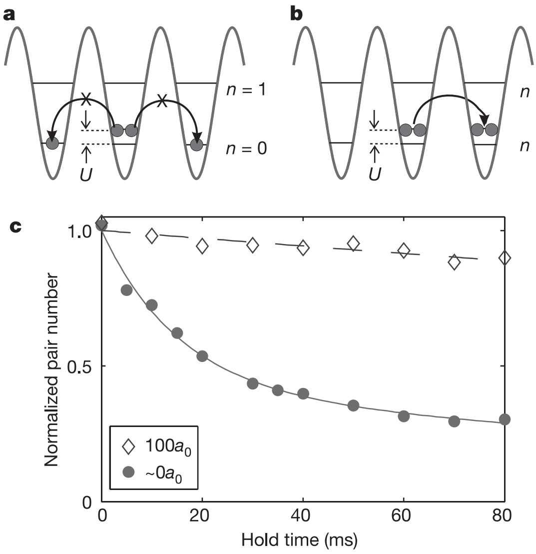

Figure 1 | Atom pairs in an optical lattice. **a**, Repulsive interaction (scattering length $a > 0$) between two atoms sharing a lattice site in the lowest band ($n = 0$) gives rise to an interaction energy U. Breaking up of the pair is suppressed owing to the lattice band structure and energy conservation. **b**, The pair is a composite object that can tunnel through the lattice. **c**, Long lifetime of repulsively bound atom pairs that are held in a 3D optical lattice. The potential depth is $(10 \pm 0.5)E_\mathrm{r}$ in one direction and $(35 \pm 1.5)E_\mathrm{r}$ in the perpendicular directions. Shown is the remaining fraction of pairs for a scattering length of $100a_0$ (open diamonds; a_0 is the Bohr radius) and a scattering length of about $(0 \pm 10)a_0$ (filled circles) as a function of the hold time. The lines are fitted curves of an exponential (dashed line) and the sum of two exponentials (solid line).

---

[1]Institute for Experimental Physics, [2]Institute for Theoretical Physics, University of Innsbruck, A-6020 Innsbruck, Austria. [3]Institute for Quantum Optics and Quantum Information of the Austrian Academy of Sciences, A-6020 Innsbruck, Austria.

© 2006 **Nature Publishing Group**

bound dimers using a magnetic-field sweep across a Feshbach resonance[13–20] at 1,007.40 G. The initial state is prepared from a pure sample of Rb_2 Feshbach molecules in the vibrational ground state of the lattice where each lattice site is occupied by not more than a single molecule (see Methods). Sweeping across the Feshbach resonance, we adiabatically dissociate the dimers and obtain a lattice correspondingly filled with 2×10^4 atom pairs, at an effective filling factor of typically 0.3. Away from the Feshbach resonance, the effective interaction between the atoms is repulsive with scattering length $a_s = +100a_0$ (where a_0 is the Bohr radius).

In order to demonstrate the stability of repulsively bound pairs, we lower the lattice potential in one direction from its initial depth of $V_0 = 35E_r$ (corresponding to $J/\hbar \approx 2\pi \times 0.7$ Hz and $U/J \approx 3{,}700$, where $E_r = 2\pi^2\hbar^2/m\lambda^2$ and m is the mass of the atoms) in 1 ms to a depth of $V_0 = 10E_r$. This increases dramatically the tunnelling rates along this direction to $J/\hbar \approx 2\pi \times 63$ Hz ($U/J \approx 30$), potentially allowing the atom pairs to quickly separate. After a variable hold time we determine the number of remaining pairs. This is done by adiabatically raising the lattice to its full initial depth of $V_0 = 35E_r$, and converting doubly occupied sites to Feshbach molecules with near unit efficiency[13]. A purification pulse[13] then removes all remaining atoms due to dissociated pairs. Afterwards the molecules are again converted back into atoms, and can then be detected by conventional absorption imaging.

The results of these lifetime measurements are shown in Fig. 1c. For repulsive interaction ($a_s = 100a_0$), the atom pair sample exhibits the remarkably long lifetime of 700 ms (exponential fit). This lifetime is mainly limited by inelastic scattering of lattice photons[13], and greatly exceeds the calculated time for an atom to tunnel from one site to the next, $2\pi\hbar/(4J) \approx 4$ ms. In contrast, if we turn off the on-site interaction by tuning the scattering length near zero, we observe a much faster decay in the number of doubly occupied sites owing to the rapid diffusion of unbound atoms through the lattice (Fig. 1c). This observation clearly demonstrates that the stability of the pairs is induced by the on-site interaction U.

We can more deeply understand these repulsively bound pairs through an exact solution of the two-particle Lippmann–Schwinger scattering equation based on the Bose–Hubbard model. We write the two-atom wavefunction as $\Psi(\mathbf{x}, \mathbf{y})$, where the positions of the two particles are denoted $\mathbf{x} = \Sigma_i x_i \mathbf{e}_i$ and $\mathbf{y} = \Sigma_i y_i \mathbf{e}_i$, with $\mathbf{e}_i$ being the primitive lattice vectors, and x_i, y_i integer numbers. Introducing centre of mass, $\mathbf{R} = (\mathbf{x} + \mathbf{y})/2$, and relative coordinates, $\mathbf{r} = \mathbf{x} - \mathbf{y}$, we can solve the Schrödinger equation with the ansatz $\Psi(\mathbf{x}, \mathbf{y}) = \exp(i\mathbf{KR})\psi_K(\mathbf{r})$, where $\mathbf{K}$ is the quasi-momentum of the centre of mass motion and $\psi_K(\mathbf{r})$ is the pair wavefunction. We derive two types of solutions (for details see Methods), each of which are eigenstates of $\mathbf{K}$. These states, as illustrated in Fig. 2a, correspond to (1) unbound scattering solutions (shaded area in Fig. 2a), where the two particles move on the lattice, and scatter from each other according to the interaction U, and (2) repulsively bound pairs for which $\psi_K(\mathbf{r})$ is square integrable. In one and two dimensions, states of repulsively bound pairs always exist for non-zero U, while in three dimensions they exist above a critical value $U_{\mathrm{crit}} \approx 0.5J$.

In this Letter, we focus primarily on the 1D situation, which in the experiment corresponds to a low depth of the lattice along one direction, whilst the lattice in the perpendicular directions remains very deep ($35E_r$). Here the energy of the bound pairs is $E(K) = 2J\left[\sqrt{4(\cos\frac{Ka}{2})^2 + (U/2J)^2} + 2\right]$. This is plotted in Fig. 2a as the Bloch band of a stable composite object above the continuum of two-particle scattering states. In the limit of strong interaction, $U \gg J$, this reduces to $E(K) \approx 4J + U + (4J^2/U)(1 + \cos Ka)$, which shows that the bound pairs indeed have binding energy of $\sim U$ and hop through the lattice with an effective tunnelling rate $J^2/(\hbar U)$.

Figure 2b shows the pair wavefunctions $\psi_K(r)$ for repulsively bound pairs ($a_s = 100a_0$) in one dimension with $K = 0$, for $U/J = 30$ ($V_0 \approx 10E_r$) and $U/J = 3$ ($V_0 \approx 3E_r$). For large U/J, bound pairs essentially consist of two atoms occupying the same site, whereas for small U/J, the pair is delocalized over several lattice sites. The corresponding quasi-momentum distribution can be found from the Fourier transform $\tilde{\psi}_0(k)$ of the pair wavefunction (Fig. 2c), where k is the relative quasi-momentum. Because $K = 0$, $|\tilde{\psi}_0(k)|^2$ is also equal to the single-particle quasi-momentum distribution. When the two particles are localized on the same site, the quasi-momentum distribution is essentially flat. However, for lower U/J the wavefunction is characteristically peaked at the edges of the Brillouin zone. This occurs because the energy of the repulsively bound state is above that of the continuum, and thus the contribution to the corresponding wavepacket of single-particle quasi-momentum states with higher energy is favoured. In contrast, if we had $U < 0$, the pair would be attractively bound, and would have energy lower than that in the continuum. Thus contributions from the low-energy quasi-momentum states would be favoured, leading to a single peak in the centre of the Brillouin zone. In both cases, the amplitude of the peaks grows with increasing width $4J$ of the Bloch band. In general, the stable bound pairs will not be prepared in a fixed quasi-momentum state K in an experiment, but rather in a superposition of different momentum states. For non-zero K, the peaks in the single-particle quasi-momentum distribution are translated by K, but their strength is also reduced. As a consequence, for typical symmetric distributions of K, the peak at the edge of the Brillouin zone remains present, but is less strong than in the optimal case of vanishing K. We have verified this using many-body numerical simulations, which were performed using time-dependent density-matrix renormalization group methods[21–23].

We have experimentally investigated the quasi-momentum distribution of the pairs in various regimes by mapping it onto a spatial distribution, which we measured using standard absorption imaging. For this, we first adiabatically lower the lattice depth in the X

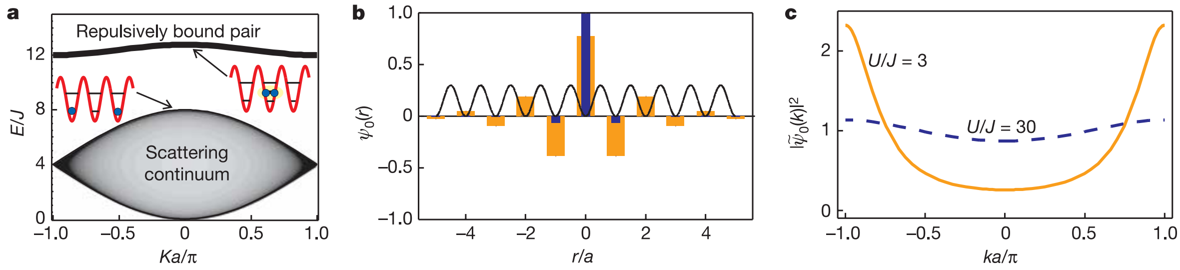

Figure 2 | Atom pair states in one dimension. **a**, Spectrum of energy E of the 1D hamiltonian for $U/J = 8$ ($V_0 \approx 6E_r$) as a function of centre of mass quasi-momentum K. The Bloch band for repulsively bound pairs is located above the continuum of unbound states. The grey level for the shading of the continuum is proportional to the density of states. **b**, The pair wavefunction $\psi_0(r)$, showing the amplitude at each site with $U/J = 30$ ($V_0 \approx 10E_r$, blue bars) and $U/J = 3$ ($V_0 \approx 3E_r$, orange bars). **c**, The square modulus of the corresponding momentum space wavefunctions $|\tilde{\psi}_0(k)|^2$, which are equivalent to the single-particle momentum distributions, as $K = 0$. Note the characteristic peaks at the edge of the Brillouin zone.

© 2006 Nature Publishing Group

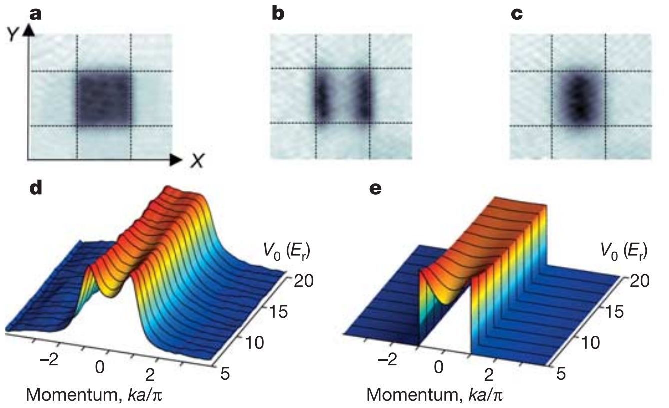

Figure 3 | **Quasi-momentum distribution of atoms in the lattice.** **a**–**c**, Absorption images of the atomic distribution after release from the 3D lattice and a subsequent 15-ms time of flight. The horizontal and vertical black lines enclose the first Brillouin zone. **a**, Distribution when lattice sites are occupied by single atoms; **b**, distribution for repulsively bound atom pairs (see text for details); **c**, same as **b** but pairs are attractively bound. **d**, **e**, The quasi-momentum distribution for pairs in the X direction as a function of lattice depth V_0, after integration over the Y direction. **d**, Experiment; **e**, numerical calculation. See Methods for a definition of E_r.

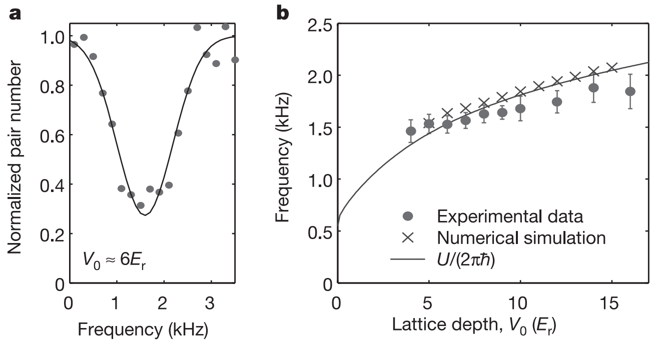

Figure 4 | **Modulation spectroscopy of repulsively bound pairs.** **a**, Typical resonance dip showing the remaining number of atom pairs as a function of the modulation frequency, for $V_0 \approx 6E_r$. The solid line is a gaussian fit, a choice that was justified by numerical calculations. **b**, Plot showing the measured resonance frequencies (filled circles) as a function of the lattice depth. They show good agreement with numerical simulations (crosses) and also coincide with the on-site collisional energy shift U (line). Experimental error bars correspond to the 95% confidence interval for the gaussian fit parameters of the resonance dips.

direction (Fig. 3a) at a rate of $1.3E_r$ (ms^{-1}) to a pre-chosen height while the lattice depth in the other two directions is kept high ($35E_r$). This will prepare repulsively bound pairs at the chosen lattice depth. We then turn off the lattice rapidly enough for the pair wavefunction not to change, but slowly with respect to the bandgap, so that single-particle quasi-momenta are mapped to real momenta[24,25]. We have typically employed linear ramps with rates of $0.2E_r\,\mu\text{s}^{-1}$. The resulting momentum distribution is converted to a spatial distribution after ~15 ms time of flight.

Figure 3a–c shows typical measured quasi-momentum distributions that were obtained after adiabatically lowering the lattice depth in the X direction to the lowest values, below $3E_r$. If only empty sites and sites with single atoms are present in the lattice, then the first Brillouin zone is homogeneously filled[24] (Fig. 3a). For repulsively bound pairs, the momentum distribution is, in general, peaked at the edges of the first Brillouin zone (Fig. 3b), whereas for attractively bound pairs, it is peaked in the centre of the first Brillouin zone (Fig. 3c). In order to change the interaction between the atoms from repulsive to attractive, we change the scattering length, making use of the Feshbach resonance[26] at 1,007.40 G. Figure 3d and e shows the dependence on lattice depth V_0 of the single-particle quasi-momentum distribution for repulsively bound pairs from experiment and numerical simulation, respectively. As expected, the peak structure is more pronounced for lower values of V_0, and diminishes for larger V_0. This characteristic is a clear signature of the pair wavefunction for repulsively bound pairs.

We also performed spectroscopic measurements, determining the binding energy from pair dissociation produced by modulating the depth of the lattice at a chosen frequency. On resonance, the modulation allows pairs to release their binding energy. Figure 4a shows the number of remaining pairs as a function of the modulation frequency. This was repeated for a variety of lattice depths V_0 in one direction while keeping the lattice in the other two directions at $35E_r$. The behaviour of the binding energy as a function of the lattice depth provides an additional key signature of repulsively bound pairs. As shown in Fig. 4b, the resonance positions are in good agreement with numerical simulations and essentially coincide with the interaction energy, U.

It is important to note that for sufficiently large U/J, repulsively bound pairs are stable under collisions with each other. This is particularly evident in the limit $U \gg J$ where, by energy arguments, the elastic scattering between pairs is the only open channel. This means that even a relatively dense quantum lattice gas of these objects can be long-lived. When the lattice height is lowered so that U/J becomes sufficiently small, it is possible for a certain fraction of the pairs to dissociate by collision with other pairs. In our experiments, we observe the onset of this behaviour for lattice depths lower than $6E_r$, that is, $U/J \approx 9$. The dynamics of the collisions and details of the decay depend crucially on lattice depth and the local density of pairs across the lattice. Further details of these processes will be discussed elsewhere.

In conclusion, we have demonstrated the formation of a novel composite object in an optical lattice: a stable bound state that arises from the lattice band structure and repulsion between the constituents. Although no direct analogue to repulsively bound atomic pairs is known to exist, the formation of a metastable state is reminiscent of trapping light in photonic bandgap materials[27], or extended lifetimes of excited atoms in cavity quantum electrodynamics[28]. In both cases, decay is suppressed by restriction of the accessible light field modes. Stable repulsively bound objects should be viewed as a general phenomenon, and their existence will be ubiquitous in cold atom lattice physics. They also give rise to new potential composites with fermions[29] or Bose–Fermi mixtures[30], and can be formed in an analogous manner with more than two particles. The stability of repulsively bound objects could thus be the basis of a wealth of new quantum many-body states or phases. In particular, the next experimental step in investigating repulsively bound atomic pairs is the possible realization of a condensate of pairs, together with the means to characterise long-range order in this system.

METHODS

Preparation of pure molecular sample. We use a set-up which was described in detail in ref. 13, starting with a Bose–Einstein condensate of 6×10^5 ^{87}Rb atoms in an Ioffe-type magnetic trap with trap frequencies $\omega_{x,y,z} = 2\pi \times (7, 19, 20)$ Hz). Within 100 ms the Bose–Einstein condensate is adiabatically loaded into the cubic 3D optical lattice which is $35E_r$ deep. After turning off the magnetic trap, we flip the spins of our atoms from their initial state $|F = 1, m_F = -1\rangle$ to $|F = 1, m_F = +1\rangle$ by suddenly reversing the bias magnetic field of a few gauss. This spin state features a 210-mG-wide Feshbach resonance at 1,007.40 G (ref. 26). By adiabatically ramping over this resonance we convert pairs of atoms in multiply occupied lattice sites into Rb$_2$ Feshbach molecules. Fast inelastic collisions of molecules within lattice sites and a subsequent combined radio-frequency and optical purification pulse remove all chemically unbound atoms, thus creating a pure molecular sample of about 2×10^4 molecules.

Exact solution for single pair bound state. Within the Bose–Hubbard model (equation (1)), the Schrödinger equation describing two particles in a

© 2006 Nature Publishing Group

homogenous optical lattice takes the form

$$\left[-J\left(\tilde{\Delta}_{\mathbf{x}}^{0}+\tilde{\Delta}_{\mathbf{y}}^{0}\right)+U\delta_{\mathbf{x},\mathbf{y}}\right]\Psi(\mathbf{x},\mathbf{y})=E\Psi(\mathbf{x},\mathbf{y}) \tag{2}$$

where the vectors **x** and **y** describe the positions of the two particles as defined in the main text. The operator $\tilde{\Delta}_{\mathbf{x}}^{\mathbf{K}}\Psi(\mathbf{x})=\sum_{i=1}^{d}\cos(\mathbf{K}\mathbf{e}_i/2)[\Psi(\mathbf{x}+\mathbf{e}_i)+\Psi(\mathbf{x}-\mathbf{e}_i)-2\Psi(\mathbf{x})]$ denotes the discrete lattice laplacian with d the dimensionality in the cubic lattice, and $\delta_{\mathbf{x},\mathbf{y}}$ is a Kronecker delta. Writing the wavefunction in relative and centre of mass coordinates $\Psi(\mathbf{x},\ \mathbf{y})=\exp(i\mathbf{K}\mathbf{R})\psi_K(\mathbf{r})$, the Schrödinger equation (2) then reduces to a single-particle problem in the relative coordinate

$$\left[-2J\tilde{\Delta}_{\mathbf{r}}^{\mathbf{K}}+E_{\mathbf{K}}+U\delta_{\mathbf{r},0}\right]\psi_K(\mathbf{r})=E\psi_K(\mathbf{r}) \tag{3}$$

with $E_{\mathbf{K}}=4J\Sigma_i[1-\cos(\mathbf{K}\mathbf{e}_i/2)]$ being the kinetic energy of the centre of mass motion.

The short range character of the interaction potential allows for a resummation of the perturbation expansion generated by the corresponding Lippmann–Schwinger equation. We obtain the scattering states

$$\psi^{(+)}(\mathbf{r})=\exp(i\mathbf{k}\mathbf{r})-8\pi Jf_E(\mathbf{K})G_{\mathbf{K}}(E,\mathbf{r}) \tag{4}$$

with scattering amplitude

$$f_E(\mathbf{K})=-\frac{1}{4\pi}\frac{U/(2J)}{1-G_K(E,0)U} \tag{5}$$

where the total energy $E=\varepsilon_{\mathbf{k},\mathbf{K}}+E_{\mathbf{K}}$, and $\varepsilon_{\mathbf{k},\mathbf{K}}=4J\Sigma_i\cos(\mathbf{K}\mathbf{e}_i/2)[1-\cos(\mathbf{k}\mathbf{e}_i)]$. Furthermore, $G_{\mathbf{K}}(E,\ \mathbf{r})$ denotes the Green's function of the non-interacting problem, which in Fourier space takes the form $\tilde{G}_{\mathbf{K}}(E,\mathbf{k})=1/(E-\varepsilon_{\mathbf{k},\mathbf{K}}+i\eta)$.

The energy spectrum for these states in one dimension is shown as a function of K by the shaded region in Fig. 2a. In addition, the pole in the scattering amplitude indicates the presence of an additional bound state. The energy E_{bs} of the bound state is determined by $G_{\mathbf{K}}(E_{\mathrm{bs}},0)U=1$ and the bound state wavefunction takes the form $\psi^{\mathrm{bs}}(\mathbf{r})=cG_{\mathbf{K}}(E_{\mathrm{bs}},\mathbf{r})$, with c being a normalization factor.

Received 1 April; accepted 18 May 2006.

1. Jaksch, D. & Zoller, P. The cold atom Hubbard toolbox. *Ann. Phys.* **315,** 52–79 (2005).
2. Bloch, I. Ultracold quantum gases in optical lattices. *Nature Phys.* **1,** 23–30 (2005).
3. Fisher, M. P. A., Weichman, P. B., Grinstein, G. & Fisher, D. S. Boson localization and the superfluid insulator transition. *Phys. Rev. B.* **40,** 546–570 (1989).
4. Greiner, M., Mandel, O., Esslinger, T., Hänsch, T. W. & Bloch, I. Quantum phase transition from a superfluid to a Mott insulator in a gas of ultracold atoms. *Nature* **415,** 39–44 (2002).
5. Paredes, B. *et al.* Tonks–Girardeau gas of ultracold atoms in an optical lattice. *Nature* **429,** 277–281 (2004).
6. Stöferle, T., Moritz, H., Schori, C., Köhl, M. & Esslinger, T. Transition from a strongly interacting 1D superfluid to a Mott insulator. *Phys. Rev. Lett.* **92,** 130403 (2004).
7. Kinoshita, T., Wenger, T. & Weiss, D. S. Observation of a one-dimensional Tonks-Girardeau gas. *Science* **305,** 1125–1128 (2004).
8. Laburthe Tolra, B. *et al.* Observation of reduced three-body recombination in a correlated 1D degenerate Bose gas. *Phys. Rev. Lett.* **92,** 190401 (2004).
9. Fallani, L., Lye, J. E., Guarrera, V., Fort, C. & Inguscio, M. Onset of a Bose-glass of ultra-cold atoms in a disordered crystal of light. Preprint at ⟨http://arxiv.org/abs/cond-mat/0603655⟩ (2006).
10. Fedichev, P. O., Bijlsma, M. J. & Zoller, P. Extended molecules and geometric scattering resonances in optical lattices. *Phys. Rev. Lett.* **92,** 080401 (2004).
11. Ryu, C. *et al.* Raman-induced oscillation between an atomic and a molecular quantum gas. Preprint at ⟨http://arxiv.org/abs/cond-mat/0508201⟩ (2005).
12. Stöferle, T., Moritz, H., Günter, K., Köhl, M. & Esslinger, T. Molecules of fermionic atoms in an optical lattice. *Phys. Rev. Lett.* **96,** 030401 (2006).
13. Thalhammer, G. *et al.* Long-lived Feshbach molecules in a 3D optical lattice. *Phys. Rev. Lett.* **96,** 050402 (2006).
14. Donley, E. A., Claussen, N. R., Thompson, S. T. & Wieman, C. E. Atom–molecule coherence in a Bose–Einstein condensate. *Nature* **417,** 529–533 (2002).
15. Regal, C. A., Ticknor, C., Bohn, J. L. & Jin, D. S. Creation of ultracold molecules from a Fermi gas of atoms. *Nature* **424,** 47–50 (2003).
16. Herbig, J. *et al.* Preparation of a pure molecular quantum gas. *Science* **301,** 1510–1513 (2003).
17. Xu, K. *et al.* Formation of quantum-degenerate sodium molecules. *Phys. Rev. Lett.* **91,** 210402 (2003).
18. Cubizolles, J., Bourdel, T., Kokkelmans, S. J. J. M. F., Shlyapnikov, G. V. & Salomon, C. Production of long-lived ultracold Li_2 molecules from a Fermi gas. *Phys. Rev. Lett.* **91,** 240401 (2003).
19. Dürr, S., Volz, T., Marte, A. & Rempe, G. Observation of molecules produced from a Bose-Einstein condensate. *Phys. Rev. Lett.* **92,** 020406 (2004).
20. Koehler, T., Goral, K. & Julienne, P. S. Production of cold molecules via magnetically tunable Feshbach resonances. Preprint at ⟨http://arxiv.org/abs/cond-mat/0601420⟩ (2006).
21. Vidal, G. Efficient classical simulation of slightly entangled quantum computations. *Phys. Rev. Lett.* **91,** 147902 (2003).
22. Daley, A. J., Kollath, C., Schollwöck, U. & Vidal, G. Time-dependent density-matrix renormalization-group using adaptive effective Hilbert spaces. *J. Stat. Mech. Theor. Exp.* P04005 (2004).
23. White, S. R. & Feiguin, A. E. Real-time evolution using the density matrix renormalization group. *Phys. Rev. Lett.* **93,** 076401 (2004).
24. Greiner, M., Bloch, I., Mandel, O., Hänsch, T. W. & Esslinger, T. Exploring phase coherence in a 2D lattice of Bose-Einstein condensates. *Phys. Rev. Lett.* **87,** 160405 (2001).
25. Hecker Denschlag, J. *et al.* A Bose-Einstein condensate in an optical lattice. *J. Phys. B.* **35,** 3095–3110 (2002).
26. Volz, T., Dürr, S., Ernst, S., Marte, A. & Rempe, G. Characterization of elastic scattering near a Feshbach resonance in ^{87}Rb. *Phys. Rev. A* **68,** 010702 (2003).
27. Joannopoulos, J. D., Meade, R. D. & Winn, J. N. *Photonic Crystals: Molding the Flow of Light* (Princeton Univ. Press, Princeton, 1995).
28. Berman, P. (ed.) *Cavity Quantum Electrodynamics* (Academic, New York, 1994).
29. Hofstetter, W., Cirac, J. I., Zoller, P., Demler, E. & Lukin, M. D. High-temperature superfluidity of fermionic atoms in optical lattices. *Phys. Rev. Lett.* **89,** 220407 (2002).
30. Lewenstein, M., Santos, L., Baranov, M. A. & Fehrmann, H. Atomic Bose-Fermi mixtures in an optical lattice. *Phys. Rev. Lett.* **92,** 050401 (2004).

Acknowledgements We thank H. Ritsch for discussions, and M. Theis and S. Schmid for help in setting up the experiment. We acknowledge support from the Austrian Science Fund (FWF) within the Spezialforschungsbereich 15, from the European Union within the OLAQUI and SCALA networks, from the TMR network 'Cold Molecules', and from the Tiroler Zukunftsstiftung.

Author Contributions This work is a collaboration between teams of experimental (K.W., G.T., F.L., R.G. and J.H.D.) and theoretical (A.J.D., A.K., H.P.B. and P.Z.) physicists.

Author Information Reprints and permissions information is available at npg.nature.com/reprintsandpermissions. The authors declare no competing financial interests. Correspondence and requests for materials should be addressed to J.H.D. (Johannes.Denschlag@uibk.ac.at).

© 2006 Nature Publishing Group

New Journal of Physics
The open–access journal for physics

Long distance transport of ultracold atoms using a 1D optical lattice

Stefan Schmid, Gregor Thalhammer, Klaus Winkler,
Florian Lang and Johannes Hecker Denschlag
Institut für Experimentalphysik, Universität Innsbruck, Technikerstraße 25,
6020 Innsbruck, Austria
E-mail: johannes.denschlag@uibk.ac.at

New Journal of Physics **8** (2006) 159
Received 30 May 2006
Published 30 August 2006
Online at http://www.njp.org/
doi:10.1088/1367-2630/8/8/159

Abstract. We study the horizontal transport of ultracold atoms over macroscopic distances of up to 20 cm with a moving 1D optical lattice. By using an optical Bessel beam to form the optical lattice, we can achieve nearly homogeneous trapping conditions over the full transport length, which is crucial in order to hold the atoms against gravity for such a wide range. Fast transport velocities of up to 6 m s^{-1} (corresponding to about 1100 photon recoils) and accelerations of up to 2600 m s^{-2} are reached. Even at high velocities the momentum of the atoms is precisely defined with an uncertainty of less than one photon recoil. This allows for construction of an atom catapult with high kinetic energy resolution, which might have applications in novel collision experiments.

Contents

© IOP Publishing Ltd and Deutsche Physikalische Gesellschaft

1. Introduction

Fast, large-distance transport of Bose–Einstein condensates (BEC) from their place of production to other locations is of central interest in the field of ultracold atoms. It allows for exposure of BECs to all different kinds of environments, spawning progress in BEC manipulation and probing.

Transport of cold atoms has already been explored in various approaches using magnetic and optical fields. Magnetic fields have been used to shift atoms, e.g. on atom chips (for a review see [1]) and to move laser-cooled clouds of atoms over macroscopic distances of tens of centimetres, e.g. [2, 3]. By changing the position of an optical dipole trap, a BEC has been transferred over distances of about 40 cm within several seconds [4]. This approach consisted of mechanically relocating the focusing lens of the dipole trap with a large translation stage. A moving optical lattice offers another interesting possibility to transport ultracold atoms. Acceleration of atoms with lattices is intimately connected to the techniques of Raman transitions [5], STIRAP [6, 7] and the phenomenon of Bloch oscillations [8, 9]; (for a recent review on atoms in optical lattices see [10]). Acceleration with optical lattices allows for precise momentum transfer in multiples of two photon recoils to the atoms. Transport of single, laser-cooled atoms in a deep optical lattice over short distances of several mm has been reported in [11]. Coherent transport of atoms over several lattice sites has been described in [12]. Even beyond the field of ultracold atoms, applications of optical lattices for transport are of interest, e.g. to relocate submicron sized polystyrene spheres immersed in heavy water [13].

Here, we experimentally investigate transporting BECs and ultracold thermal samples with an optical lattice over macroscopic distances of tens of centimetres. Our method features the combination of the following important characteristics. The transport of the atoms is in the quantum regime, where all atoms are in the vibrational ground state of the lattice. With our setup, mechanical noise is avoided and we achieve precise positioning (on the order of the imaging resolution of 1 μm). We demonstrate high transport velocities of up to 6 m s^{-1}, which are accurately controlled on the quantum level. The velocity spread of the atoms is not more than 2 mm s^{-1}, corresponding to 1/3 of a photon recoil.

2. Basic principle of transport

Horizontal transport of atoms over larger distances holds two challenges: how to move the atoms and how to support them against gravity. Our approach here is to use a special 1D optical lattice trap, which is formed by a Bessel laser beam and a counterpropagating Gaussian beam. The lattice part of the trap moves the atoms axially, whereas the Bessel beam leads to radial confinement holding the atoms against gravity.

In brief, lattice transport works like this. We first load the atoms into a 1D optical lattice, which in general is a standing wave interference pattern of two counterpropagating laser beams far red-detuned from the atomic resonance line (see figure 1). Afterwards the optical lattice is carefully moved, ‘dragging’ along the atoms. Upon arrival at the destination, the atoms are released from the lattice.

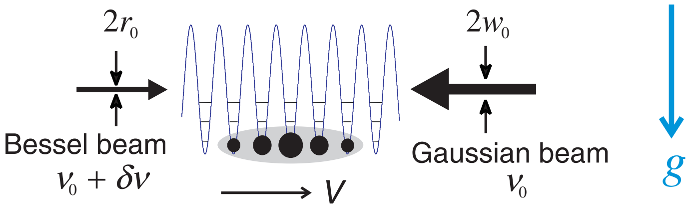

Figure 1. Scheme for atom transport. Two counterpropagating laser beams form a standing wave dipole trap. A BEC is loaded adiabatically into the vibrational ground state of this 1D optical lattice. A relative frequency detuning $\Delta\nu$ between the two laser beams results in a lattice motion at a velocity $v = \Delta\nu \cdot \lambda/2$ which drags along the trapped atoms. We chose the counterpropagating laser beams to consist of a Gaussian beam with diameter $2w_0$ and a Bessel beam with a central spot diameter of $2r_0$. The (in principle) diffraction-free propagation of the Bessel beam leads to tight radial confinement of the atoms over long distances, which supports the atoms against gravity during horizontal transport.

The lattice motion is induced by dynamically changing the relative frequency detuning $\Delta\nu$ of the two laser beams, which corresponds to a lattice velocity

$$v = \frac{\lambda}{2}\Delta\nu, \tag{1}$$

where λ is the laser wavelength of the lattice.

In comparison to the classical notion of simply 'dragging' along the atoms in the lattice, atom transport is more subtle on the quantum level. Here, only momenta in multiples of two photon recoil momenta, $2\hbar k = 4\pi\hbar/\lambda$ can be transferred to the atoms. This quantized momentum transfer can be understood in several ways, e.g. based on stimulated Raman transitions or based on the concept of Bloch-like oscillations in lattice potentials. For a more thorough discussion in this context, the reader is referred to [14].

In order to prevent the atoms from falling in the gravitational field, the lattice has to act as an optical dipole trap in the radial direction. It turns out that for radial trapping, optical lattices formed by Bessel beams have a clear advantage over Gaussian beam lattices. To make this point clear, we now show, that a standard optical lattice based on Gaussian beams is not well suited for long distance transports on the order of 50 cm. During transport, we require the maximum radial confining force $F_{\max}$ to be larger than gravity mg, where m is the atomic mass and $g \approx 9.81\ \mathrm{m\,s^{-2}}$ is the acceleration due to gravity. For a Gaussian beam this is

$$F_{\max} = \frac{3}{4\pi^3\sqrt{\mathrm{e}}}\frac{\lambda^3}{c}\frac{\Gamma}{\Delta}\frac{P_0}{w(z)^3} > mg, \tag{2}$$

where Γ is the natural linewidth of the relevant atomic transition, Δ the detuning from this transition, $w(z)$ the beam radius and P_0 the total power of the beam. The strong dependence on the beam radius $w(z)$ suggests, that $w(z) = w_0\sqrt{1 + (z/z_{\mathrm{R}})^2}$ should not vary too much over the transport distance. If we thus require the Rayleigh range $z_{\mathrm{R}} = \pi w_0^2/\lambda$ to equal the distance of 25 cm, the waist has to be $w_0 \approx 260\ \mu\mathrm{m}$. For a lattice beam wavelength of e.g. $\lambda = 830\ \mathrm{nm}$, the detuning from the D-lines of ^{87}Rb is $\Delta \approx 2\pi \times 130\ \mathrm{THz}$. To hold the atoms against gravity for

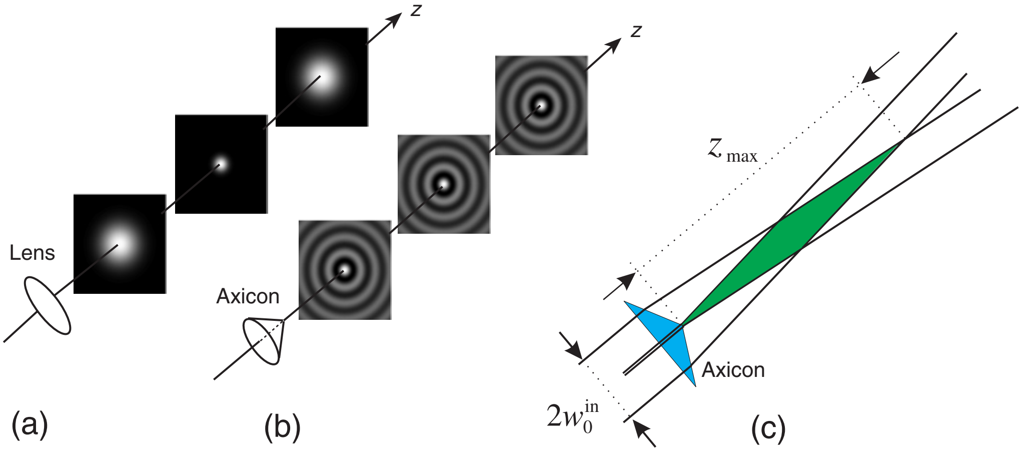

Figure 2. Gaussian and Bessel beams. (a) The radial intensity distribution of a Gaussian beam changes as it propagates. The smaller the waist w_0 of the beam, the higher its divergence (for a given wavelength). (b) Bessel beam: the radial distribution and in particular the radius of the central spot r_0 do not change with z (see equation (8)). (c) Within a certain axial range $z_{\max}$ a Bessel-like beam can be produced by illuminating an axicon lens with a collimated laser beam.

all z, where $|z| < z_R$, a total laser power of $P_0 \approx 10\,\mathrm{W}$ is needed, which is difficult to produce. In addition, the spontaneous photon scattering rate

$$\Gamma_{\mathrm{scatt}} = \frac{3}{8\pi^3\hbar}\frac{\lambda^3}{c}\left(\frac{\Gamma}{\Delta}\right)^2\frac{P_0}{w(z)^2} \qquad (3)$$

would reach values on the order of $\Gamma_{\mathrm{scatt}} = 2\,\mathrm{s}^{-1}$. For typical transport times of 200 ms, this means substantial heating and atomic losses.

A better choice for transport are zero order Bessel beams (figure 2). They exhibit an intensity pattern which consists of an inner intensity spot surrounded by concentric rings and which does *not* change during propagation. In our experiments, we have formed a standing light wave by interfering a Bessel beam with a counterpropagating Gaussian beam, giving rise to an optical lattice which is radially modulated according to the Bessel beam.[1] Atoms loaded into the tightly confined inner spot of the Bessel beam can be held against gravity for moderate light intensities, which minimizes the spontaneous photon scattering rate. In comparison to the transport with a Gaussian beam, the scattering rate in a Bessel beam transport can be kept as low as $0.05\,\mathrm{s}^{-1}$ by using the beam parameters of our experiment.

3. Bessel beams

Bessel beams are a solution of the Helmholtz equation and were first discussed and experimentally investigated about two decades ago [15, 16].

---

[1] In principle, one could also use a pure Bessel lattice (produced by two counterpropagating Bessel beams) for transport. This would improve radial confinement, however, alignment is more involved.

In cylindrical coordinates, the electric field distribution of a Bessel beam of order l is given by

$$E(r,\varphi,z) = E_0\,\mathrm{e}^{\mathrm{i}\beta z}\,\mathrm{e}^{\mathrm{i}l\varphi}\,J_l(\alpha r), \tag{4}$$

where $J_l(\alpha r)$ is the Bessel function of the first kind with integer order l. The beam is characterized by the parameters α and β. In the following, we restrict the discussion to order $l = 0$ which we have used in the experiment. By taking the absolute square of this expression, one gets the intensity distribution given by

$$I(r,z) = I_0 J_0^2(\alpha r), \tag{5}$$

where α determines the radius r_0 of the central spot via the first zero crossing of $J_0(\alpha r)$

$$r_0 \approx \frac{4.81}{2\alpha}. \tag{6}$$

As pointed out before, r_0 and I_0 do not change with the axial position z. Because of this axial independence, the Bessel beams are said to be 'diffraction-free'.

Bessel-like beams were realized experimentally for the first time by illuminating a circular slit [16]. Since this method is very inefficient, two other ways are common now-a-days. To generate Bessel beams of arbitrary order, holographic elements, such as phase-gratings, are used [17]. In our setup, we use a zero order Bessel beam, which can be produced efficiently by simply illuminating an axicon (conical lens) with a collimated laser beam [18]. How this comes about can be understood by looking at the Fourier transform of the Bessel field

$$\widetilde{E}(k_\perp,\varphi_k,k_z) = \int \mathrm{d}^3 r E(r,\varphi,z)\mathrm{e}^{-\mathrm{i}k_\perp r\cos(\varphi-\varphi_k)}\mathrm{e}^{-\mathrm{i}k_z z} \propto \mathrm{e}^{\mathrm{i}l\varphi_k}\delta(k_z-\beta)\delta(k_\perp-\alpha). \tag{7}$$

Thus a Bessel beam is a superposition of plane waves with $(k_\perp, k_z) = (\alpha, \beta)$. The **k**-vectors of the plane waves all have the same magnitude $|\mathbf{k}| = k = 2\pi/\lambda = \sqrt{\alpha^2+\beta^2}$ and they are forming a cone with radius $k_\perp$ and height k_z. Using an axicon with apex angle δ and index of refraction n, α and β are given by

$$\alpha = \frac{\pi(n-1)}{2\lambda\tan\delta/2} \tag{8}$$

and

$$\beta = \sqrt{k^2-\alpha^2}. \tag{9}$$

These experimentally produced Bessel beams are not ideal in the sense that their range $z_{\max} = kw_0^{\mathrm{in}}/\alpha$ is limited by the finite size (waist w_0^{in}) of the beam impinging on the axicon lens (see figure 2(c)). Also, the intensity of the Bessel beams might not be independent of the axial coordinate z, as it is also determined by the radial intensity distribution of the impinging beam (e.g. see figure 4(b)).

4. Experimental setup

We work with a ^{87}Rb-BEC in the internal state $|F = 1, m_F = -1\rangle$, initially held in a Ioffe-type magnetic trap with trap frequencies of $2\pi\nu_{x,y,z} = 2\pi$ (7, 19 and 20 Hz) [19, 20]. From the magnetic trap, the condensate is adiabatically loaded in about 100 ms into the inner core of the 1D optical lattice formed by a Bessel beam of central spot radius $r_0 = 36\,\mu$m and a counterpropagating Gaussian beam with a waist of $w_0 = 85\,\mu$m. About 70 lattice sites are occupied with atoms in the vibrational ground state. The lattice periodicity is 415 nm, corresponding to the laser wavelength of 830 nm. For our geometry (see below) the total power needed for the Bessel beam to support the atoms against gravity is typically 200 mW, since only a few per cent ($\approx$10 mW) of the total power are stored in the central spot. For the Gaussian beam, a power of roughly 20 mW is chosen, leading to an optical trapping potential at the centre ($r = 0$) of $U(z) = -U_0 + U_{\mathrm{latt}} \sin^2(kz)$, where the lattice depth (effective axial trap depth) is $U_{\mathrm{latt}} \approx 10E_{\mathrm{r}}$ and the total trap depth $U_0 \approx 11E_{\mathrm{r}}$. Here, $E_{\mathrm{r}} = (\hbar k)^2/(2m)$ is the recoil energy.

The corresponding trap frequencies are $\nu_\perp = 4.81\sqrt{U_0/(8mr_0^2)}/(2\pi) = 97$ Hz in the radial direction and $\nu_z = k\sqrt{2U_{\mathrm{latt}}/m}/(2\pi) = 21$ kHz in the axial direction. In order to better analyse the transport properties, we mostly perform round trips, where the atoms are first moved to a distance D and then back to their initial spot, which lies in the field of vision of our CCD camera. Once back, the atoms are adiabatically reloaded into the Ioffe-type magnetic trap. To obtain the resulting atomic momentum distribution, a standard absorption imaging picture is taken after sudden release from the magnetic trap and typically 12 ms of time-of-flight.

The lattice beams for the optical lattice are derived from a Ti:Sapphire-laser operating at 830 nm. The light is split into two beams, each of which is controlled in amplitude, phase and frequency with an acousto-optical modulator (AOM). For both AOMs, the radio-frequency (RF) driver consists of a home-built 300 MHz programmable frequency generator, which gives us full control over amplitude, frequency and phase of the radio-wave at any instant of time. The frequency generator is based on an AD9854 digital synthesizer chip from Analogue Devices and a 8-bit micro-controller ATmega162 from Atmel, on which the desired frequency ramps are stored and from which they are sent to the AD9854 upon request. After passing the AOMs, the two laser beams are mode-cleaned in single-mode fibres and converted into collimated Gaussian beams. One of the Gaussian beams passes the axicon lens (apex angle = 178°, radius = 25.4 mm, Del Mar Photonics) with a waist of $w_0^{\mathrm{in}} = 2$ mm, producing the Bessel beam. From there the beam propagates towards the condensate, which—before transport—is located 5 cm away.

5. Transport of ultracold atoms

Figure 3 shows results of a first experiment, where we have transported atoms over short distances of up to 1 mm (round trip), so that they never leave the field of view of the camera. The atoms move perpendicularly to the direction of observation. *In situ* images of the atomic cloud in the optical lattice are taken at various times during transport and the centre of mass position of the cloud is determined. As is clear from figure 3(a), we find very good agreement between the expected and the measured position of the atoms. In figures 3(b) and (c), calculations are shown for the corresponding velocity $v(t)$ and acceleration $a(t)$ of the optical lattice, respectively. As discussed before (see equation (1)), the velocity v of the lattice translates directly into a relative detuning $\Delta\nu$ of the laser beam, which we control via the AOMs. In order to suppress unwanted heating and losses of atoms during transport, we have chosen very smooth frequency ramps $\Delta\nu(t)$ such that the acceleration is described by a cubic spline interpolation curve which is continuously differentiable (details are given in the appendix). In this way, also the derivative of the acceleration (commonly called the jerk) is kept small.

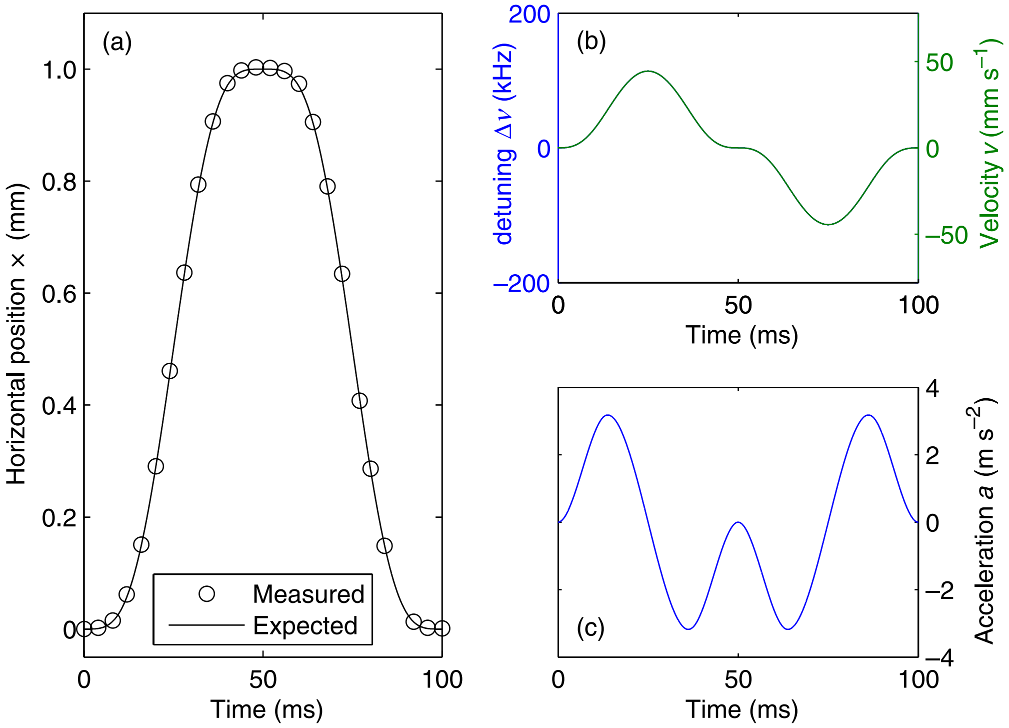

Figure 3. (a) Position, (b) velocity and (c) acceleration of the atomic cloud as a function of time for a typical transport sequence, here a round-trip over a short distance of 1 mm. Piecewise defined cubic polynomials are used for the acceleration ramp (see appendix for an analytical expression). By integrating over time, velocity and position are obtained. The frequency detuning $\Delta\nu$, which is used to program the RF synthesizers, corresponds directly to the velocity v via equation (1). The position ramp is compared with *in situ* measurements of the cloud's position (○).

In the next set of experiments, we extended the atomic transport to more macroscopic distances of up to 20 cm (40 cm round trip), where we moved the atoms basically from one end of the vacuum chamber to the other and back. However, the transport distance was always limited by the finite range z_{max} of the Bessel beam (see figures 2(c) and 4). As shown in figure 4, the total number of atoms abruptly decreases at the axial position, where the maximum radial force drops below gravity. It is also clear from the figure how the range of the Bessel beam is increased by enlarging the waist w_0^{in} of the incoming Gaussian beam. Of course, for a given total laser power, the maximum radial force decreases as the Bessel beam diameter is increased. For the transport distances of 12 and 20 cm, the total power in the Bessel beam was approximately 400 mW. For comparison, we have also transported atoms with a lattice formed by two counterpropagating Gaussian beams (see figure 4(a)). For this transport, both laser beams have a Rayleigh range of $z_{\mathrm{R}} \approx 2$ cm corresponding to a waist of 70 μm. The laser power of the two beams was $\approx$130 and $\approx$35 mW, respectively. We observe a sudden drop in atom number when the transport distance exceeds the Rayleigh range. Using the scaling law given in equation (2), it should be clear that transports of atoms over tens of centimetres with a Gaussian lattice is hard to achieve.

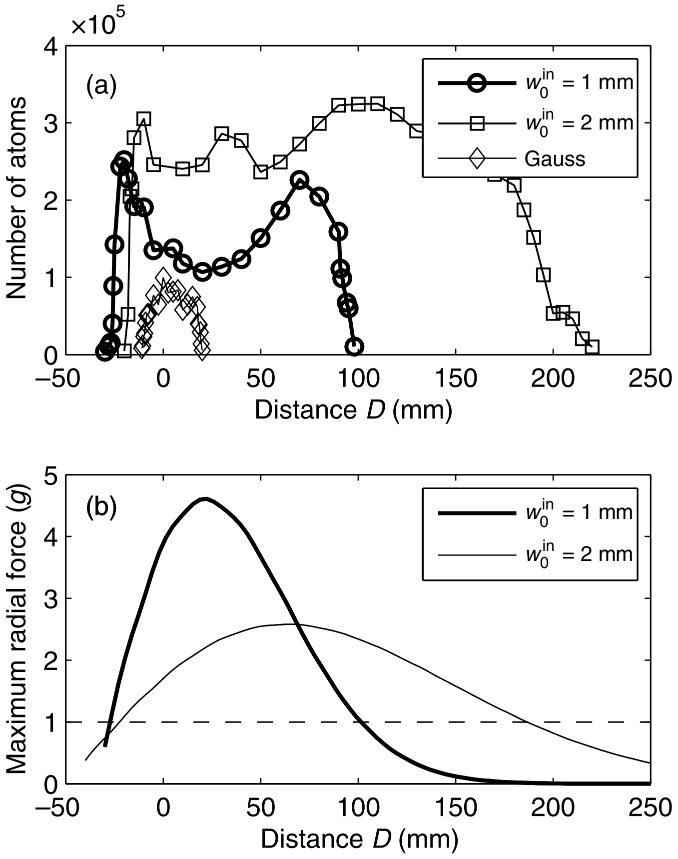

Figure 4. Long distance transports. (a) Shown is the number of remaining atoms after a round-trip transport (see figure 3) over various one-way distances D. The first two data sets are obtained with two different Bessel beams which are created by illuminating an axicon with a Gaussian beam with a waist $w_0^{\mathrm{in}} = 1$ and 2 mm, respectively. The transport time T was kept constant at $T = 130\,\mathrm{ms}$ and $T = 280\,\mathrm{ms}$, respectively. The third data set (◇) corresponds to a transport in a Gaussian beam lattice (see text). The calculated maximum radial trapping force of the two Bessel beam lattice traps is shown in (b) in units of mg, where $g \approx 9.81\,\mathrm{m\,s^{-2}}$ denotes the gravitational acceleration. The variation of the trapping force with distance is an imperfection of the Bessel beam and reflects its creation from a Gaussian beam. When the maximum radial force drops below $1\,g$, gravity pulls the atoms out of the trap, as can be clearly seen in (a).

Interestingly, the curve corresponding to the Bessel beam with waist $w_0^{\mathrm{in}} = 1\,\mathrm{mm}$ in figure 4(a) exhibits a pronounced minimum in the number of remaining atoms at a distance of about 3 cm. The position of this minimum coincides with the position, where the lattice depth has a maximum (see figure 4(b)). This clearly indicates, that high light intensities adversely affect atom lifetimes in the lattice. Although we have not studied in detail the origin of the atomic losses in this work, they should partially originate from spontaneous photon scattering and three body recombination. In the deep lattice here ($60E_{\mathrm{r}}$), the calculated photon scattering rate is $\Gamma_{\mathrm{scatt}} = 0.4\,\mathrm{s}^{-1}$. The tight lattice confinement leads to a high calculated atomic density

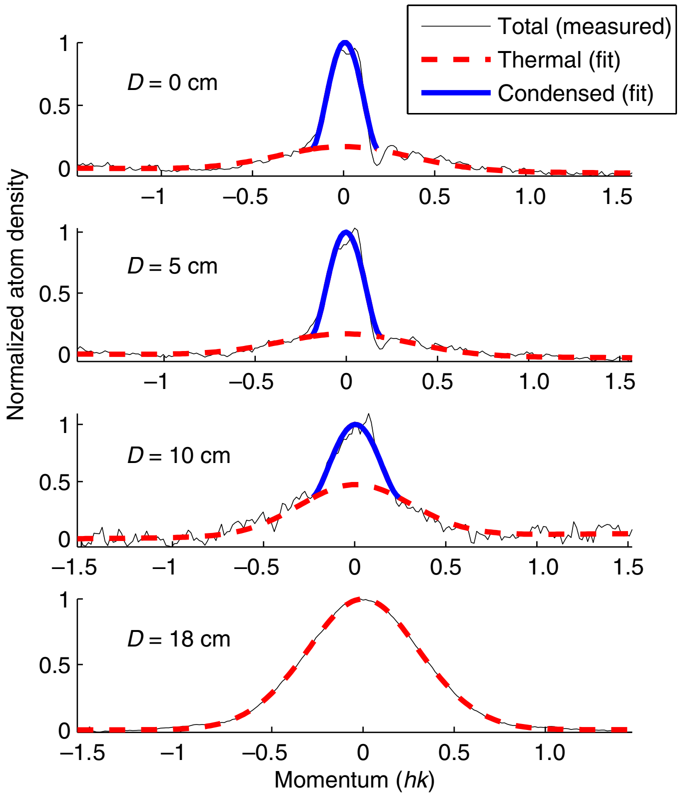

Figure 5. Transporting BEC. Shown are the momentum distributions (thin black lines) of the atoms after a return-trip transport over various one-way distances D. A bimodal distribution (a blue parabolic distribution for the condensed fraction and a red Gaussian distribution for the thermal fraction) is fit to the data. For D below 10 cm, a significant fraction of the atomic cloud is still condensed. For $D = 18$ cm, ($\approx$ the limit in our experiments) only a thermal cloud remains, however, with a temperature below the recoil limit ($T < 0.2E_r/k_B \approx 30$ nK).

of $n_0 \approx 2 \times 10^{14}\,\text{cm}^{-3}$. Adopting $L = 5.8 \times 10^{-30}\,\text{cm}^6\,\text{s}^{-1}$ as rate coefficient for the three body recombination [21], we expect a corresponding loss rate $Ln_0^2 = 0.3\,\text{s}^{-1}$.

In figure 5, we have studied the transport of a BEC, which is especially sensitive to heating and instabilities. It is important to determine, whether the atoms are still Bose-condensed after the transport and what their temperature is afterwards. Figure 5 shows momentum-distributions for various transport distances D, which were obtained after adiabatically reloading the atoms into the magnetic trap by ramping down the lattice and subsequent time-of-flight measurements.

Before discussing these results, we point out that loading the BEC adiabatically into the stationary optical lattice is already critical. We observe a strong dependence of the condensate fraction on the lattice depth. For too low lattice depths, most atoms fall out of the lattice trap due to the gravitational field. For too high lattice depths, all atoms are trapped but the condensate fraction is very small. One explanation for this is that high lattice depths lead to the regime of 2D pancake shaped condensates where tunnelling between adjacent lattice sites is suppressed. Relative dephasing of the pancake shaped condensates will then reduce the condensate fraction after release from the lattice. We obtain the best loading results for a $11\,E_r$ deep trap, where we lose about 65% of the atoms, but maximize the condensate fraction. Because high lattice intensities are detrimental for the BEC, we readjust the power of the lattice during transport, such that the intensity is kept constant over the transport range. The adjustments are based on the calculated axial intensity distribution of the Bessel beam. In this way, we reach transport distances for BEC of 10 cm. We believe, that more sophisticated fine tuning of the power adjustments should increase the transport length considerably. After transport distances of $D = 18$ cm (36 cm round trip), the atomic cloud is thermal. Its momentum spread, however, is merely $0.3\hbar k$, which corresponds to a temperature of 30 nK. Additionally, we want to point out that the loss of atoms due to the transport is negligible ($<10\%$) compared to the loss through loading and simply holding in such a low lattice potential ($\approx 65\%$).

An outstanding feature of the lattice transport scheme is the precise positioning of the atomic cloud. Aside from uncontrolled phase shifts due to residual mechanical noise, such as vibrating optical components, we have perfect control over the relative phase of the lattice lasers with our RF/AOM setup. This would in principle result in an arbitrary accuracy in positioning the optical lattice. We have experimentally investigated the positioning capabilities in our setup. For this, we measured in many runs the position of the atomic cloud in the lattice after it had undergone a return trip with a transport distance of $D = 10$ cm. The position jitter, i.e. the standard deviation from the mean position, was slightly below 1 μm. For comparison, we obtain very similar values for the position jitter when investigating BECs in the lattice before transport. Hence, the position jitter introduced through the transport scheme is negligible.

Another important property of the lattice transport scheme is its high speed. For example, for a transport over 20 cm (40 cm round trip) with negligible loss, a total transport time of 200 ms turns out to be sufficient. This is more than an order of magnitude faster than in the MIT experiment [4], where an optical tweezer was mechanically relocated. The reason for this speed up as compared to the optical tweezer is mainly the much higher axial trapping frequency of the lattice and the non-mechanical setup.

In order to determine experimentally the lower limit of transportation time, we have investigated round-trip transports ($D = 5$ mm), where we have varied the maximum acceleration and the lattice depth (figure 6(a)). The number of atoms, which still remain in the lattice after transport, is measured. As soon as the maximum acceleration exceeds a critical value, the number of atoms starts to drop. For a given lattice depth, we define a critical acceleration a_{crit} as the maximum acceleration of the particular transport where 50% of the atoms still reach their final destination. Figure 6(b) shows the critical acceleration a_{crit} as a function of lattice depth. The upper bound on acceleration observed here can be understood from classical considerations. In our lattice, the maximum confining force along the axial direction is given by $U_{\mathrm{latt}}k$, where k is the wave vector of the light field. Thus in order to keep an atom bound to the lattice, we require the acceleration a to be small enough such that

$$ma < U_{\mathrm{latt}}k. \tag{10}$$

Our data in figure 6 are in good agreement with this limit.[2]

There is in principle also a lower bound on the acceleration, which is due to instabilities exhibited by BECs with repulsive interactions loaded into periodic potentials [23]–[26]. Due to the fact that these instabilities mainly occur at the edge of the Brillouin zones, the time spent

---

[2] In the weak lattice regime ($U_{\mathrm{latt}} \ll 10E_{\mathrm{r}}$) transport losses would be dominated by Landau–Zener tunnelling, see e.g. [14, 22].

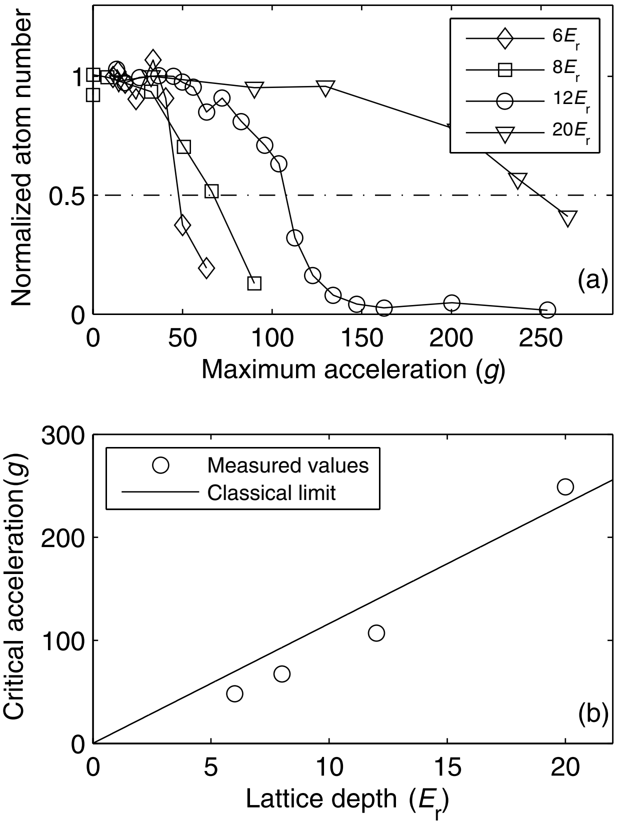

Figure 6. Critical acceleration in lattice. (a) For several round-trip transports with varying maximum acceleration a and lattice depth (see legend), the number of remaining atoms after transport is shown. As the maximum acceleration exceeds a critical value, the number of atoms starts to drop significantly. We define a critical acceleration as the maximum acceleration for transports in which 50% of the atoms still reach their final destination. This critical acceleration is shown as a function of the lattice depth in (b). The experimentally determined values are compared with the limit expected from classical considerations: $a_{\mathrm{crit}} = U_{\mathrm{latt}}k/m$.

in this critical momentum range should be kept small. For our lattice parameters, nearly half of the Brillouin zone is an unstable region, where the lifetime of the BEC is only on the order of 10 ms [25]. Thus we tend to sweep through the Brillouin zone in much less than $\Delta t = 20$ ms, which corresponds to an acceleration of $a = \dot{v} \gg 2v_{\mathrm{r}}/\Delta t \simeq 0.6\,\mathrm{m\,s^{-2}}$. In this way, BECs may be transported without introducing too much heating through these instabilities.

In contrast to acceleration, the transport velocity in our experiment is only technically limited due to the finite AOM bandwidth. As discussed before, the lattice is set in motion by introducing a detuning between the two beams via AOMs (equation (1)). For detunings exceeding the bandwidth of the AOM, the diffraction efficiency of the modulator starts to drop significantly. Consequently the lattice confinement vanishes, and the atoms are lost. In our setup, we can conveniently reach velocities of up to $v = 6\,\mathrm{m\,s^{-1}} \approx 1100v_{\mathrm{r}}$, corresponding to a typical AOM bandwidth of 15 MHz. This upper bound actually limits the transport time for long distance transports ($D > 5$ cm).

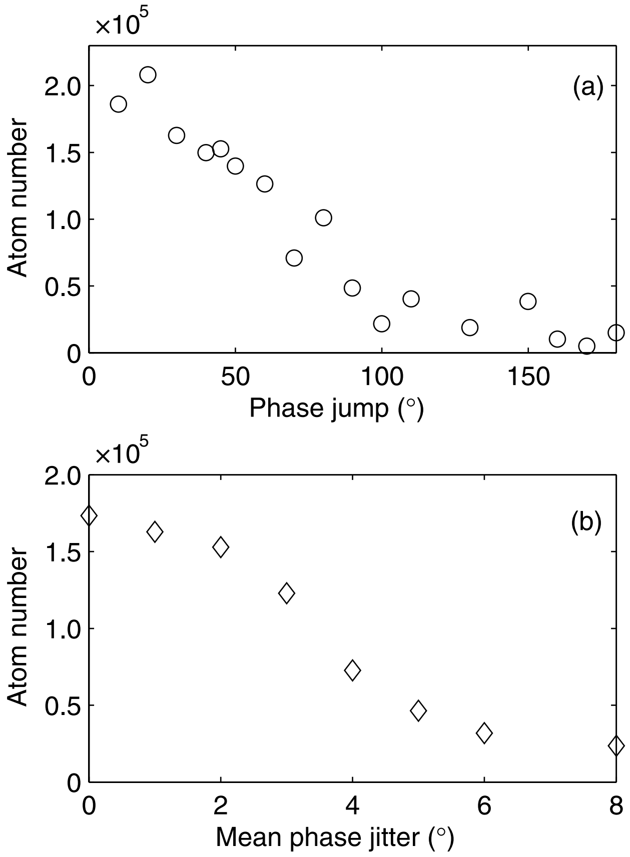

Figure 7. Stability requirements for transport. Sudden phase jumps are introduced in the relative phase of the two counterpropagating lattice laser beams. The corresponding abrupt displacements of the optical lattice lead to heating and loss of the atoms. We measure the number of atoms which remain in the lattice after transport. (a) Data obtained after a single relative phase jump of variable magnitude. (b) A phase jitter (200 positive Poissonian-distributed phase jumps with a variable mean value) is introduced during transport. Mean values on the order of a few degrees already lead to a severe loss of atoms.

Finally we have investigated the importance of phase stability of the optical lattice for the transport (see figure 7). For this, we purposely introduced sudden phase jumps during transport to one of the lattice beams. The timescale for the phase jumps, as given by AOM response time of about 100 ns, was much smaller than the inverse trapping frequencies. The phase jumps lead to abrupt displacements of the optical lattice, causing heating and loss of atoms. In figure 7(a), the atomic losses due to a single phase jump during transport are shown. Phase jumps of 60° typically induce a 50% loss of atoms. For continuous phase jitter (see figure 7(b)), the sensitivity is much larger.

6. Atom catapult

In addition to transport of ultracold atoms, acceleration of atoms to precisely defined velocities is another interesting application of the moving optical lattice. For instance, it could be used

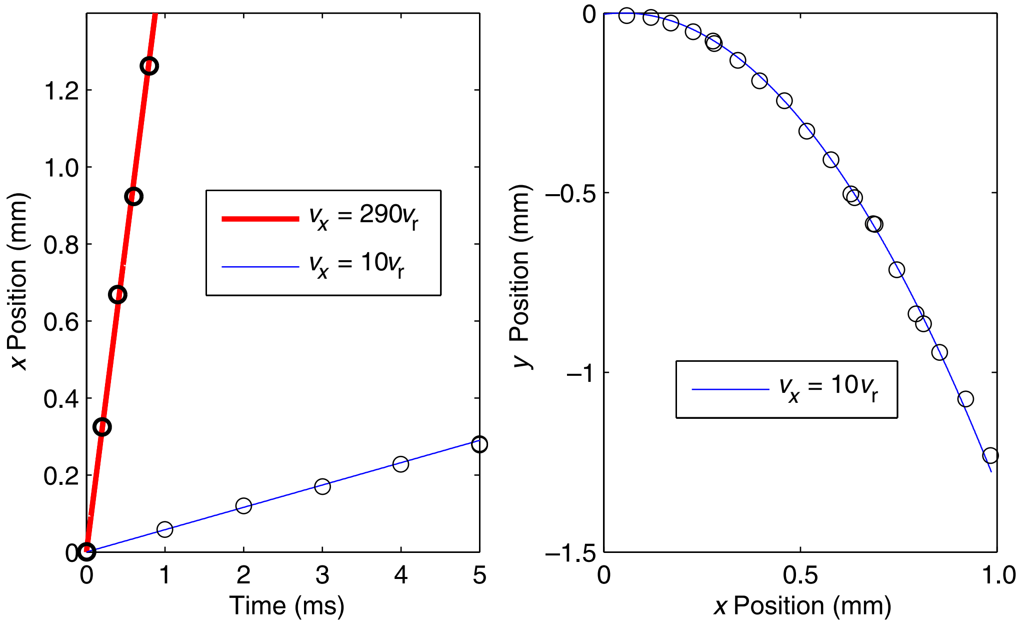

Figure 8. Atom catapult. After acceleration in x-direction and subsequent release from the lattice, the position of the atomic cloud is tracked as it flies ballistically through the field of view of the CCD camera. Shown are two data sets where atoms were accelerated to velocities of either $v_x = 10v_\mathrm{r}$ or $v_x = 290v_\mathrm{r}$. (a) The horizontal position x as a function of time. (b) For the slower cloud ($v_x = 10v_\mathrm{r}$) a parabolic trajectory $y = -g/2 \cdot (x/v_x)^2$ is observed as it falls under the influence of gravity.

to study collisions of BECs with a very high but well-defined relative velocity, similar to the experiments described in [27, 28]. As already shown above, we have precise control to impart a well-defined number of up to 1100 photon recoils to the atoms. This corresponds to a large kinetic energy of $k_\mathrm{B} \times 200\,\mathrm{mK}$. At the same time, the momentum spread of the atoms is about 1/3 of a recoil (see figure 5). To illustrate this, we have performed two sets of experiments, where we accelerate a cloud of atoms to velocities $v = 10v_\mathrm{r}$ and $v = 290v_\mathrm{r} \approx 1.6\,\mathrm{m\,s^{-1}}$. After adiabatic release from the lattice, we track their position in free flight (see figure 8). Initially the atomic cloud is placed about 8 cm away from the position of the magnetic trap. It is then accelerated back towards its original location. Before the atoms pass the camera's field of vision, the lattice beams are turned off within about 5 ms, to allow a ballistic flight of the cloud. Using absorption imaging, the position of the atomic cloud as a function of time is determined. The slope of the straight lines in figure 8(a) corresponds nicely to the expected velocity. However, due to a time jitter problem, individual measurements are somewhat less precise than one would expect.[3] For $v = 10v_\mathrm{r}$, figure 8(b) shows the trajectory of the ballistic free fall of the atoms in gravity.

---

[3] This is linked to the fact that our clock for the system control is synchronized to the 50 Hz of the power grid. Fluctuations of the line frequency lead to shot to shot variations in the ballistic flight time of the atoms, which translates into an apparent position jitter.

7. Conclusion

In conclusion, we have realized a long distance optical transport for ultracold atoms, using a moveable standing wave dipole trap. With the help of a diffraction-free Bessel beam, macroscopic distances are covered for both BEC and ultracold thermal clouds. The lattice transport features a fairly simple setup, as well as a fast transport speed and high positional accuracy. Limitations are mainly technical and leave large room for improvement. In addition to transport, the lattice can also be used as an accelerator to impart a large but well-defined number of photon recoils to the atoms.

Acknowledgments

We thank U Schwarz for helpful information on the generation of Bessel beams and for lending us phase-gratings for testing purposes. Furthermore, we thank R Grimm for discussions and support. This work was supported by the Austrian Science fund (FWF) within SFB 15 (project part 17) and the Tiroler Zukunftsstiftung.

Appendix. Transport ramp

We give here the analytic expression for the lattice acceleration $a(t)$ as a function of time t which was implemented in our experiments (see for example figure 3). $a(t)$ is a smooth piecewise defined cubic polynomial,

$$a(t) = \begin{cases} \frac{D}{T^2}\left(-\frac{7040}{9}\left(\frac{t}{T}\right)^3 + 320\left(\frac{t}{T}\right)^2\right) & \text{for } 0 < t \leqslant T/4, \\ \frac{D}{T^2}\left(\frac{3200}{9}\left(\frac{t}{T}\right)^3 - \frac{1600}{3}\left(\frac{t}{T}\right)^2 + \frac{640}{3}\frac{t}{T} - \frac{160}{9}\right) & \text{for } T/4 < t \leqslant 3T/4, \\ \frac{D}{T^2}\left(-\frac{7040}{9}\left(\frac{t}{T}\right)^3 + \frac{6080}{3}\left(\frac{t}{T}\right)^2 - \frac{5120}{3}\frac{t}{T} + \frac{4160}{9}\right) & \text{for } 3T/4 < t \leqslant T. \end{cases}$$

Here, D is the distance over which the lattice is moved and T is the duration of the transport. From $a(t)$, both the velocity $v(t)$ and the location $x(t)$ may be derived via integration over time. Our choice for the acceleration $a(t)$ features a very smooth transport. The acceleration $a(t)$ and its derivative $\dot{a}(t)$ are zero at the beginning ($t = 0$) and at the end ($t = T$) of the transport. At $t = T/4$ and $t = 3T/4$, the absolute value of the acceleration reaches a maximum.

References

[1] Folman R, Krüger P, Schmiedmayer J, Denschlag J and Henkel C 2002 *Adv. At. Mol. Opt. Phys.* **48** 263–352

[2] Greiner M, Bloch I, Hänsch T W and Esslinger T 2001 *Phys. Rev.* A **63** 031401

[3] Lewandowski H J, Harber D M, Whitaker D L and Cornell E A 2002 *Phys. Rev. Lett.* **88** 070403

[4] Gustavson T L, Chikkatur A P, Leanhardt A E, Görlitz A, Gupta S, Pritchard D E and Ketterle W 2002 *Phys. Rev. Lett.* **88** 020401

[5] Kasevich M and Chu S 1991 *Phys. Rev. Lett.* **67** 000181

[6] Berg-Sørensen K and Mølmer K 1998 *Phys. Rev.* A **58** 1480

[7] Pötting S, Cramer M, Schwalb C H, Pu H and Meystre P 2001 *Phys. Rev.* A **64** 023604

[8] Dahan M B, Peik E, Reichel J, Castin Y and Salomon C 1996 *Phys. Rev. Lett.* **76** 4508–11

[9] Morsch O, Müller J H, Cristiani M, Ciampini D and Arimondo E 2001 *Phys. Rev. Lett.* **87** 140402

[10] Morsch O and Oberthaler M 2006 *Rev. Mod. Phys.* **78** 179–215

[11] Kuhr S, Alt W, Schrader D, Müller M, Gomer V and Meschede D 2001 *Science* **293** 278

[12] Mandel O, Greiner M, Widera A, Rom T, Hänsch T W and Bloch I 2003 *Phys. Rev. Lett.* **91** 010407

[13] Cizmar T, Garces-Chavez V, Dholakia K and Zemanek P 2005 *Appl. Phys. Lett.* **86** 174101

[14] Denschlag J H, Simsarian J E, Häffner H, McKenzie C, Browaeys A, Cho D, Helmerson K, Rolston S L and Phillips W D 2002 *J. Phys. B: At. Mol. Opt. Phys.* **35** 3095–110

[15] Durnin J 1987 *J. Opt. Soc. Am.* B **4** 651–4

[16] Durnin J, Miceli J J and Eberly J H 1987 *Phys. Rev. Lett.* **58** 1499–501

[17] Niggl L, Lanzl T and Maier M 1997 *J. Opt. Soc. Am.* A **14** 27–33

[18] Niggl L 1999 *PhD Thesis* Universität Regensburg

[19] Thalhammer G, Winkler K, Lang F, Schmid S, Grimm R and Denschlag J H 2006 *Phys. Rev. Lett.* **96** 050402

[20] Thalhammer G, Theis M, Winkler K, Grimm R and Denschlag J H 2005 *Phys. Rev.* A **71** 033403

[21] Söding J, Guéry-Odelin D, Desbiolles P, Chevy F, Inamori H and Dalibard J 1999 *Appl. Phys.* B **69** 257–61

[22] Peik E, Dahan M B, Bouchoule I, Castin Y and Salomon C 1997 *Phys. Rev.* A **55** 4

[23] Choi D I and Niu Q 1999 *Phys. Rev. Lett.* **82** 2022

[24] Wu B and Niu Q 2003 *New J. Phys.* **5** 104.1–104.24

[25] Fallani L, De Sarlo L, Lye J E, Modugno M, Saers R, Fort C and Inguscio M 2004 *Phys. Rev. Lett.* **93** 140406

[26] Cristiani M, Morsch O, Malossi N, Jona-Lasinio M, Anderlini M, Courtade E and Arimondo E 2004 *Opt. Express* **12** 4

[27] Thomas N R, Kjaergaard N, Julienne P S and Wilson A C 2004 *Phys. Rev. Lett.* **93** 173201

[28] Buggle C, Léonard J, von Klitzing W and Walraven J T M 2004 *Phys. Rev. Lett.* **93** 173202

Long-Lived Feshbach Molecules in a Three-Dimensional Optical Lattice

G. Thalhammer,[1] K. Winkler,[1] F. Lang,[1] S. Schmid,[1] R. Grimm,[1,2] and J. Hecker Denschlag[1]
[1]*Institut für Experimentalphysik, Universität Innsbruck, 6020 Innsbruck, Austria*
[2]*Institut für Quantenoptik und Quanteninformation, Österreichische Akademie der Wissenschaften, 6020 Innsbruck, Austria*

(Received 27 October 2005; published 8 February 2006)

We have created and trapped a pure sample of $^{87}Rb_2$ Feshbach molecules in a three-dimensional optical lattice. Compared to previous experiments without a lattice, we find dramatic improvements such as long lifetimes of up to 700 ms and a near unit efficiency for converting tightly confined atom pairs into molecules. The lattice shields the trapped molecules from collisions and, thus, overcomes the problem of inelastic decay by vibrational quenching. Furthermore, we have developed an advanced purification scheme that removes residual atoms, resulting in a lattice in which individual sites are either empty or filled with a single molecule in the vibrational ground state of the lattice.

DOI: 10.1103/PhysRevLett.96.050402 PACS numbers: 03.75.Lm, 03.75.Nt, 32.80.Lg, 34.50.−s

Using magnetic Feshbach resonances [1] to create ultracold diatomic molecules in their highest rovibrational state has become a key to exciting developments and breakthroughs. Feshbach molecules made of bosonic atoms behave in a strikingly different way from Feshbach molecules made of fermionic atoms. For weakly bound dimers of fermionic atoms, vibrational quenching and inelastic decay are strongly suppressed by a Pauli blocking effect in a close encounter of two molecules [2]. This has been vital to the experimental creation of molecular Bose-Einstein condensates (BEC) and investigations of the crossover to a strongly interacting fermionic superfluid [3]. For dimers of bosonic atoms [4–7], however, progress has been hampered by strong inelastic decay due to atom-molecule and molecule-molecule collisions. Therefore, the experiments have been focused on the transient regime, studying, e.g., the collision and dissociation dynamics [6–11].

A three-dimensional optical lattice offers many interesting opportunities for research on ultracold molecules. Lattice sites occupied with exactly two atoms represent a perfectly controlled quantum system which can be rigorously treated theoretically. Matrix elements for atom-molecule coupling are strongly enhanced with the prospect of efficient atom-molecule conversion. Moreover, it is expected that the lattice can isolate molecules from each other and shield them from detrimental collisions so that a long-lived sample can be created also with dimers of bosonic atoms. Recently, first experiments with molecules in a lattice have studied photoassociation [12,13] or demonstrated modifications of the binding energy of tightly confined Feshbach molecules [14].

In this Letter, we report on the creation of a pure sample of ultracold Rb_2 Feshbach molecules trapped in a 3D optical lattice. The observed long lifetimes of up to 700 ms greatly exceed previous values reported for dimers of bosonic atoms [6,7,9,10]. Further, we experimentally investigate association and dissociation of the Feshbach molecules and reach efficiencies of 95% for converting pairs of atoms into molecules. In brief, we adiabatically load a ^{87}Rb BEC into the vibrational ground state of the lattice. For our experimental conditions, about 20% of the condensate atoms are grouped in pairs of two into the lattice sites. By ramping adiabatically over a magnetic Feshbach resonance at 1007.4 G, we convert these pairs into molecules. Another 20% of atoms are located in triply and more highly occupied lattice sites. After the Feshbach ramp, however, inelastic collisions between the created molecules and atoms within the high occupancy sites quickly remove these particles from the lattice. Finally, the remaining 60% of the condensate atoms are found in singly occupied sites and are unaffected by the Feshbach ramp. Using a novel resonant purification scheme, we can remove these atoms from the lattice, which results in a pure molecular sample with each molecule being shielded from the others by the lattice potential.

The starting point for our experiments is an almost pure BEC of about 6×10^5 ^{87}Rb atoms in the spin state $|F = 1, m_F = -1\rangle$ [15]. It is transferred from a quadrupole Ioffe configuration trap (QUIC) into another Ioffe-type magnetic trap with trap frequencies $\omega_{x,y,z} = 2\pi \times (7, 19, 20)$ Hz, leading to a peak density of the BEC of about 4×10^{13} cm^{-3}. Our 3D lattice is cubic and consists of three retroreflected intensity-stabilized laser beams which propagate orthogonally to each other. They are derived from a frequency-stable single-mode Ti:sapphire laser (≈500 kHz linewidth) with a wavelength of $\lambda = 830.44$ nm. For this wavelength, the laser is detuned by about 100 GHz from the closest transition to an excited molecular level, minimizing light induced losses as a precondition for long molecular lifetimes. The laser beams are polarized perpendicularly to each other, and their frequencies differ by several tens of megahertz to avoid disturbing interference effects. The waists of all three beams are about 160 μm, and the maximum obtainable power is about 110 mW per beam, which results in calculated lattice depths of up to 40 recoil energies ($E_r = h^2/2m\lambda^2$, where m is the atomic mass of ^{87}Rb and h is Planck's constant). We have verified the lattice depths by measuring the energy

© 2006 The American Physical Society

gap between bands of the lattice [16]. The relative uncertainty of our lattice depth is ±15%.

After the BEC is adiabatically loaded into a $35E_r$ deep 3D optical lattice within 100 ms, we turn off the magnetic trap. By suddenly reversing the bias magnetic field of a few gauss, we flip the spins of our atoms to the high field seeking state $|F = 1, m_F = +1\rangle$ with an efficiency higher than 99% (see also [17]). This state features the Feshbach resonance at 1007.4 G. Afterwards, we ramp up a homogeneous magnetic field in 3 ms to about 1015 G using the QUIC quadrupole coils in Helmholtz configuration. The current through the coils is actively stabilized to a relative accuracy of about 10^{-4}. The fast diabatic crossing of the Feshbach resonance has basically no effect on the atoms in the lattice. If we slowly ramp in 5 ms from 1015 to 1000 G (crossing the Feshbach resonance at 1007 G), molecules are adiabatically produced in the multiply occupied lattice sites. If, however, we cross the Feshbach resonance very quickly, e.g., by simply switching off the magnetic field, less than 10% of the atoms are converted into molecules. Note that, after the first Feshbach ramp, we observe an immediate irretrievable loss of 20% of the atoms. We attribute this loss to inelastic collisions involving molecules for sites initially occupied by 3 or more atoms. The remaining occupied sites each contain either a single atom or a single molecule.

Atom numbers are measured with absorption imaging at low magnetic fields (≈2 G) after release from the optical lattice and 11 ms of ballistic expansion. In order to determine molecule numbers, they are first dissociated into atoms by slowly ramping back across the Feshbach resonance and then quickly switching off the magnetic field. We also use absorption imaging to map out the band occupation of the lattice. For this, the lattice is ramped down in 2 ms, and we typically observe a momentum distribution which is fully contained in a cube of width $2\hbar k$ corresponding to the first Brillouin zone of the lattice [18]. This demonstrates that atoms and molecules are in the vibrational ground state of the lattice sites.

In order to create a pure molecular sample, we have developed an advanced purification scheme to remove all atoms which combines the great selectivity of microwave excitation with the high efficiency of atom removal through resonant light pressure [7]. We apply a combined microwave and light pulse at a magnetic field of 1000 G for 3 ms. The microwave drives the transition at a frequency of 9113 MHz between levels which correlate with $|F = 1, m_F = +1\rangle$ and $|F = 2, m_F = +2\rangle$. The light pulse drives the closed transition $|F = 2, m_F = +2\rangle \longrightarrow |F = 3, m_F = +3\rangle$. The optical transition frequency is 1402 MHz blue detuned compared to the transition at zero magnetic field. After this pulse, which heats the atoms out of the lattice and an additional hold time (~20 ms), no more atoms can be detected. The direct effect of the microwave and light field pulse on the molecules is negligible because the radiation is off resonance. As an indirect effect, however, we find that during the first purification pulse we still lose about 40% of the molecules, probably due to inelastic collisions with the blown away atoms. Further losses are not observed in subsequent purification pulses. We end up with a pure molecular sample formed from about 10% of the initial atoms, which corresponds to 3×10^4 molecules.

We have investigated the lifetimes of the Feshbach molecules in the lattice under various conditions (see Figs. 1 and 2). Figure 1 shows the decay of molecules at a lattice depth of $10E_r$. The pure molecular sample exhibits a remarkably long lifetime of 700 ms. For the case of an unpurified sample, where the atoms at singly occupied sites have not been removed, the lifetime of the molecules is considerably reduced to ≈ 35 ms. This observation suggests that the molecular decay is based on a process where an atom tunnels to a site occupied by a molecule and inelastically collides with it. These inelastic collisions can, in principle, also happen between two molecules. However, compared to an atom, a molecule has a much lower tunneling rate, since it experiences twice the dipole potential and has twice the mass of a single atom. Using simple scaling arguments, for a molecule to have the same tunneling rate as an atom, the lattice light intensity needs to be more than 4 times smaller. This explains the comparatively long lifetime of the purified molecular samples. We note that, if molecular decay is based on inelastic collisions, its time dependence is intrinsically nonexponential. However, exact modeling of the decay would be quite involved and requires precise knowledge of atom or molecule distributions in the lattice. Since these distributions are not known to us, we simply base our estimates for the molecular lifetimes on an exponential decay law.

Figure 2 shows the measured lifetimes of the molecules for various lattice depths. For sufficiently high lattice

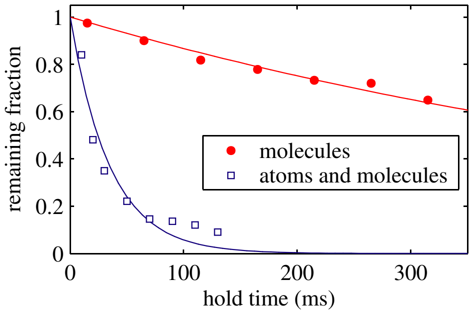

FIG. 1 (color online). Decay of molecules in a 3D optical lattice with a potential depth of $(10 \pm 2)E_r$. Shown is the remaining fraction of molecules in purified (solid circles) and unpurified (squares) samples as a function of hold time. The continuous lines are exponential fits to the data indicating a lifetime of 700 and 35 ms for purified and unpurified molecular samples, respectively. In order to determine molecule numbers in the unpurified sample, purification was performed at the end of the hold time. The hold time was limited to below 400 ms due to the heating up of the coils.

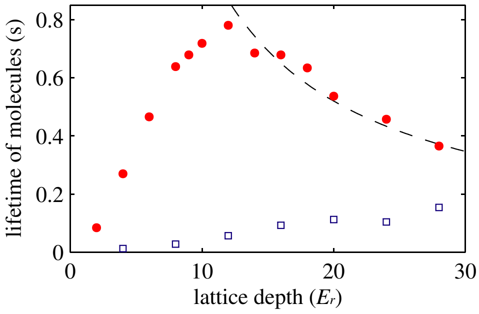

FIG. 2 (color online). Molecular lifetimes for purified molecular samples (circles) and for unpurified samples (squares) as a function of the lattice depth. For this measurement, the lattice depth was reduced from $35E_r$ to the given value after the creation of the molecules. The dashed line is inversely proportional to the lattice depth.

depths, we observe a lifetime for the purified molecular sample inversely proportional to the lattice depth (see dashed line in Fig. 2). From this, we conclude that above a lattice depth of about $12E_r$ the tunneling of the molecules is strongly suppressed, and the lifetime is limited by light induced losses due to off-resonant transitions to an excited molecular state which subsequently decays. Below this value, decay is dominated by tunneling [19] and following inelastic collisions. Thus, the molecular lifetime is maximized in a tradeoff between tunneling and light induced losses. As already shown in Fig. 1, the presence of atoms considerably reduces the lifetime of the molecules, even at larger lattice depths. In the limit of vanishing lattice depths, our experimental lifetimes decrease to values similar to those observed in Refs. [6–10]. Figure 2 clearly demonstrates that shielding of the molecules against inelastic collisions grows with increasing lattice depth.

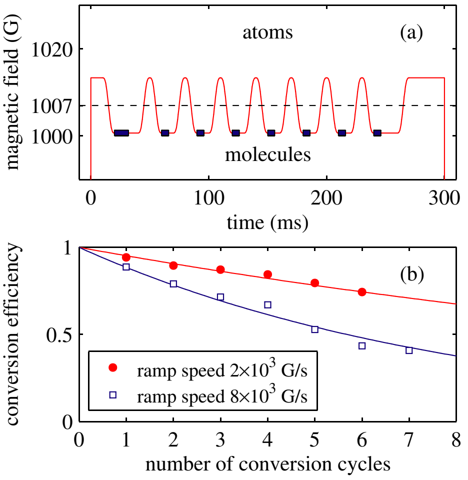

FIG. 3 (color online). (a) Scheme for measurement of conversion efficiency, shown for 7 dissociation-association cycles. The shaded areas indicate the application of our purification procedure to remove atoms. The dashed line at 1007 G shows the position of the Feshbach resonance. (b) Conversion efficiency for a given number of complete dissociation-association cycles for two different ramp speeds of the magnetic field. We measure a conversion efficiency of 95% per cycle for the slow ramp and 89% per cycle for the fast ramp. The solid lines are described by exponential fit curves as described in the text. The lattice depth is $35E_r$.

We now investigate the dynamics for both association and dissociation of a single Feshbach molecule in a lattice site during Feshbach ramping. This fundamental system is of special interest since it can be theoretically treated exactly and solved analytically [21]. We prepare a purified sample of molecules at 1000 G in a lattice of $35E_r$ depth. We then ramp the magnetic field in a symmetric way across the Feshbach resonance up to 1015 G and back (see Fig. 3). Afterwards, purification is applied to remove atoms which have not recombined to form molecules. In a last step, the molecule number is measured. If dissociation and association are not fully adiabatic in a conversion cycle, a loss of molecules will result; e.g., during the association ramp, a pair of atoms might not be converted into a molecule or during dissociation the molecule might break up into two atoms which, after tunneling, are located in separate sites. For slow ramps, we observe small loss signals indicating high adiabaticity for the dissociation-association cycle. In order to increase the loss signal, to improve its accuracy, and to check for consistency, we repeated this experiment with a higher number of cycles (see Fig. 3). The two data sets in Fig. 3(b) correspond to two different ramp speeds (2×10^3 G/s, 8×10^3 G/s) and can be described by the exponential functions 0.95^n and 0.89^n, respectively, where n is the number of cycles. Thus, for a slow Feshbach ramp (2×10^3 G/s), we observe an unprecedented high efficiency of up to 95% for the whole dissociation-association cycle. For a faster ramp (8×10^3 G/s), the efficiency drops to 89%. We have taken care that light induced losses have been corrected for in the data [Fig. 3(b)]. Our high conversion efficiencies in the optical lattice are in strong contrast to the low values of ~10% observed previously in a ^{87}Rb BEC [10] which were presumably limited by strong inelastic collisions. In our deep lattice, however, inelastic collisions are suppressed.

After having determined the efficiency for the full dissociation-association cycle, we now study dissociation and association individually. Figure 4(a) shows the measured conversion efficiency of atom pairs to molecules for different ramp speeds. The atom pairs were prepared by creating a pure molecular sample and then dissociating the molecules by slowly (2×10^3 G/s) ramping backward over the Feshbach resonance. Then, again, the magnetic field was swept across the Feshbach resonance at various speeds, and, finally, after switching off completely the magnetic field, the remaining nonconverted atoms are detected. The dashed line in Fig. 4(a) is based on a Landau-Zener expression without adjustable parameters [21] and is given by

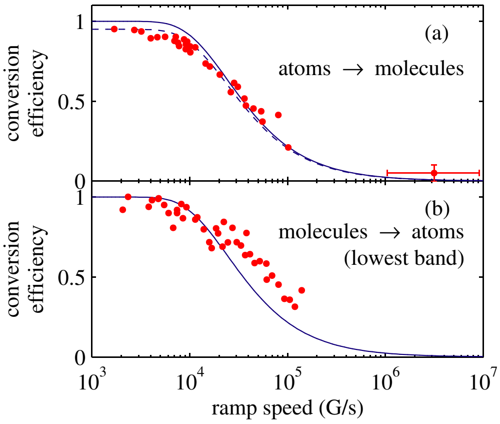

FIG. 4 (color online). (a) Conversion efficiency of atoms (mostly pairs) into molecules as a function of the ramp speed. (b) A purified sample of molecules is dissociated into atom pairs at different ramp speeds. We measure the number of atoms which are observed in the first Brillouin zone of the lattice after release, i.e., atoms that populate the lowest energy band of the lattice. The data is normalized to the atom number at the lowest ramp speeds. The continuous lines in (a) and (b) are calculations as described in the text.

$$p = 1 - \exp\left(-\frac{2\sqrt{6}\hbar}{m a_{\mathrm{ho}}^3}\left|\frac{a_{\mathrm{bg}}\Delta B}{\dot{B}}\right|\right), \tag{1}$$

where p is the probability of creating a molecule, $a_{\mathrm{bg}} = 100.5a_0$ the background scattering length, $\Delta B = 0.21$ G [10] the width of the Feshbach resonance, $\dot{B}$ the ramp speed at the Feshbach resonance, and $a_{\mathrm{ho}} = \sqrt{\hbar/m\omega}$ the harmonic oscillator length. Using the best estimate for our trapping frequency of $\omega = 2\pi \times (39 \pm 3)$ kHz (corresponding to a lattice depth of $35 \pm 5E_r$), we get good agreement with our data. We note that, even for the slowest ramp speeds, the measured conversion efficiency never reaches unity but levels off at 95%, in agreement with the results in Fig. 3. This, however, does not exclude a true unit conversion efficiency for atom pairs into molecules, because it is possible that 5% of the atoms are not grouped in pairs, e.g., due to nonadiabaticity in dissociation and tunneling. In order to facilitate the comparison of the data distribution and theory, we have scaled the Landau-Zener curve by a factor of 0.95 (dashed line). The maximum controllable ramp speed ($\sim 10^5$ G/s; see Fig. 4) is limited by the performance of our current supply for the magnetic field coils. The data point at 3×10^6 G/s was obtained by simply switching off the coil currents with an external switch. The abrupt switching induces eddy currents, which results in a less controlled ramp with a large error margin. For fast switching, we measured a conversion efficiency of $5 \pm 5\%$.

In Fig. 4(b), we study the dissociation of a purified sample of molecules. We measure the number of atoms which populate the lowest band of the lattice after dissociation. At low ramp speeds, Feshbach molecules get adiabatically converted to pairs of atoms in the lattice ground state. At higher speeds, molecules are energetically lifted above the molecule threshold and can decay into higher lattice bands or into the continuum. Assuming the reversibility of the Landau-Zener transition, we use the same theory curve as in Fig. 4(a). For higher ramp speeds, we measure larger atom numbers than expected. This is probably due to imperfections of our data analysis which can overestimate the atom number in the lowest band by adding in some atoms from higher bands.

To summarize, we have demonstrated that ultracold Feshbach molecules can be created with high conversion efficiency in a 3D optical lattice. After purification, we observe long molecular lifetimes up to 700 ms. These strong improvements over previous experiments open promising perspectives for applications, e.g., in high resolution molecular spectroscopy and quantum information processing in optical lattices. They may also represent an important step in the creation of a stable BEC of molecules in their vibrational ground state.

We appreciate the assistance of Matthias Theis and Carlo Sias. We thank Thorsten Köhler and Todd Meyrath for fruitful discussions. This work was supported by the Austrian Science Fund (FWF) within SFB 15 (project part 17) and the European Union in the frame of the Cold Molecules TMR Network under Contract No. HPRN-CT-2002-00290.

---

[1] D. Kleppner, Phys. Today **57**, No. 8, 12 (2004).
[2] D. S. Petrov, C. Salomon, and G. V. Shlyapnikov, Phys. Rev. Lett. **93**, 090404 (2004).
[3] F. Chevy and C. Salomon, Phys. World **18**, 43 (2005).
[4] E. A. Donley *et al.*, Nature (London) **417**, 529 (2002).
[5] J. Herbig *et al.*, Science **301**, 1510 (2003).
[6] S. Dürr *et al.*, Phys. Rev. Lett. **92**, 020406 (2004).
[7] K. Xu *et al.*, Phys. Rev. Lett. **91**, 210402 (2003).
[8] E. Hodby *et al.*, Phys. Rev. Lett. **94**, 120402 (2005).
[9] T. Mukaiyama *et al.*, Phys. Rev. Lett. **92**, 180402 (2004).
[10] S. Dürr, T. Volz, and G. Rempe, Phys. Rev. A **70**, 031601(R) (2004).
[11] C. Chin *et al.*, Phys. Rev. Lett. **94**, 123201 (2005).
[12] T. Rom *et al.*, Phys. Rev. Lett. **93**, 073002 (2004).
[13] C. Ryu *et al.*, cond-mat/0508201.
[14] T. Stöferle *et al.*, Phys. Rev. Lett. **96**, 030401 (2006).
[15] G. Thalhammer *et al.*, Phys. Rev. A **71**, 033403 (2005).
[16] J. Hecker Denschlag *et al.*, J. Phys. B **35**, 3095 (2002).
[17] T. Volz *et al.*, Phys. Rev. A **68**, 010702(R) (2003).
[18] M. Greiner *et al.*, Phys. Rev. Lett. **87**, 160405 (2001).
[19] Tunneling rates can be calculated (see [20]); e.g., lattice depths of 5, 8, and $16E_r$ correspond to molecular tunneling rates J of 4, 0.6, and 0.009 Hz, respectively, which are consistent with our measured lifetimes.
[20] D. Jaksch *et al.*, Phys. Rev. Lett. **81**, 3108 (1998).
[21] P. Julienne, E. Tiesinga, and T. Köhler, J. Mod. Opt. **51**, 1787 (2004); cond-mat/0312492.

Bibliography

[Abo 01] J. R. Abo-Shaeer, C. Raman, J. M. Vogels, and W. Ketterle. “Observation of vortex lattices in Bose-Einstein condensates”. *Science*, Vol. 292, p. 476, 2001.

[Ande 95] M. H. Anderson, J. R. Ensher, M. R. Matthews, C. E. Wieman, and E. A. Cornell. “Observation of Bose-Einstein condensation in a dilute atomic vapor”. *Science*, Vol. 269, pp. 198–201, 1995.

[Andr 97] M. R. Andrews, C. G. Townsend, H.-J. Miesner, D. S. Durfee, M. Kurn, and W. Ketterle. “Observation of interference between two Bose condensates”. *Science*, Vol. 275, p. 637, 1997.

[Arim 76] E. Arimondo and G. Orriols. “Nonabsorbing atomic coherences by coherent two-photon transitions in a three-level optical pumping”. *Nuovo Cimento Soc. Ital. Fis.*, Vol. 17, pp. 333–338, 1976.

[Autl 55] S. H. Autler and C. H. Townes. “Stark effect in rapidly varying fields”. *Phys. Rev.*, Vol. 100, pp. 703–722, 1955.

[Bart 04] M. Bartenstein, A. Altmeyer, S. Riedl, S. Jochim, C. Chin, J. H. Denschlag, and R. Grimm. “Crossover from a molecular Bose-Einstein condensate to a degenerate Fermi gas”. *Phys. Rev. Lett.*, Vol. 92, p. 120401, 2004.

[Baue 09] D. Bauer, M. Lettner, C. Vo, G. Rempe, and S. Dürr. “Control of a magnetic Feshbach resonance with laser light”. *Nat. Phys.*, Vol. 5, pp. 339–342, 2009.

[Berg 98] K. Bergmann, H. Theuer, and B. W. Shore. “Coherent population transfer among quantum states of atoms and molecules”. *Rev. Mod. Phys.*, Vol. 70, pp. 1003–1025, 1998.

[Bert 06] J. F. Bertelsen and K. Mølmer. “Molecule formation in optical lattice wells by resonantly modulated magnetic fields”. *Phys. Rev. A*, Vol. 73, p. 013811, 2006.

[Best 04] T. Best. *Ultrakalte Moleküle in optischen Gittern.* PhD thesis, Ludwig Maximilians Universität München, 2004.

[Beth 99] H. L. Bethlem, G. Berden, and G. Meijer. “Decelerating neutral dipolar molecules”. *Phys. Rev. Lett.*, Vol. 83, pp. 1558–1561, 1999.

[Bose 24] S. Bose. “Plancks Gesetz und Lichtquantenhypothese”. *Z. Phys.*, Vol. 26, p. 178, 1924.

[Bove 88] F. Bovey, L. Jelinski, and P. Mirau. *Nuclear magnetic resonance spectroscopy.* Academic Press, 1988.

[Bran 07] B. Brandstätter. *Radio frequency transitions in ultracold Rubidium.* Master’s thesis, Universität Innsbruck, 2007.

[Buch 07] H. P. Büchler, A. Micheli, and P. Zoller. “Three-body interactions with cold polar molecules”. *Nat. Phys.*, Vol. 3, p. 726, 2007.

[Chin 04] C. Chin, M. Bartenstein, A. Altmeyer, S. Riedl, S. Jochim, J. H. Denschlag, and R. Grimm. “Observation of the pairing gap in a strongly interacting Fermi gas”. *Science*, Vol. 305, pp. 1128–1130, 2004.

[Chin 08] C. Chin, R. Grimm, P. Julienne, and E. Tiesinga. “Feshbach Resonances in ultracold gases”. *Rev. Mod. Phys.*, 2008.

[Chu 04] S.-I. Chu and D. A. Telnovc. “Beyond the Floquet theorem: Generalized Floquet formalisms and quasienergy methods for atomic and molecular multiphoton processes in intense laser fields”. *Phys. Rep.*, Vol. 390, pp. 1–131, 2004.

[Cohe 77] C. Cohen Tannoudji, B. Diu, and F. Laloe. *Quantum Mechanics.* John Wiley & Sons, 2 Ed., 1977.

[Cour 98] P. Courteille, R. S. Freeland, and D. J. Heinzen. “Observation of a Feshbach resonance in cold atom scattering”. *Phys. Rev. Lett.*, Vol. 81, pp. 69–72, 1998.

[Cran 47] J. Crank and P. Nicolson. “A practical method for numerical evaluation of solutions of partial differential equations of the heat-conduction type”. *Proc. Camb. Phil. Soc.*, Vol. 43, pp. 50–67, 1947.

[Cubi 03] J. Cubizolles, T. Bourdel, S. J. J. M. F. Kokkelmans, G. V. Shlyapnikov, and C. Salomon. “Production of long-lived ultracold Li_2 molecules from a Fermi gas”. *Phys. Rev. Lett.*, Vol. 91, p. 240401, 2003.

[Danz 08] H. Danzl, E. Haller, M. Gustavsson, M. Mark, R. Hart, N. Bouloufa, O. Dulieu, H. Ritsch, and H.-C. Nägerl. “Quantum gas of deeply bound ground state molecules”. *Science*, Vol. 321, pp. 1062–1066, 2008.

[Danz 09] J. G. Danzl, M. J. Mark, E. Haller, M. Gustavsson, N. Bouloufa, O. Dulieu, H. Ritsch, R. Hart, and H.-C. Nägerl. "Precision molecular spectroscopy for ground state transfer of molecular quantum gases". *Faraday Discuss.*, 2009.

[Davi 95] K. B. Davis, M. O. Mewes, M. R. Andrews, N. J. van Druten, D. S. Durfee, D. M. Kurn, and W. Ketterle. "Bose-Einstein condensation in a gas of Sodium atoms". *Phys. Rev. Lett.*, Vol. 75, pp. 3969–3973, Nov 1995.

[Deig 08] J. Deiglmayr, A. Grochola, M. Repp, K. Mörtlbauer, C. Glück, J. Lange, O. Dulieu, R. Wester, and M. Weidemüller. "Formation of ultracold polar molecules in the rovibrational ground state". *Phys. Rev. Lett.*, Vol. 101, p. 133004, 2008.

[DeMi 02] D. DeMille. "Quantum computation with trapped polar molecules". *Phys. Rev. Lett.*, Vol. 88, p. 067901, 2002.

[DeMi 08] D. DeMille, S. Sainis, J. Sage, T. Bergeman, S. Kotochigova, and E. Tiesinga. "Enhanced sensitivity to variation of m_e/m_p in molecular spectra". *Phys. Rev. Lett.*, Vol. 100, p. 043202, 2008.

[Dens 00] J. Denschlag, J. E. Simsarian, D. L. Feder, C. W. Clark, L. A. Collins, J. Cubizolles, L. Deng, E. W. Hagley, K. Helmerson, W. P. Reinhardt, S. L. Rolston, B. I. Schneider, and W. D. Phillips. "Generating solitons by phase engineering of a Bose-Einstein condensate". *Science*, Vol. 287, p. 97, 2000.

[Dres 99] K. Drese and M. Holtaus. "Floquet theory for short laser pulses". *Eur. Phys. J. D*, Vol. 5, pp. 119–134, 1999.

[Drev 83] R. W. P. Drever, J. L. Hall, F. V. Kowalski, J. Hough, G. M. Ford, A. Munley, and H. Ward. "Laser phase and frequency stabilisation using an optical resonator". *Appl. Phys. B*, Vol. 31, pp. 97–105, 1983.

[Duli 95] O. Dulieu and P. S. Julienne. "Coupled channel bound states calculations for alkali dimers using the Fourier grid method". *J. Chem. Phys.*, Vol. 103, pp. 60–66, 1995.

[Durr 04] S. Dürr, T. Volz, A. Marte, and G. Rempe. "Observation of molecules produced from a Bose-Einstein condensate". *Phys. Rev. Lett.*, Vol. 92, p. 020406, 2004.

[Eins 25] A. Einstein. "Quantentheorie des einatomigen idealen Gases. Zweite Abhandlung,". *Sitzber. Kgl. Preuss. Akad. Wiss.*, Vol. 3, 1925.

[Elio 03] M. Elioff, J. Valentini, and D. Chandler. “Subkelvin cooling NO molecules via billiard-like collisions with Argon”. *Science*, Vol. 302, p. 1940, 2003.

[Essl 98] T. Esslinger, I. Bloch, and T. W. Hänsch. “Bose-Einstein condensation in a quadrupole-Ioffe configuration trap”. *Phys. Rev. A*, Vol. 58, pp. R2664–R2667, 1998.

[Fate 00] F. K. Fatemi, K. M. Jones, and P. D. Lett. “Observation of optically induced Feshbach resonances in collisions of cold atoms”. *Phys. Rev. Lett.*, Vol. 85, pp. 4462–4465, 2000.

[Fesh 64] H. Feshbach. “Unified theory of nuclear reactions”. *Rev. Mod. Phys.*, Vol. 36, pp. 1076–1078, 1964.

[Fior 01] A. Fioretti, C. Amiot, C. M. Dion, O. Dulieu, M. Mazzoni, G. Smirne, and C. Gabbanini. “Cold Rubidium molecule formation through photoassociation: A spectroscopic study of the 0_g^- long-range state of $^{87}\mathrm{Rb}_2$”. *Eur. Phys. J. D*, Vol. 15, pp. 189–198, 2001.

[Flam 07] V. Flambaum and M. G. Kozlov. “Enhanced sensitivity to the time variation of the fine-structure constant and m_p/m_e in diatomic molecules”. *Phys. Rev. Lett.*, Vol. 99, p. 150801, 2007.

[Floq 83] G. Floquet. “Sur les quations diffrentielles linaires coefficients priodiques”. *Ann. cole Norm. Sup.*, Vol. 12, pp. 47–88, 1883.

[Foll 06] S. Fölling, A. Widera, T. Müller, F. Gerbier, and I. Bloch. “Formation of spatial shell structure in the superfluid to Mott insulator transition”. *Phys. Rev. Lett.*, Vol. 97, p. 060403, 2006.

[Gao 08] Y. Gao, S.-J. Xiong, and Y.-M. Zhong. “Floquet states and geometrical phase of a multi-level system in cyclic evolution”. *Phys. Lett. A*, Vol. 372, pp. 3071–3077, 2008.

[Grei 01] M. Greiner, I. Bloch, T. W. Hänsch, and T. Esslinger. “Magnetic transport of trapped cold atoms over a large distance”. *Phys. Rev. A*, Vol. 63, p. 031401, 2001.

[Grei 02] M. Greiner, O. Mandel, T. Esslinger, T. W. Hänsch, and I. Bloch. “Quantum phase transition from a superfluid to a Mott insulator in gas of ultracold atoms”. *Nature*, Vol. 415, pp. 39–44, 2002.

[Grei 03a] M. Greiner, C. A. Regal, and D. S. Jin. “Emergence of a molecular Bose-Einstein condensate from a Fermi gas”. *Nature*, Vol. 426, pp. 537–540, 2003.

[Grei 03b] M. Greiner. *Ultracold quantum gases in three-dimensional optical lattice potentials*. PhD thesis, Ludwig-Maximilians-Universität München, 2003.

[Grei 05] M. Greiner, C. A. Regal, and D. S. Jin. “Probing the excitation spectrum of a Fermi Gas in the BCS-BEC crossover regime”. *Phys. Rev. Lett.*, Vol. 94, p. 070403, 2005.

[Grim 00] R. Grimm, M. Weidemüller, and Y. B. Ovchinnikov. “Optical dipole traps for neutral atoms”. *Adv. At. Mol. Opt. Phys.*, Vol. 42, pp. 95–170, 2000.

[Hein 00] D. J. Heinzen, R. Wynar, P. D. Drummond, and K. Kheruntsyan. “Superchemistry: Dynamics of coupled atomic and molecular Bose-Einstein condensates”. *Phys. Rev. Lett.*, Vol. 84, pp. 5029–5033, 2000.

[Herb 03] J. Herbig, T. Kraemer, M. Mark, T. Weber, C. Chin, H.-C. Nägerl, and R. Grimm. “Preparation of a pure molecular quantum gas”. *Science*, Vol. 301, pp. 1510–1513, 2003.

[Hind 97] E. A. Hinds. “Testing time reversal symmetry using molecules”. *Phys. Scr.*, Vol. T70, pp. 34–41, 1997.

[Ho 83] T.-S. Ho, S. Chu, and J. V. Tietz. “Semiclassical many-mode Floquet theory”. *Chem. Phys. Lett.*, Vol. 96, pp. 464–471, 1983.

[Hsu 06] H. Hsu and L. E. Reichl. “Floquet-Bloch states, quasienergy bands, and high-order harmonic generation for single-walled Carbon nanotubes under intense laser fields”. *Phys. Rev. B*, Vol. 74, p. 115406, 2006.

[Huds 05] J. J. Hudson, H. T. Ashworth, P. C. Condylis, M. R. Tarbutt, B. E. Sauer, and E. A. Hinds. “Towards a new measurement of the electron’s dipole moment”. In: E. A. Hinds, E. Ferguson, and E. Riis, Eds., *Proceedings of the 17th International Conference on Laser Spectroscopy*, pp. 129–136, World Scientific Publ., Singapore, 2005.

[Ingr 56] D. J. E. Ingram. “Spectroscopy at radio and microwave frequencies”. *J. Electrochem. Soc.*, Vol. 103, pp. 124–125, 1956.

[Inou 98] S. Inouye, M. R. Andrews, J. Stenger, H.-J. Miesner, D. M. Stamper-Kurn, and W. Ketterle. “Observation of Feshbach resonances in a Bose-Einstein condensate”. *Nature*, Vol. 392, pp. 151–154, 1998.

[Jaks 02] D. Jaksch, V. Venturi, J. I. Cirac, C. J. Williams, and P. Zoller. “Creation of a molecular condensate by dynamically melting a Mott insulator”. *Phys. Rev. Lett.*, Vol. 89, p. 040402, Jul 2002.

[Jaks 98] D. Jaksch, C. Bruder, J. I. Cirac, C. W. Gardiner, and P. Zoller. “Cold bosonic atoms in optical lattices”. *Phys. Rev. Lett.*, Vol. 81, p. 3108, 1998.

[Jaks 99] D. Jaksch. *Bose-Einstein condensation and applications.* PhD thesis, Naturwissenschaftliche Fakultät der Leopold-Franzens-Universität Innsbruck, 1999.

[Joch 03] S. Jochim, M. Bartenstein, A. Altmeyer, G. Hendl, C. Chin, J. H. Denschlag, and R. Grimm. “Pure gas of optically trapped molecules created from fermionic atoms”. *Phys. Rev. Lett.*, Vol. 91, p. 240402, 2003.

[Jone 06] K. M. Jones, E. Tiesinga, P. D. Lett, and P. S. Julienne. “Ultracold photoassociation spectroscopy: Long-range molecules and atomic scattering”. *Rev. Mod. Phys.*, Vol. 78, p. 483, 2006.

[Kett 99] W. Ketterle, D. S. Durfee, and D. M. Stamper-Kurn. “Making, probing and understanding Bose-Einstein condensates”. In: M. Inguscio, S. Stringari, and C. E. Wieman, Eds., *Bose-Einstein Condensation in Atomic Gases*, IOS Press, 1999.

[Kins 05] I. Kinski. *Magnetic trapping apparatus and frequency stabilization of a ring cavity laser for Bose-Einstein condensation experiments.* Master’s thesis, Freie Universität Berlin, 2005.

[Knoo 09] S. Knoop, F. Ferlaino, M. Mark, M. Berninger, H. Schoebel, H.-C. Nägerl, and R. Grimm. “Observation of an Efimov-like resonance in ultracold atom-dimer scattering”. *Nat. Phys.*, Vol. 5, pp. 227–230, 2009.

[Koch 07] C. Koch. “Private communication”. 2007.

[Kohl 06] T. Köhler, K. Goral, and P. S. Julienne. “Production of cold molecules via magnetically tunable Feshbach resonances”. *Rev. Mod. Phys.*, Vol. 78, p. 1311, 2006.

[Kohn 73] W. Kohn. “Construction of Wannier functions and applications to energy bands”. *Phys. Rev. B*, Vol. 7, pp. 4388–4398, 1973.

[Krae 06] T. Kraemer, M. Mark, P. Waldburger, J. G. Danzl, C. Chin, B. Engeser, A. D. Lange, K. Pilch, A. Jaakkola, H.-C. Nägerl, and R. Grimm. “Evidence for Efimov quantum states in an ultracold gas of Caesium atoms”. *Nature*, Vol. 440, p. 315, 2006.

[Krem 08] R. V. Krems. “Cold controlled chemistry”. *Phys. Chem. Chem. Phys.*, Vol. 10, pp. 4079–4092, 2008.

[Lang 08a] F. Lang, P. v. d. Straten, B. Brandstätter, G. Thalhammer, K. Winkler, P. S. Julienne, R. Grimm, and J. H. Denschlag. “Cruising through molecular bound state manifolds with radio frequency”. *Nat. Phys.*, Vol. 4, p. 223, 2008.

[Lang 08b] F. Lang, K. Winkler, C. Strauss, R. Grimm, and J. H. Denschlag. “Ultracold molecules in the rovibrational triplet ground state”. *Phys. Rev. Lett.*, Vol. 101, p. 133005, 2008.

[Lang 09] F. Lang, C. Strauss, K. Winkler, T. Takekoshi, R. Grimm, and J. H. Denschlag. “Dark state experiments with ultracold, deeply-bound triplet molecules”. *Faraday Discuss.*, Vol. 142, pp. 1–12, 2009.

[Luit 96] O. J. Luiten, M. W. Reynolds, and J. T. M. Walraven. “Kinetic theory of the evaporative cooling of a trapped gas”. *Phys. Rev. A*, Vol. 53, pp. 381–389, 1996.

[Mark 07] M. Mark, T. Kraemer, P. Waldburger, J. Herbig, C. Chin, H.-C. Nägerl, and R. Grimm. “Stückelberg interferometry with ultracold molecules”. *Phys. Rev. Lett.*, Vol. 99, p. 113201, 2007.

[Mart 02] A. Marte, T. Volz, J. Schuster, S. Dürr, G. Rempe, E. G. M. v. Kempen, and B. J. Verhaar. “Feshbach resonances in Rubidium 87: Precision measurement and analysis”. *Phys. Rev. Lett.*, Vol. 89, p. 283202, 2002.

[Matt 99] M. R. Matthews, B. P. Anderson, P. C. Haljan, D. S. Hall, C. E. Wieman, and E. A. Cornell. “Vortices in a Bose-Einstein condensate”. *Phys. Rev. Lett.*, Vol. 83, p. 2498, 1999.

[Metc 02] H. J. Metcalf and P. van der Straten. *Laser cooling and trapping.* Springer, 2002.

[Mewe 97] M.-O. Mewes, M. R. Andrews, D. M. Kurn, D. S. Durfee, C. G. Townsend, and W. Ketterle. “Output coupler for Bose-Einstein condensed atoms”. *Phys. Rev. Lett.*, Vol. 78, p. 582, 1997.

[Mies 00] F. H. Mies, E. Tiesinga, and P. S. Julienne. “Manipulation of Feshbach resonances in ultracold atomic collisions using time-dependent magnetic fields”. *Phys. Rev. A*, Vol. 61, p. 022721, 2000.

[Ni 08] K.-K. Ni, S. Ospelkaus, M. H. G. de Miranda, A. Pe’er, B. Neyenhuis, J. J. Zirbel, S. Kotochigova, P. S. Julienne, D. S. Jin, and J. Ye. “A high phase-space-density gas of polar molecules”. *Science*, Vol. 322, p. 231, 2008.

[Ospe 06] C. Ospelkaus, S. Ospelkaus, L. Humbert, P. Ernst, K. Sengstock, and K. Bongs. "Ultracold heteronuclear molecules in a 3D optical lattice". *Phys. Rev. Lett.*, Vol. 97, p. 120402, 2006.

[Petr 04] D. S. Petrov, C. Salomon, and G. V. Shlyapnikov. "Weakly bound dimers of fermionic atoms". *Phys. Rev. Lett.*, Vol. 93, p. 090404, 2004.

[Potv 88] R. M. Potvliege and R. Shakeshaft. "Time-independent theory of multiphoton ionization of an atom by an intense field". *Phys. Rev. A*, Vol. 38, pp. 4597–4621, 1988.

[Rabi 38] I. I. Rabi, J. R. Zacharias, S. Millman, and P. Kusch. "A new method of measuring nuclear magnetic moment". *Phys. Rev.*, Vol. 53, p. 318, 1938.

[Rega 03] C. A. Regal, C. Ticknor, J. L. Bohn, and D. S. Jin. "Creation of ultracold molecules from a Fermi gas of atoms". *Nature*, Vol. 424, pp. 47–50, 2003.

[Rieg 05] T. Rieger, T. Junglen, S. Rangwala, P. Pinkse, and G. Rempe. "Continuous loading of an electrostatic trap for polar molecules". *Phys. Rev. Lett.*, Vol. 95, p. 173002, 2005.

[Robe 98] J. L. Roberts, N. R. Claussen, J. P. B. Jr., C. H. Greene, E. A. Cornell, and C. E. Wieman. "Resonant magnetic field control of elastic scattering in cold ^{85}Rb". *Phys. Rev. Lett.*, Vol. 81, pp. 5109–5112, 1998.

[Samb 73] H. Sambe. "Steady states and quasienergies of a quantum-mechanical system in an oscillating field". *Phys. Rev. A*, Vol. 7, pp. 2203–2213, 1973.

[Sant 00] L. Santos, G. V. Shlyapnikov, and P. Z. abd M. Lewenstein. "Bose-Einstein condensation in trapped dipolar gases". *Phys. Rev. Lett.*, Vol. 85, pp. 1791–1794, 2000.

[Schm 06] S. Schmid. *Long distance transport of ultracold atoms using a 1D optical lattice.* Master's thesis, Universität Innsbruck, 2006.

[Shir 65] J. Shirley. "Solution of the Schrödinger equation with a Hamiltonian periodic in time". *Phys. Rev.*, Vol. 138, pp. B979–B987, 1965.

[Staa 06] P. Staanum, S. D. Kraft, J. Lange, R. Wester, and M. Weidemller. "Experimental investigation of ultracold atom-molecule collisions". *Phys. Rev. Lett.*, Vol. 96, p. 023201, 2006.

[Syas 07] N. Syassen, D. M. Bauer, M. Lettner, D. Dietze, T. Volz, S. Duerr, and G. Rempe. "Atom-molecule Rabi oscillations in a Mott insulator". *Phys. Rev. Lett.*, Vol. 99, p. 033201, 2007.

[Thal 05] G. Thalhammer, M. Theis, K. Winkler, R. Grimm, and J. Hecker Denschlag. “Inducing an optical Feshbach resonance via stimulated Raman coupling”. *Phys. Rev. A*, Vol. 71, p. 033403, 2005.

[Thal 06] G. Thalhammer, K. Winkler, F. Lang, S. Schmid, R. Grimm, and J. H. Denschlag. “Long-lived Feshbach molecules in a threedimensional optical lattice”. *Phys. Rev. Lett.*, Vol. 96, p. 050402, 2006.

[Thal 07] G. Thalhammer. *Ultrakalte gepaarte Atome in kohärenten Lichtfeldern*. PhD thesis, Universität Innsbruck, 2007.

[Thei 04] M. Theis, G. Thalhammer, K. Winkler, M. Hellwig, G. Ruff, R. Grimm, and J. Hecker Denschlag. “Tuning the scattering length with an optically induced Feshbach resonance”. *Phys. Rev. Lett.*, Vol. 93, p. 123001, 2004.

[Thei 05] M. Theis. *Optical Feshbach resonances in a Bose-Einstein condensate*. PhD thesis, Universität Innsbruck, 2005.

[Thom 05] S. T. Thompson, E. Hodby, and C. E. Wieman. “Ultracold molecule production via a resonant oscillating magnetic field”. *Phys. Rev. Lett.*, Vol. 95, p. 190404, 2005.

[Tiem 08] E. Tiemann. “Private communication”. 2008.

[Ties 98] E. Tiesinga, C. J. Williams, and P. S. Julienne. “Photoassociative spectroscopy of highly excited vibrational levels of alkali dimers: Green function approach for eigenvalue solvers”. *Phys. Rev. A*, Vol. 57, pp. 4257–4267, 1998.

[Vita 01] N. V. Vitanov, T. Halfmann, B. Shore, and K. Bergmann. “Laser-induced population transfer by adiabatic passage techniques”. *Annu. Rev. Phys. Chem.*, Vol. 52, pp. 763–809, 2001.

[Vita 96] N. V. Vitanov and B. M. Garraway. “Landau Zener model: Effects of finite coupling duration”. *Phys. Rev. A*, Vol. 53, pp. 4288–4304, 1996.

[Vite 08] M. Viteau, A. Chotia, M. Allegrini, N. Bouloufa, O. Dulieu, D. Comparat, and P. Pillet. “Optical pumping and vibrational cooling of molecules”. *Science*, Vol. 321, p. 232, 2008.

[Volz 03] T. Volz, S. Dürr, S. Ernst, A. Marte, and G. Rempe. “Characterization of elastic scattering near a Feshbach resonance in ^{87}Rb”. *Phys. Rev. A*, Vol. 68, p. 010702, 2003.

[Wall 94] D. F. Walls and G. J. Milburn. *Quantum optics*. Springer-Verlag, Berlin, 1994.

[Wein 98] J. D. Weinstein, R. deCarvalho, T. Guillet, B. Friedrich, and J. M. Doyle. "Magnetic trapping of Calcium monohydride molecules at millikelvin temperatures". *Nature*, Vol. 395, p. 148, 1998.

[Wink 02] K. Winkler. *Aufbau einer magnetischen Transportapparatur für ultrakalte Atome*. Master's thesis, Universität Innsbruck, 2002.

[Wink 07a] K. Winkler, F. Lang, G. Thalhammer, P. v. d. Straten, R. Grimm, and J. H. Denschlag. "Coherent optical transfer of Feshbach molecules to a lower vibrational state". *Phys. Rev. Lett.*, Vol. 98, p. 043201, 2007.

[Wink 07b] K. Winkler. *Ultracold molecules and atom pairs in optical lattice potentials*. PhD thesis, Universität Innsbruck, 2007.

[Xu 03] K. Xu, T. Mukaiyama, J. R. Abo-Shaeer, J. K. Chin, D. E. Miller, and W. Ketterle. "Formation of quantum-degenerate Sodium molecules". *Phys. Rev. Lett.*, Vol. 91, p. 210402, 2003.

[Zahz 06] N. Zahzam, T. Vogt, M. Mudrich, D. Comparat, and P. Pillet. "Atom-molecule collisions in an optically trapped gas". *Phys. Rev. Lett.*, Vol. 96, p. 023202, 2006.

[Zele 08] T. Zelevinsky, S. Kotochigova, and J. Ye. "Precision test of mass-ratio variations with lattice-confined ultracold molecules". *Phys. Rev. Lett.*, Vol. 100, p. 043201, 2008.

[Zwie 03] M. W. Zwierlein, C. A. Stan, C. H. Schunck, S. M. F. Raupach, S. Gupta, Z. Hadzibabic, and W. Ketterle. "Observation of Bose-Einstein condensation of molecules". *Phys. Rev. Lett.*, Vol. 91, p. 250401, 2003.

Danksagung

An dieser Stelle möchte ich mich bei allen bedanken, die zum Gelingen meiner Doktorarbeit beigetragen haben: Johannes Hecker Denschlag, unter dessen ausgezeichneter Betreuung ich diese Arbeit absolvieren konnte. Sein physikalischen Gespür und sein für Fragen und Anliegen stets offenes Ohr haben wesentlich zum Gelingen dieses Projektes beigetragen. Ebenso bei Rudi Grimm, der die Gruppe mit ausserordentlichem Einsatz und großem Weitblick leitet, und so ihren weltweiten Ruf etabliert hat.

Besonderer Dank gilt auch Klaus, Gregor und Matthias, meinen Vorgängern als Doktoranden am Rubidium-Projekt. Von ihnen konnte ich unglaublich viel lernen, und mich stets auf ihre Hilfe und Unterstützung verlassen. Meinem Nachfolger Christoph, der die Geschicke des Experimentes zukünftig in Ulm weiterführen wird, sowie den früheren Diplomanden Stefan, Birgit, Sascha und Christian, die mit vollem Einsatz am Erfolg des Projektes mitgebarbeitet haben. Danken möchte ich auch Russel und speziell Tetsu für das sorgfältige Korrekturlesen dieser Arbeit, und für lehrreiche Diskussionen über die Subtilitäten der englischen Sprache. Den "Barbies" Stefan (trotz seines Fremdgehens), Arne und Albert, sowie all den anderen Gruppenmitgliedern - vielen Dank euch allen für die zahlreichen unterhaltsamen Stunden inner- und außerhalb des Labors!

Ebenfalls Dank gebührt Peter van der Straten und Herman Batelaan, die in ihrer Zeit als Gastprofessoren wertvolle Hilfe geleistet haben. All die hehre Wissenschaft wäre jedoch ohne die Unterstützung durch die Sekretariate und Wertstätten undenkbar - ein großes Dankeschön ergeht deshalb an Christine, Karin, Gabriel, Nicole und Patricia, sowie Toni, Helmut, Josef, Manuel und Arthur.

Zu guter Letzt, dafür aber mit besonderer Herzlichkeit möchte ich mich bei meinen Eltern, die mir diese Ausbildung ermöglicht haben, sowie meiner Schwester und meinen Freunden bedanken. Sie haben in all den Jahren dafür gesorgt, daß neben der Physik auch der Kontakt zum "richtigen" Leben nicht ganz verloren ging...